



**INVESTIGATION OF  
FLAW GEOMETRY AND LOADING EFFECTS  
ON PLANE STRAIN FRACTURE  
IN METALLIC STRUCTURES**

**CASE FILE  
COPY**

*By*

*L. R. Hall and R. W. Finger*

THE **BOEING** COMPANY

*Prepared For*

NATIONAL AERONAUTICS AND SPACE ADMINISTRATION

NASA LEWIS RESEARCH CENTER

Contract NAS3-12016

Gordon T. Smith, Project Manager

#### NOTICE

This report was prepared as an account of Government sponsored work. Neither the United States, nor the National Aeronautics and Space Administration (NASA), nor any person acting on behalf of NASA:

- A.) Makes any warranty or representation, expressed or implied, with respect to the accuracy, completeness, or usefulness of the information contained in this report, or that the use of any information, apparatus, method, or process disclosed in this report may not infringe privately owned rights; or
- B.) Assumes any liabilities with respect to the use of, or for damages resulting from the use of any information, apparatus, method or process disclosed in this report.

As used above, "person acting on behalf of NASA" includes any employee or contractor of NASA, or employee of such contractor, to the extent that such employee or contractor of NASA, or employee of such contractor prepares, disseminates, or provides access to, any information pursuant to his employment or contract with NASA, or his employment with such contractor.

Requests for copies of this report should be referred to

National Aeronautics and Space Administration  
Office of Scientific and Technical Information  
Attention: AFSS-A  
Washington, D.C. 20546

Final Report

INVESTIGATION OF FLAW GEOMETRY AND LOADING EFFECTS  
ON PLANE STRAIN FRACTURE IN METALLIC STRUCTURES

by

L. R. Hall and R. W. Finger

Research and Engineering Division  
THE BOEING COMPANY  
Seattle, Washington

Prepared for

NATIONAL AERONAUTICS AND SPACE ADMINISTRATION

December 18, 1971

Contract NAS 3-12016

NASA Lewis Research Center  
Cleveland, Ohio

Gordon T. Smith, Project Manager

## PREFACE

This report describes an investigation of fracture and flaw growth in cryogenic tank materials performed by The Boeing Company from July 1968 to March 1970 under Contract NAS 3-12016. The work was administered by Mr. Gordon T. Smith of the NASA Lewis Research Center.

Boeing personnel who participated in the investigation include J. N. Masters, project leader; L. R. Hall, principal investigator; R. C. Shah and R. W. Finger, research engineers. Program support was provided by A. A. Ottlyk, non-hazardous testing; H. M. Olden, C. C. Mahnken and G. E. Vermilion, liquid hydrogen testing; L. Albertin, titanium welding; C. W. Bosworth, aluminum welding; A. L. Esquirel, residual stress measurements; C. R. Pond, holography; E. C. Roberts, R. E. Regan and R. E. Smith, metallurgical support; and D. G. Good, technical illustrations and art work.



# INVESTIGATION OF FLAW GEOMETRY AND LOADING EFFECTS ON PLANE STRAIN FRACTURE IN METALLIC STRUCTURES

by

L. R. Hall and R. W. Finger

## ABSTRACT

This experimental program evaluated effects on fracture and flaw growth of weld-induced residual stresses, combined bending and tension stresses, and stress fields adjacent to circular holes in 2219-T87 aluminum and 5Al-2.5Sn(ELI) titanium alloys. Static fracture tests were conducted in liquid nitrogen; fatigue tests were performed in room air, liquid nitrogen and liquid hydrogen. Evaluation of results was based on linear elastic fracture mechanics concepts and was directed to improving existing methods of estimating minimum fracture strength and fatigue lives for pressurized structure in spacecraft and booster systems.

Effects of specimen design in plane-strain fracture toughness testing were investigated. Four different specimen types were tested in room air, liquid nitrogen and liquid hydrogen environments using 2219-T87 aluminum and 5Al-2.5Sn(ELI) titanium alloys. Interferometry and holograph were used to measure crack-opening displacements in surface-flawed plexiglass test specimens. Comparisons were made between stress intensities calculated using displacement measurements, and approximate analytical solutions.

## CONTENTS

	<u>PAGE</u>
ABSTRACT	iv
SYMBOLS	vii
SUMMARY	1
1.0 INTRODUCTION	3
2.0 BACKGROUND	5
3.0 MATERIALS AND PROCEDURES	9
3.1 Materials	9
3.2 Procedures	10
4.0 FRACTURE AT FLAWS PROTRUDING FROM CIRCULAR HOLES	13
4.1 Results	14
4.2 Analysis	15
4.2.1 Static Fracture Tests	15
4.2.2 Fatigue Tests	17
4.3 Summary	18
5.0 FRACTURE AT SURFACE FLAWS SUBJECTED TO COMBINED BENDING AND TENSION STRESSES	21
5.1 Background	21
5.2 Test Program	22
5.3 Description and Analysis of Results	23
5.3.1 Specimen Calibration	23
5.3.2 Static Fracture Tests	23
5.3.3 Fatigue Tests	24
6.0 INFLUENCE OF SPECIMEN DESIGN IN PLANE STRAIN FRACTURE TOUGHNESS TESTING	27
6.1 Procedures	28
6.1.1 Specimen Configuration Effect Tests	28
6.1.2 Specimen Thickness Effect Tests	30
6.2 Results and Discussion	31
6.2.1 Specimen Configuration Effect Tests	31
6.2.2 Specimen Thickness Effect Tests	34
6.3 Summary and Recommendation	36

	<u>PAGE</u>
7.0 FRACTURE AT FLAWS IN RESIDUAL STRESS FIELDS	39
7.1 Background	39
7.2 Analysis	43
7.3 Test Program and Procedures	45
7.3.1 Static Fracture Tests	46
7.3.2 Fatigue Tests	49
7.4 Description and Interpretation of Results	49
7.4.1 Titanium Alloy Static Fracture Tests	49
7.4.2 Aluminum Alloy Static Fracture Tests	54
7.4.3 Titanium Alloy Fatigue Tests	56
7.4.4 Aluminum Alloy Fatigue Tests	57
8.0 EXPERIMENTAL STRESS INTENSITY ANALYSIS	59
8.1 Holographic Technique	59
8.2 Procedures	61
8.3 Results	62
REFERENCES	65
APPENDIX A - WELDING PROCEDURES	69
Procedures for One-Inch-Thick 2219-T87 Aluminum	69
Procedures for Internally Flawed One-Inch-Thick 2219-T87 Aluminum	69
Procedures for Three-Eighths-Inch Thick 5Al-2.5Sn(ELI) Titanium	70
APPENDIX B - CONVERSION OF U.S. CUSTOMARY UNITS TO SI UNITS	73

## SYMBOLS

$K_I$	Opening mode stress intensity factor
$K_{Ii}$	Opening mode stress intensity factor at initial conditions
$K_{IE}$	Critical stress intensity or plane strain fracture toughness for surface flaws
$K_{Ic}$	Plane strain fracture toughness determined according to ASTM E399-70T
$K_Q$	Fracture toughness value determined per ASTM E399-70T except for crack length and specimen thickness requirements
$K_f$	Stress intensity used to fatigue crack a precracked test specimen
$a$	Crack depth of semi-elliptical surface flaw or semi-minor axis of ellipse $x^2/c^2 + y^2/a^2 = 1$
$2c$	Crack length of semi-elliptical surface flaw
$\Phi$	Complete elliptical integral of the second kind corresponding to modules $k = [(c^2 - a^2)/c^2]^{1/2}$
$\sigma$	Uniform tensile stress acting perpendicular to the plane of a crack.
$\sigma_R$	Residual stress
$\sigma_P$	Load stress
$\sigma_{ys}$	Uniaxial tensile yield stress
$Q$	$\Phi^2 - 0.212 (\sigma/\sigma_{ys})^2$
$E$	Young's modulus
$\mu$	Poisson's ratio
$r$	Radius of circular hole
$t$	Thickness of test specimen at the flaw plane
$W$	Width of test specimen at flaw plane
$c_e$	Effective flaw length for quarter-elliptically shaped flaws originating at circular holes
$M_B$	Scalar factor depending on $a/t$ and $a/2c$ used in stress intensity expression for surface flaws subjected to bending stress
$M_K$	Scalar factor depending on $a/t$ and $a/2c$ used to account for effect of stress free back specimen surface on stress intensity expression for surface flaws
$M_F$	Scalar factor depending on $a/2c$ used to account for effect of stress free front specimen surface on stress intensity for surface flaws

## LIST OF FIGURES

<u>No.</u>	<u>Title</u>	<u>Page</u>
2-1	Shape Parameter Curves For Surface And Internal Flaws	75
2-2	$M_K$ Curves For 5Al-2.5Sn(ELI) Titanium Alloy	76
2-3	$M_K$ Curves For 2219-T87 Aluminum Alloy	76
2-4	Effect Of Surface Flaw Size On Failure Stress For 5Al-2.5Sn (ELI) Titanium Alloy At -320°F	77
2-5	Cyclic Life Data For 2219-T87 Aluminum Surface-Flawed Specimens (Reference 1)	78
2-6	Cyclic Life Data For 5Al-2.5Sn(ELI) Titanium Surface-Flawed Specimens (Reference 1)	79
3-1	Microstructure Of Mill Annealed 0.375-Inch Thick 5Al-2.5Sn (ELI) Titanium Plate	80
3-2	Layered Microstructure Observed In Mill Annealed 5Al-2.5Sn (ELI) Titanium (0.375-Inch (9.53 mm) Thick Plate)	81
3-3	Microstructural Changes Resulting From Annealing 5Al-2.5Sn (ELI) Titanium 0.375-Inch (9.53mm) Thick Plate	82
3-4	Microstructure Of Mill Annealed 0.80-Inch (20.3 mm) Thick 5Al-2.5Sn(ELI) Titanium Plate	83
3-5	Microstructural Changes At Center Of 0.80-Inch (20.3 mm) Thick 5Al-2.5Sn(ELI) Titanium Plate Due To Various Annealing Cycles	84
3-6	Tensile Specimen For Mechanical Property Measurements (Used For 2219-T87 Aluminum Parent and Weld Metal, 5Al-2.5Sn(ELI) Titanium Parent Metal, and Plexiglas)	85
3-7	All Weld Metal Tensile Specimen For Mechanical Property Measurements Of Titanium Welds	85
4-1	Geometry For Specimens With Flaws Protruding From Holes	86
4-2	Gross Failure Stresses As A Function Of Test Variables For Specimens With Flaws Protruding From Holes	87
4-3	Effect of Hole Diameter On Failure Stress For Specimens With Flaws Protruding From Holes	88
4-4	Fracture Faces Of Specimens Containing Flaws Protruding From Holes	89
4-5	Plots Of $\sigma \sqrt{a}$ VS (a/c) For Specimens With Flaws Protruding From Holes	90

## LIST OF FIGURES (Cont.)

<u>No.</u>	<u>Title</u>	<u>Page</u>
4-6	Plots of $\sigma \sqrt{a}$ VS Flaw Length to Hole Size Ratios for Titanium Specimens With Flaws Protruding From Holes	91
4-7	Plots of $\sigma \sqrt{a}$ VS Flaw Length to Hole Size Ratios for Aluminum Specimens With Flaws Protruding From Holes	92
4-8	Failure Criterion for Flaws Protruding From Holes	93
4-9	Comparison of Failure Criteria for Through-the Thickness and Embedded Flaws Protruding From Holes	94
4-10	F(c/r) in Failure Criterion for Flaws Protruding From Holes (Reference 12)	95
4-11	Values of Effective Flaw Length for Embedded Flaws Protruding From Holes	96
4-12	Fatigue Data for 2219-T87 Aluminum Specimens with Flaws Protruding From Circular Holes	97
4-13	Fatigue Data for 5Al-2.5Sn(ELI) Titanium Specimens with Flaws Protruding From Holes	98
5-1	Stress Intensity for Surface-Flawed Plates Subjected to Bending Stresses	99
5-2	Specimen Configuration for Combined Bending/Tension Tests	100
5-3	Instrumentation for Calibrating Combined Bending/Tension Specimens	101
5-4	Load-Bending Stress Calibrations for Combined Bending and Tension Specimens	102
5-5	Fracture Face of Surface-Flawed Specimen Fatigue Tested Under Combined Bending and Tension Stresses	103
5-6	Fatigue Data for 2219-T87 Aluminum Surface-Flawed Specimens Subjected to Combined Bending/Tension Stresses or Pure Tensile Stresses	104
5-7	Fatigue Data for 5Al-2.5Sn(ELI) Titanium Surface-Flawed Specimens Subjected to Combined Bending/Tension Stresses or Pure Tensile Stresses	105
6-1	Specimen Location Within Plate	106
6-2	Details of SENB, SENT and CT Specimens	107
6-3	Specimen Dimensions for SF Specimens Used in Configuration Effect Tests	108

## LIST OF FIGURES (Cont.)

<u>No.</u>	<u>Title</u>	<u>Page</u>
6-4	Crack Starter Details for SENB, SENT and CT Specimens	109
6-5	Fracture Faces of Test Specimens	110
6-6	Stress Intensity Expressions for SENB, SENT and CT Specimens	111
6-7	Specimen Configurations for Thickness Effect Tests	112
6-8	Test Records for Single-Edge-Notched-Tension Specimens	113
6-9	Test Records for Single-Edge-Notched-Bend Specimens	114
6-10	Test Records for Compact Tension Specimens	115
6-11	Test Records for Surface-Flawed Specimens	116
6-12	Plane Strain Fracture Toughness Data for 2219-T87 Aluminum and 5Al-2.5Sn(ELI) Titanium	117
6-13	Microstructural Indications of Thickness and Rolling Direction in 2219-T87 Aluminum CT Specimens	118
6-14	Fracture Data for 2219-T87 Aluminum Base Metal (Varied Thickness Surface-Flawed Specimen Tests)	119
6-15	Fracture Data for 5Al-2.5Sn(ELI) Titanium Base Metal (Varied Thickness Surface-Flawed Specimen Tests)	120
7-1	Typical Residual Stress Distribution in Flat Butt Welded Steel Plates (Reference 19)	121
7-2	Distribution of Yield Strength and Longitudinal Residual Stresses in a Welded 5456-H321 Plate (Reference 20)	122
7-3	Longitudinal and Transverse Residual Stresses in As-Welded Ti-5Al-2.5Sn Panels (Reference 23)	122
7-4	Effects of Sharp Notch and Residual Stress on Fracture Strength of Steel Welds (Reference 29)	123
7-5	Crack Tip Stress Intensity Values for Butt Welded Specimens (Reference 33)	124
7-6	Illustrative Example of the Application of Fracture Mechanics to Analysis of Crack Stability in a Butt Welded Plate	125
7-7	Production Sequences for Residual Stress Test Series I and II	126
7-8	EB Welding for 5Al-2.5Sn(ELI) Titanium Test Series I and II	127
7-9	Residual Stress Measurements for 5Al-2.5Sn(ELI) Titanium Alloy Test Series I and II	128
7-10	5Al-2.5Sn(ELI) Titanium Test Specimen for Residual Stress Test Series III	129

## LIST OF FIGURES (Cont.)

<u>No.</u>	<u>Title</u>	<u>Page</u>
7-11	Residual Stress Measurements for 5Al-2.5Sn(ELI) Titanium Alloy Test Series III	130
7-12	EB Welding for 2219-T87 Aluminum Residual Stress Test Series I and II	131
7-13	Residual Stresses at Surfaces of 2219-T87 Aluminum Series I Test Specimens	132
7-14	Residual Stresses at Surfaces of 2219-T87 Aluminum Series II Test Specimens	133
7-15	Internally Flawed 2219-T87 Aluminum Weld Panels	134
7-16	EB Welding of 2219-T87 Aluminum Internally Flawed Residual Stress Specimens	135
7-17	Effect of Residual Stress on Gross Failure Stress for 5Al-2.5Sn(ELI) Titanium Test Series I and II	136
7-18	Gross Failure Stresses for 5Al-2.5Sn(ELI) Titanium Test Series III	137
7-19	Test Specimen Used for Evaluating Effect of Thermal Cycles on Fracture Toughness of 5Al-2.5Sn(ELI) Titanium Weld Centerlines	138
7-20	Crack Displacement VS Load Test Records for 5Al-2.5Sn(ELI) Titanium GTA Weld Centerlines in SENT Specimens	139
7-21	Crack Displacement VS Load Test Records for Surface Flaws at 1-Inch-Thick 2219 Aluminum GTA Weld Centerlines	140
8-1	Schematic Representation of Holographic Test Setup	141
8-2	Plexiglas Test Specimens	142
8-3	2000 Pound Load Fixture for Laser Experiment	143
8-4	Schematic Representation of Results	144
8-5	Crack-Opening Displacements Along Semi-Minor Axis of First Plexiglas Surface-Flawed Specimen	145
8-6	Crack-Opening Displacements Along Semi-Minor Axis of Second Plexiglas Surface-Flawed Specimen	146
8-7	Crack-Opening Displacements Along Semi-Minor Axis of Third Plexiglas Surface-Flawed Specimen	147
A-1	Weld Panels for 5Al-2.5Sn(ELI) Titanium Specimens	148



## LIST OF TABLES

<u>No.</u>	<u>Title</u>	<u>Page</u>
3-1	Chemical Composition of Materials	149
3-2	Mechanical Properties for 2219-T87 Aluminum Parent Metal and Weld Metal	150
3-3	Mechanical Properties for 5Al-2.5Sn(ELI) Titanium Parent Metal and Weld Metal	151
3-4	Summary of 5Al-2.5Sn(ELI) Titanium Processing Details	152
3-5	Mechanical Properties of Cast Acrylic Material	153
4-1	Test Program for Evaluating Fracture at Flaws Protruding from Circular Holes	154
4-2	Fracture Data for 2219-T87 Aluminum with Flaws Protruding from Holes ( $2r/t = 0.5$ )	155
4-3	Fracture Data for 2219-T87 Aluminum with Flaws Protruding from Holes ( $2r/t = 1.0$ )	156
4-4	Fracture Data for 5Al-2.5Sn(ELI) Titanium with Flaws Protruding from Holes ( $2r/t = 0.5$ )	157
4-5	Fracture Data for 5Al-2.5Sn(ELI) Titanium with Flaws Protruding from Holes ( $2r/t = 1.0$ )	158
4-6	Fatigue Data for Specimens Containing Flaws Protruding from Holes	159
4-7	Fracture Toughness Test Results for Materials Used in Fracture Tests of Specimens with Flaws Protruding From Holes	160
4-8	Summary of Calculated Parameters Used to Estimate Cyclic Life for Specimens with Flaws Protruding from Holes	161
5-1	Combined Bending and Tension Stress Test Program	162
5-2	Test Results for Surface-Flawed Specimens Subjected to Combined Bending and Tension Stresses	163
5-3	Evaluation of Test Results for Surface-Flawed Specimens Subjected to Combined Bending and Tension Stresses	164
5-4	Results for Fatigue Tests of Surface-Flawed Specimens Subjected to Combined Bending and Tension Stresses	165
6-1	Test Program	166
6-2	Fracture Toughness Test Results for 2219-T87 Aluminum (SENB, SENT and CT Specimens)	167
6-3	Fracture Toughness Test Results for 5Al-2.5Sn(ELI) Titanium (SENB, SENT and CT Specimens)	168

## LIST OF TABLES (Cont.)

<u>No.</u>	<u>Title</u>	<u>Page</u>
6-4	Fracture Toughness Test Results for 2219-T87 Aluminum (SF Specimens)	169
6-5	Fracture Toughness Test Results for 5Al-2.5Sn(ELI) Titanium (SF Specimens)	169
6-6	Results for Fracture Tests of 2219-T87 Aluminum Surface-Flawed Specimens Tested at 72°F in Room Air (Specimen Thickness & Flaw Shape Varied)	170
6-7	Results for Fracture Tests of 2219-T87 Aluminum Surface-Flawed Specimens Tested at -320°F in LN <sub>2</sub> (Specimen Thickness & Flaw Shape Varied)	170
6-8	Results for Fracture Tests of 2219-T87 Aluminum Surface-Flawed Specimens Tested at -423°F in LH <sub>2</sub> (Specimen Thickness & Flaw Shape Varied)	171
6-9	Results for Fracture Tests of Mill Annealed 5Al-2.5Sn(ELI) Titanium Surface-Flawed Specimens Tested at -320°F in LN <sub>2</sub> (Specimen Thickness & Flaw Shape Varied)	171
6-10	Results for Fracture Tests of Re-Annealed 5Al-2.5Sn(ELI) Titanium Surface-Flawed Specimens Tested at -320°F in LN <sub>2</sub> (Specimen Thickness & Flaw Shape Varied)	172
6-11	Results for Fracture Tests of Re-Annealed 5Al-2.5Sn(ELI) Titanium Surface-Flawed Specimens Tested at -423°F in LH <sub>2</sub> (Specimen Thickness & Flaw Shape Varied)	172
7-1	Test Program for Evaluating Residual Stress Effects in 5Al-2.5Sn(ELI) Titanium	173
7-2	Test Program for Evaluating Residual Stress Effects in 2219-T87 Aluminum	173
7-3	Test Program for Evaluating Residual Stress Effects on Cyclic Flaw Growth Rates	174
7-4	Test Results for 5Al-2.5Sn(ELI) Titanium Residual Stress Test Series I	175
7-5	Test Results for 5Al-2.5Sn(ELI) Titanium Residual Stress Test Series II	176
7-6	Test Results for 5Al-2.5Sn(ELI) Titanium Residual Stress Test Series III	177
7-7	Fracture Test Results for 5Al-2.5Sn(ELI) Titanium GTA Weld Centerlines Subjected to Various Thermal Cycles	178
7-8	Results for 2219-T87 Aluminum Residual Stress Test Series I (Surface-Flawed Specimens Fractured at -320°F in LN <sub>2</sub> )	179
7-9	Results for 2219-T87 Aluminum Residual Stress Test Series II (Surface-Flawed Specimens Fractured at -320°F in LN <sub>2</sub> )	180

LIST OF TABLES (Cont.)

<u>No.</u>	<u>Title</u>	<u>Page</u>
7-10	Results for 2219-T87 Aluminum Residual Stress Test Series III (Internally Flawed Welds Fractured at $-320^{\circ}\text{F}$ in $\text{LN}_2$ )	181
7-11	Results for Cyclic Tests of 5Al-2.5Sn(ELI) Titanium Specimens Containing Residual Stresses	182
7-12	Evaluation of Cyclic Flaw Growth Data for 5Al-2.5Sn(ELI) Titanium Surface-Flawed Specimens Containing Residual Stresses	183
7-13	Results for Cyclic Tests of 2219-T87 Aluminum Specimens Containing Residual Stresses	184

## SUMMARY

This experimental program was undertaken to refine existing methods of estimating minimum performance capabilities of cryogenic pressure vessels and other medium to high strength metallic structure. Performance estimates reflect the knowledge that crack-like defects in fabricated structure can grow during service use to a size sufficiently large to initiate failure, and are based on fracture strength and subcritical flaw growth data from tests of precracked test specimens.

The two alloys selected for testing (2219-T87 aluminum and 5Al-2.5Sn(ELI) titanium) are primary candidates for cryogenic pressure vessel applications and have been previously used to develop fracture and flaw growth data at cryogenic temperatures. Previous data were developed by testing precracked specimens under uniform tension stress fields acting perpendicular to the plane of the crack. However, potential fracture origins are often subjected to stress fields influenced by weld residual stresses, weld land buildups, and circular holes. Hence, the major part of this investigation was devoted to tests of surface-flawed specimens containing residual stresses or simulated weld land buildups, and specimens containing partially embedded cracks originating at circular holes. Both static fracture and fatigue tests were performed under zero-to-tension loading profiles; fracture tests were performed in liquid nitrogen; fatigue tests were conducted in room air, liquid nitrogen and liquid hydrogen environments. Methods of estimating fracture strength were developed using linear elastic fracture mechanics concepts. Data obtained from fatigue tests were insufficient to fully characterize the effect of weld residual stresses, weld loads, and circular holes on subcritical crack growth. However, approximate methods for estimating fatigue strength are suggested.

Effects of specimen configuration in plane strain fracture toughness testing were evaluated by testing single-edge-notched-bend (SENB), single-edge-notched-tension (SENT), compact tension (CT), and surface-flawed (SF) specimens. Fracture toughness values were compared at ambient,  $-320^{\circ}\text{F}$  and  $-423^{\circ}\text{F}$

temperatures for both 2219-T87 aluminum and 5Al-2.5Sn(ELI) titanium alloys. For the aluminum alloy, good agreement was obtained between fracture toughness values obtained from tests of SENB, SENT and SF specimens at all three test temperatures; CT specimens yielded consistently lower fracture toughness values than did the other three types of specimens. For the titanium alloy, fracture toughness values from tests of SF specimens fell in the central region of the scatter band of results for the other specimens at  $-423^{\circ}\text{F}$ , and above the scatter band at  $-320^{\circ}\text{F}$ . Room temperature tests were invalidated by inadequate specimen size.

The influence of surface-flawed specimen thickness on fracture toughness were evaluated at room temperature,  $-320^{\circ}\text{F}$  and  $-423^{\circ}\text{F}$  for the 2219-T87 aluminum alloy, and at  $-320^{\circ}\text{F}$  and  $-423^{\circ}\text{F}$  for the 5Al-2.5Sn(ELI) titanium alloy. When fracture toughness calculations were based on the assumption that negligible flaw growth preceded the onset of unstable flaw propagation, consistent fracture toughness values were obtained from specimens with thicknesses greater than  $(K_{IE}/\sigma_{ys})^2$  where  $K_{IE}$  is the fracture toughness and  $\sigma_{ys}$  is the uniaxial yield strength of the material.

An attempt was made to develop experimental stress intensity analysis techniques based on measurement of crack opening displacement in the immediate vicinity of a crack tip. Crack-tip displacements were measured in three plexiglass surface-flawed specimens using both interferometry and holography. Measured displacements were approximately 50 percent of displacements calculated using approximate analytical solutions. Despite this discrepancy, it is believed that this experimental technique can be developed into a useful method of determining stress intensity with additional refinement of experimental procedures.

## 1.0 INTRODUCTION

Failures in aerospace hardware have originated at undetected crack-like flaws that enlarged during service use under the influence of loads and environment. Accordingly, methods have been developed for estimating minimum performance capabilities of medium-to-high strength metallic structure that makes use of crack growth and fracture data derived from tests of precracked specimens.

Tests of surface-flawed specimens provide representative data concerning the effects of loads and environment on crack growth in aerospace structure. Surface flaws are commonly found in aerospace hardware, and are subjected to plane strain deformations that result in minimum fracture toughness and minimum resistance to stress corrosion cracking. A second flaw geometry of practical interest is the partially embedded flaw originating at a bolt hole. If the parent structure is sufficiently thick, such flaws can grow under plane strain conditions and initiate failure prior to growing through the section thickness.

This experimental program was undertaken to refine existing methods of estimating minimum performance capabilities of cryogenic pressure vessels and other medium to high strength metallic structure. The two alloys selected for testing (2219-T87 aluminum and 5Al-2.5Sn(ELI) titanium) are primary candidates for cryogenic pressure vessel applications and have been previously tested (1-5)\* to develop fracture and subcritical flaw growth data at cryogenic temperatures. The previous programs have emphasized testing surface-flawed specimens under uniform tension stress fields. However, potential fracture origins are often subjected to stress fields influenced by weld residual stresses, weld land buildups, and circular holes. Hence, the major part of this investigation was devoted to tests of surface-flawed specimens containing residual stresses or simulated weld land buildups, and specimens containing partially embedded cracks originating at circular holes. Both static fracture and fatigue tests were performed under

---

\* Numbers in parentheses refer to references at end of report.

zero-to-tension loading profiles; fracture tests were performed in a liquid nitrogen environment; fatigue tests were conducted in room air, liquid nitrogen and liquid hydrogen environments.

There is in existence a considerable body of plane strain fracture toughness data derived from the testing of several different specimen configurations. However, there has been no systematic comparison of fracture toughness values determined from the testing of through-cracked and surface-flawed specimens. To this end, single-edge-notched-bend, single-edge-notched-tension, compact tension, and surface-flawed specimens were tested. Fracture toughness values were compared at 72°F, -320°F and -423°F temperatures for both 2219-T87 aluminum and 5Al-2.5Sn (ELI) titanium alloys. The influence of surface-flawed specimen thickness on fracture toughness was also investigated at room temperature, -320°F, and -423°F for the same two alloys.

An attempt was made to develop experimental stress intensity analysis techniques based on measurements of crack-opening displacement in the immediate vicinity of a crack tip. Crack tip displacements were measured in three plexiglass surface-flawed specimens using both interferometry and holography.

The experimental approach was emphasized in the program because of the lack of applicable analytical solutions. Whenever possible, analytical solutions were checked for validity or were used to gain insight regarding possible methods of data correlation. Considerable use was made of linear elastic fracture mechanics in the evaluation of the experimental results; in particular, extensive use was made of the stress intensity parameter in the design and analysis of the various test programs.

## 2.0 BACKGROUND

The surface flaw is an excellent model of actual failure origins in many metallic structures. Consequently, surface-flawed specimens have been tested to develop data for use in failure analyses and fracture prevention of metallic hardware. Most surface-flawed data have been evaluated and correlated in terms of the opening mode stress intensity parameter defined by linear elastic fracture mechanics. Some background information relating to stress intensity analyses for surface flaws and experimental results derived from tests of surface-flawed specimens are summarized in the following paragraphs.

The first solution for stress intensity at surface flaws was due to Irwin (6) and took the form

$$K_I = 1.1 \sigma \sqrt{\frac{\pi a}{Q}} (\sin^2 \phi + (a/c)^2 \cos^2 \phi)^{1/4} \quad (2-1)$$

where  $\sigma$  is a uniform tensile stress acting perpendicular to the plane of the flaw,  $x = c \cos \phi$  and  $y = a \sin \phi$  are parametric equations of the semi-elliptical flaw periphery, and other variables are defined in Figure 2-1. Equation 2-1 contains some small approximations that are valid for flaw depth-to-length ( $a/c$ ) ratios less than 1.0, and flaw depth-to-thickness ( $a/t$ ) ratios less than 0.5.

A number of approximate solutions for stress intensity at the tips of surface flaws deeper than 50 percent of the parent plate thickness have been proposed (7,8,9,10). Although the solutions have become increasingly sophisticated, there still is some uncertainty in calculations of stress intensity for surface flaws for which  $a/t$  exceeds 50 percent.

Masters et al (3) recently conducted an experimental program to study fracture and fatigue induced crack growth of deep surface flaws in uniaxially stressed surface-flawed specimens. Tests were performed on 2219-T87 aluminum and 5Al-2.5Sn(ELI) titanium alloy specimens. It was concluded that when the parent



section thickness was relatively large with respect to surface flaw plastic zone size, failure occurs when

$$1.1 \sigma \sqrt{\pi a/Q} M_K = K_{IE} \quad (2-2)$$

where  $K_{IE}$  is the fracture toughness of the parent material derived from tests of surface-flawed specimens. Experimentally determined values of  $M_K$  were found to be material dependent as shown in Figures 2-2 and 2-3.

In view of the uncertainties in calculation of stress intensity for deep surface flaws, most fracture and flaw growth data for surface flaws have been developed through the testing of specimens in which flaw depth was less than 50 percent of the specimen thickness. Some characteristics of the resulting data are described in the following paragraphs.

Fracture tests of surface-flawed specimens have shown that fracture occurs when the maximum applied stress intensity at the flaw tip reaches a particular value of stress intensity called fracture toughness of the parent material. Fracture toughness values determined from tests of surface-flawed specimens will hereafter be designated by the symbol  $K_{IE}$ . An example of fracture data obtained from tests of surface-flawed specimens (1) is shown in Figure 2-4. Failure stress is plotted as a function of flaw size for 5A1-2.5Sn(ELI) titanium alloy specimens. Data are included for uniaxially stressed specimens loaded to failure either monotonically (static specimens), or cyclically under both zero-to-tension (0-100-0) and half-tension-to-tension (50-100-50) loading cycles; one data point for a surface-flawed cylindrical tank cycled to failure under zero-to-tension loading profile is also shown. The failure criterion  $(K_I)_{max} = K_{IE}$  is represented by the solid curve drawn through the data points. Good agreement is evidenced between test data and failure criterion.

Fatigue tests of surface-flawed specimens have shown that, when critical flaw size is less than one-half the specimen thickness, the number of uniform loading cycles required to grow a flaw from some initial size to the critical size is

dependent primarily on the maximum stress intensity applied to the flaw tip during the initial loading cycle ( $K_{Ii}$ ). Consequently, fatigue data for surface flawed specimens are usually plotted on graphs of  $K_{Ii}/K_{IE}$  versus cycles to failure where data for given loading profiles and test conditions can be reasonably represented by a single curve called a cyclic life curve. This approach requires knowledge of only initial and final conditions for each test and is called an "end-point" approach. Cyclic life curves and data (1) for 2219-T87 aluminum and 5Al-2.5Sn (ELI) titanium alloys for room air, liquid nitrogen and liquid hydrogen environments are shown in Figures 2-5 and 2-6. These data were developed by testing surface-flawed specimens under uniform cyclic tensile stresses. The cyclic life curves in Figures 2-5 and 2-6 are used in this report as reference curves against which to compare cyclic life data for test specimens containing flaws subjected to stress fields adjacent to circular holes, combined bending and tension stresses, and weld-induced residual stresses.

Flaw growth rates corresponding to a cyclic life curve are found to be inversely proportional to the square of the peak cyclic stress level for which the rates are evaluated (11). Although no systematic investigation of the stress level dependence of plane strain flaw growth rates has been undertaken over large ranges of peak cyclic stress, it is experimentally justified to consider flaw growth rates to be stress level dependent for ranges of peak cyclic stress normally encountered in spacecraft pressure vessels.

**Page Intentionally Left Blank**

### 3.0 MATERIALS AND PROCEDURES

#### 3.1 MATERIALS

All metallic specimens were machined from hot rolled plates of 2219-T87 aluminum or 5Al-2.5Sn(ELI) titanium alloys. Aluminum plates, 1.0 by 36 by 84 inches (25.4 by 914 by 2134 mm) and 2.5 by 48 by 120 inches (63.5 by 1219 by 3048 mm) were purchased in the T-87 condition per Boeing MBS 7-105C (equivalent to MIL-A-8920 (ASG) military specification). Specified limits on chemical composition are listed in Table 3-1. Mechanical properties of aluminum base metal and weldments are located in Table 3-2. Titanium plates, 0.375 by 36 by 84 inches (9.53 by 914 by 2134 mm) and 0.80 by 36 by 60 inches (203 by 914 by 1524 mm) were obtained in the mill annealed condition per MIL-T-9046E after a treatment of 1500°F (1089°K), 0.5 hour, A.C. Ingot composition provided by the vendor is listed in Table 3-1. Mechanical properties of titanium base metal and weldments are included in Table 3-3.

The surfaces of the 1.0 inch (25.4 mm) thick 2219-T87 aluminum plates contained blistered regions and inclusions of foreign matter. Metallurgical samples taken from the blistered regions showed that surface imperfections extended to a maximum depth of 0.002 inch (0.05 mm) and the remaining thickness exhibited a uniform normal microstructure. The contaminated surface layers were machined away during the preparation of all test specimens. With one exception, all aluminum specimens were machined from 1.0 inch (25.4 mm) thick 2219-T87 plates. The excepted specimens were tested to evaluate specimen configuration effects in plane strain fracture toughness testing and were machined from a 2.5 inch (63.5 mm) thick plate.

Two different 5Al-2.5Sn(ELI) titanium plate thicknesses and several different thermal treatments were used in preparing titanium test specimens. The various combinations of material thickness and thermal processing are summarized in Table 3-4.

Specimens used to evaluate effects of combined bending and tension stresses and stress fields adjacent to circular holes were fabricated from 0.375 inch (9.53 mm)

thick plate in the mill annealed condition. A micrograph of the mill annealed material in Figure 3-1a shows inhomogeneity in the microstructure resulting from an incomplete anneal. For comparison, a micrograph of completely annealed 5Al-2.5Sn(ELI) titanium tested in Reference 3 is included in Figure 3-1b.

Specimens used to evaluate surface-flawed specimen thickness effects were machined from a second 0.375 inch (9.53 mm) thick 5Al-2.5Sn(ELI) titanium plate. After six initial tests, it was noted that the microstructure of the plate was layered as illustrated by the micrograph in Figure 3-2. To evaluate effects of further annealing treatments on the microstructure of the remaining specimens, samples were heat treated at 1350°F (1005°K), 1450°F (1061°K) and 1550°F (1117°K) for 4 and 8 hours. Micrographs of the samples annealed for 8 hours are included in Figure 3-3. The 1550°F (1117°K) - 8 hour anneal recrystallized the microstructure into a reasonably homogeneous matrix of equiaxed grains. Accordingly, all remaining specimens were annealed at 1550°F (1117°K) for 8 hours prior to being tested.

Specimens tested to evaluate effects of specimen configuration in plane strain fracture toughness testing were machined from a 0.80 inch (20.3 mm) thick 5Al-2.5Sn(ELI) titanium plate. This plate was found to be partially annealed at mid-thickness as shown by the micrographs in Figure 3-4. Metallurgical samples were cut from the plate and annealed at 1550°F (1117°K) and 1700°F (1200°K) for 8 and 16 hours. Micrographs of the heat treated samples are included in Figure 3-5. The 1550°F (1117°K) - 16 hour thermal cycle proved to be the most effective annealing treatment. Accordingly, all specimen blanks taken from the 0.80 inch (20.3 mm) thick plate were annealed at 1550°F (1117°K) for 16 hours prior to machining of test specimens.

Plexiglas specimens used for experimental stress analysis were machined from 10 by 12 by 12 inches (254 by 305 by 305 mm) cast acrylic blocks obtained from Catalogue Plastics and Chemical Company. Mechanical properties of the acrylic material are included in Table 3-5.

## 3.2 PROCEDURES

Experimental procedures used throughout the test program are described in this

section. Procedures applicable to a given series of tests are reported in the section describing those tests. Welding procedures are described in Appendix A.

All test specimens were precracked by growing fatigue cracks from starter slots under low stress fatigue loadings. Starter slots with dimensions slightly less than the required final flaw dimensions were introduced using an electrical discharge machine. Specimens were then fatigue loaded using maximum cyclic stress levels of 20 ksi and 50 ksi for the aluminum and titanium alloys, respectively, a frequency of 1800 cpm, and a stress ratio of 0.06. Crack surfaces were perpendicular to the rolling direction for the 5Al-2.5Sn(ELI) titanium alloy specimen and parallel to the rolling direction for the 2219-T87 aluminum alloy specimens.

Tests at  $-423^{\circ}\text{F}$  ( $20^{\circ}\text{K}$ ) were conducted with specimens completely submerged in liquid hydrogen within an enclosed cryostat. Liquid level was monitored by means of liquid level sensors. After the liquid reached the desired level, specimens were soaked for 15 minutes to stabilize test conditions. Maximum cyclic loads applied during the first loading cycle were controlled by means of a hand-operated valve. To avoid overloads, the initially applied maximum load was limited to 90 percent of the required maximum load. Minor load adjustments were made during subsequent cycles to raise the load to the required value. The specified load level was always reached within three to five cycles.

Tests at  $-320^{\circ}\text{F}$  ( $78^{\circ}\text{K}$ ) were conducted by submerging test specimens in liquid nitrogen. Titanium alloy specimens and aluminum alloy specimens less than 16 inches (40.6 cm) in length were completely submerged within a closed cryostat. Aluminum alloy specimens greater than 16 inches (40.6 cm) in length were submerged only in the gage area using a wrap-around cryostat. Thermocouple temperature measurements showed that the gage areas were maintained at  $-320^{\circ}\text{F}$  ( $78^{\circ}\text{K}$ ). Prior to the installation of the cyclic test specimens, a dummy specimen was used to adjust cyclic loads to the required values. The test specimen was then substituted for the dummy specimen, cooled to  $-320^{\circ}\text{F}$  ( $78^{\circ}\text{K}$ ), soaked for 15 minutes, and tested. Due to the prior load adjustment, the required maximum cyclic load was applied on the first loading cycle.

Tests at room temperature were conducted within an air-conditioned laboratory in room air. Temperature and relative humidity were neither controlled nor measured. Ambient temperatures were very close to 72°F (295°K) for all tests. All maximum cyclic loads were preset using dummy specimens.

Mechanical properties were determined by testing specimens with uniform gage areas as shown in Figures 3-6 and 3-7. Specimen configuration for 2219-T87 aluminum parent metal and weld metal, 5Al-2.5Sn(ELI) titanium parent metal, and plexiglas is detailed in Figure 3-6. Specimen configuration for 5Al-2.5Sn(ELI) titanium weld metal is detailed in Figure 3-7. Titanium weld metal tensile specimens were machined so that the specimen centerline coincided with the weld centerline and the gage area consisted entirely of weld metal. All metallic specimens were instrumented with 2.0-inch (5.08 cm) gage length extensometer. Plexiglas specimens were instrumented with back-to-back pairs of strain gages.

Loading rates can be summarized as follows. Mechanical property tests were conducted using a strain rate of 0.005 inch/inch/minute until the material yield strength was exceeded; the strain rate was then increased to 0.02 inch/inch/minute until failure. The loading rates for static fracture specimens were such that failure resulted at about one minute after initial load application. All cyclic loading profiles were sinusoidal with a cyclic frequency of 20 cycles per minute at 72°F (295°K) and -320°F (78°K), and two cycles per minute at -423°F (20°K).

#### 4.0 FRACTURE AT FLAWS PROTRUDING FROM CIRCULAR HOLES

Rivet and bolt holes are a common origin of fatigue cracks in aerospace structure. Cracks often originate at the corner formed by the hole wall and structure surface and propagate initially as partially embedded flaws with peripheries that resemble quarter-ellipses as illustrated in Figure 4-1. Under certain combinations of material thickness, fracture toughness, and applied stress, such cracks can be the origins for fast running fractures prior to growing through the section thickness. Under other combinations of the same variables, such cracks can propagate through the section thickness and form through-the-thickness cracks growing from a circular hole. A good stress intensity analysis (12) is available for through-the-thickness cracks growing from a circular hole and this analysis can be used in conjunction with fracture toughness data to estimate critical crack lengths, failure stresses, and desirable inspection frequencies for potential through crack origins. However, no stress intensity analysis exists for partially embedded flaws protruding from circular holes and only rough estimates of critical crack sizes, failure stresses, and inspection intervals can be made for such flaws. Hence, the experimental program outlined in Table 4-1 was undertaken to evaluate the effects of partially embedded flaws on fracture strength and fatigue life of parent structure. The experimental approach was chosen in view of the immense difficulty of performing an applicable stress analysis.

Both static fracture and fatigue tests were performed on 2219-T87 aluminum and 5Al-2.5Sn(ELI) titanium alloy uniaxially stressed specimens. All specimens contained circular holes with peripheral cracks as illustrated in Figure 4-1. For static fracture tests, specimen geometry was varied using two hole diameter-to-thickness ( $2r/t$ ) ratios, three flaw depth-to-thickness ( $a/t$ ) ratios, and three flaw depth-to-length ( $a/c$ ) ratios. Specimen thickness was varied for the aluminum alloy specimens to avoid excessively large specimen dimension and load requirements. All tests were conducted at  $-320^{\circ}\text{F}$  ( $78^{\circ}\text{K}$ ) in liquid nitrogen. Fatigue tests were conducted at  $72^{\circ}\text{F}$  ( $295^{\circ}\text{K}$ ) in room air,  $-320^{\circ}\text{F}$  ( $78^{\circ}\text{K}$ ) in liquid nitrogen, and at  $-423^{\circ}\text{F}$  ( $20^{\circ}\text{K}$ ) in liquid hydrogen using specimens with  $2r/t = 0.50$ ,  $a/t = 0.2$  and  $a/c = 1.0$ .



Materials and test procedures are described in Section 3 of this report.

#### 4.1 RESULTS

Tables 4-2 through 4-5 summarize test variables and gross fracture stress for the seventy-two fracture tests of specimens with flaws originating at circular holes. Failure stresses are plotted in terms of flaw depth-to-length ratio in Figure 4-2. Separate plots are included for each material and for each hole diameter-to-thickness ratio tested. The effect of hole diameter on failure stress is illustrated in Figure 4-3 where it can be seen that the effect is reasonably constant for all  $a/c$  and  $a/t$  ratios and both materials.

All failures originated at the flaw under elastic net section stresses. Crack propagation completely severed the flawed half of the specimen and, simultaneously, the unflawed ligament underwent an ultimate strength failure. Fracture surfaces on the flawed side of all test specimens were very flat and exhibited only small shear lips as evidenced by the pictured fracture faces in Figure 4-4a. The fracture surface of one aluminum specimen (1 HA52-2) exhibited extensive delamination along the flaw periphery. Fracture surfaces of several other aluminum specimens (1 HA22-2, 5 HA22-1, and -2, and 1 HA51-2) exhibited small amounts of delamination along the flaw periphery.

Table 4-6 includes test results for specimens subjected to fatigue loadings. All specimens except titanium/room air were cycled to failure. Critical flaw sizes were not clearly visible and only initial flaw sizes are reported. It did appear that all specimens failed when flaw depth was significantly less than the specimen thickness. Titanium/room air specimens were subjected to 1000 loading cycles and were then pulled to failure. Both initial and final flaw sizes for the cyclic loading sequence were clearly outlined on the fracture surfaces. Fracture surfaces of all specimens tested in  $LN_2$  and  $LH_2$  showed very little evidence of shear lips as illustrated by the fracture surfaces pictures in Figure 4-4b. Aluminum/room air specimens delaminated near maximum flaw depth and resulting fracture faces were flat only in the vicinity of the flaw as shown in Figure 4-4c.

Table 4-7 contains fracture toughness ( $K_{IE}$ ) values obtained from tests of surface-flawed specimens. For the 5Al-2.5Sn(ELI) titanium alloy, test specimens were fabricated using specimens previously tested with flaws originating at holes. Fracture faces were cut from the broken halves of specimens 1HT81-1 and -2, and 1HT55-1 and -2, and the specimen halves were welded together using the electron beam (EB) process. Surface flaws were located 0.4 inch (12.7 mm) away from the edge of the EB weld in order to avoid the heat affected zone associated with the weld. Average fracture toughness values were 43 ksi  $\sqrt{\text{in}}$  (47 MN/m<sup>3/2</sup>) and 75 ksi  $\sqrt{\text{in}}$  (82 MN/m<sup>3/2</sup>) for the aluminum and titanium alloys respectively.

## 4.2 ANALYSIS

### 4.2.1 Static Fracture Tests

An analysis was undertaken to develop a failure criterion for partially embedded flaws protruding from circular holes. It was assumed that failure originated along the peripheries of the flaws under conditions of plane strain at the location of maximum applied stress intensity,  $K_{\text{max}}$ . Pertinent variables include specimen thickness 't', flaw dimensions 'a' and 'c', and hole diameter 'r'. Hence the failure criterion took the form

$$K_{\text{max}}(a, c, r, t) = K_{IE} \quad (4-1)$$

where  $K_{IE}$  is the fracture toughness from tests of surface-flawed specimens. Because of the combined stress concentrations of hole and flaw in the vicinity of the intersection of the flaw periphery and hole surface, it was felt that failure would very likely initiate near that intersection and the most significant flaw dimension would be 'a'. Dimensional considerations then led to the following criterion:

$$\sigma \sqrt{a} \cdot F(a, c, r, t) = K_{IE} \quad (4-2)$$

To gain insight into the form of  $F(a, c, r, t)$ , values of  $\sigma \sqrt{a}$  were plotted in

terms of different independent variables in Figures 4-5 through 4-7. It was at first thought that it might be possible to modify a failure criterion for surface flaws (3) to predict failure stresses for flaws originating from holes. The surface flaw failure criterion assumes the form

$$C \sigma \sqrt{a} \cdot F(a/c) \cdot G(a/t) = K_{IE} \quad (4-3)$$

where  $C$  is a constant and  $G(a/t)$  is both material and  $(a/c)$  dependent. However the  $\sigma \sqrt{a}$  versus  $(a/c)$  data plots in Figure 4-5 show that any attempts to modify Equation (4-3) to account for hole effects would not be successful. Data plots of  $\sigma \sqrt{a}$  versus  $c/r$  in Figures 4-6 and 4-7 expressed the test results in an orderly manner. Accordingly, a failure criterion of the form

$$C \sigma \sqrt{a} \cdot F(c/2r) \cdot G(a/t) \cdot H(r/t) = K_{IE} \quad (4-4)$$

was evaluated. Using functions  $F(c/2r)$  and  $G(a/t)$  shown in Figure 4-8, it was found that calculated failure stresses agree with actual failure stresses within  $\pm 10$  percent with  $C = 1.1$  and  $H(r/t) = \sqrt{4(r/t)}$ . The single exception was specimen 1HA82-1 for which actual failure stress was 12 percent lower than the calculated value. Since only two  $(r/t)$  ratios were tested, the form of  $H(r/t)$  could not be properly evaluated. However, reasonable agreement between actual and calculated failure stresses was obtained in this set of tests using  $H(r/t) = \sqrt{4(r/t)}$ .

A second failure criterion was evaluated after it was noted that the  $(c/r)$  ratio had a marked effect on fracture stress, and that the effect of hole size on fracture stress decreased as flaw length increased. These observations led to an attempt to calculate effective flaw lengths ( $c_e$ ) for each test specimen which, when substituted into the Bowie (12) analytical stress intensity solution for through-the-thickness cracks originating at a hole, could be used to estimate failure stress for each specimen. This approach is illustrated in Figure 4-9 where geometry and failure criterion for a through-crack are compared to geometry and failure criterion for a partially embedded flaw. Values of  $F(c/r)$  from (12) are included in Figure 4-10. Assuming the failure criterion

$$K_{IE} = C \sigma \sqrt{\pi c_e} \cdot F(c_e/r) \quad (4-5)$$

values of  $(c_e/c)$  were found to relate to  $(a/c)$  and  $(a/t)$  in an orderly manner for  $C = 0.87$  as shown in Figure 4-11. Failure stresses calculated using Equation (4-5) with  $C = 0.87$  and the  $c_e/c$  curves in Figure 4-11 differed from actual failure stresses by less than 10 percent for all but two specimens: 1HA82-1A and 5HT22-1 yielded failure stresses that were respectively 18 percent lower and 15 percent higher than the calculated failure stress.

Of the two failure criteria, Equation (4-5) is thought to be more attractive than Equation (4-4) because of its relationship to an existing stress intensity solution (12). Since Equation (4-5) was found to be applicable to two distinctly different materials, it is hoped that it will also be applicable to materials other than those tested in this program.

#### 4.2.2 Fatigue Tests

Cyclic life data for specimens containing flaws originating at holes were compared to cyclic life data for surface-flawed specimens reported in Reference 1. It was hoped that the comparison would yield a consistent relationship between cyclic life for the two different flaw types so that future estimates of minimum cyclic life for flaws originating at holes could be based on cyclic life data for surface flaws. Since cycles-to-failure data for surface-flawed specimens have a strong tendency to fall within a reasonably narrow scatter band on  $(K_{II}/K_{IE})$  versus cycles-to-failure plots ( $K_{II}$  is the maximum stress intensity generated along the flaw periphery during the first loading cycle), data for the two different flaw configurations were compared on such plots in Figures 4-12 and 4-13. Values of  $K_{II}$  for specimens containing flaws originating at holes were estimated by substituting initial flaw parameters and peak cyclic stress into the equation

$$K_I = 0.87 \sigma \sqrt{\pi c_e} \cdot F(c_e/r) \quad (4-6)$$

taken from Section 4.2.1 of this report. Resulting values of  $K_{II}$  and  $K_{II}/K_{IE}$  for each specimen are summarized in Table 4-8. For given  $K_{II}/K_{IE}$  ratios, agreement between cyclic life data for both flaws originating at holes and

surface flaws is very good except for the aluminum/LH<sub>2</sub> tests. For the 2219-T87 aluminum alloy, a reduction in test temperature from -320°F (78°K) to -423°F (20°K) had very little effect on cyclic life for surface-flawed specimens but significantly reduced cyclic life for specimens containing flaws originating at holes.

For titanium/air tests in which specimens were subjected to 1000 loading cycles without failing, final flaw dimensions were compared to estimated final flaw dimensions based on flaw growth rate data for surface flaws reported in (1). To estimate flaw growth, it was assumed that the initial quarter-circular flaw would remain quarter-circular throughout each test. For different assumed final flaw sizes, stress intensities calculated for initial and final conditions using Equation (4-6) were averaged to obtain an average applied stress intensity for the 1000 loading cycles. Crack growth rate corresponding to the average stress intensity was obtained from data in (1). The average growth rate was multiplied by 1000 to calculate the total anticipated flaw growth due to 1000 loading cycles. The flaw radius for which assumed and calculated flaw sizes agreed was 0.20 inch (5 mm) for both specimens. In the actual tests, the flaw did not remain quarter-circular in shape. Rather, the depthwise flaw growth was greater than the lateral growth and the maximum final flaw dimensions were less than the calculated values.

The cyclic life data contained in Figures 4-12 and 4-13 were all generated from specimens in which flaw depth-to-thickness (a/t) ratio at failure did not significantly exceed 50 percent of the specimen thickness. For such restricted geometries, it does appear that cyclic-life and flaw-growth-rate data for surface flawed specimens can be used in the manner employed in the foregoing analysis to make reasonable estimates of cyclic life for tension-loaded structure containing corner flaws originating from holes. However, there may be material/environment combinations for which estimated life will be somewhat greater than actual life as in the 2219-T87 aluminum/LH<sub>2</sub> tests conducted herein.

#### 4.3 SUMMARY

Two failure criterion were developed using fracture data for 2219-T87 aluminum

and 5Al-2.5Sn(ELI) titanium test specimens containing partially embedded flaws protruding from circular holes (see Figure 4-1). Of the two criteria, Equation (4-5) is thought to be more attractive than Equation (4-4) because of its relationship to an existing stress intensity solution (12). Since Equation (4-5) was found to be applicable to two distinctly different materials, it is hoped that it will also be applicable to materials other than those tested in this program.

A method of comparing cyclic life data for surface flaws and partially embedded flaws protruding from holes was evaluated. It does appear that fatigue data for surface-flawed specimens can be used to make reasonable estimates of cyclic life for tension loaded structure containing corner flaws originating from circular holes. However, there may be material/environment combinations for which estimated life will be moderately greater than actual life.

**Page Intentionally Left Blank**

## 5.0 FRACTURE AT SURFACE FLAWS SUBJECTED TO COMBINED BENDING AND TENSION STRESSES

Potential flaw locations in aerospace hardware are often subjected to combined bending and tension stresses. Estimates of critical flaw size and minimum cyclic life for these conditions can be calculated using approximate stress intensity analyses for surface flaws subjected to combined bending and tension stresses. The following experimental program constitutes an initial attempt to experimentally evaluate effects of combined bending and tension stresses on stability of surface flaws.

### 5.1 BACKGROUND

Two approximate solutions have been derived for stress intensity at the tip of semi-elliptical surface flaws in plates subjected to bending. Both analyses are limited to flaws with  $(a/t)$  values less than 0.5. Stress intensity due to bending ( $K_{Ib}$ ) is expressed in the form

$$K_{Ib} = M_B \sigma_B \sqrt{\frac{\pi a}{Q}} \quad (5-1)$$

where  $M_B$  is a scalar factor depending on  $a/t$  and  $a/2c$ ;  $t$  is the plate thickness; and  $\sigma_B$  is the maximum bending stress at the outer fibers of the plate.

Smith (10) obtained approximate  $M_B$  values for  $a/2c = 0$  and 0.5 using two existing stress intensity solutions and interpolated to derive  $M_B$  values for intermediate flaw shapes. Smith's results are plotted in Figure 5-1a. The upper curve for  $a/2c = 0$  was obtained from the Gross (13) solution for an edge-notched plate subjected to pure bending; the lower curve for  $a/2c = 0.5$  was derived from the Smith (14) solution for a semi-circular surface flaw in a thick plate subjected to pure bending.

Shah obtained approximate  $M_B$  values using a solution (15) for an embedded elliptical flaw in a large beam subjected to pure bending moment. The stress intensity



was expressed by Equation (5-1) with  $M_B$  values given by

$$M_B = M_F - \frac{2 (a/t) k^2 E(k)}{(1+k^2) E(k) - (1-k^2) K(k)} \quad (5-2)$$

where  $M_F = 1 + 0.12 (1-a/2c)^2$  is a correction factor accounting for the effect of the stress free face from which the flaw originates;  $K(k)$  and  $E(k)$  are complete elliptic integrals of the first and second kind corresponding to the modulus  $k = [1-(a/c)^2]^{1/2}$ . Values of  $M_B$  calculated from Equation (5-2) are plotted in Figure 5-1b. Both Shah and Smith  $M_B$  values agree for  $a/2c = 0.5$  but the Smith values become increasingly larger than the Shah values as  $a/2c$  is decreased from 0.5.

Stress intensity at the tips of semi-elliptical flaws in plates subjected to combined bending and tension can be estimated using the principle of superposition, i.e.,  $K_I = K_{It} + K_{Ib}$  where  $K_{Ib}$  and  $K_{It}$  are stress intensities due to bending and tension stresses respectively.  $K_{It}$  can be calculated using the Irwin (6) solution, i.e.,

$$K_{It} = 1.1 \sqrt{\pi} \sigma_T \sqrt{a/Q} \quad (5-3)$$

where  $\sigma_T$  is the tension stress acting perpendicular to the plane of the flaw. Stress intensity for combined bending and tension stresses is obtained by combining Equations (5-2) and (5-3) as follows:

$$K_I = 1.1 \sqrt{\pi} \sigma_T \sqrt{a/Q} + M_B \sigma_B \sqrt{a/Q} \quad (5-4)$$

Equation (5-4) was used to evaluate the results of the following test program.

## 5.2 TEST PROGRAM

Effects of combined bending and tension stresses on fracture and fatigue growth or surface flaws were experimentally evaluated according to the test program outlined in Table 5-1. Test specimen configuration is illustrated in Figure 5-2. Surface flaws having two nominal  $a/2c$  ratios (0.125 and 0.250) and  $a/T$  ratios (0.25 and 0.50) were tested under uniform tension stresses (using  $T/t = 1.5$  and 2.0). Uniform thickness specimens were tested to determine fracture toughness data using

surface flaws identical to those tested under combined bending and tension stresses. All static fracture tests were performed at  $-320^{\circ}\text{F}$  ( $78^{\circ}\text{K}$ ) in liquid nitrogen. Fatigue tests were conducted at room temperature in ambient air, at  $-320^{\circ}\text{F}$  ( $78^{\circ}\text{K}$ ) in liquid nitrogen, and at  $-423^{\circ}\text{F}$  ( $20^{\circ}\text{K}$ ) in liquid hydrogen.

### 5.3 DESCRIPTION AND ANALYSIS OF RESULTS

#### 5.3.1 Specimen Calibration

Load versus bending stress calibrations were established for each different specimen configuration. This was accomplished by testing unflawed specimens instrumented with four pair of back-to-back strain gages as illustrated in Figure 5-3. Each specimen was incrementally loaded at  $-320^{\circ}\text{F}$  ( $78^{\circ}\text{K}$ ) and strain readings were taken after the addition of each load increment. In all specimens, the measured strains were quite uniform across the specimen width at all load levels. Bending stresses were calculated using the following procedure. Applied stress was divided by average tensile strain to determine the modulus of elasticity for the material. The calculated moduli were  $11.5 \pm 0.1 \times 10^6$  and  $18.1 \pm 0.1 \times 10^6$  psi for the aluminum and titanium alloys respectively. Average bending strains were multiplied by the appropriate modulus in order to calculate bending stress. The resultant load versus bending stress curves are plotted in Figure 5-4.

#### 5.3.2 Static Fracture Tests

Static fracture test results are summarized in Table 5-2. For the 2219-T87 aluminum alloy, four uniform thickness and two asymmetrical specimens failed in the grip area. For the 5Al-2.5Sn(ELI) titanium alloy, two uniform thickness and two asymmetrical specimens failed at the flaw plane, two uniform thickness specimens did not fail at the test machine capacity of 160 kips, and five asymmetrical specimens failed in the grip area. Pronounced delaminations were observed at the flaw tip on the failure surfaces of uniform thickness aluminum specimens A11-1, A21-1 and A22-1. Fracture surfaces of all other specimens were very flat in the vicinity of the flaw.

Fracture toughness values ( $K_{IE}$ ) were obtained from only one aluminum specimen (A21-1) and one titanium specimen (T21-1). The other uniform thickness specimens tested either delaminated at the flaw tip (A11-1, A21-1 and A22-1) or were inadequately fatigue cracked (T22-1), and the resultant data were not evaluated. The  $K_{IE} = 45 \text{ ksi} \sqrt{\text{in}}$  ( $49 \text{ MN/m}^{3/2}$ ) calculated for specimen A21-1 agrees with comparable data included in Figure 6-13b. The  $K_{IE} = 77 \text{ ksi} \sqrt{\text{in}}$  ( $85 \text{ MN/m}^{3/2}$ ) calculated for specimen T21-1 compares favorably with comparable data in Table 4-7.

Maximum loads applied to several test specimens are compared to estimated failure loads in Table 5-3. Failure load estimates were calculated using Equation (5-4) and  $K_{IE}$  values of  $45 \text{ ksi} \sqrt{\text{in}}$  ( $49 \text{ MN/m}^{3/2}$ ) and  $77 \text{ ksi} \sqrt{\text{in}}$  ( $85 \text{ MN/m}^{3/2}$ ) for the aluminum and titanium alloys respectively. Values of  $\sigma_B$  were estimated by extrapolating the  $\sigma_B$  versus  $P$  curves in Figure 5-3 to the observed failure load. The first four specimens listed in Table 5-3 failed at the flaw plane. Slightly better agreement between actual and calculated failure load was obtained when calculations were made using  $M_B$  values from Figure 5-1a rather than 5-1b. The remaining specimens listed in Table 5-3 failed in the grips. The flawed cross-section of most specimens were subjected to loads greater than 90 percent of the calculated failure loads without failing.

Table 5-3 shows that reasonable estimates of failure load can be made for structure containing surface flaws subjected to combined bending and tension stresses. It follows that critical flaw sizes can also be estimated for given applied stresses. At the present time, estimating procedures are available only for flaws having depth-to-thickness ratios less than 0.5. The limited experimental data in Table 5-2 agreed slightly better with estimates made using  $M_B$  values from Figure 5-1a rather than from Figure 5-1b.

### 5.3.3 Fatigue Tests

Test results for both 2219-T87 aluminum and 5Al-2.5Sn(ELI) titanium alloys are included in Table 5-4. All aluminum alloy specimens were cycled to failure. Specimens tested at room temperature and  $-320^\circ\text{F}$  ( $78^\circ\text{K}$ ) delaminated in the

vicinity of the flaw tip during cycling. At room temperature, depthwise flaw growth was completely inhibited as illustrated in Figure 5-5. At  $-320^{\circ}\text{F}$  ( $78^{\circ}\text{K}$ ), limited depthwise growth occurred before delaminations became sufficiently pronounced to halt further growth, and considerable growth occurred laterally in the flaw plane. At  $-423^{\circ}\text{F}$  ( $20^{\circ}\text{K}$ ), no delaminations were observed on any of the fracture faces, but final flaw peripheries were not sufficiently distinct to permit reliable measurements of critical flaw size.

Aluminum alloy fatigue results are compared to previously reported fatigue data (1) for surface-flawed specimens tested under uniform tension stresses in Figure 5-6. Comparisons are made on semi-log plots of  $K_{II}/K_{IE}$  versus cycles to failure.  $K_{II}$  values were calculated using Equation (5-4) and  $M_B$  values from Figure 5-1a.  $K_{IE}$  values of 41, 43 and 45  $\text{ksi}\sqrt{\text{in}}$  (45, 47, and 49  $\text{MN}/\text{m}^{3/2}$ ) were obtained from Figure 6-13 for room temperature,  $-320^{\circ}\text{F}$  ( $78^{\circ}\text{K}$ ) and  $-423^{\circ}\text{F}$  ( $20^{\circ}\text{K}$ ), respectively. At room temperature and  $-320^{\circ}\text{F}$  ( $78^{\circ}\text{K}$ ), cyclic lives at a given  $K_{II}/K_{IE}$  ratio were significantly greater for specimens subjected to combined bending and tension stresses than for specimens subjected to uniform tension stresses. Since delaminations in aluminum surface-flawed specimens tend to prolong cyclic life, most of noted differences in cyclic life were probably due to the effects of delaminations in the specimens tested under combined bending and tension stresses. At  $-423^{\circ}\text{F}$  ( $20^{\circ}\text{K}$ ) no delaminations were observed and there was much closer agreement between the data for combined bending and tension stresses and uniform tension stresses.

Titanium alloy results are compared to previously reported data (1) for surface-flawed specimens tested under uniform tension stresses in Figure 5-7. At  $-320^{\circ}\text{F}$  ( $78^{\circ}\text{K}$ ) all bending/tension specimens were cycled to failure. Flaw depths were greater than 50 percent of the specimen thickness throughout each test. However, initial flaw depths were sufficiently close to 50 percent of specimen depth to permit reasonable estimates of  $K_{II}$  using Equation (5-4) and  $M_B$  values from Table 5-1a;  $K_{II}/K_{IE}$  ratios for each specimen were based on  $K_{IE} = 77 \text{ ksi}\sqrt{\text{in}}$  ( $85 \text{ MN}/\text{m}^{3/2}$ ). Room temperature and  $-423^{\circ}\text{F}$  ( $20^{\circ}\text{K}$ ) data comparisons were made on stress intensity versus flaw growth rate  $[K_I \text{ versus } d(a/Q)/dN]$  plots in

Figure 5-7. Rates for uniform tension stresses were calculated using Reference 1 data and two different stress levels including (1) maximum bending plus tension, and (2) uniform tension stress components of the stress fields used in the combined bending and tension stress tests. Flaw-growth rates were assumed to be inversely proportional to the square of the stress level (11). Rates for bending-tension specimens were calculated by dividing the observed changes in flaw size ( $\Delta a/Q$ ) by the number of applied loading cycles, and were plotted against the arithmetic average of initial and final stress intensities at the flaw tip calculated using Equation (5-4) and  $M_B$  values from Figure 5-1a. At room temperature, flaw growth rates for combined bending and tension stresses agreed with Reference 1 rates evaluated for a stress level equal to the maximum bending plus tension stress. At  $-423^{\circ}\text{F}$  ( $20^{\circ}\text{K}$ ) flaw growth rates for combined bending and tension specimens were less than comparable rates for uniform tension stresses reported in Reference 1.

In conclusion, these limited data provide an incomplete characterization of the subcritical fatigue growth behavior of surface flaws subjected to combined bending and tension stresses. Until further experimental or analytical work is undertaken, estimates of cycles to failure for surface flaws subjected to combined bending and tension stresses can be based on cyclic life and flaw growth rate data for surface-flawed specimens tested under uniform tension stresses. The data developed herein indicate that for given  $K_{II}/K_{IE}$  ratios, cyclic life for flaws subjected to combined bending and tension stresses will range from slightly less to significantly greater than cyclic life for flaws subjected to uniform tension stresses.

## 6.0 INFLUENCE OF SPECIMEN DESIGN IN PLANE STRAIN FRACTURE TOUGHNESS TESTING

Plane strain fracture toughness is receiving increased attention in material selection and design considerations for medium-to-high strength metallic structure. There is in existence considerable plane strain fracture toughness data obtained from tests of surface-flawed specimens (1,2,3,16,17, for example) since the surface-flawed specimen is the best available model of potential failure origins in aerospace pressure vessels. However, a recently proposed ASTM test method (18) for plane strain fracture toughness ( $K_{Ic}$ ) testing of metallic materials presently covers tests of only single-edge-notched bend and compact tension specimens. To assess the usefulness of such specimens in the design of aerospace hardware, a systematic comparison of plane strain fracture toughness data obtained from tests of through-cracked and surface-flawed specimens was undertaken. To this end, duplicate 2219-T87 and 5Al-2.5Sn(ELI) titanium single-edge-notched-bend (SENB), single-edge-notched-tension (SENT), compact tension (CT) and surface flawed (SF) specimens were fractured at 72°F (295°K) in room air, -320°F (78°K) in liquid nitrogen, and at -423°F (20°K) in liquid hydrogen as summarized in Table 6-1.

The proposed test method (18) specifies minimum specimen thicknesses and crack lengths required to obtain acceptable  $K_{Ic}$  values from tests of SENB and CT specimens. To investigate the applicability of these requirements to SF specimens, tests of 2219-T87 aluminum and 5Al-2.5Sn(ELI) titanium SF specimens were undertaken in which specimen thickness and flaw shape were varied, as summarized in the lower part of Table 6-1. For tests of each alloy, four specimen thicknesses and two flaw shapes were used and flaw depth-to-thickness ratios were less than 50 percent for all but the thinnest specimens. Aluminum alloy specimens were tested at 72°F (295°K), -320°F (78°K), and -423°F (20°K). Titanium alloy specimens were tested at -320°F (78°K) and -423°F (20°K).

## 6.1 PROCEDURES

### 6.1.1 Specimen Configuration Effect Tests

All specimens were cut from either one 2.5 inch (6.35 cm) thick 2219-T87 aluminum alloy plate or one 0.80 inch (2.03 cm) thick 5Al-2.5Sn(ELI) titanium alloy plate as illustrated in Figure 6-1. Orientation of crack plane with respect to rolling direction was the same in all specimens of a given alloy, i.e., parallel to the rolling direction for the aluminum alloy and perpendicular to the rolling direction for the titanium alloy. The tips of all cracks in SENB, SENT and SF specimens were located very close to the mid plane of the parent plate. Crack tips in CT specimens were respectively 0.35 inch (0.89 cm) and 0.075 inch (0.19 cm) away from mid plane of the aluminum and titanium alloy parent plates.

Specimen details for SENB, SENT and CT specimens are shown in Figure 6-2. All specimens were fabricated with the largest depth (W) dimensions that could be obtained from the parent plates, i.e., 2.50 inches (6.35 cm) for the aluminum specimens and 0.75 inches (1.91 cm) for the titanium specimens. Specimen thicknesses were 1.25 inches (3.18 cm) and 0.40 inches (1.02 cm) for aluminum and titanium specimens respectively. Thicknesses were chosen to exceed estimated values of  $2.5 (K_{Ic} / \sigma_{ys})^2$  for all material-environment combinations except titanium/air. For the titanium/air tests, it was estimated that  $2.5 (K_{Ic} / \sigma_{ys})^2$  exceeded 2.5 inches (6.35 cm), and specimens sufficiently large to measure  $K_{Ic}$  could not be machined from the available 0.80 inch (2.03 cm) thick plate. Loading pin hole locations in the CT specimens were smaller and more widely separated than the hole locations recommended in Reference 18 since CT specimens were designed prior to the release of the proposed test method. However, CT specimen proportions agreed with Reference 18 requirements in all other respects.

Surface-flawed specimen details are summarized in Figure 6-3. Specimen thickness was selected to be greater than estimated values of  $2.5 (K_{IE} / \sigma_{ys})^2$  where  $K_{IE}$  is fracture toughness resulting from the SF specimen tests.

Specimens were precracked by growing fatigue cracks from starter slots. Details of starter slots used in SENB, SENT and CT specimens are summarized in Figure 6-4. An electrical discharge machine (EDM) was used to produce a sharp tip at the end of a milled slot. For the aluminum alloy, starter slots fell within the required envelope specified in Reference 18; for the titanium alloy, the 0.10 inch (0.25 cm) milled slot was wider than the maximum allowable (18) value of  $0.05 W$  (0.038 inch or 0.096 cm). In SF specimens, starter slots were produced using an EDM machine and 0.06 inch (0.15 cm) thick circular electrodes; electrode tips were machined to a radius of about 0.003 inch (0.008 cm) and an included angle of less than 20 degrees. All specimens were cracked under tension-tension fatigue at 72°F (295°K) in room air. The ratio of maximum cyclic stress intensity to Young's modulus ( $K_f/E$ ) was less than  $0.0012 \text{ inch}^{1/2}$  ( $0.0019 \text{ cm}^{1/2}$ ) for all but the titanium alloy SENB specimens tested at -320°F (78°K) and titanium alloy CT specimens tested at -423°F (20°K) for which  $K_f/E$  was  $0.0014 \text{ inch}^{1/2}$  ( $0.0022 \text{ cm}^{1/2}$ ). The resulting fatigue cracks in SENB, SENT and CT specimens were quite uniform across the specimen width and were approximately 0.10 inch long (0.25 cm). Fatigue cracks in SF specimens were about 0.04 inch (0.10 cm) and 0.02 inch (0.05 cm) long in the aluminum and titanium alloy specimens respectively and the crack peripheries approximated semi-ellipses.

Tests at 72°F (295°K) were conducted within an enclosed air conditioned laboratory. Relative humidity was neither controlled nor measured. Tests at -320°F (78°K) and -423°F (20°K) were conducted with test specimens completely submerged in liquid nitrogen and liquid hydrogen respectively. Specimens were soaked for 15 minutes prior to loading to stabilize test conditions. All specimens were tested in standard test machines. SENB specimens were supported on lightly greased rollers separated by a fixed span.

Continuous recordings of crack-opening displacement versus load were obtained for all tests except SF specimens tested at -423°F (20°K). Crack displacements were measured using a clip gage spring loaded against integrally machined knife edges. Knife edge details for all specimens are shown in Figure 6-4. For SF specimens, the knife edges were machined into the specimen surface at the mouth of the surface



crack. One such knife edge appears as a small rectangle within the dark colored EDM slot on the fracture face of the aluminum alloy SF specimen pictured in Figure 6-5. Clip gage details corresponded to those given in Reference 18 and both clip gage and load cell were connected to an X-Y recorder to obtain the test records.

Fracture toughness values for SENB, SENT and CT specimens were calculated using the equations summarized in Figure 6-6. Loads used in the calculations were obtained by drawing secant lines through the origin of each crack-opening displacement versus load record having a slope 5 percent less than the slope of the initial straight line part of the test record. The load corresponding to the intersection of secant offset and test record was designated as  $P_Q$  and was substituted into the equations in Figure 6-6 to calculate fracture toughness.

Fracture toughness values for SF specimens were calculated by substituting maximum applied gross stress and initial flaw dimensions into Equation 2-1 with  $\phi = 90^\circ$ . This procedure implies that fracture originates at the point of maximum flaw depth and unstable flaw propagation is preceded by negligible amounts of slow crack propagation. This implication is discussed in light of the test results in the "Results and Discussion" section.

#### 6.1.2 Specimen Thickness Effect Tests

All specimens were taken from either 1.0 inch (2.54 cm) thick 2219-T87 aluminum or 0.38 inch (0.97 cm) thick 5Al-2.5Sn(ELI) titanium plate stock. Three different specimen configurations were used and designated as configurations A, B and C. Specimen configurations are illustrated in Figure 6-7 and specimen dimensions are listed in the tables of results. Crack planes were parallel to the rolling direction in aluminum alloy specimens and perpendicular to the rolling direction in titanium alloy specimens. All specimens were precracked and tested using the same procedures that were employed in the specimen configuration effect tests, except that crack-opening displacement versus load records were not obtained.

## 6.2 RESULTS AND DISCUSSION

### 6.2.1 Specimen Configuration Effect Tests

Tables 6-2 and 6-3 contain test results and specimen details for 2219-T87 aluminum and 5A1-2.5Sn(ELI) titanium SENT, SENB and CT specimens. Tables 6-4 and 6-5 contain similar data for SF specimens. Test records for one of each set of duplicate instrumented specimens are included in Figures 6-8 through 6-11. Plane strain fracture toughness values obtained from tests of SENB, SENT and CT specimens along with fracture toughness values obtained from SF specimen tests are given as a function of test temperature in Figure 6-12 for both 2219-T87 aluminum and 5A1-2.5Sn(ELI) titanium alloys.

Crack displacement-versus-load records for all SENB, SENT and CT specimens (with the exception of the inadequately sized titanium alloy specimens tested at 72°F) indicated a reasonably abrupt onset of unstable crack propagation. The  $P_Q$  load was usually slightly less than the maximum load but always greater than loads corresponding to all points on the test record preceding that at  $P_Q$ . Deviations from linearity at  $0.8 P_Q$  were less than 25 percent of comparable deviations measured at  $P_Q$  as required for valid test records (18).

Crack displacement versus load record for SF specimens exhibited moderate nonlinearity at loads above about 90 percent of the maximum applied loads. It is believed that the nonlinearity observed in these tests was due primarily to small amounts of slow crack extension that preceded rapid crack propagation. Unreported tests of 2219-T87 aluminum and 5A1-2.5Sn(ELI) titanium SF specimens conducted at The Boeing Company have shown that moderate amounts of slow crack extension do occur when such specimens are loaded to stress intensity levels near  $K_{IE}$  and then immediately unloaded prior to failure. Moderate amounts of crack extension in SF specimens at stress intensity levels less than  $K_{IE}$  has been previously reported (2) for both 2219-T87 aluminum and 5A1-2.5 Sn(ELI) titanium in the environments of room air, liquid nitrogen and liquid hydrogen.

Plane strain fracture toughness data for the 2219-T87 aluminum alloy SENB, SENT and SF specimens are in good agreement as illustrated in the lower part of Figure 6-12.

The scatter band was drawn for illustrative purposes and includes all SENB and SENT data. The SENB, SENT and SF fracture toughness data are in good agreement, but the CT data fall consistently below data for the other specimen types. There were some small differences between SENB, SENT and SF data, some of which were temperature independent and others temperature dependent. For example, SENB data fell moderately higher than SENT data at all test temperatures. The SENB data also fell above SF data at  $-320^{\circ}\text{F}$  ( $78^{\circ}\text{K}$ ) and  $-423^{\circ}\text{F}$  ( $20^{\circ}\text{K}$ ), but agreed closely with SF data at  $72^{\circ}\text{F}$  ( $295^{\circ}\text{K}$ ). Small variations in fracture toughness data for SENB, SENT and SF specimens are not surprising. However, the substantial disagreement between CT data and all other data was unexpected.

Limited efforts to determine possible reasons for the discrepancies noted in the aluminum alloy fracture toughness data were not successful. Since there was a remote possibility that the CT specimens could have been inadvertently fabricated with cracks located in the TR rather than the WT plane, rolling and thickness directions were determined for each CT specimen. The variation of microstructure with direction is illustrated in Figure 6-13 and shows that the crack planes were properly oriented in the WT plane of the parent plate. Two additional CT specimens were tested in room air to determine whether increase in length of ligament between the crack tip and back specimen surface would elevate measured fracture toughness values. To this end, specimens ACL-1 and ACL-2 were fabricated with a crack length to specimen depth ( $a/W$ ) ratio of 0.27 and an uncracked ligament length of 1.5 inches (3.81 cm) as compared to ( $a/W$ ) ratios and ligament lengths of 0.55 and 0.9 inches (2.29 cm) for other CT specimens. The resulting data is plotted in Figure 6-12 where it can be seen that the data points fell above those obtained from CT specimens with ( $a/W$ )  $\approx$  0.55, but still below the SENB, SENT and SF data points. Since crack lengths in specimens ACL-1 and ACL-2 were less than  $2.5 (K_Q/\sigma_{ys})^2$  it is possible that the increase in fracture toughness values for these specimens was due in part to insufficient crack length rather than increase in uncracked ligament length. It should also be noted again that diameter and spacing of loading holes in the CT specimens were different from comparable dimensions in specimens used in round robin evaluations of the CT specimen prior to the release of Reference 18. Since stress intensity in CT specimens is very sensitive to boundary conditions, there is a possibility that the loading method used in these tests did not satisfy the boundary

conditions assumed in the stress intensity analyses of the CT specimen. At this time, discrepancies noted in the test program between  $K_{Ic}$  values obtained from tests of CT specimens and  $K_{Ic}$  values obtained from tests of SENB and SENT specimens cannot be explained.

Plane strain fracture toughness data for the 5Al-2.5Sn(ELI) titanium alloy show a considerable degree of scatter and some disagreement between through-cracked and surface cracked specimen data at  $-320^{\circ}\text{F}$  ( $78^{\circ}\text{K}$ ). The scatter band shown in the upper part of Figure 6-12 was drawn for illustrative purposes and includes all  $-423^{\circ}\text{F}$  ( $20^{\circ}\text{K}$ ) data at all but SF data at  $-320^{\circ}\text{F}$  ( $78^{\circ}\text{K}$ ). The SENB, SENT and CT data indicate little change in fracture toughness between  $-320^{\circ}\text{F}$  ( $78^{\circ}\text{K}$ ) and  $-423^{\circ}\text{F}$  ( $20^{\circ}\text{K}$ ). Other reported SENB data (5) have shown a higher toughness at  $-320^{\circ}\text{F}$  ( $78^{\circ}\text{K}$ ) than at  $-423^{\circ}\text{F}$  ( $20^{\circ}\text{K}$ ) for the RT direction. The  $K_Q$  values obtained at  $72^{\circ}\text{F}$  ( $295^{\circ}\text{K}$ ) from inadequately sized specimens are considerably less than previously reported (1, 5) room temperature plane strain fracture toughness values in excess of  $100 \text{ ksi } \sqrt{\text{in}}$  ( $110 \text{ MN/m}^{3/2}$ ). At  $-423^{\circ}\text{F}$  ( $20^{\circ}\text{K}$ ) fracture toughness values for two SENT, one SENB, one CT and three SF specimens are in good agreement. At  $-320^{\circ}\text{F}$  ( $78^{\circ}\text{K}$ ), the SF data fell above the scatter band enclosing the SENT, SENB and CT data.

The possibility that disagreement between  $-320^{\circ}\text{F}$  ( $78^{\circ}\text{K}$ ) SF and through-cracked specimen data for the 5Al-2.5Sn(ELI) titanium alloy was due to inadequate crack depths in the SF specimens was examined. In SF specimens, both crack depth ( $a$ ) and distance between the crack tip and back specimen face ( $t - a$ ) must be sufficiently large multiples of  $(K_{IE} / \sigma_{ys})^2$  in order to ensure that  $K_{IE}$  is the controlling mechanical parameter in the fracturing process. Data in the following section of this report show that 5Al-2.5Sn(ELI) titanium SF specimens yield essentially constant values of  $K_{IE}$  at  $-320^{\circ}\text{F}$  ( $78^{\circ}\text{K}$ ) and  $-423^{\circ}\text{F}$  ( $20^{\circ}\text{K}$ ) when both ' $a$ ' and ( $t - a$ ) exceed  $0.5 (K_{IE} / \sigma_{ys})^2$ . In these tests, ' $a$ ' and ( $t - a$ ) values exceeded  $0.5 (K_{IE} / \sigma_{ys})^2$  in all  $-320^{\circ}\text{F}$  ( $78^{\circ}\text{K}$ ) specimens and so it was concluded that increases in crack depth and specimen dimensions would probably not have resulted in better agreement between the SF and through-cracked specimen data for the 5Al-2.5Sn(ELI) titanium alloy at  $-320^{\circ}\text{F}$  ( $78^{\circ}\text{K}$ ).

The significant change in fracture toughness values between  $-423^{\circ}\text{F}$  ( $20^{\circ}\text{K}$ ) and  $-320^{\circ}\text{F}$  ( $78^{\circ}\text{K}$ ) for the titanium alloy SF specimens suggests that a fracture mode transition may

have occurred between the two test temperatures. Other evidence of a change in plane strain fracture behavior in 5Al-2.5Sn(ELI) titanium alloy between  $-423^{\circ}\text{F}$  ( $20^{\circ}\text{K}$ ) and  $-320^{\circ}\text{F}$  ( $78^{\circ}\text{K}$ ) was reported in Reference 1 where it was observed that surface-flawed cylindrical tanks failed at  $-320^{\circ}\text{F}$  ( $78^{\circ}\text{K}$ ) by splitting open, whereas tanks failed at  $-423^{\circ}\text{F}$  ( $20^{\circ}\text{K}$ ) by complete shattering of the vessel. It was also noted that areas of fatigue induced flaw growth in 5Al-2.5Sn(ELI) surface-flawed specimens and cylindrical tanks were characterized by fatigue striations at  $-320^{\circ}\text{F}$  ( $78^{\circ}\text{K}$ ) but were completely devoid of striations at  $-423^{\circ}\text{F}$  ( $20^{\circ}\text{K}$ ). In contrast to SF specimens, through-the-thickness cracked specimens yielded no evidence of differences in fracture behavior between  $-423^{\circ}\text{F}$  ( $20^{\circ}\text{K}$ ) and  $-320^{\circ}\text{F}$  ( $78^{\circ}\text{K}$ ). Since the crack planes in all through-cracked specimens were subjected to significant bending stresses whereas crack planes in SF specimens are subjected primarily to tensile stresses, there is a possibility that differences in titanium alloy  $-320^{\circ}\text{F}$  ( $78^{\circ}\text{K}$ ) fracture toughness data are related to bending stresses. To date, no effort has been made to evaluate this possibility.

#### 6.2.2 Surface-Flawed Specimen Thickness Effects

Tables 6-6 through 6-11 contain fracture stress, flaw dimensions, and specimen dimensions for all test specimens. Data for the 2219-T87 aluminum alloy specimens tested at  $72^{\circ}\text{F}$  ( $295^{\circ}\text{K}$ ),  $-320^{\circ}\text{F}$  ( $78^{\circ}\text{K}$ ) and  $-423^{\circ}\text{F}$  ( $20^{\circ}\text{K}$ ) are summarized in Tables 6-6, 6-7 and 6-8 respectively. The six 5Al-2.5Sn(ELI) titanium specimens listed in Table 6-9 were tested in the mill annealed condition. The resulting fracture faces were exceptionally jagged and contained no areas of flat fracture. The microstructure of these specimens is illustrated in Figure 3-2. The titanium specimens listed in Tables 6-10 and 6-11 were tested at  $-320^{\circ}\text{F}$  ( $78^{\circ}\text{K}$ ) and  $-423^{\circ}\text{F}$  ( $20^{\circ}\text{K}$ ) after having been annealed at  $1550^{\circ}\text{F}$  ( $1117^{\circ}\text{K}$ ) for 8 hours to improve the microstructure.

Fracture data for 2219-T87 aluminum and 5Al-2.5Sn(ELI) titanium alloy SF specimens of varied thickness are plotted in Figures 6-14 and 6-15 respectively. Data are plotted for all tests in which flaw depth to specimen thickness ratios were less than one-half. Apparent fracture toughness ( $K_{\text{cr}}$ ) values were calculated by substituting gross failure stress and initial flaw parameters in Equation 2-2 ( $\phi = 90^{\circ}$ ) and plotted as a function of specimen thickness. Specimen thickness is given both in inches and in multiples of

$(K_{IE}/\sigma_{ys})^2$  where  $K_{IE}$  is the average fracture toughness value obtained from the thickest test specimens. For purposes of comparison, data obtained from surface-flawed specimens tested in the specimen configuration effect tests are represented in Figures 6-14 and 6-15 by solid circles. The data plots show that consistent fracture toughness values were obtained for all material/environment combinations from specimens thicker than about  $1.0 (K_{IE}/\sigma_{ys})^2$ .

Flaw growth prior to specimen fracture was observed only during room temperature tests of the thinnest surface-flawed specimens. In 0.125 inch (0.138 cm) thick aluminum specimens containing flaws with  $a/2c = 0.25$  and  $a/t = 0.8$ , the flaws were observed to grow through the specimen thickness prior to the onset of unstable flaw propagation. In Specimen 3A3R-2 (Table 6-6), the flaw penetrated the specimen thickness at a gross stress level of 46.5 ksi (320.6 MN/m<sup>2</sup>). Applied load was then held constant for five minutes while the flaw was observed through a magnifying glass. No flaw growth could be detected under constant load. The load was then increased until the specimen failed at 50.5 ksi (348.2 MN/m<sup>2</sup>). In specimen 3A3R-1, (Table 6-6), the flaw penetrated the specimen thickness at a gross stress level of 50.9 ksi (351.0 MN/m<sup>2</sup>). The stress was then held constant for twenty seconds during which time the flaw grew sufficiently to result in failure of the specimen. In 0.125 inch (0.318 cm) thick aluminum specimens containing flaws with  $a/2c = 0.10$  and  $a/t = 0.70$ , i.e., 3A1R-1 and -2, a slight amount of dimpling was observed on the back specimen face opposite the flaw tip. However, the flaw did not penetrate the specimen thickness prior to failure. Specimens tested at -320°F (78°K) and -423°F (20°K) were completely submerged in the test media and could not be visually monitored. However, there was indirect evidence that flaws in the 0.02 inch (0.051 cm) thick titanium specimens tested at -423°F (20°K) grew through the specimen thickness at loads less than the fracture load. While loading at a constant rate of head travel, a reasonably abrupt interruption in the rate of load increase was noted at a load less than the failure load, after which the test specimen became more compliant. The observed change in load rate behavior probably occurred when the flaw grew through the specimen thickness. Other -423°F (20°K) test data have been published (3) for 0.02 inch (0.051 cm) thick 5Al-2.5Sn(ELI) titanium surface-flawed specimens that indicate surface flaws deeper than 60 percent of the specimen thickness can be expected to grow through the specimen thickness at loads less than the failure load.

The effect of flaw shape on  $K_{IE}$  values was small. There was a slight tendency for specimens containing flaws with  $a/2c = 0.10$  to yield smaller  $K_{IE}$  values than specimens containing flaws with  $a/2c = 0.25$ . This trend is in agreement with a stress intensity analysis for surface-flawed specimens (15) that shows for constant  $a/t$ , the ratio of applied stress intensity to load increases moderately for decreasing  $a/2c$ . Since Equation (1) does not account for this effect, there appeared to be a small effect of  $a/2c$  on  $K_{IE}$  values in the test results as seen in Figures 6-14 and 6-15.

The data in Figures 6-14 and 6-15 can be used to draw some conclusions with respect to crack depth and specimen thickness requirements for 2219-T87 aluminum and 5Al-2.5Sn(ELI) titanium surface-flawed specimens. Most of the data were developed by testing specimens with  $a/t \simeq 0.5$ . Since consistent fracture toughness values were obtained for specimens thicker than about  $1.0 (K_{IE}/\sigma_{ys})^2$ , it is concluded that a characteristic fracture toughness value ( $K_{IE}$ ) can be used to predict fracture strength of surface-flawed structure for which both crack depth and depth of ligament between the flaw tip and back specimen face are greater than  $0.5 (K_{IE}/\sigma_{ys})^2$ . In four of five material/environment combinations tested, the characteristic fracture toughness had a numerical value that was in agreement with  $K_{Ic}$  values determined according to Reference 18 requirements. The excepted material/environment combination is 5Al-2.5 Sn(ELI) titanium/LN<sub>2</sub> for which  $K_{Ic}$  values were less than  $K_{IE}$  values determined from SF tests.

### 6.3 SUMMARY AND RECOMMENDATION

This experimental program provides the first comparison between plane strain fracture toughness data obtained from tests of both surface-flawed and through-cracked fracture specimens for a single direction of crack propagation. Good agreement was obtained between fracture toughness data derived from tests of 2219-T87 aluminum surface-flawed (SF), single-edge-notched-bend (SENB), and single-edge-notched-tension (SENT) specimens at 72°F (295°K), -320°F (78°K) and -423°F (20°K). However, fracture toughness values derived from tests of 2219-T87 aluminum compact tension (CT) specimens were consistently lower than the other aluminum alloy data. Similar tests of

5Al-2.5Sn(ELI) titanium SF, SENB, SENT and CT specimens yielded fracture toughness data that showed reasonable agreement at  $-423^{\circ}\text{F}$  ( $20^{\circ}\text{K}$ ); however, at  $-320^{\circ}\text{F}$  ( $78^{\circ}\text{K}$ ) fracture toughness data from tests of SF specimens were higher than data obtained from tests of SENB, SENT and CT specimens.

Fracture tests of 2219-T87 aluminum and 5Al-2.5Sn(ELI) titanium SF specimens in which specimen thickness was varied yielded consistent fracture toughness values for specimens in which both flaw depth and distance between the flaw tip and back specimen face exceeded  $0.5 (K_{IE} / \sigma_{ys})^2$ , and flaw depth was approximately 50 percent of the specimen thickness. The fracture toughness values were in good agreement with plane strain fracture toughness data determined from tests of SENB and SENT specimens for 2219-T87 aluminum at  $72^{\circ}\text{F}$  ( $295^{\circ}\text{K}$ ),  $-320^{\circ}\text{F}$  ( $78^{\circ}\text{K}$ ) and  $-423^{\circ}\text{F}$  ( $20^{\circ}\text{K}$ ), and from tests of SENB, SENT, and CT specimens for 5Al-2.5Sn(ELI) titanium tested at  $-423^{\circ}\text{F}$  ( $20^{\circ}\text{K}$ ). For 5Al-2.5Sn(ELI) titanium at  $-320^{\circ}\text{F}$  ( $78^{\circ}\text{K}$ ) fracture toughness values from tests of SF specimens were greater than plane strain fracture toughness values determined from tests of SENB, SENT and CT specimens.

These tests show that fracture toughness values from tests of specimens designed to yield plane strain fracture toughness can vary with specimen configuration. Consequently, it is recommended that fracture toughness data for use in design applications be developed using specimen configurations that simulate potential failure origins. For example, part-through cracks are best simulated by surface-flawed specimens and through-the-thickness cracks by specimens containing through-the-thickness cracks.



**Page Intentionally Left Blank**

## 7.0 FRACTURE AT FLAWS IN RESIDUAL STRESS FIELDS

Crack growth in residual stress fields is a problem of considerable practical significance. For example, fusion welds are a common source of both crack-like defects and residual stresses. Hence, potential detrimental effects of residual stresses on subcritical crack growth and crack stability must be quantitatively understood so that better estimates of quality requirements and service performance can be made for welded aerospace structure. This experimental program was undertaken to study the effects of weld-induced residual stresses on crack stability in 2219-T87 aluminum and 5Al-2.5Sn(ELI) titanium alloys. Both static fracture and fatigue tests were conducted on specimens containing surface flaws in residual stress fields. Static fracture tests are summarized in Table 7-1 and 7-2 and fatigue tests are summarized in Table 7-3. Prior to initiation of the test programs, a literature review was undertaken to collect existing knowledge on the effect of residual stresses on fracture and crack growth in metallic structures. The resulting information is summarized in Section 7-1. A method for quantitatively evaluating residual stress effects on flaw stability was then selected as described in Section 7.2. The method was evaluated using results of the experimental program for which procedures are described in Section 7.3 and results are presented and interpreted in Section 7.4.

### 7.1 BACKGROUND

Previous investigations dealing with residual stresses have been directed to:

- (1) measurement of magnitudes and distributions of residual stresses in welds;
- (2) determination of effects of weld-induced residual stresses on brittle fracture characteristics of welded specimens; and
- (3) development of methods for calculating magnitudes and distributions of weld-induced residual stresses.

Considerable information has been collected concerning magnitudes and distributions of residual stresses at butt welds in mild steel alloys. A typical residual stress pattern (19) for flat butt welded steel plates is schematically illustrated in Figure 7-1 where it can be seen that the maximum residual stress is tensile

and acts parallel to the weld axis. In carbon steel weldments, the maximum tensile residual stresses are usually as high as the yield stress of the weld metal. In high strength steel weldments, the maximum residual stress is usually less than the weld metal yield strength. A limited amount of residual stress data has been developed for welds in aluminum and titanium alloys (20 through 24). Distributions of residual stress in an aluminum and titanium alloy are pictured in Figures 7-2 and 7-3 respectively. In aluminum alloys, the weld metal yield strength is often less than the parent metal yield strength and the longitudinal tensile residual stresses are maximum in the heat affected zone rather than at the weld centerline.

Most experiments undertaken to determine effects of weld residual stresses on brittle fracture of weldments have been performed on mild steel alloy specimens. Fracture of steel weldments under low applied stress has been demonstrated by several investigators (25 through 28). Tests are usually conducted at low temperatures on specimens consisting of pairs of rectangular plates joined by butt welding after placing saw cut notches in the prepared edges. The general trend of results derived from such tests has been diagrammatically summarized by Kihara and Masubuchi (29) as illustrated in Figure 7-4. Smooth unnotched specimens fracture at the ultimate strength of the material at the appropriate temperature as illustrated by curve PQR. Sharply notched specimens containing no residual stress fail at stresses indicated by curve PQST. At temperatures in excess of the transition temperature ( $T_f$ ), a shear fracture occurs at stress levels in excess of the yield strength. At temperatures below  $T_f$ , fracture results at stress levels near the yield strength of the material. Specimens containing notches located in high tensile residual stress fields can fracture in one of three different manners. At temperatures greater than  $T_f$ , fracture occurs at the ultimate strength of the material and residual stresses have no effect on fracture stress. At temperatures lower than  $T_f$  but higher than the crack arresting temperature ( $T_a$ ), crack propagation may initiate at low stress levels and then arrest after propagating a short distance. Fracture initiation is influenced by both local damage to the material at the notch tip and residual stresses whereas subsequent crack propagation is influenced primarily by residual stresses. At temperatures lower than  $T_a$ , the fracture behavior is dependent on the stress level at which

crack propagation initiates. If the initiation stress is below the curve VW, the crack will arrest after propagating a short distance. Complete fracture will then occur at or near the yield stress of the material. If the initiation stress is above the curve VW, complete fracture occurs without any further increase in stress level.

Wide steel plate brittle fracture tests conducted by Hall, et al., (28), have shown that propagating cracks can be arrested by residual compressive stresses. Machined notches in the sides of the plate specimens were filled with weld metal to generate residual tensile stresses at the edges of the plate and residual compressive stresses in the central region. The specimens were subjected to small tensile stresses in a test machine, and crack propagation was initiated by impacting a wedge inserted into a starter notch in the tensile residual stress field at the edge of the specimen. It was observed that after the tip of the propagating crack entered the residual compressive stress field, the rate of crack propagation decelerated until the crack arrested. It was also noted that the minimum applied load at which crack propagation could be initiated was significantly less than that required for test specimens in which the starter notch was not located in a residual tensile stress field.

Both mechanical and thermal stress relieving have been used to increase the fracture strength of notched and welded steel plate specimens. Wells (25) and Kihara (29) have both demonstrated that the effect of a prior prestress at temperatures above the transition temperature is to elevate subsequent low temperature fracture strengths to stress levels equal to or greater than the prestress. This increase in strength has been attributed to a reduction in residual stress due to mechanical stress relief. Greene (31) and Kennedy (32) have shown that fracture strengths of notched and welded steel specimens could be significantly elevated by a furnace stress relief at 1200°F (922°K). The beneficial effect of the thermal stress relief has been attributed (33) to the combined effects of lowered residual stresses and reduction in embrittlement at the tip of the prepared notches.

Tests designed to determine the effect of residual stresses on crack growth in titanium alloys 6Al-4V, 8Al-1Mo-1V, and 5Al-2.5Sn have been reported by

Robelotto et al., (24). Through-the-thickness fatigue cracks were propagated through the longitudinal residual compressive stress field adjacent to longitudinally oriented welds. It was observed that fatigue crack growth rates were significantly less when the crack tip was located in a residual compressive stress field than when the crack tip was located in a stress field free of residual stresses.

Wells (33), Boyd (34), and Masubuchi (35) have applied fracture mechanics to the study of the effects of residual stress on fracture of notched weldments. In the most recent analysis by Wells (33), the combined effect of residual and load stresses on stress intensity were calculated for centrally cracked specimens containing a longitudinally oriented butt weld at the center of the specimen (Figure 7-5a). The contributions to stress intensity from applied stress ( $K_p$ ) and residual stress ( $K_R$ ) were calculated from the formulae

$$K_p = \sigma_p \left[ W \tan \left( \frac{\pi a}{W} \right) \right]^{1/2}$$

$$K_R = 2 \left( \frac{a}{\pi} \right)^{1/2} \int_0^a \frac{\sigma_R dx}{(a^2 - x^2)^{1/2}}$$

where 'a' is the half crack length, W is plate width,  $\sigma_p$  is applied stress, and  $\sigma_R$  is residual stress. Calculations were made for fixed grip conditions and the resultant decrease in  $\sigma$  with increase in crack length was taken into account. Typical stress intensity versus crack length curves are shown in Figure 7-5b. Individual curves are shown for residual stress only, for an applied stress of 10 ksi and for combined applied and residual stress. For applied stress levels less than about 10 ksi and half crack lengths between about 2 and 10 inches (4.9 and 25 cm), the total applied stress intensity tends to decrease with increasing crack length. This result is consistent with the experimental observations that cracks initiating from butt welds at very low stress levels tend to arrest after propagating short distances.

In summary, the foregoing information from the literature shows that:

1. Weld-induced residual stresses affect fracture strength and fatigue crack growth rates for precracked test specimens.
2. Thermal and mechanical stress relief treatments can increase fracture strength of flawed weldments through lowering residual tensile stress levels.
3. Fracture mechanics theory can be used to assess potential effects of residual stresses on growth of crack-like defects in weldments.

## 7.2 ANALYSIS

In the following analysis, the stress intensity factor defined by linear elastic fracture mechanics will be used to superpose the effects of applied and residual stress on stability of cracks. Stress intensity is related to both applied stress and relative displacement of the crack surfaces and appears to be the most attractive parameter with which to correlate effects of both residual and applied stress on crack stability.

Quantitative analyses of potential residual stress effects on fracture of welded structure must account for several variables including: material properties (yield and ultimate strength, fracture toughness, strain rate sensitivity), metallurgical conditions (strain aging effects, cooling rate effects), and residual stresses (magnitude and distribution). The roles of the above variables in stability analyses of cracks is illustrated by the following qualitative analysis of the structure shown in Figure 7-6a in which a butt weld is located at the center of an infinitely wide plate. The plate is subjected to a fixed stress acting parallel to the butt weld. If a through-the-thickness crack propagates as shown, stress intensity at the crack tip due to applied and residual stress is related to crack length by the following expressions:

$$K_{IP} = \sigma_p \sqrt{\pi a}$$

$$K_{IR} = 2 \left( \frac{a}{\pi} \right)^{1/2} \int_0^a \frac{\sigma_R(x) dx}{\sqrt{a^2 - x^2}}$$

where  $K_{IP}$  and  $K_{IR}$  are stress intensity factors due to applied stress ( $\sigma_p$ ) and residual stress ( $\sigma_R$ ). Figure 7-6b schematically illustrates typical distributions of  $K_{IP}$  and  $K_{IR}$  for the through cracked butt welded structure shown in Figure 7-6a. Figure 7-6b also includes curves depicting stress intensity levels required to initiate unstable crack propagation ( $K_{cr}$ ), and stress intensity levels at which unstable crack propagation could be expected to arrest ( $K_{ar}$ ). The variations in  $K_{cr}$  and  $K_{ar}$  illustrate possible differences in properties between the cast weld metal (WM), wrought plate material (PM), and heat-affected zone (HAZ) which is subjected to variable maximum temperatures and cooling rates during the welding process. In strain rate sensitive materials,  $K_{ar}$  is usually less than  $K_{cr}$ . Testing of precracked specimens has shown that fracture originates when stress intensity at the crack tip reaches the critical stress intensity value for the particular material and thickness used in the tests. Hence, the failure criterion is:

$$K_{IR} + K_{IP} = K_{cr}$$

If the butt welded plate shown in Figure 7-6a is loaded at a constant rate to a maximum applied stress of  $\sigma_o$ , fracture characteristics are dependent on initial crack length and relative magnitudes of  $K_{cr}$ ,  $K_{ar}$  and  $K_{IT}$  where  $K_{IT} = K_{IR} + K_{IP}$ . If  $K_{IT}$  is less than  $K_{cr}$  at  $\sigma_o$ , rapid crack propagation would not be expected to initiate, if  $K_{IT}$  reaches  $K_{cr}$  at a stress level less than  $\sigma_o$ , rapid crack propagation would initiate during loading. If rapid crack propagation does initiate, one of three possible crack propagation modes will occur: (1) if the  $K_{IT}$  curve lies above the  $K_{ar}$  curve for all crack lengths in excess of the initial value, crack propagation will not arrest; (2) if the  $K_{IT}$  curve crosses and drops below the  $K_{ar}$  curve, crack

propagation will arrest at a crack length of  $a_1$ , as illustrated in Figure 7-6b. If crack arrest occurs at or near  $\sigma_o$ ,  $K_{IT}$  could remain less than  $K_{cr}$  for applied stresses equal to or less than  $\sigma_o$  and no further crack propagation would ensue; (3) if applied stress is increased a sufficient amount after crack arrest, then  $K_{IT}$  could be increased to the  $K_{cr}$  level and rapid crack propagation would once again initiate. All of the foregoing fracture characteristics have been observed in tests of center-cracked butt welded steel plates as noted in Section 7.1.

The foregoing analysis can be extended to include surface or internal defects as potential failure origins. Such an analyses would change the characteristics of the  $K_{IT}$  curve in Figure 7-6b but would not alter the conclusions resulting from this analysis.

In summary, it appears that effects of residual stresses on crack stability and subcritical crack growth can be estimated by accounting for the effects of stress intensity due to both applied and residual stresses. Stress intensity due to residual stresses can be calculated by solving the stress problem in which stresses equal and opposite to residual stresses that would have existed at the crack locus in an uncracked structure are applied to the crack surfaces. In practice, residual stress magnitudes and distributions are not usually precisely known and so potential effects of residual stresses on crack stability will have to be estimated. However, it is better to make reasonable estimates than to ignore the problem completely.

The foregoing conclusions will now be evaluated in light of results from the following test program.

### 7.3 TEST PROGRAM AND PROCEDURES

An experimental program was undertaken to investigate the effects of weld-induced residual stresses on flaw growth in 5Al-2.5Sn(ELI) titanium and 2219-T87 aluminum alloys. Residual stress effects on both fracture initiation under monotonically increasing loads, and on flaw growth rates under cyclically varying loads were studied. Static fracture tests and cyclic loading tests are discussed separately in the following two sub-sections.



### 7.3.1 Static Fracture Tests

Test programs for studying effects of residual stresses on fracture initiations in 5Al-2.5Sn(ELI) titanium and 2219-T87 aluminum are summarized in Tables 7-1 and 7-2 respectively. Each program was divided into three series of tests.

Test Series I for the titanium alloy was designed to investigate the effects of residual stresses on fracture initiation at embedded flaws in GTA welds. Surface-flawed test specimens were fabricated as shown in Figure 7-7. Specimens were machined from GTA welded panels and stress relieved using a 1300°F (978°K) - one hour retort cool thermal cycle. Weld procedures are included in Appendix A. Surface-flaws were placed at the GTA weld centerline with the flaw plane parallel to the weld axis. Two different flaw depth-to-thickness ratios were tested in an attempt to effect fractures at gross stress levels both slightly below, and well below the uniaxial yield stress of the weld metal. Subsequent to flaw preparation, specimens were electron beam (EB) welded as shown in Figures 7-7 and 7-8 to generate residual stresses at the flaw location. Gage area widths were then reduced from 6 to 4 inches (15.2 to 10.2 cm) for the specimens containing circular EB welds, and from 9 to 6 inches (22.9 to 15.2 cm) for specimens containing the linear EB welds in the flaw plane.

Residual stress measurements were made using 6 inch by 12 inch (15.2 by 30.5 cm) test panels fabricated using procedures identical to those used in fabricating Series I test specimens. Measurements were made using the hole drilling compliance technique (35) in which measurements are made of strain relaxation resulting from drilling a flat bottomed hole in successive increments at the location where residual stresses are to be measured. The center of the 0.125 inch (3.18 mm) diameter drill hole coincided with the intersection of center lines drawn longitudinally through two mutually perpendicular strain gages positioned such that their active grid edges were located  $5/32 \pm 0.010$  inch ( $4 \pm .25$  mm) from the hole center. Incremental strain gage readings were read from an Automatron Industries Model P-350 strain indicator during interruptions in drilling. Readings were taken after each 0.005-inch (0.13 mm) increment up to a depth of 0.050 inch (1.27 mm) and after each 0.010-inch (0.25 mm) increment thereafter. Holes were

drilled from only one side of each panel and it was assumed that the residual stress distributions were symmetrical with respect to mid-plane of the panel. The resultant distributions of calculated residual stress are illustrated in Figure 7-9. The transverse residual stresses in the stress relieved weld were less than 2 ksi ( $13.8 \text{ MN/m}^2$ ) except over a 0.02-inch (5 mm) layer next to the panel surface where the stresses increased to about 6.5 ksi ( $44.8 \text{ MN/m}^2$ ). In the panels with the circular EB welds, transverse and longitudinal stresses of 19 ksi ( $131 \text{ MN/m}^2$ ) were measured. In the panels with the linear EB welds, peak transverse residual stresses of about 29 ksi ( $200 \text{ MN/m}^2$ ) were measured. It was concluded that, at the flaw location in the test specimens, the circular EB welds generated transverse tensile residual stresses of about 17 ksi ( $117 \text{ MN/m}^2$ ), and the linear EB welds induced residual compressive stresses of about -30 ksi ( $-207 \text{ MN/m}^2$ ).

Test series II for the 5Al-2.5Sn(ELI) titanium alloy was very similar to test series I except that the surface flaws were located in base metal rather than weld metal. Residual stresses generated at the flaw location in Series II specimens were taken to be the same as those measured for the Series I specimens.

Titanium test series III was designed to investigate the effects of longitudinal weld residual stresses on fracture initiation at surface flaws oriented perpendicular to the longitudinal weld axis. Surface-flawed test specimens were prepared as shown in Figure 7-10. After each specimen was machined to the configuration shown, a two pass GTA weld was deposited without edge preparation. One pass was laid from each side of the specimen with the first pass penetrating to 100 percent of the specimen thickness, and the second pass penetrating to 90 percent of the specimen thickness. The weld beads were ground flush in the specimen gage areas. Weld procedures are included in Appendix A. The magnitude of longitudinal weld residual stresses in each specimen was controlled by subjecting test specimens to different thermal cycles. Maximum residual stresses were obtained by leaving specimens in the as-welded condition. A  $1000^\circ\text{F}$  ( $811^\circ\text{K}$ ) 4 hour retort cool thermal cycle was used to partially relieve residual stresses in some specimens. Other specimens were fully stress relieved using a  $1300^\circ\text{F}$  ( $978^\circ\text{K}$ ) one hour retort cool thermal cycle. Surface flaws were introduced at the geometric center of

the test specimens after application of the required thermal cycle. Flaw planes were oriented perpendicular to the longitudinal weld axis. Cyclic stress used to fatigue extend EDM starter notches was kept sufficiently low so that the sum of cyclic and residual stress was less than the weld metal uniaxial yield stress.

Residual stress measurements were made at the geometric center of one as-welded, one partially stress relieved, and one fully stress relieved weld panel using the hole drilling compliance technique. The measured distributions of residual stress are included in Figure 7-11. Residual stress levels were reasonably constant up to a depth of 0.07 inch (1.78 mm). The peak longitudinal stress for the as-welded condition was 70 ksi ( $483 \text{ MN/m}^2$ ). The thermal cycle of  $1000^\circ\text{F}$  ( $811^\circ\text{K}$ ) for 4 hours reduced the peak longitudinal stress to 24 ksi ( $165 \text{ MN/m}^2$ ). The thermal cycle of  $1300^\circ\text{F}$  ( $978^\circ\text{K}$ ) for one hour completely stress relieved the weld and reduced the peak tensile longitudinal stress to 0.4 ksi ( $3 \text{ MN/m}^2$ ).

Test Series I and II for the 2219-T87 aluminum alloy were identical to Series I and II for the titanium alloy except for necessary changes in weld procedures, specimen dimensions and flaw sizes. Test specimens were prepared using the configuration and production sequences summarized in Figure 7-7. In Series I specimens, flaws were located at the GTA weld centerline. In Series II specimens, the weld was omitted and flaws were located in base metal. Details of the EB welding used to generate the residual stresses are included in Figure 7-12.

Residual stress measurements made in 8-inch (20.3 cm) square test panels fabricated using procedures identical to those employed in fabricating specimens for the Series I aluminum alloy tests are summarized in Figures 7-13 and 7-14.

Test Series III for the 2219-T87 aluminum alloy was undertaken to investigate the effects of residual stress on failure initiation at internal-lack-of-fusion flaws in GTA welds. Test specimens were cut from one-inch (2.5 cm) thick weld panels prepared according to Figure 7-15. First, weld parameters were developed to produce full penetration two-pass square butt weld. When the panels were welded, the current required for complete penetration was manually reduced over 3.5 inches (8.9 cm) lengths in order to produce the lack of fusion defects. Details of the welding procedure are included in Appendix A. A typical internal flaw is illustrated in Figure 7-15.

Residual stress levels at the location of the internal flaw were varied through using EB welding as was done for the Series I and II tests. EB welding details are included in Figure 7-16. No residual stress measurements were made for the internally flawed specimens.

### 7.3.2 Fatigue Tests

The test program for studying effects of tensile residual stresses on cyclic flaw growth rates is summarized in Table 7-3. Surface-flawed specimens containing flaws located in base metal at the center of a circular EB weld were cycled at three different temperatures; ambient,  $-320^{\circ}\text{F}$  ( $78^{\circ}\text{K}$ ), and  $-423^{\circ}\text{F}$  ( $20^{\circ}\text{K}$ ). Fabrication procedures were identical to those used for manufacturing Series II test specimens in the static fracture test programs.

## 7.4 DESCRIPTION AND INTERPRETATION OF RESULTS

### 7.4.1 Titanium Alloy Static Fracture Tests

Failure stress, flaw dimensions and specimen dimensions for each 5Al-2.5Sn(ELI) titanium test specimen are listed in Tables 7-4, 7-5 and 7-6. Each table contains data for a given test series. Relationships between gross applied stress at fracture and residual stress at the flaw location are included in Figures 7-17 and 7-18.

The test data show that residual stresses can have a significant effect on fracture strength of surface-flawed specimens. This is most strongly evidenced by the test data for Series I and II specimens shown in Figure 7-17. For specimens containing flaws with  $(a/t)$  greater than 50 percent, the applied stress required to fracture the specimen increased with decrease in residual stress in such a way that the sum of applied and residual stress at fracture was reasonably constant for all specimens. For specimens containing flaws with  $(a/t)$  less than 50 percent, the applied stress required to fracture the specimens increased with decreasing residual stress until the applied stress reached the yield stress of the flawed material. Further reduction of residual stress had no effect on failure stress.

Since the spread between yield and ultimate strength is small for both titanium alloy parent metal and weld metal, it is not possible to obtain fracture stresses much in excess of yield stress, particularly in the presence of flaws.

A review of the data in Figure 7-18 for titanium alloy Test Series III led to the speculation that thermal cycles used to vary residual stress levels also effected changes in fracture toughness of the titanium welds. To evaluate this possibility, six single-edge-notched-tension (SENT) specimens were prepared and tested. Specimens were precracked along the weld centerline as shown in Figure 7-19. Two specimens were subjected to a 1300°F (978°K)/one hour/retort cool thermal cycle; two other specimens were subjected to a 1000°F (811°K)/4 hour/retort cool thermal cycle; two additional specimens were left in the as-welded condition. All specimens were instrumented with a clip gage and fractured at -320°F (78°K). Test results are summarized in Table 7-7 and redrawn load-displacement records are included in Figure 7-20.  $P_Q$  loads correspond to points at which a 5 percent secant offset intersects the test record and  $K_Q$  values were calculated by substituting  $P_Q$  loads into the SENT stress intensity formula included in Figure 6-6. It is evident that both the 1300°F (978°K) and 1000°F (811°K) thermal cycles decreased the fracture toughness of the welds. The 1000°F (811°K) thermal cycle was particularly detrimental.

Test results were used to evaluate the validity of a failure criterion for surface flaws subjected to combined applied and residual stresses. The criterion was based on the assumption that failure would occur when

$$K_{IR} + K_{IP} = K_{cr} \quad (7-1)$$

where  $K_{IR}$  and  $K_{IP}$  are stress intensities corresponding to residual stress ( $\sigma_R$ ) and load stress ( $\sigma_P$ ), and  $K_{cr}$  is the critical stress intensity or fracture toughness of the flawed material. Stress intensities due to residual stresses were calculated

using Equation 2-2 with  $\sigma = \sigma_R$ . This procedure is strictly applicable when residual stress that would have existed at the flaw location in the absence of the flaw are uniform over the entire area occupied by the flaw, and the presence of the flaw does not perturb the source of residual and/or applied stresses. It is believed that both of these conditions were satisfied by Series I and II titanium alloy specimens. These specimens were designed so that the source of residual stresses (the EB welds) were several crack dimensions away from the surface crack. Hence, residual stresses were undoubtedly reasonably uniform at the crack area and local deformations due to the presence of the crack had a negligibly small effect on the incompatible strains in the EB weld. In Series II titanium alloy test specimens,  $\sigma_R$  was taken to be uniform over the crack surface and equal to the peak value measured at the weld centerline. Since the distribution of longitudinal residual stresses in Series III specimens was similar to that illustrated in Figure 7-3 and flaw length was equal to a slightly greater than weld bead width, this procedure probably resulted in small over-estimates of  $K_{IR}$  for Series III specimens.

Previous tests (1,3) have shown that fracture toughness of 5Al-2.5Sn(ELI) titanium alloy surface-flawed specimens is reasonably constant for failure stresses less than about 90 percent of the uniaxial yield strength. In Series I and II titanium alloy tests, specimens containing flaws with  $a/t$  less than 50 percent failed at stress levels (applied plus residual) greater than 90 percent of yield strength and specimens containing flaws with  $a/t$  greater than 50 percent failed at stress levels less than 90 percent of yield strength. Hence, only results obtained from tests of specimens with similar flaw sizes were directly compared.

In Series I and II tests,  $K_{cr}$  values listed in Tables 7-4 and 7-5 are in reasonable agreement for all " $a/t > 0.5$ " specimens regardless of the residual stress level. For welds,  $K_{cr}$  varied from 103 to 127 ksi  $\sqrt{\text{in}}$  (113 to 140 MN/m<sup>3/2</sup>). For base metal,  $K_{cr}$  ranged from 94 to 113 ksi  $\sqrt{\text{in}}$  (103 to 124 MN/m<sup>3/2</sup>). If residual stresses are not accounted for in  $K_{cr}$  calculations, i.e., if  $K_{cr}$  is assumed to be equal to  $K_{IP}$ ,  $K_{cr}$  values range from 86 to 154 ksi  $\sqrt{\text{in}}$  (95 to 169 MN/m<sup>3/2</sup>) for weld metal and from 81 to 136 ksi  $\sqrt{\text{in}}$  (89 to 149 MN/m<sup>3/2</sup>) for base metal. For " $a/t < 0.5$ " specimens,  $K_{cr}$  values were in reasonable agreement for all specimens

except those containing residual compressive stresses at the flaw location (RC-1, RC-2, RMC-1 and RMC-2). Since the excepted specimens failed at applied net stress levels at or above the uniaxial yield strength, residual stress had probably been mechanically relieved by yielding prior to failure to the extent that  $K_{IR} \approx 0$  and  $K_{cr} \approx K_{IP}$ . This possibility is substantiated by the observation that  $K_{IP}$  values at failure for the excepted specimens were in good agreement with  $K_{cr}$  values for all other specimens. Taking  $K_{cr} = K_{IP}$  for specimen width residual compressive stresses,  $K_{cr}$  varied from 97 to 104 ksi  $\sqrt{\text{in}}$  (107 to 114 MN/m<sup>3/2</sup>) for weld metal and from 93 to 104 ksi  $\sqrt{\text{in}}$  (102 to 114 MN/m<sup>3/2</sup>) for base metal. As anticipated,  $K_{cr}$  values were moderately lower for "a/t < 0.5" specimens than for "a/t > 0.5" specimens. On the basis of the foregoing results, it was concluded that Equation 7-1 is a useful criterion for evaluating potential effects of residual stresses on stability of surface flaws in 5Al-2.5Sn(ELI) titanium base metal or weld metal.

It was difficult to evaluate the applicability of Equation 7-1 to the Series III test specimens since both fracture toughness ( $K_{cr}$ ) and residual stress ( $\sigma_R$ ) were simultaneously varied by specimen processing techniques. In an attempt to estimate fracture toughness for the various surface-flawed (SF) specimens, results of SENT specimen tests summarized in Table 7-7 were used. It was decided to base estimates of fracture toughness on SENT specimen failure loads rather than  $P_Q$  loads since calculations of fracture stress for SF specimens relate to failure load. For specimens stress relieved at 1300°F (978°K) for one hour, SENT and SF specimens yielded average  $K_{cr}$  values of 69 and 89 ksi  $\sqrt{\text{in}}$  (76 and 98 MN/m<sup>3/2</sup>) respectively. It was assumed that the ratio between fracture toughness for SF and SENT specimens subjected to as-welded and 1000°F (811°K) 4 hour thermal cycles was the same as that for the 1300°F (978°K) one hour thermal cycle, i.e.,  $89/69 = 1.29$ . The resulting estimates of fracture toughness for SF specimens subjected to as-welded and 1000°F (811°K) four hour thermal cycles were  $1.29 (88) = 114$  ksi  $\sqrt{\text{in}}$  (125 MN/m<sup>3/2</sup>) and  $1.29 (58) = 75$  ksi  $\sqrt{\text{in}}$  (82 MN/m<sup>3/2</sup>).

The estimated fracture toughness of 75 ksi  $\sqrt{\text{in}}$  (82 MN/m<sup>3/2</sup>) for SF specimens

RLR-1 through -4 is in good agreement with  $K_{cr}$  values calculated using Equation 7-1 and included in Table 7-6. This result indicates that Equation 7-1 properly accounted for the effect of residual stress on fracture initiation in these tests.

For the as-welded specimens, the sum of applied plus peak residual stress (70 ksi or  $483 \text{ MN/m}^2$ ) reached the weld metal yield strength of 184 ksi ( $1268 \text{ MN/m}^2$ ) well before the specimens failed. For specimens RLT-1 and RLT-2, this behavior would be expected if the estimated fracture toughness of  $114 \text{ ksi}\sqrt{\text{in}}$  ( $125 \text{ MN/m}^{3/2}$ ) is reasonably accurate since failure stresses calculated using Equation 2-2 and  $K_{IE} = 114 \text{ ksi}\sqrt{\text{in}}$  are about 215 ksi ( $1490 \text{ MN/m}^2$ ). Similar calculations of failure stress for specimens RLT-3 and RLT-4 yielded an estimated failure stress of 178 ksi ( $1227 \text{ MN/m}^2$ ). Since the estimated peak residual stress level was 70 ksi, use of Equation 7-1 would lead to an estimated applied stress at failure of  $(178-70) = 108 \text{ ksi}$  ( $745 \text{ MN/m}^2$ ) as compared to the actual failure stresses of 130 and 140 ksi ( $896$  and  $965 \text{ MN/m}^2$ ). Although actual failure stresses were higher than estimated values, they were significantly lower than failure stress estimated without accounting for residual stress, i.e., 178 ksi ( $1227 \text{ MN/m}^2$ ). This discrepancy is not surprising since the 70 ksi ( $483 \text{ MN/m}^2$ ) is a peak residual stress value and some areas of the flaw were undoubtedly under the influence of residual stresses somewhat smaller than the peak value (see Figure 7-11).

In summary, residual stresses were shown to have a significant effect on fracture stress of surface-flawed specimens fabricated from 5Al-2.5Sn(ELI) titanium alloy. For specimens in which failure stresses were elastic, residual stresses at the flaw location changed the applied fracture stress by an amount equal to the residual stress. Tensile and compressive residual stresses respectively lowered and elevated applied fracture stress relative to residual-stress-free specimens. For specimens in which yield stress levels were reached prior to failure, residual stresses had a smaller effect on applied fracture stress than in specimens in which no yielding occurred. Finally, it was found that the effect of residual stress on applied fracture stress of surface-flawed specimens could be quantitatively evaluated using Equation 7-1.

The foregoing information leads to the conclusion that residual stresses should be taken into account in estimates of critical flaw sizes for peak proof test stress levels. Tensile residual stresses can reduce critical flaw sizes from those calculated for nominal stress fields and place more stringent requirements on sensitivity of non-



destructive inspection techniques required to avoid proof test failures. If the peak nominal proof stress levels are at or near the yield strength of the parent metal, mechanical stress relieving should substantially reduce both the magnitude and effects of tensile residual stresses during subsequent loadings. If peak proof stress levels are significantly below the parent metal yield strength, tensile residual stresses may be unaffected by the proof overload and continue to reduce critical flaw sizes during subsequent operation of the structure.

#### 7.4.2 Aluminum Alloy Static Fracture Tests

Test results for 2219-T87 aluminum Test Series I, II and III are included in Tables 7-8, 7-9 and 7-10 respectively. The first group of specimens listed in each table were tested in either the as-rolled (base metal specimens) or as-welded (weld metal specimens) conditions to provide baseline data against which to compare data for specimens containing superimposed tensile or compressive residual stresses. Residual stress measurements were made only up to depths of 0.07-inch (1.78 mm) from the specimen surfaces and the resulting residual stress trends (shown in Figures 7-13 and 7-14) were not sufficiently well established to be reliably extrapolated to the interiors of the test specimens. Accordingly, the tables of results contain indications of relative residual stress levels thought to exist in the vicinity of the flaw prior to load application.

Two Series I test specimens (RASR-1 and RASR-2) were instrumented with clip gages to obtain continuous recordings of load versus flaw-opening displacement at the centerline of the surface of each specimen. Since flaw-opening displacement is related to flaw size (6), the test records (shown in Figure 7-21) provide indicators of flaw size throughout each test. There was no evidence of an abrupt flaw size instability at loads less than the failure load and the test records began to exhibit considerable nonlinearity at loads above about 80 kips (355 kN). Other unreported tests of surface-flawed 2219 welds have shown that under rising loads, flaw extension starts to occur at stress intensity levels above 12-15 ksi  $\sqrt{\text{in}}$  (13 to 16 MN/m<sup>3/2</sup>). Stress intensity corresponding to the 80 kip (356 kN) load in these tests was about 12.5 ksi  $\sqrt{\text{in}}$  (13.7 MN/m<sup>3/2</sup>) and so the nonlinearity of the test records is probably largely due to increase in flaw size with increasing load. Accordingly,  $K_{cr}$  values were not calculated for the 2219-T87 aluminum specimens subjected to combined load and residual stresses since flaw size at failure was uncertain.

The most significant results of the aluminum alloy tests can be summarized as follows:

1. Methods used to generate residual compressive stresses had very little effect on failure stress of surface- and internally-flawed weld metal, and surface-flawed base metal.
2. Methods used to generate residual tensile stresses had opposite effects on failure stress of welded and parent metal test specimens. For surface- and internally-flawed weld metal, failure stresses were lowered by 1-7 ksi (28-48 MN/m<sup>2</sup>) or about 4 - 25%. In parent metal specimens, failure stresses were increased by 9 ksi (62 MN/m<sup>2</sup>) or about 28%. This increase was probably due to a redistribution of load paths within the test specimen due to yielding of the circular EB weld. The EB weld had a lower yield strength than the surrounding parent metal and was subjected to yield stress levels at about 60 percent of the failure load. After yielding, the weld became more compliant than the surrounding base metal and diverted load away from the flaw location.

Effects of residual stress on fracture of 2219-T87 aluminum flawed specimens could not be quantitatively evaluated for the following reasons:

1. Magnitudes and distributions of residual stress in the interiors of the test specimens were uncertain.
2. All specimens failed at net section stress levels in excess of the weld metal uniaxial yield stress. The resulting mechanical stress relieving and load path alterations could not be quantitatively evaluated.

These tests show that for 2219 aluminum welds less than one inch (2.5 cm) thick, very large flaws are required to effect fracture at stress levels below the weld metal yield strength. This result was most apparent in the as-welded internally flawed specimens that contained flaw planes having an area of 9.25 square inches (592 cm<sup>2</sup>) and flaws with an area of 2.5 square inches (16.3 cm<sup>2</sup>), and still failed at gross applied stress levels near the weld metal yield strength. It was also concluded that the initial loading of flawed 2219 weld metal can result in significant amounts of flaw extension at stress levels considerably less than the failure stress. Any future evaluations of residual stress effects on 2219 welds should be directed to investigating the effect of residual stress on stress intensity level at which flaw growth initiates both during initial and subsequent loadings.

### 7.4.3 Titanium Alloy Fatigue Tests

Test results and specimen details for 5Al-2.5Sn(ELI) titanium alloy SF specimens cycled under the influence of both applied and residual stresses are summarized in Table 7-11. Specimen configuration is shown in the upper part of Figure 7-8 except that the GTA weld was omitted and the flaw was located at the center of the parent metal enclosed by the circular EB weld. The circular EB weld generated a residual tensile stress of about 19 ksi (131 MN/m<sup>2</sup>) at the flaw location. Tests were conducted at 72°F (295°K) in room air, at -320°F (78°K) in liquid nitrogen, and at -423°F (20°K) in liquid hydrogen. Specimens cycled in room air were subjected to 1000 loading cycles and were then pulled to failure. Flaw peripheries both at the beginning and termination of the test were visible on the fracture surfaces. Specimens cycled in LN<sub>2</sub> and LH<sub>2</sub> were cycled to failure. Flaw peripheries existent at failure could not be detected and only initial flaw sizes are reported in Table 7-11.

The fatigue data were evaluated using the following growth rate equation for surface flaws (11):

$$d(a/Q)/dN = C \left( \sigma_o / \sigma \right)^2 (1 + \lambda)^m (\Delta K)^n (1 - K_{\max}/K_{IE})^p \quad (7-3)$$

where:

C is a constant dependent on material and test variables;

$\sigma$  is peak cyclic stress;

$\sigma_o$  is an arbitrarily chosen peak cyclic stress for which C is evaluated;

$K_{\max}$  is peak stress intensity during a loading cycle;

$K_{\min}$  is minimum stress intensity corresponding to  $K_{\max}$ ;

$\Delta K$  is ( $K_{\max} - K_{\min}$ );

$\lambda$  is  $K_{\min} / \Delta K$ ;

$m, n, p$  are experimentally evaluated

Values of  $n = 4$ ,  $m = 2$ , and  $p = -0.2$  were found to be applicable to 6Al-4V(ELI) titanium surface-flawed specimens cycled in room air, LN<sub>2</sub>, and LH<sub>2</sub> (11), and were used to evaluate and compare the 5Al-2.5Sn(ELI) titanium results included in Table 7-11 and Reference 1.

Values of  $C$  were calculated for each specimen in Table 7-11 using the assumption that residual and applied stresses were additive, i.e.,  $K_{\max} = K_{IR} + K_{IP}$  and  $K_{\min} = K_{IR}$ . Since values of  $K_{IE}$  were not determined from the individual tests,  $K_{IE}$  values of  $120 \text{ ksi}\sqrt{\text{in}}$  ( $131.9 \text{ MN/m}^{3/2}$ ),  $94 \text{ ksi}\sqrt{\text{in}}$  ( $103.3 \text{ MN/m}^{3/2}$ ), and  $62 \text{ ksi}\sqrt{\text{in}}$  ( $68.1 \text{ MN/m}^{3/2}$ ) were used in evaluating room air,  $\text{LN}_2$  and  $\text{LH}_2$  data in Table 7-11. The  $K_{IE}$  value for room air tests was obtained from previously reported fracture toughness data (1,5) for the 5Al-2.5Sn(ELI) titanium alloy.  $K_{IE}$  values for  $\text{LN}_2$  and  $\text{LH}_2$  tests were taken from Tables 7-5 and 6-11, respectively.  $K_{IE}$  values reported for the 5Al-2.5Sn(ELI) titanium alloy tested in Reference 1 were  $120 \text{ ksi}\sqrt{\text{in}}$  ( $131.9 \text{ MN/m}^{3/2}$ ),  $61 \text{ ksi}\sqrt{\text{in}}$  ( $67.0 \text{ MN/m}^{3/2}$ ) and  $50 \text{ ksi}\sqrt{\text{in}}$  ( $55.0 \text{ MN/m}^{3/2}$ ) for room air,  $\text{LN}_2$  and  $\text{LH}_2$  environments respectively. Values of  $C$  both for data included in Table 7-11 and in Reference 1 are summarized in Table 7-12, where it can be seen that  $C$  values for the Table 7-11 data were less than  $C$  values for Reference 1 data by factors ranging from two to six. However, the microstructure and fracture toughness of the 5Al-2.5Sn(ELI) plate used for tests reported in Table 7-11 were considerably different from the same characteristics of the plate material tested in Reference 1. Hence, the discrepancy in  $C$  values was probably largely due to material differences rather than effects of residual stress. If residual stresses had not been accounted for in evaluating the data in Table 7-11, the discrepancies in  $C$  values would have been even larger.

No conclusions were drawn with regard to the effect of residual stresses on fatigue growth of surface flaws. Cyclic flaw growth data are required for residual-stress-free SF specimens taken from the same plate as specimens tested in Table 7-11 before any conclusions can be drawn. The comparison of Table 7-11 data with Reference 1 data was inconclusive due to differences in microstructure and fracture toughness between the two heats of material for which data were compared.

#### 7.4.4 Aluminum Alloy Fatigue Tests

Test results and specimen details for 2219-T87 aluminum SF specimens cycled under the influence of applied and residual stresses are summarized in Table 7-13. Specimen configuration is shown in the upper part of Figure 7-12 except that

the GTA weld was omitted and the flaw was located at the center of the parent metal enclosed by the EB weld. As discussed in Section 7.4.2, magnitudes and distributions of residual stress measured in the outer 0.07 inch (1.8 mm) thick layers of the specimens provided an inadequate basis for estimating residual stresses in the interiors of the specimens. Hence, absolute values of residual stress are not reported in Table 7-13. Three specimens were cycled to failure in room air at 72°F (295°K) and in liquid nitrogen at -320°F (78°K). Depthwise flaw growth in aluminum specimens 5 and 6 was completely inhibited by delaminations. In aluminum specimens 3 and 4 tested in LN<sub>2</sub>, depthwise flaw growth was partially inhibited by delaminations. In view of the delamination effects, no attempt was made to assess the effect of residual stresses on test results.

## 8.0 EXPERIMENTAL STRESS INTENSITY ANALYSIS

Stress intensity is related to crack opening displacements over a small inward distance from the crack border in the crack plane. Hence, if crack tip displacements ( $w$ ) can be measured at known distances ( $r$ ) from the crack border, stress intensity ( $K_I$ ) can be calculated using the relationship;

$$w \Big|_{\substack{r \rightarrow 0 \\ z \rightarrow 0}} = \frac{2(1 - \mu^2)}{E} \left[ \frac{2r}{\pi} \right]^{1/2} K_I \quad (8-1)$$

where  $\mu$  is Poisson's ratio and  $E$  is the Young's modulus of the material. Since analytical stress intensity calculations are prohibitively difficult for many geometries of practical interest, this investigation was undertaken to determine the applicability of holography to measurements of crack-opening displacements and stress intensity for complex geometries.

### 8.1 HOLOGRAPHIC TECHNIQUE

A schematic optical diagram of the holographic technique is shown in Figure 8-1. The sample is illuminated with a collimated laser beam. The test beam passes through the sample, while the reference beam is directed around the sample as shown. The two beams cross at the plane of the hologram recording cell. The lenses,  $L'$  and  $L''$ , image the crack onto the image plane,  $P$ .

Three variations of the holographic method were used in these tests. These are as follows:

1. Differential holography. Two holograms are recorded sequentially on the same substrate. The first hologram records the unstressed condition of the sample while the second records the stressed condition. Upon illumination of the hologram with only the reference beam, an interferogram of the change in optical path length through the sample caused by the change in stress appears at the image plane. The interference fringes on the image are contours of equal change in optical path length and the fringe spacing represents a change in path length of one wavelength.

2. Stored-beam holographic interferometry. A hologram of the initial sample condition is recorded, then after stressing, the holographic reconstruction is compared interferometrically with the direct test beam. The hologram reconstructs the image of the sample in the initial condition, while the image formed by the test beam refracted through the crack forms an image of the crack as it appears under stress. These images are temporarily coherent, so they form an interferogram of the change in optical path length through the sample caused by the applied stress.

If the lens,  $L'$ , forms an image of the crack on the hologram, while the lens,  $L''$ , re-images this image onto the plane,  $P'$ , then the tilt between the reconstructed and direct images can be adjusted by varying the angle of the reference beam with the adjustable mirror. In this manner, the spacing and direction of the fringes can be controlled.

3. Two reference beam differential holography. This method is a variation of the usual differential holographic technique wherein the two holograms are made on the same photographic plate, but a separate reference beam is used for each hologram. The two separate reference beams are obtained by using two adjustable mirrors. The first hologram records load condition 1, while the second records load condition 2. The hologram is formed at an image plane of the crack.

In the reconstruction, reference beam  $R_1$  reconstructs load condition 1 and reference beam  $R_2$  reconstructs load condition 2. At any subsequent image plane, load conditions 1 and 2 are superimposed resulting in the interferometric contour map of the crack opening. Since the optical phase across each image depends on the angle of the corresponding reference beam, a slight variation in the angle of either reference beam introduces a linear phase variation across the image, altering the fringe spacing and direction.

Although the differential holography method is easier to apply, more information can be obtained by variation of the direction and spacing of

the fringes using the stored-beam method. Two reference beam differential holography has the advantages of both stored beam and ordinary differential holography, i.e., the high contrast fringes and the ability to change fringe space and direction in order to simplify the data reduction. In addition, the hologram pair can be recorded in a short time interval (less than 15 seconds) thus eliminating problems due to creep.

## 8.2 PROCEDURES

Initial tests were carried out on surface-flawed plexiglass specimens since approximate analytically based stress intensity solutions (6,8) are available against which to compare the experimental results. Test specimen configuration is shown in Figure 8-2. Specimen blanks were cut from 10 by 12 by 12 inches (254 by 305 by 305 mm) cast acrylic block (see Table 3-5 for mechanical properties). Each specimen was rough machined to within 0.10 inch (2.54 mm) of final dimensions. Final machining was done in very fine cuts in a continuous spray of "Koolmist". Surface layers of completed specimens showed no evidence of residual stresses or distortion. The ends of each specimen were ground flat on a metallurgical grinding wheel.

Surface flaws were prepared by extending a machined crack starter. Crack starters were introduced with a fly cutter. A matching steel wedge was then inserted into the starter slot and subjected to a sharp blow. The resulting cracks were approximately semi-elliptical with smooth regular peripheries.

Specimens were loaded as shown in Figure 8-3. Load was applied through bearing against the specimen flanges. Uniform loading was obtained by placing an epoxy (Epon 901) between the specimen flanges and loading grips and allowing the epoxy to set under a light load. Tests of specimens instrumented with strain gages as shown in Figure 8-3 confirmed that the procedure resulted in uniform tensile stresses in the specimen gage area. Load was applied by a torque wrench through a dyne bar which sensed and recorded the magnitude of the applied loads.

Interferograms and holograms were recorded using the test setup illustrated in Figure 8-1. Records were made for both unloaded and loaded specimens. A



schematic representation of crack geometry, interferograms and holograms is shown in Figure 8-4. From interferograms, crack-opening displacements were calculated using the formula

$$w = \frac{p\lambda}{4} \quad (8-2)$$

where  $p$  is fringe order and  $\lambda$  is the wavelength of the laser beam  $2.49 \times 10^{-5}$  inch ( $6.32 \times 10^{-5}$  cm). From holograms, displacements were determined from the expression

$$w = \frac{p \lambda (n-1)}{2} \quad (8-3)$$

where  $n$  is the index of refraction between air and plexiglass ( $n = 1.5$ ).

All experimentally determined crack-opening displacements were compared to displacements calculated from an analytical solution (6) for completely embedded elliptical cracks, i.e.,

$$w = \frac{2(1-\mu^2)}{E} \times \frac{\sigma a}{\Phi} \left\{ 1 - \frac{x^2}{c^2} - \frac{y^2}{a^2} \right\}^{1/2} \quad (8-4)$$

where  $a$  and  $c$  are the semi-minor and semi-major axes of the flaw, and  $\Phi$  is a complete elliptical integral of the second kind corresponding to the modulus  $k = \left[ (c^2 - a^2)/c^2 \right]^{1/2}$ . Equation 8-4 is thought to be a close approximation of crack-opening displacements for semi-elliptical surface flaws.

### 8.3 RESULTS

Three surface-flawed plexiglass specimens were tested. The first specimen was 8 inches (20.3 cm) long and contained a surface flaw with  $a = 0.352$  inch (8.94 mm) and  $2c = 0.768$  inch (19.5 mm). An interferogram and hologram of the crack were recorded both for zero load and for a 600 lb (2670 N) load. Crack-opening displacements along the semi-minor axis of the flaw due to the 600 lb (2670 N) load are plotted against distance from the crack border in Figure 8-5. Good agreement was obtained between displacements from the interferogram and hologram. However, both methods yielded displacements that were

considerably smaller than values calculated using Equation 8-4. The second specimen was 12 inches (30.5 cm) long and contained a surface flaw for which  $a = 0.270$  inch (6.86 mm) and  $2c = 0.670$  inch (17.01 mm). Stored beam holographic interferograms were recorded for loads of 500 lb (2224 N) and 1000 lb (4448 N). Both measured and calculated displacement along the semi-minor axis of the flaw are shown in Figure 8-6. The ratio of measured to calculated displacement increased from about  $1/3$  at  $r = 0.005$  inch (0.127 mm) to a constant value of about  $1/2$  for  $r$  values greater than 0.01 inch (0.25 mm). The third specimen was 12 inches (30.5 cm) long and contained a surface flaw with  $a = 0.295$  inch (7.49 mm) and  $2c = 0.625$  inch (15.88 mm). A hologram was recorded for 500 lb (2224 N) and 1000 lb (4448 N) loads using the two reference beam differential holographic technique. Measured displacements were again found to be about  $1/2$  of the calculated displacements as shown in Figure 8-7.

An attempt was made to resolve the differences between measured and calculated crack-opening displacements. The derivation of Equations 8-2 and 8-3 were investigated but no error could be found. Other possible sources of error due to birefringence, total internal reflection, increase in optical path length due to loading, and change in index of refraction due to loading were considered. It was concluded that possible errors stemming from any of the above sources were negligibly small. The most plausible explanation for the observed discrepancies is a loss of fringes at the crack tip due to a very rapid buildup of crack-opening displacement in the immediate vicinity of the tip. This possibility could be checked by using multiple frequency lasers (such as argon lasers) to develop interferograms, or by obtaining holograms of crack displacements under very low loads.

The use of holography and interferometry to experimentally evaluate stress intensity for complex geometries appears to be feasible. It is believed that the discrepancies between measured and calculated displacements resulted from loss of fringes at the crack tip. Further improvements in experimental technique should resolve this difficulty.

**Page Intentionally Left Blank**

## REFERENCES

1. Tiffany, C.F., Lorenz, P.M., and Hall, L.R.; "Investigation of Plane Strain Flaw Growth in Thick-Walled Tanks", NASA CR-54837, February 1966.
2. Tiffany, C.F., Lorenz, P.M., and Shah, R.C.; "Extended Loading of Cryogenic Tanks", NASA CR-72252, July 1967.
3. Masters, J. N., Haese, W.P., and Finger, R.W.; "Investigation of Deep Flaws in Thin Walled Tanks", NASA CR-72606, December 1968.
4. Carman, C.M., Forney, J.W., and Catlin, J.M.; "Plane Strain Fracture Toughness of 2219-T87 Aluminum Alloy at Room and Cryogenic Temperatures", AFML-TR-67-257, Air Force Materials Laboratory, Wright-Patterson AFB, 1967.
5. Pyle, R., Schillinger, D.E., and Carman, C.M.; "Plane Strain Fracture Toughness and Mechanical Properties of 2219-T87 Aluminum and 5Al-2.5Sn (ELI) Titanium Alloy Weldments and One Inch Thick 5Al-2.5Sn(ELI) Titanium Alloy Plate", NASA-CR-72154, National Aeronautics and Space Administration, Washington, D.C., 1968.
6. Irwin, G.R., "Crack Extension Force for a Part-Through Crack in a Plate", Journal of Applied Mechanics, Vol. 29, Trans. ASME, Vol. 84, Series E, December 1962.
7. Kobayashi, A.S., "On the Magnification Factors of Deep Surface Flaws", Structural Development Research Memorandum No. 16, Research Division, Aerospace Group, The Boeing Company, December 1965.
8. Kobayashi, A.S., and Moss, W.L.; "Stress Intensity Magnification Factors for Surface-Flawed Tension Plate and Notched Round Tension Bar", Proceedings of Second International Conference on Fracture, Brighton, England, 1969.
9. Anderson, R.B., Holms, A.G., and Orange, T.W.; "Stress Intensity Magnification for Deep Surface Cracks in Sheets and Plates", NASA Technical Note NASA TN D-6054, October, 1970.
10. Smith, F. W., "Stress Intensity Factors for a Semi-Elliptical Flaw", Structural Development Research Memorandum No. 17, Research Division Aerospace Group, The Boeing Company, August 1966.
11. Hall, L.R., "Plane Strain Cyclic Flaw Growth in 2014-T62 Aluminum and 6Al-4V(ELI) Titanium", NASA CR-72396, November 1968.
12. Bowie, O.L.; "Analysis of an Infinite Plate Containing Radial Cracks Originating from the Boundary of a Circular Hole", Journal of Mathematics and Physics, Vol. 35, 1956.
13. Gross, B., Srawley, J.E., and Brown, W.F.; "Stress Intensity Factors for a Single-Edge-Notch Tension Specimen in Boundary Collocation of a Stress Function", NASA TN D-2603, January 1965.

14. Smith, F.W., "Stresses Near a Semi-Circular Edge Crack", Ph.D. Thesis, University of Washington 1966.
15. Shah, R.C., and Kobayashi, A.S.; "Stress Intensity Factor for an Elliptical Crack under Arbitrary Normal Loading", Presented at 2nd National Symposium on Fracture Mechanics, Lehigh University, June 1968.
16. Tiffany, C.F., and Lorenz, P.M.; "An Investigation of Low Cycle Fatigue Failures Using Applied Fracture Mechanics", AFML-ML-TDR-64-53, May 1964.
17. Randall, P.N.; "Severity of Natural Flaws as Fracture Origins, and a Study of the Surface-Cracked Specimen", AFML-TR-66-204, August 1966.
18. ASTM Committee E-24, "Proposed Method of Test for Plane Strain Fracture Toughness of Metallic Materials", ASTM Standards Part 31, May 1969, pps. 1099-1114 (to be approved).
19. Masubuchi, K.; "Analysis of Thermal Stresses and Metal Movement During Welding", RSIC Report RSIC-820, July 1968.
20. Hill, H.N., "Residual Welding Stresses in Aluminum Alloy", Metal Progress, 80, 1961.
21. Capel, L., "Aluminum Welding Practice", British Welding Journal, Vol. 8, No. 5, 1960.
22. Nippes, E.F., and Savage, W.F.; "Residual Stresses in Welded Titanium Plates", Welding Journal Research Supplement, Vol. 37, 1958.
23. Lindh, D.V., and Zylstra, L.B.; "Residual Stresses in Welded Titanium", Boeing Company Document D6A 10075-1, June 1966.
24. Robelloto, R., Joy, A., and Lambase, J.; "Investigation of Magnitude and Distribution of Stresses in Welded Structures", AFML Technical Report ARML-TR-67-293, September 1967.
25. Wells, A.A., "The Brittle Fracture Strength of Welded Steel Plates", Quarterly Transactions Institute of Naval Architects, Vol. 48, 1956.
26. Wells, A.A., "Influence of Residual Stresses and Metallurgical Changes on Low Stress Brittle Fracture in Welded Steel Plates", Welding Journal Research Supplement, April 1961.
27. Martin, D.C., Ryan, R.S., and Preppel, P.J.; "Evaluation of Weld-Joint Flaws as Initiating Points of Brittle Fracture", Welding Journal Research Supplement, Vol. 37, 1957.
28. Hall, W.J., and Chamberlain, A.D.; "Studies of Welding Procedures - Part III", Welding Journal Research Supplement, 1966.
29. Kihara, H., and Masubushi, K.; "Effect of Residual Stresses on Brittle Fracture", Welding Journal Research Supplement, 1959.

30. Kihara, H., et al., Document Nos. X-218-58 and X-258-60, International Institute of Welding, 1958.
31. Greene, T.W., Welding Journal Research Supplement, 1949.
32. Kennedy, R., British Welding Journal, 4, 1957.
33. Wells, A.A., "Effects of Residual Stress on Brittle Fracture", Fracture - An Advanced Treatise, Vol. 5, Chapt. 7, Academic Press, 1969.
34. Boyd, G.M., "The Conditions for Unstable Rupturing of a Wide Plate", Trans. Inst. Naval Arch., 99, (3), Part II, July 1957.
35. Masubushi, K., "Effects of Residual Stress on Fracture Behavior of Weldments", Proceedings of Symposium on Weld Imperfections, Palo Alto, California, September 19-21, 1966.
36. Godfrey, L., and Hansen, H.A., "A Fracture Toughness Interpretation of Observed Failures in Ti-13V-11Cr-3Al. Gas Tungsten Arc Welds", Welding Journal Research Supplement, November 1967.
37. Mathew, J., "Determination of Initial Stresses by Measuring the Deformation Around Drilled Holes", Trans. ASME, Vol. 56, 1934.

**Page Intentionally Left Blank**

## APPENDIX A - WELDING PROCEDURES

This appendix contains details of welding procedures used for 1.0-inch (2.54 cm) thick 2219-T87 aluminum specimens, both with and without internal flaws, and 0.375 - inch (0.953 cm) thick 5Al-2.5Sn(ELI) titanium specimens.

### Procedures For One-Inch-Thick 2219-T87 Aluminum

Weld panels, 1.0 by 24 by 36 inches (2.5 x 61.0 x 91.4 cm) were fabricated by joining two 1.0 by 12 by 36 inch (2.5 x 30.5 x 91.4 cm) panel halves. All panels were prepared with square butt edges and cleaned just prior to welding using standard aluminum pre-weld cleaning techniques (wipe with acetone and remove surface oxides by scraping). Welding was accomplished in a Sciaky 500 amp sine wave welder using three passes (one continuous tack pass and two penetration passes). Welding details were:

Weld Process:      GTA, DCSP  
Weld Position:     Downhand  
Electrode:          2% thoriated tungsten, 5/32 inch (0.40 cm) diameter  
Electrode Tip:     1/8 -inch (0.32 cm) diameter ball nose over 3/8 inch (0.95 cm) taper  
Torch:              Linde HW-27  
Shield Gas:         Helium at 110 CFH (3.1 m<sup>3</sup>/hr)  
Parameters:

	<u>Continuous Tack</u>	<u>Penetration First Side</u>	<u>Penetration Second Side</u>
Current, amps	200	396	396
Voltage, volts	12.5	11.8	11.8
Travel, In/Min (mm/sec)	15 (6.4)	3 (11.3)	3 (11.3)
Wire	None	None	None

### Procedures for Internally Flawed One-Inch-Thick 2219-T87 Aluminum

Welding details were identical to those above for the one-inch-thick aluminum welds except that current and voltage parameters for each penetration pass were manually changed at predetermined opposing locations. At 400 amps, joint penetration was 0.6 inch (1.52 cm). Penetration was decreased to 0.2 inch (0.51 cm) by rapidly



decreasing the current to 175 amps at 12.2 volts over a 3-1/2 inches (8.9 cm) length. Current and voltage were then increased to 396 amps and 11.8 volts. This procedure produced a lack-of-fusion defect approximately 4-1/2 inches (11.4 cm) long and 0.6 inch (1.52 cm) deep.

#### Procedures for Three-Eighths-Inch Thick 5Al-2.5Sn(ELI) Titanium

Weld panels for Series I residual stress specimens were fabricated per Figure A-1. Panel halves were machined from 3/8-inch (0.95 cm) thick plates. The machined surfaces were cleaned with MEK solvent. The panel halves were then clamped to a rigid copper backing bar to maintain plate alignment during welding. The backing bar was grooved to provide a channel for inert gas shielding of the underbead. Copper hold down bars and shim stock were used to clamp the plates in the reduced thickness area.

Welding was accomplished using the mechanized GTA process with no filler wire additions. Power was supplied by a Vickers 400 amp Controlarc D.C. Welder. An Airco automatic welding head and Linde Heliarc (Type HW-27) welding torch were used. Panels were welded with a single pass deposited from each side. Parameters were chosen to result in 100 percent penetration for the first pass with no measurable under fill along the edges of the weld bead as determined by visual inspection, and 90 percent penetration for the second pass. Argon gas was used for underbead shielding and helium gas for top side shielding. Secondary top side shielding was accomplished using a 5/8 inch (1.6 cm) wide by 6 inches (15.2 cm) long trailing cup with fiberglass cloth extending from the sides.

Weld schedule details can be summarized as follows:

	First Pass	Second Pass
Current, DCSP amps:	160	160
Voltage, volts:	14	14
Travel, in/min (mm/sec)	3 (1.3)	3 (1.3)

	<u>First Pass</u>	<u>Second Pass</u>
Gas Flow, CFH (m <sup>3</sup> /hr):		
1. Torch	60 (1.7) (He)	60 (1.7) (He)
2. Trailing Shield	60 (1.7) (He)	60 (1.7) (He)
3. Backing	15 (0.4) (A)	15 (0.4) (A)
Hold Down Bar Separation, in. (cm):	0.5 (1.27)	0.5 (1.27)
Backing Bar, 2 x 0.5 in (5.1 x 1.3 cm):		
1. Groove Width, in. (cm):	0.50 (1.27)	0.50 (1.27)
2. Groove Depth, in (cm):	0.06 (0.15)	0.06 (0.15)
Electrode: 2 percent thoriated tungsten, 1/8 inch (0.32 cm) diameter, 45° included angle to 0.030-inch (0.076 cm) dia. end.		

Longitudinal welds on Series III residual stress test specimens were deposited using the above welding schedule.

**Page Intentionally Left Blank**

## APPENDIX B

### CONVERSION OF U.S. CUSTOMARY UNITS TO SI UNITS

In the text of this report, all numerical values are given in U.S. customary units with corresponding SI units in parenthesis. Due to the complexity of the tables of results, only U.S. customary units are used therein. Conversion factors for converting U.S. customary to SI units are given in the following table:

To Convert From (U.S. Customary Unit)	Multiply by	To Obtain (SI Units)
in.	$2.54 \times 10^{-2}$	meter (m)
lbf	4.448	newton (n)
kip	4.448	kilonewton (kN)
ksi	6.895	meganewton/meter <sup>2</sup> (MN/m <sup>2</sup> )
ksi $\sqrt{\text{in}}$	1.099	MN/m <sup>3/2</sup>

**Page Intentionally Left Blank**

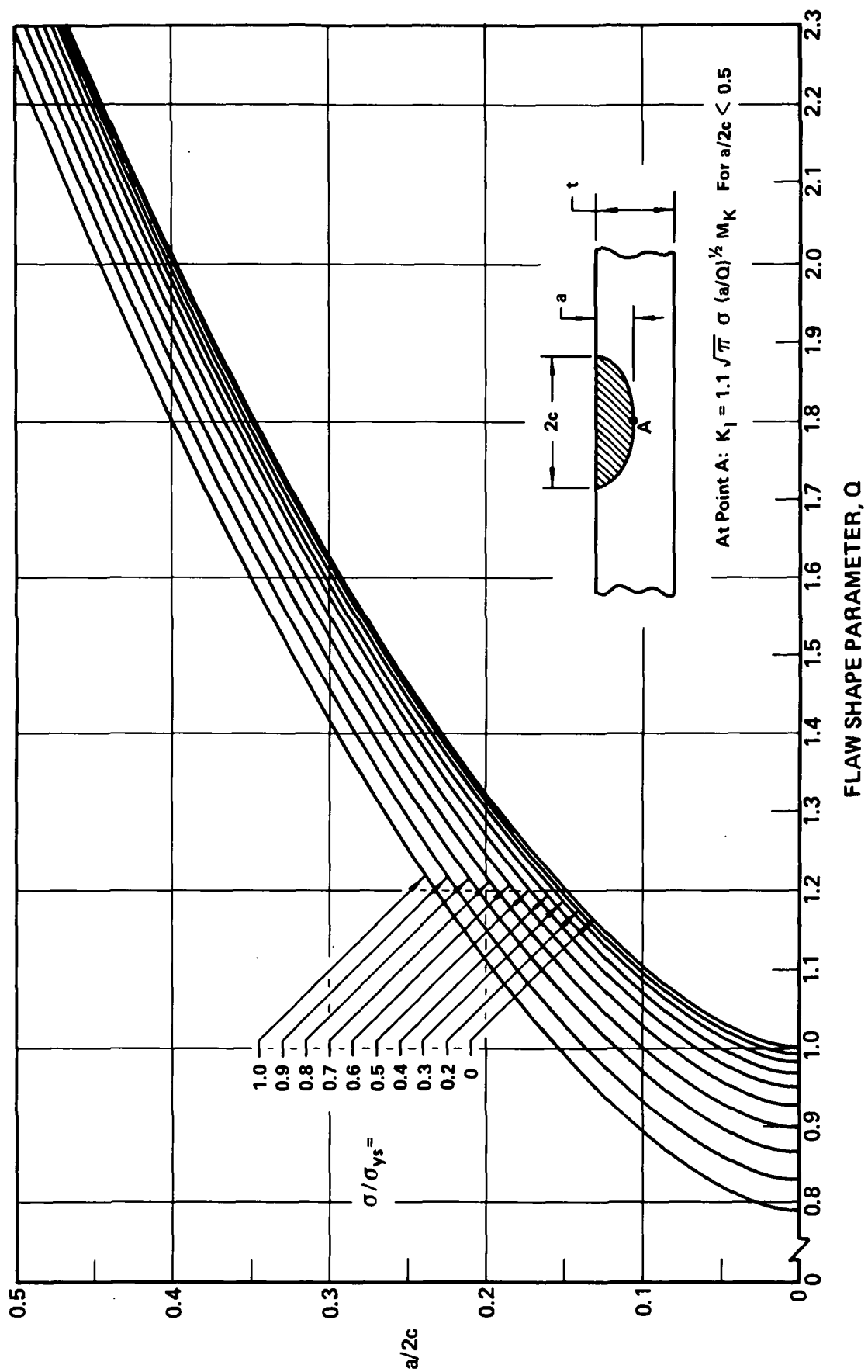
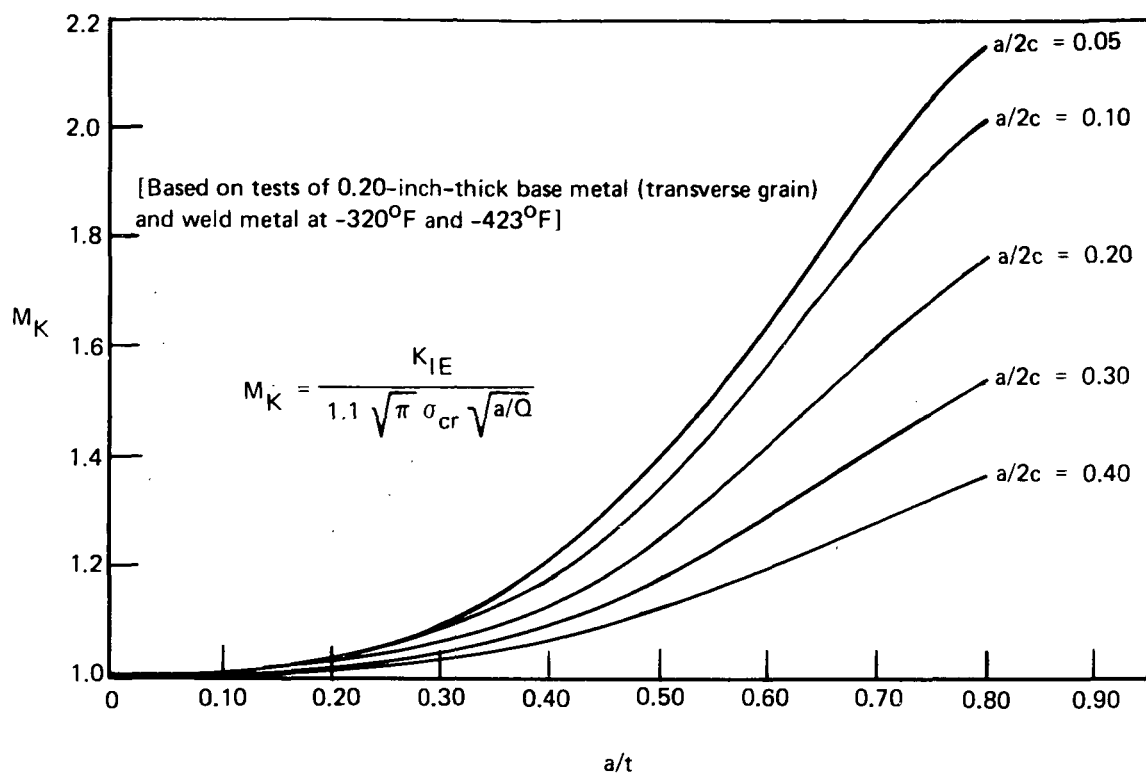
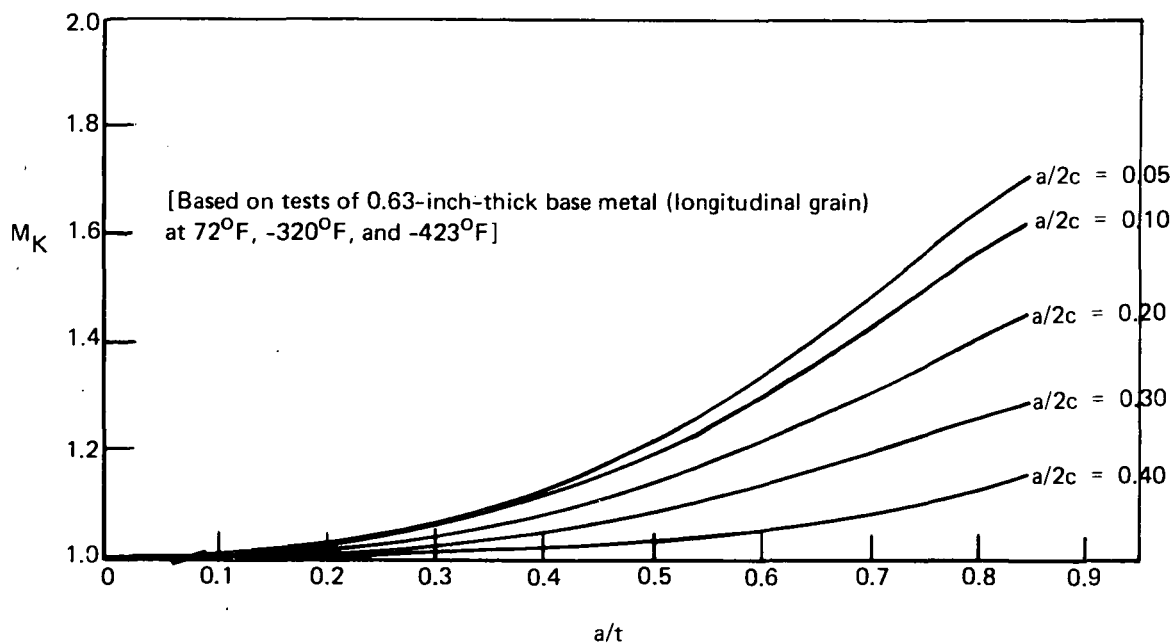


Figure 2-1: SHAPE PARAMETER CURVES FOR SURFACE AND INTERNAL FLAWS



**Figure 2-2:  $M_K$  CURVES FOR 5Al-2.5Sn (ELI) TITANIUM ALLOY**



**Figure 2-3:  $M_K$  CURVES FOR 2219-T87 ALUMINUM ALLOY**

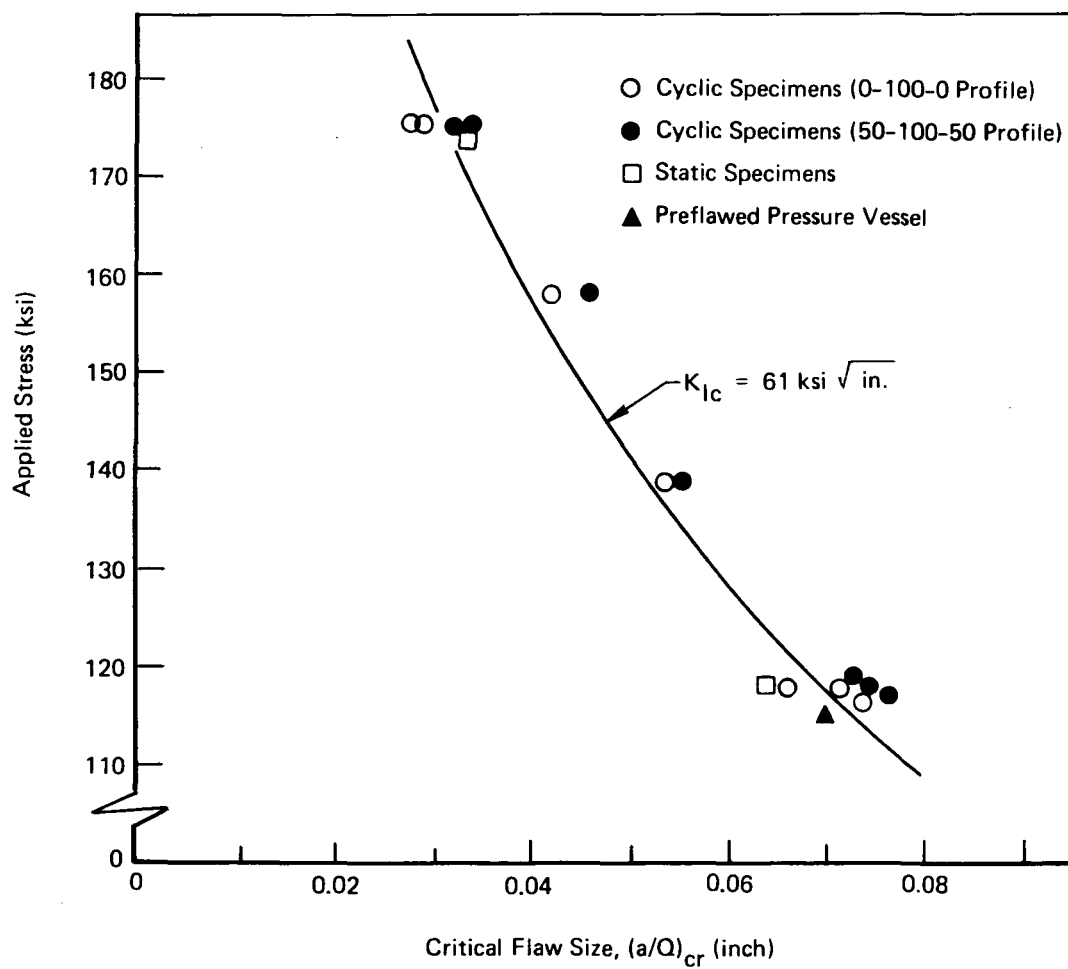
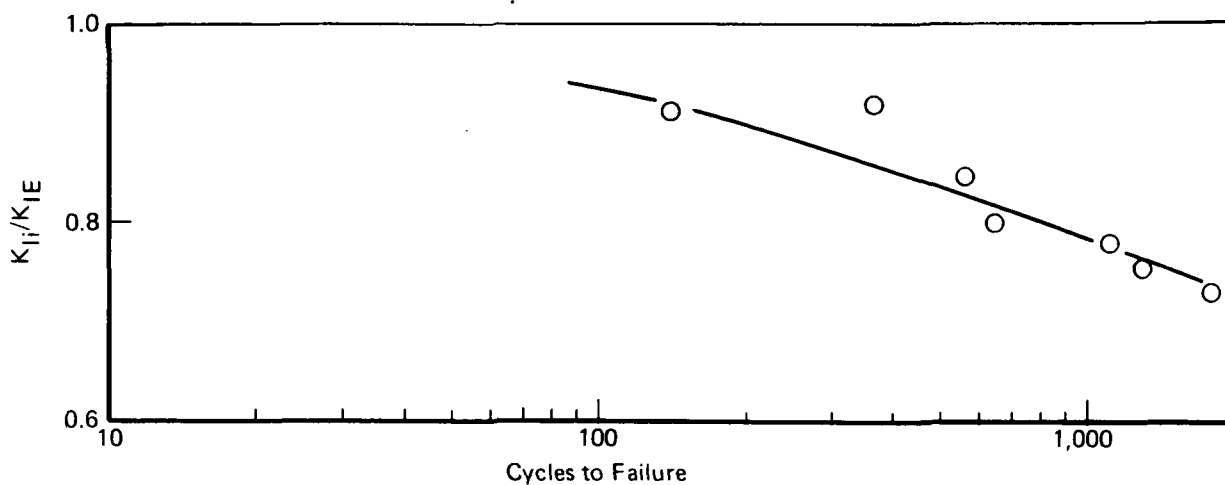
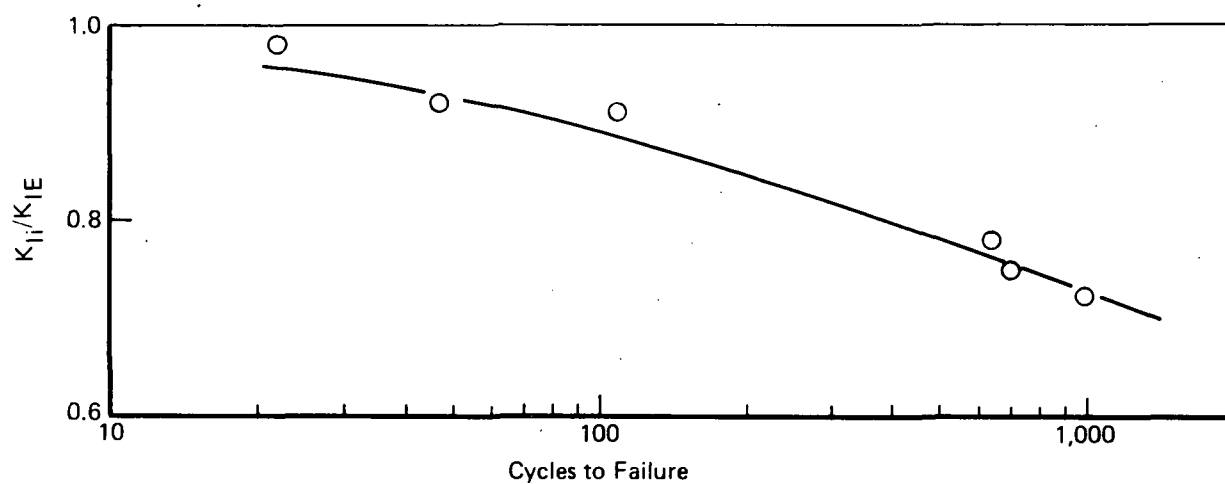


**Figure 2-4: EFFECT OF SURFACE FLAW SIZE ON FAILURE STRESS FOR 5Al-2.5Sn (ELI) TITANIUM ALLOY AT -320°F**

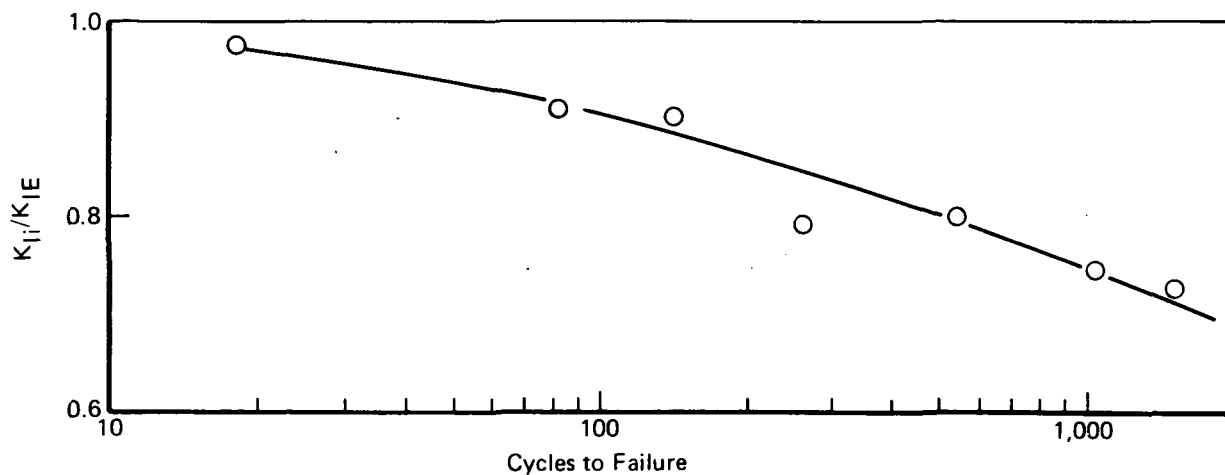




(a) ROOM AIR DATA



(b) LN<sub>2</sub> DATA



(c) LH<sub>2</sub> DATA

Figure 2-5: CYCLIC LIFE DATA FOR 2219-T87 ALUMINUM SURFACE-FLAWED SPECIMENS (REFERENCE 1)

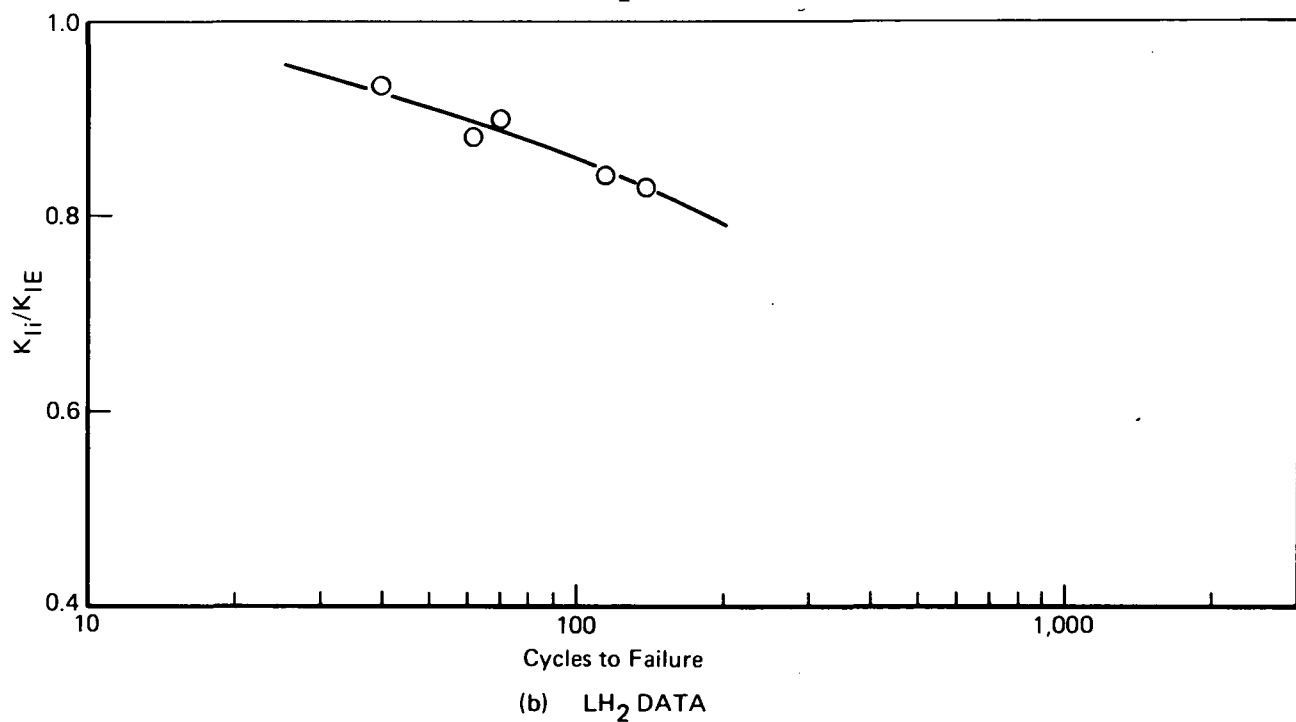
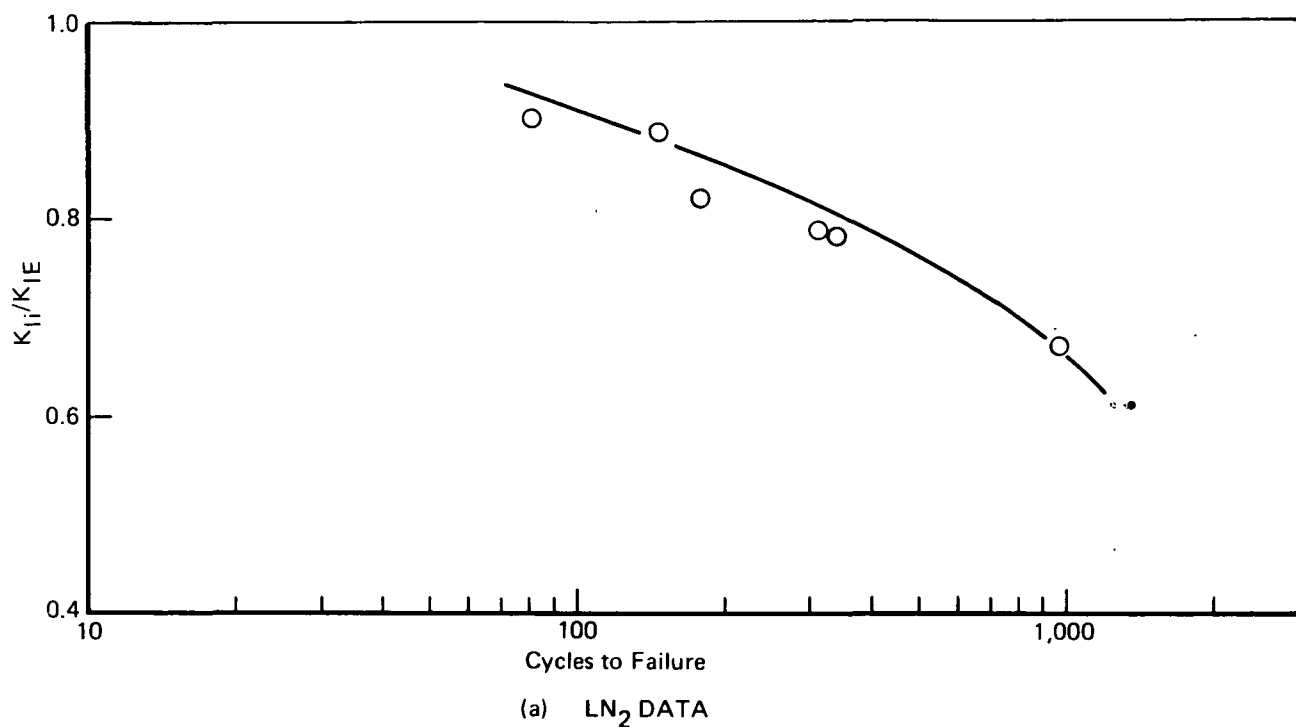
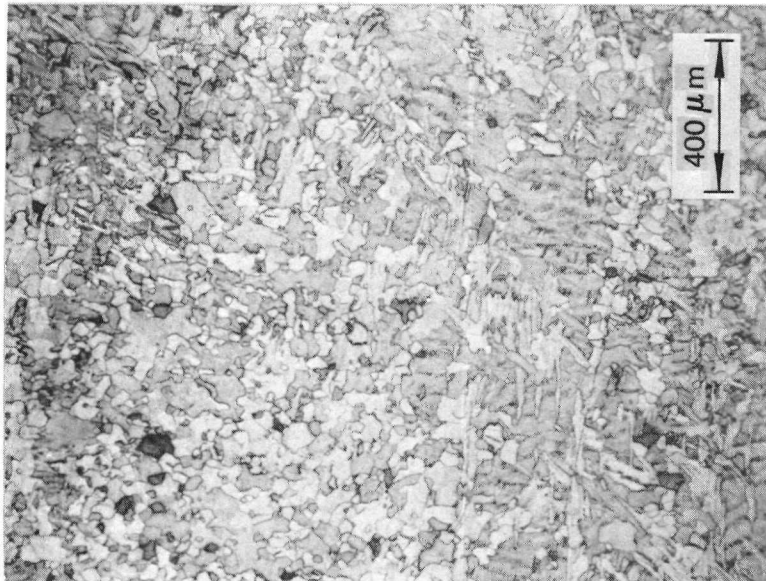
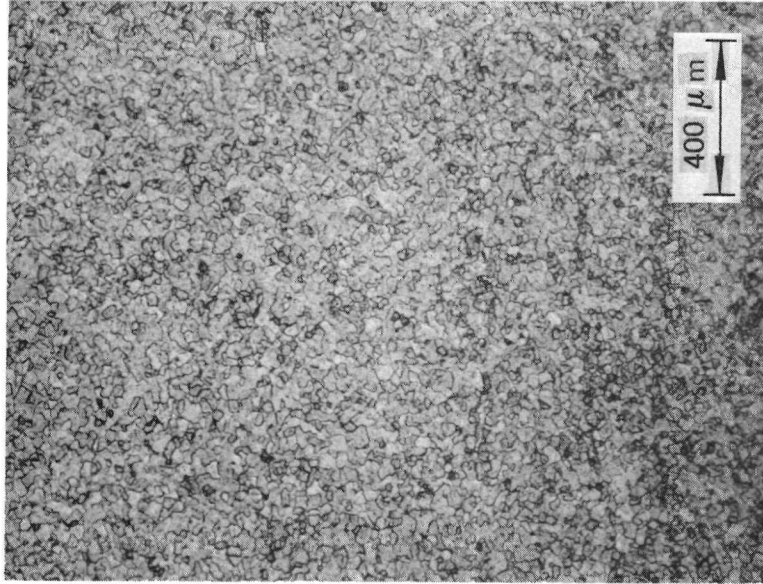


Figure 2-6: CYCLIC LIFE DATA FOR 5Al-2.5 Sn (ELI) TITANIUM SURFACE-FLAWED SPECIMENS (REFERENCE 1)



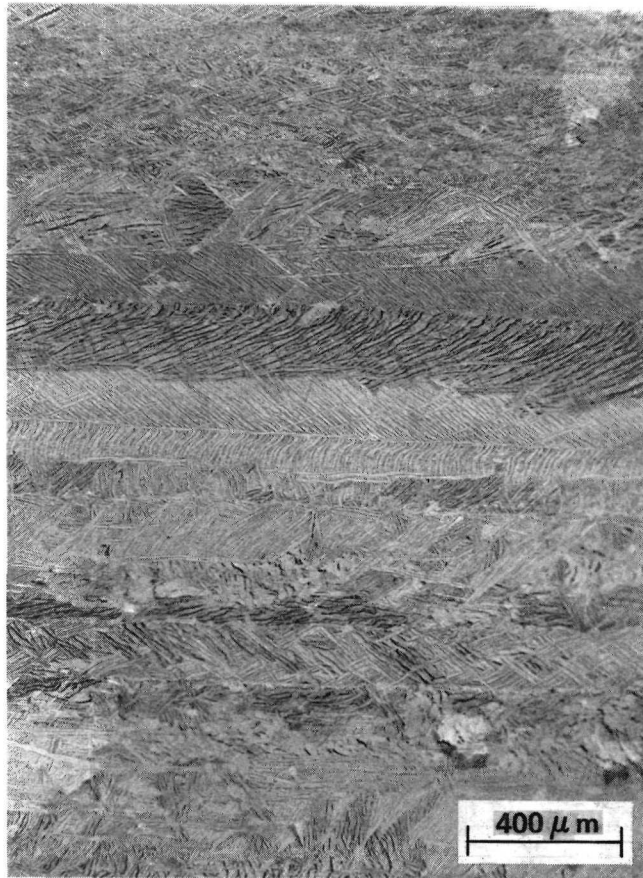
(a): INCOMPLETELY ANNEALED  
(SUBJECT PROGRAM)



(b): COMPLETELY ANNEALED  
(REFERENCE 3)

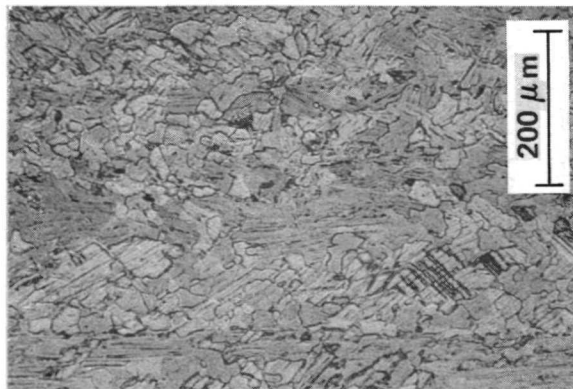
Etchant: 2% HF, 8%  $H_3PO_4$ , BAL.  $H_2O$

Figure 3-1: MICROSTRUCTURE OF MILL ANNEALED 0.375-INCH  
THICK 5Al-2.5Sn (ELI) TITANIUM PLATE



Etchant: 2% HF, 8% H<sub>3</sub>PO<sub>4</sub>, BAL. H<sub>2</sub>O

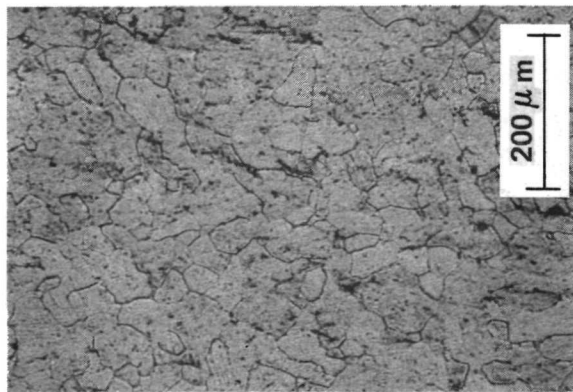
**Figure 3-2: LAYERED MICROSTRUCTURE OBSERVED IN MILL ANNEALED  
5Al-2.5 Sn (ELI) TITANIUM (0.375-Inch (9.53mm) THICK PLATE)**



1350°F FOR 8 HRS



1450°F FOR 8 HRS



1550°F FOR 8 HRS

Etchant: 2% HF, 8% H<sub>3</sub>PO<sub>4</sub>, BAL. H<sub>2</sub>O

**Figure 3-3: MICROSTRUCTURAL CHANGES RESULTING FROM ANNEALING  
5Al-2.5 Sn (ELI) TITANIUM 0.375-INCH (9.53mm) THICK PLATE**

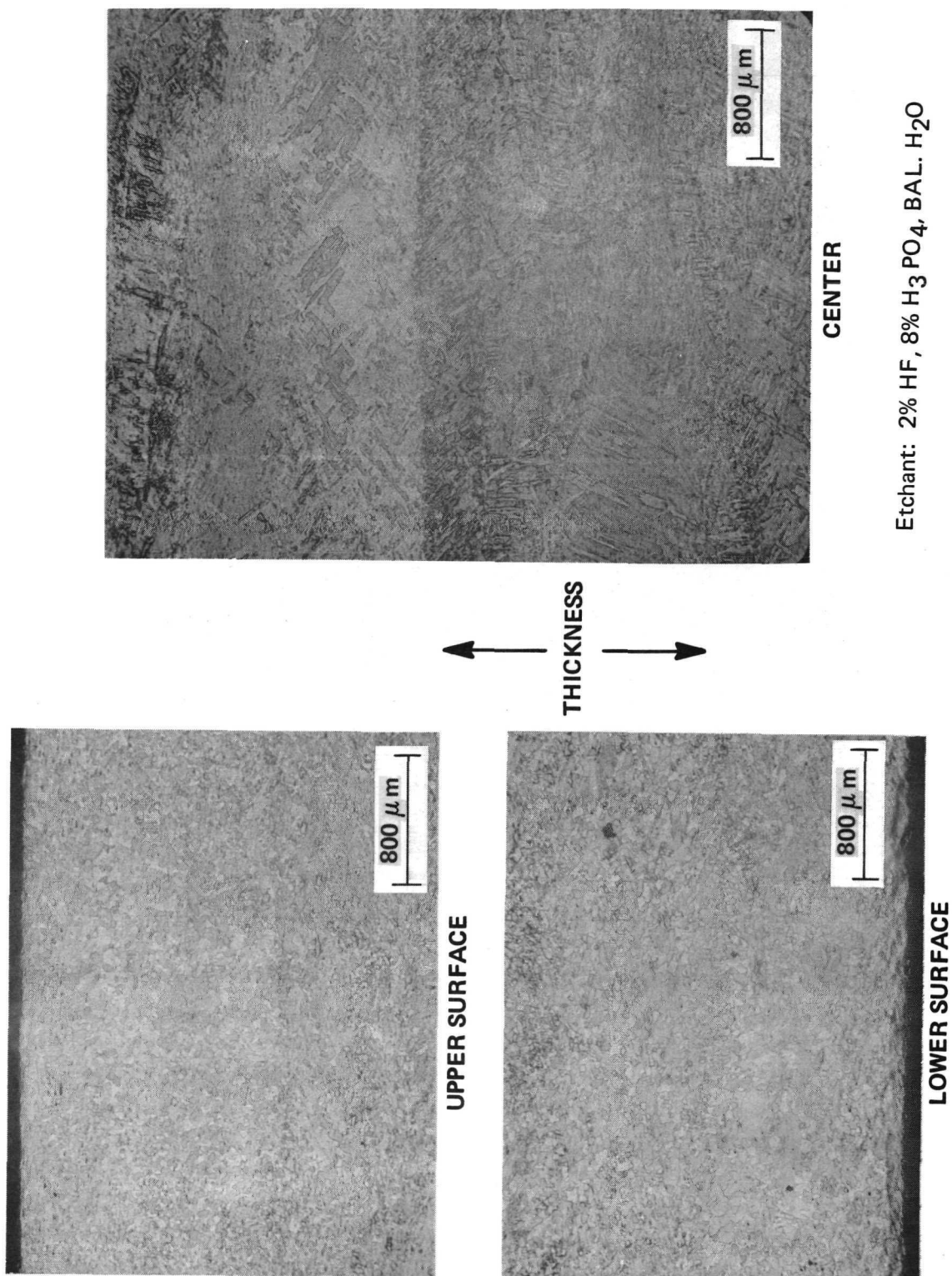
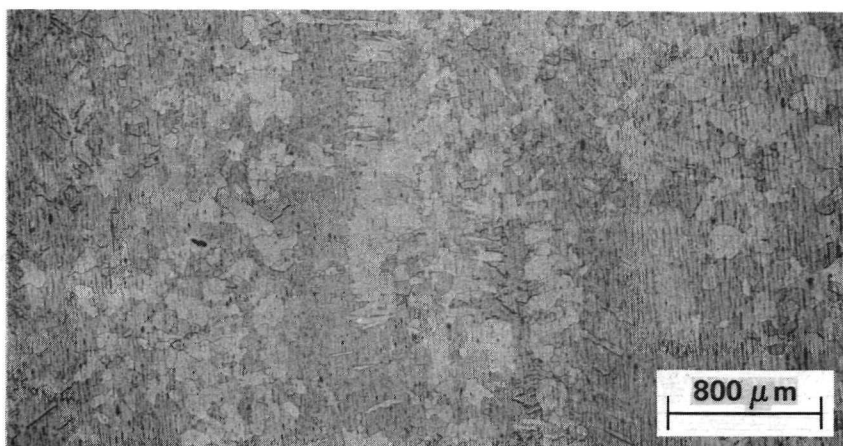
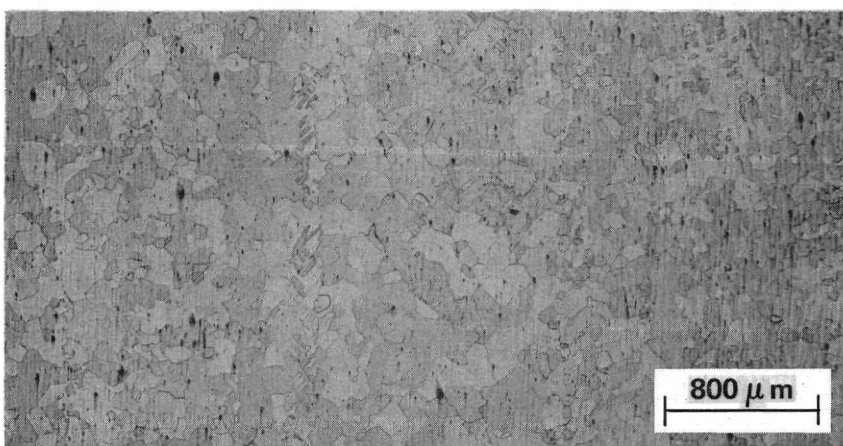


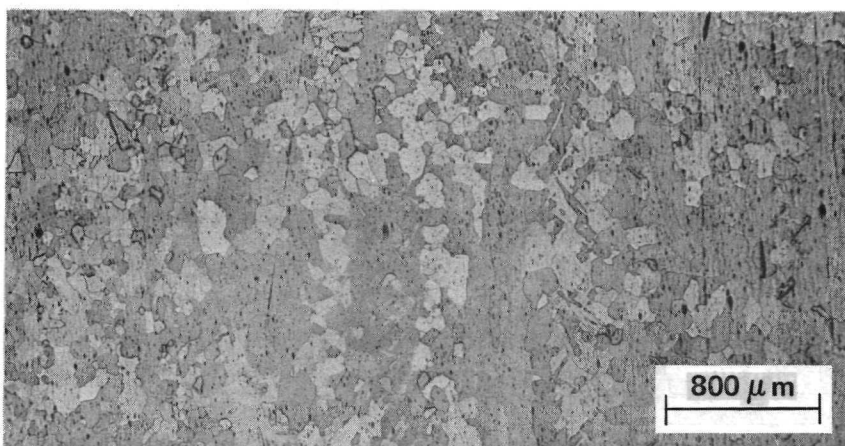
Figure 3-4: MICROSTRUCTURE OF MILL ANNEALED 0.80 - INCH (20.3 mm) THICK 5Al - 2.5 Sn(ELI) TITANIUM PLATE



**1550 deg F FOR 8 HRS**



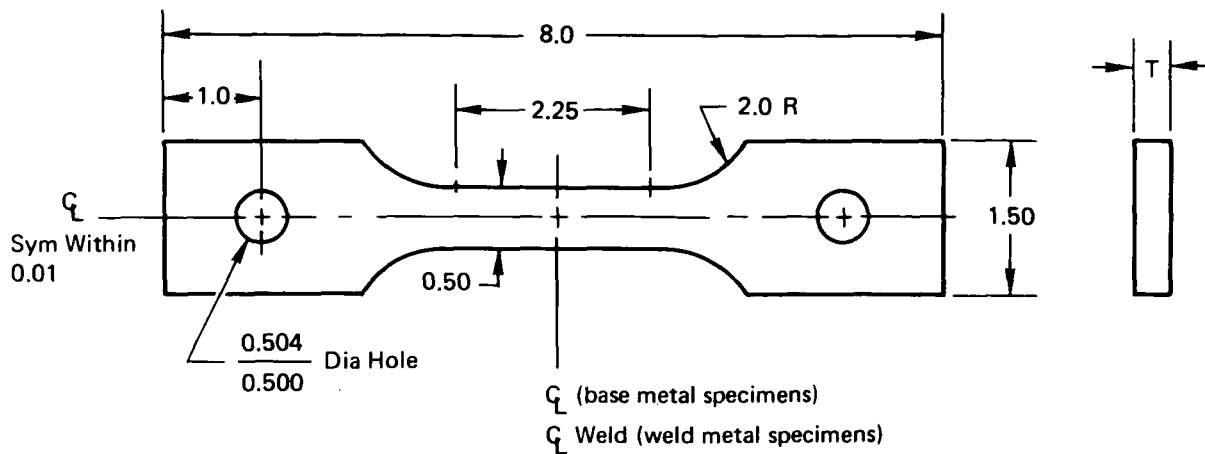
**1550 deg F FOR 16 HRS**



**1700 deg F FOR 8 HRS**

Etchant: 2% HF, 8% H<sub>3</sub> PO<sub>4</sub>, BAL. H<sub>2</sub>O

**Figure 3-5: MICROSTRUCTURAL CHANGES AT CENTER OF 0.80 - INCH (20.3 mm) THICK 5Al - 2.5 Sn (ELI) TITANIUM PLATE DUE TO VARIOUS ANNEALING CYCLES**



Alloy	Dimension "T"
2219-T87 Aluminum	0.50
5Al-2.5Sn (ELI) Titanium	0.37
Plexiglas	0.10

Figure 3-6: TENSILE SPECIMEN FOR MECHANICAL PROPERTY MEASUREMENTS  
(Used for 2219-T87 Aluminum Parent and Weld Metal, 5Al-2.5Sn (ELI)  
Titanium Parent Metal, and Plexiglas)

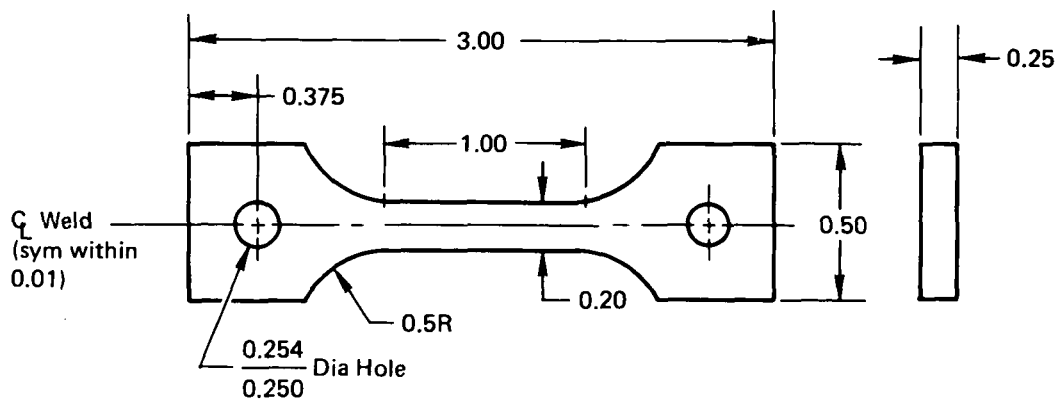


Figure 3-7: ALL WELD METAL TENSILE SPECIMEN FOR MECHANICAL PROPERTY  
MEASUREMENTS OF TITANIUM WELDS



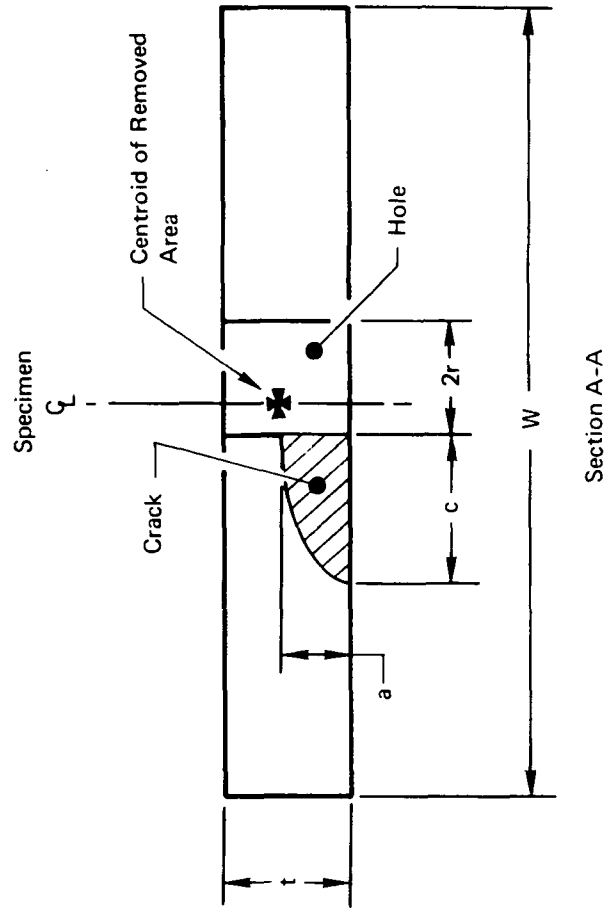
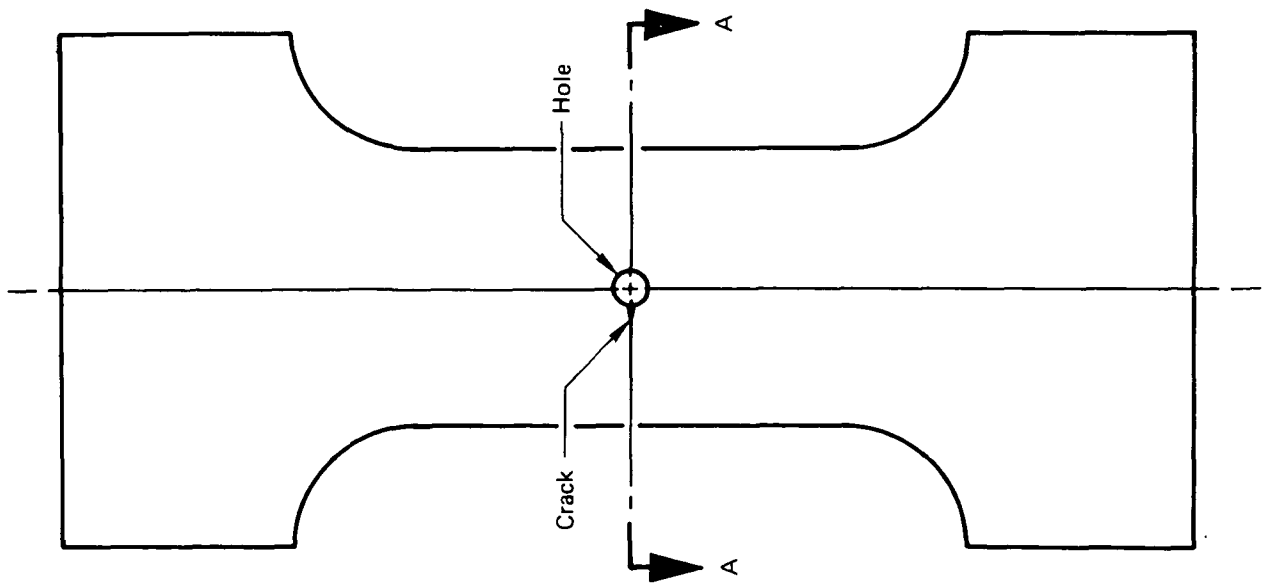


Figure 4-1: GEOMETRY FOR SPECIMENS WITH FLAWS PROTRUDING FROM HOLES

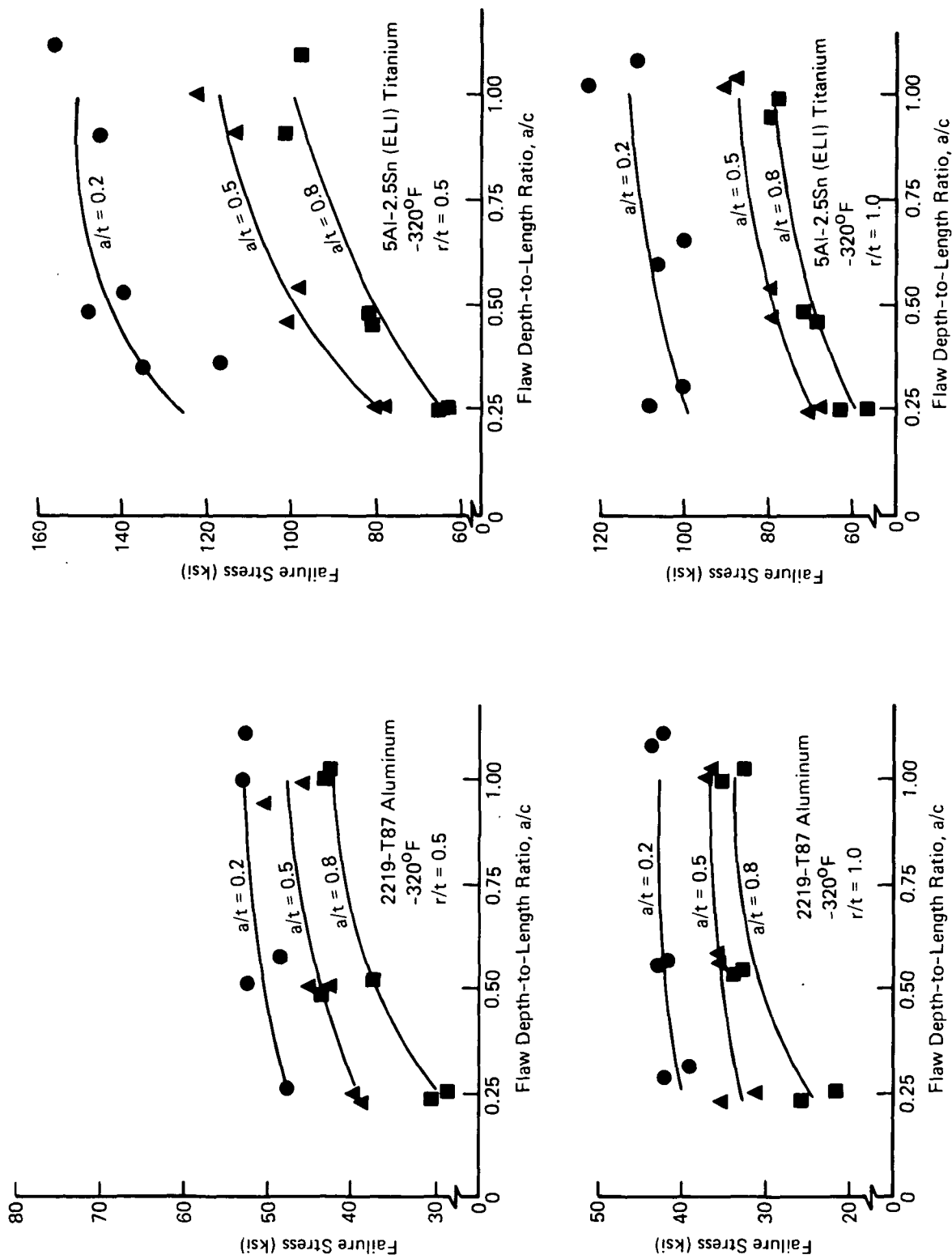


Figure 4-2: GROSS FAILURE STRESSES AS A FUNCTION OF TEST VARIABLES  
FOR SPECIMENS WITH FLAWS PROTRUDING FROM HOLES

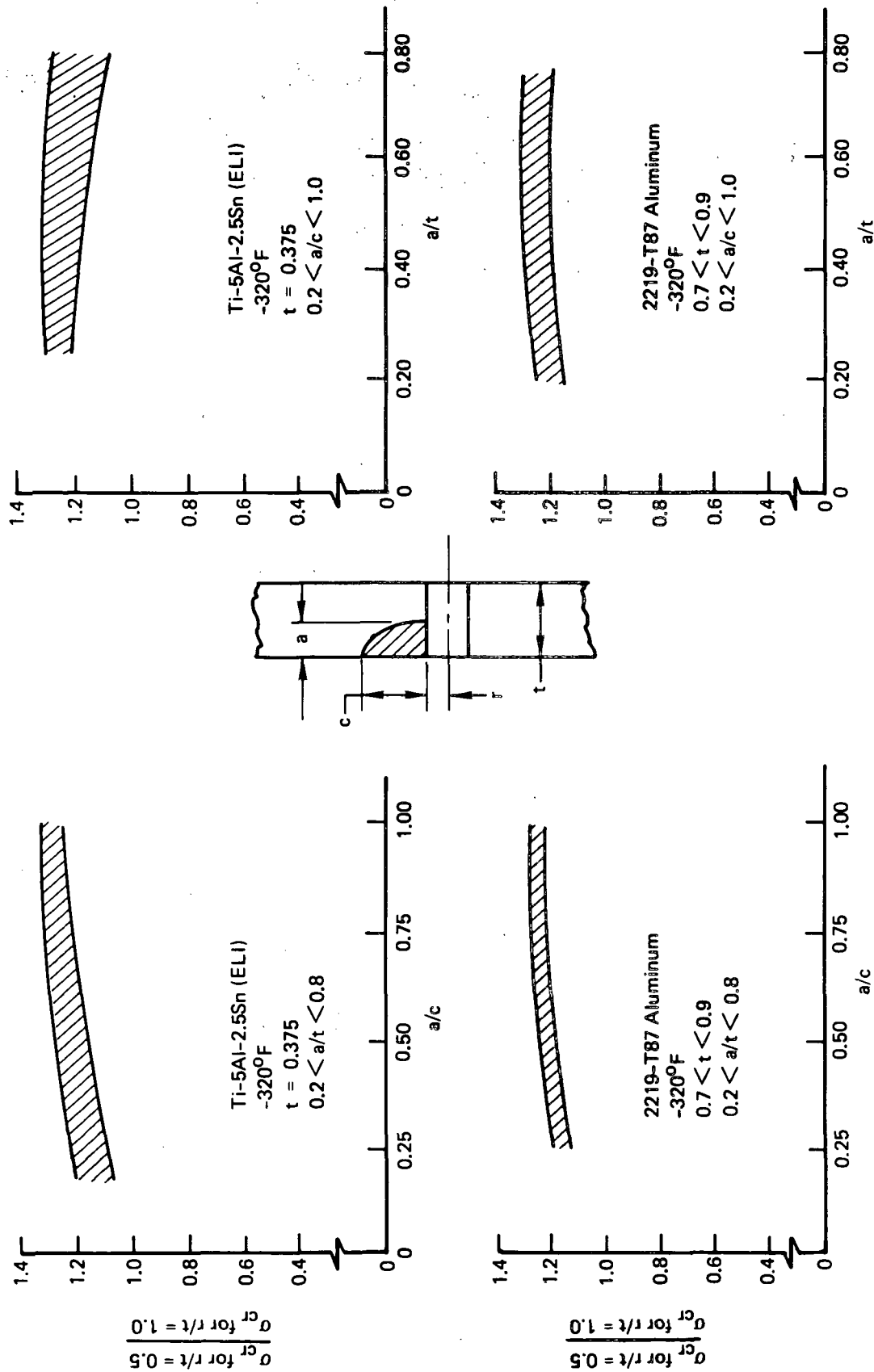
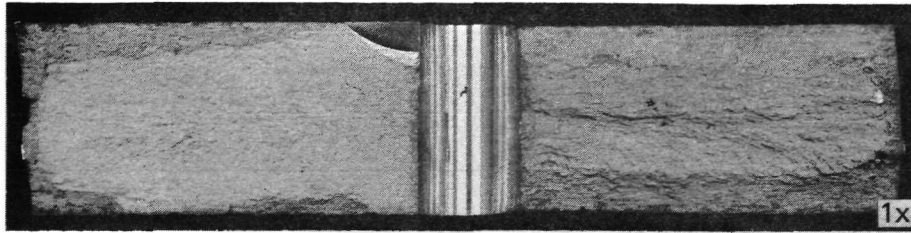


Figure 4-3: EFFECT OF HOLE DIAMETER ON FAILURE STRESS FOR SPECIMENS WITH FLAWS PROTRUDING FROM HOLES

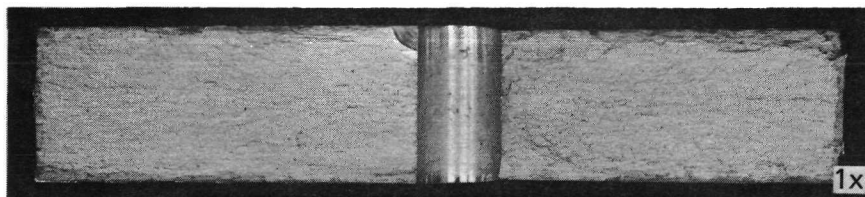


Al-2219-T87 SPECIMEN 5HA25-1

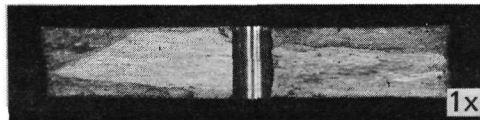


Ti-5Al-2.5Sn (ELI) SPECIMEN 1HT51-1

(a): FRACTURE FACES OF STATICALLY TESTED SPECIMENS

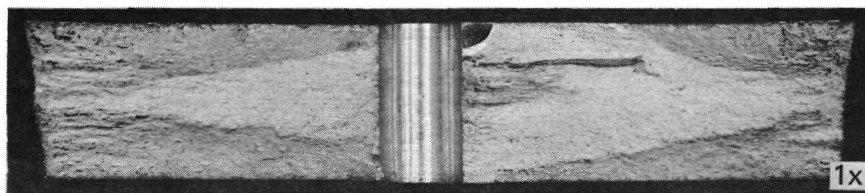


Al-2219-T87 SPECIMEN HACN-2

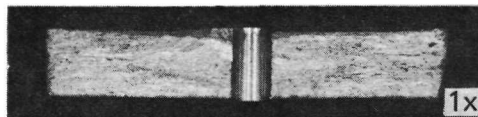


Ti-5Al-2.5Sn (ELI) SPECIMEN HTC-4N

(b): FRACTURE FACES OF SPECIMENS CYCLED IN  $LN_2$



Al-2219-T87 SPECIMEN HACR-2



Ti-5Al-2.5Sn (ELI) SPECIMEN HTC-1R

(c): FRACTURE FACES OF SPECIMENS CYCLED IN ROOM AIR

Figure 4-4: FRACTURE FACES OF SPECIMENS CONTAINING FLAWS PROTRUDING FROM HOLES

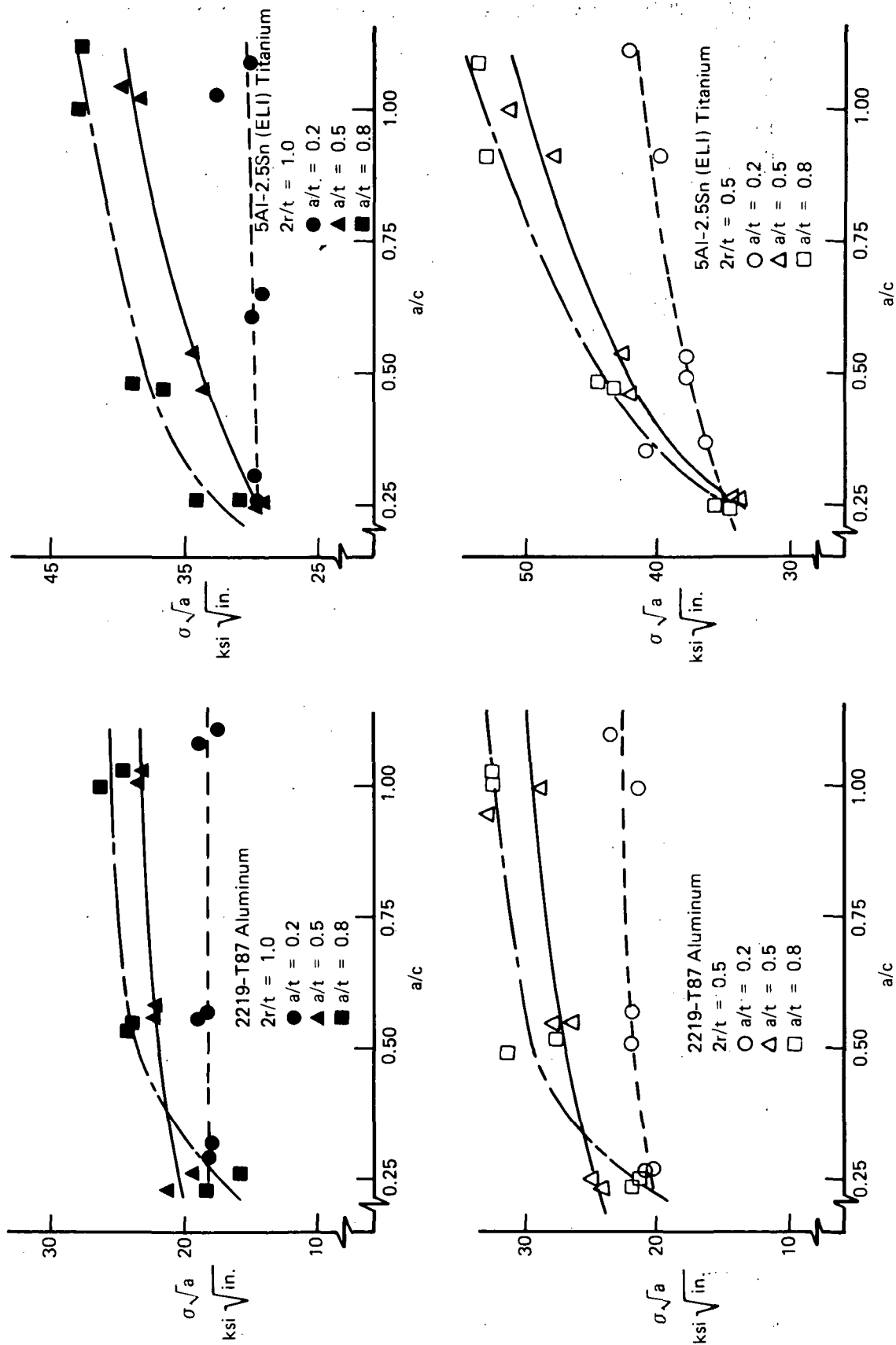


Figure 4-5: PLOTS OF  $\sigma\sqrt{a}$  VS  $(a/c)$  FOR SPECIMENS WITH FLAWS PROTRUDING FROM HOLES

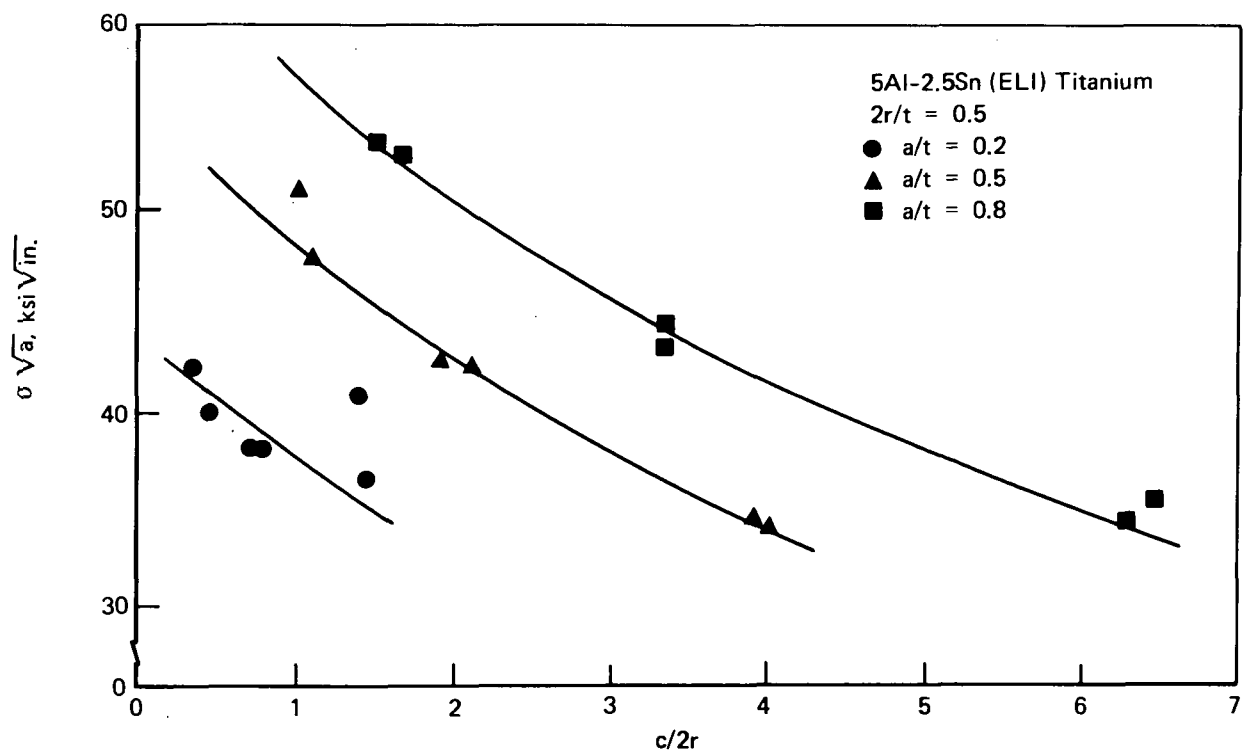
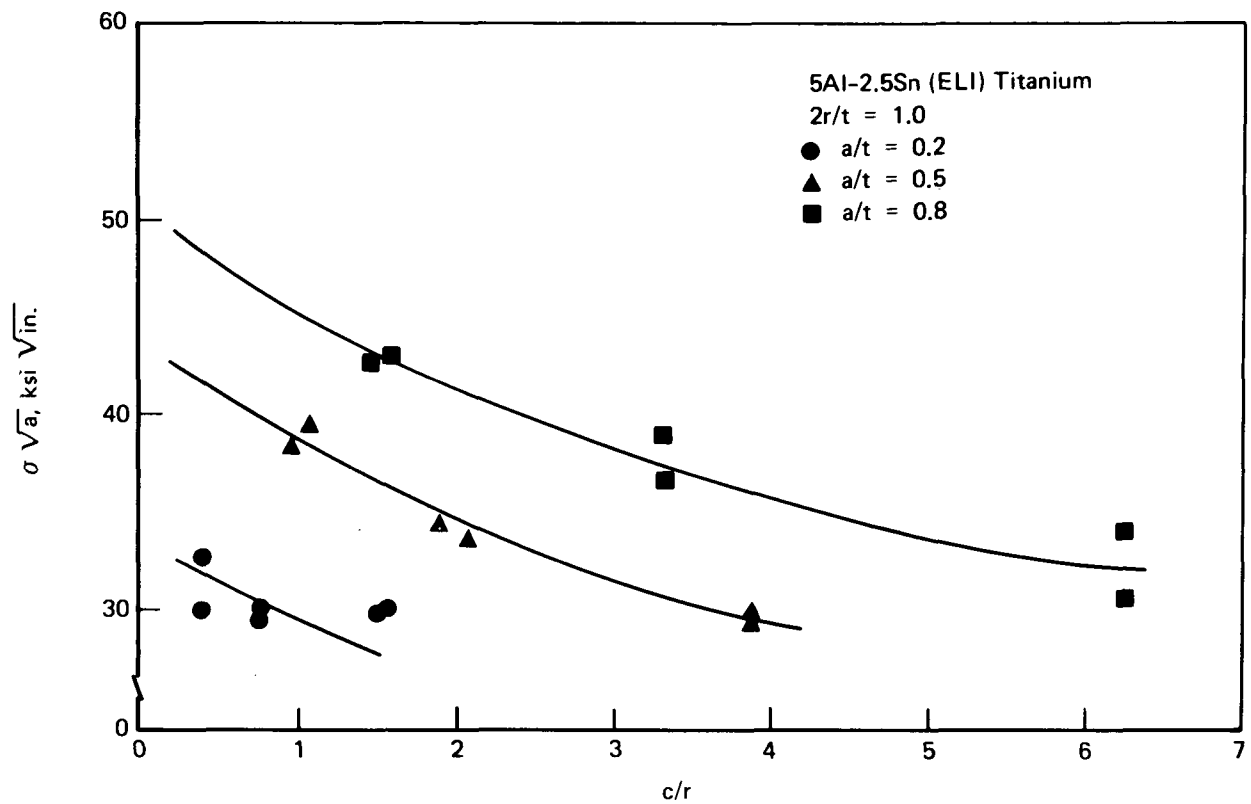


Figure 4-6: PLOTS OF  $\sigma \sqrt{a}$  VS FLAW LENGTH TO HOLE SIZE RATIOS FOR TITANIUM SPECIMENS WITH FLAWS PROTRUDING FROM HOLES

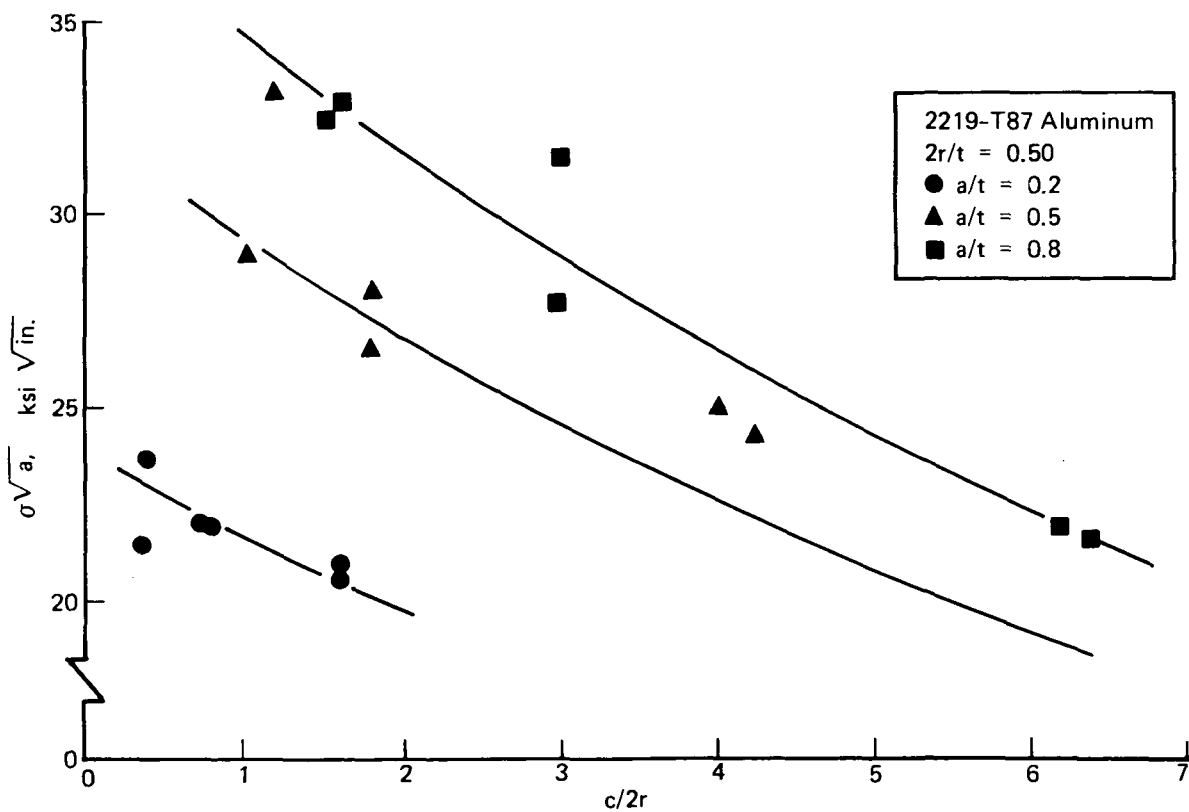
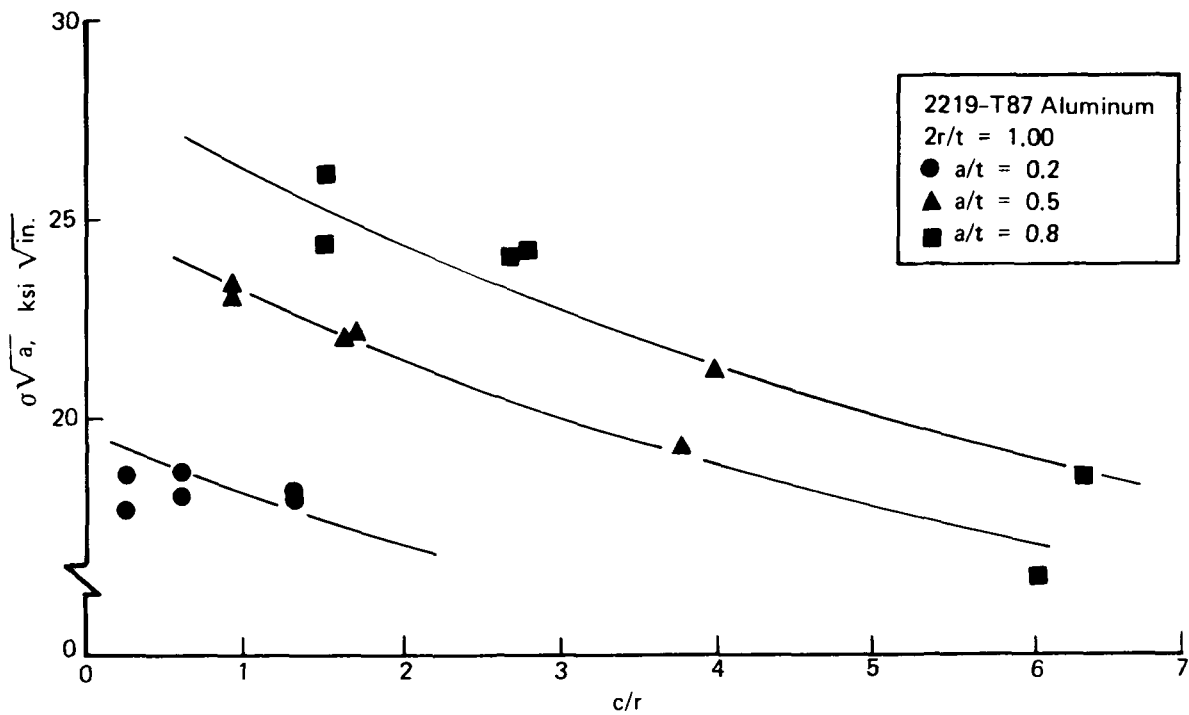
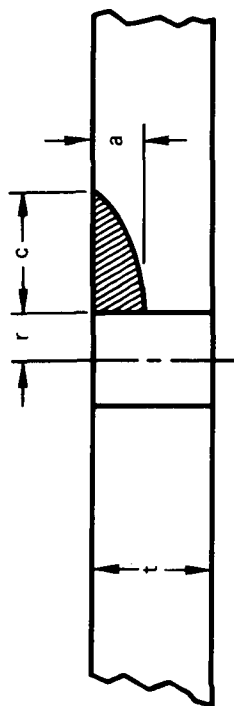
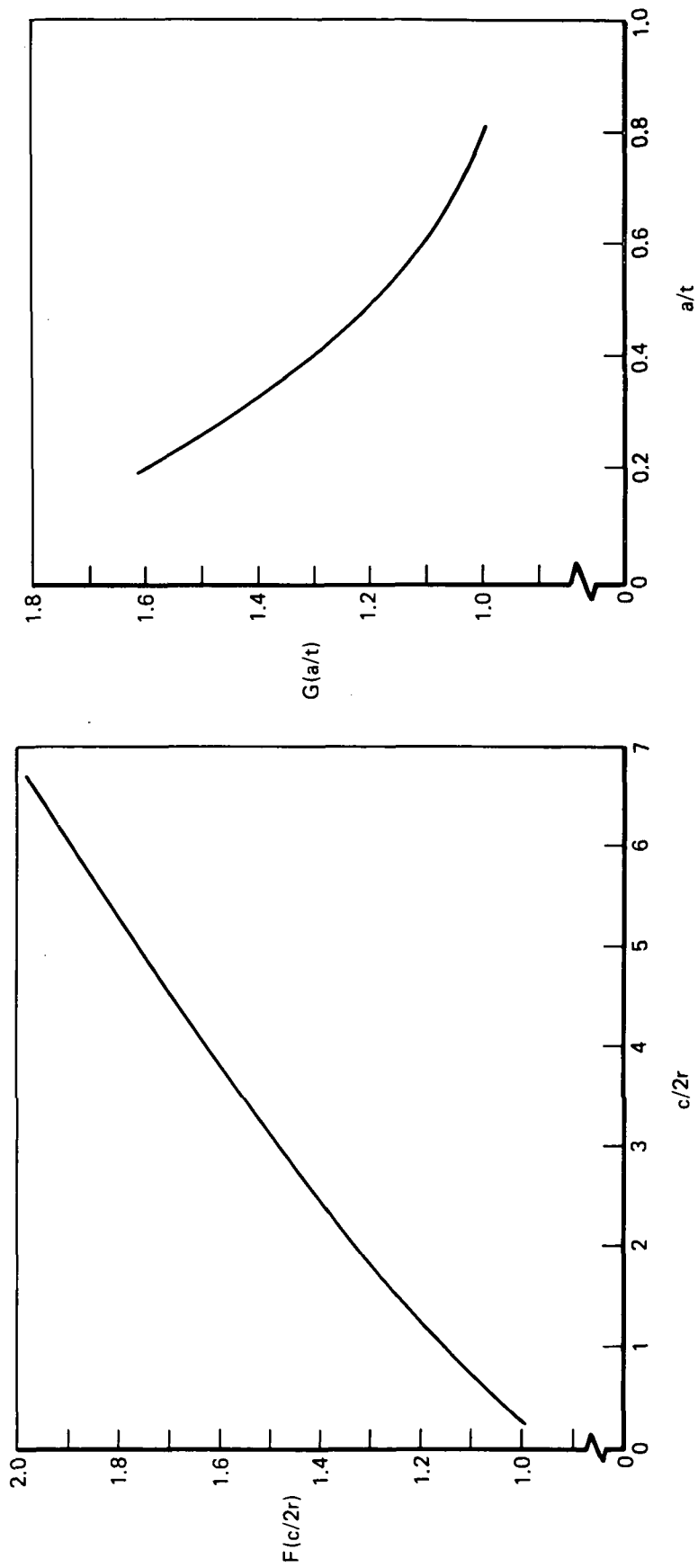


Figure 4-7: PLOTS OF  $\sigma \sqrt{a}$  VS FLAW LENGTH TO HOLE SIZE RATIOS FOR ALUMINUM SPECIMENS WITH FLAWS PROTRUDING FROM HOLES

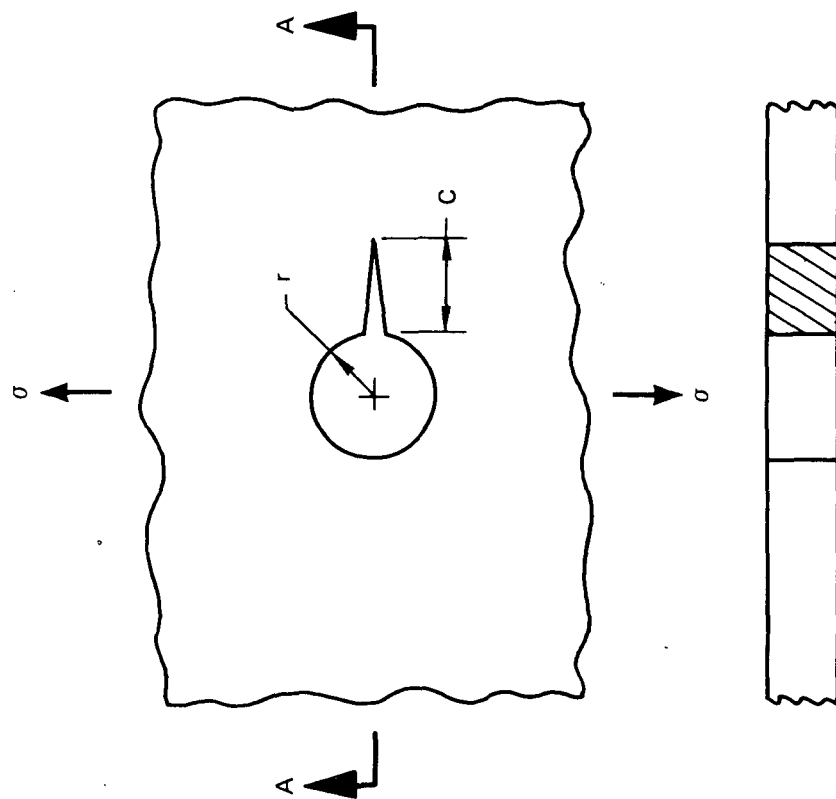


$$K_{Ic} = 1.1 \sigma \sqrt{a} \cdot F(c/2r) \cdot G(a/t) \sqrt{4r/t}$$

Figure 4-8: FAILURE CRITERION FOR FLAWS PROTRUDING FROM HOLES



## BOWIE (12) ANALYSIS

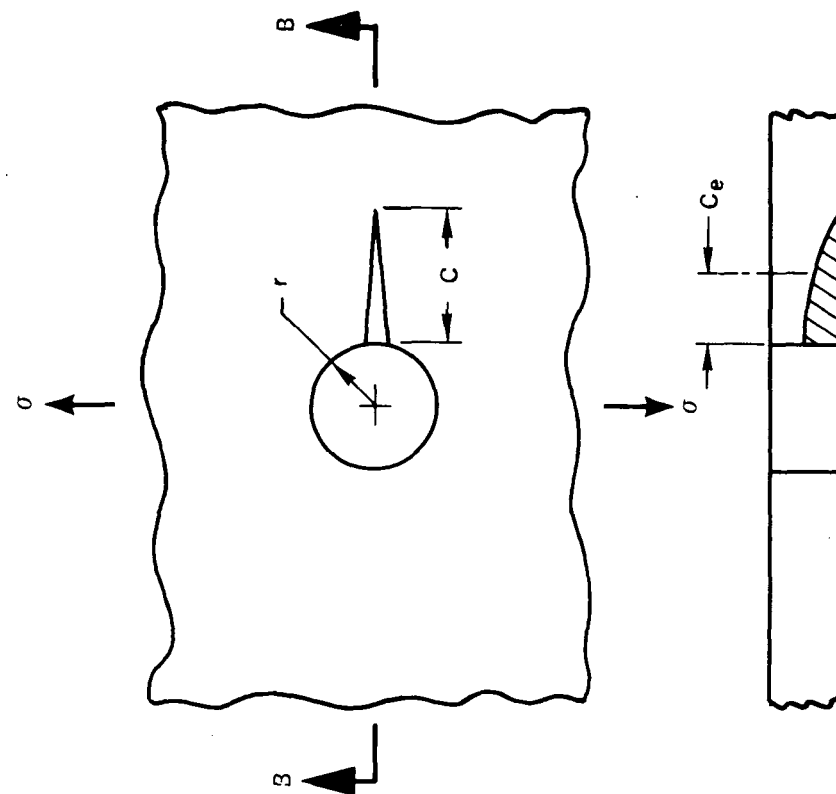


Section A-A

Stress Intensity Analysis:  $K = \sigma \sqrt{\pi c} \cdot F(c/r)$

Failure Criterion:  $K_{Gr} = \sigma \sqrt{\pi c} \cdot F(c/r)$

## EMBEDDED FLAW ANALYSIS



Section B-B

None

$K_{Gr} = \sigma \sqrt{\pi c_e} \cdot F(c_e/r)$

Figure 4-9: COMPARISON OF FAILURE CRITERIA FOR THROUGH-THE-THICKNESS AND EMBEDDED FLAWS PROTRUDING FROM HOLES

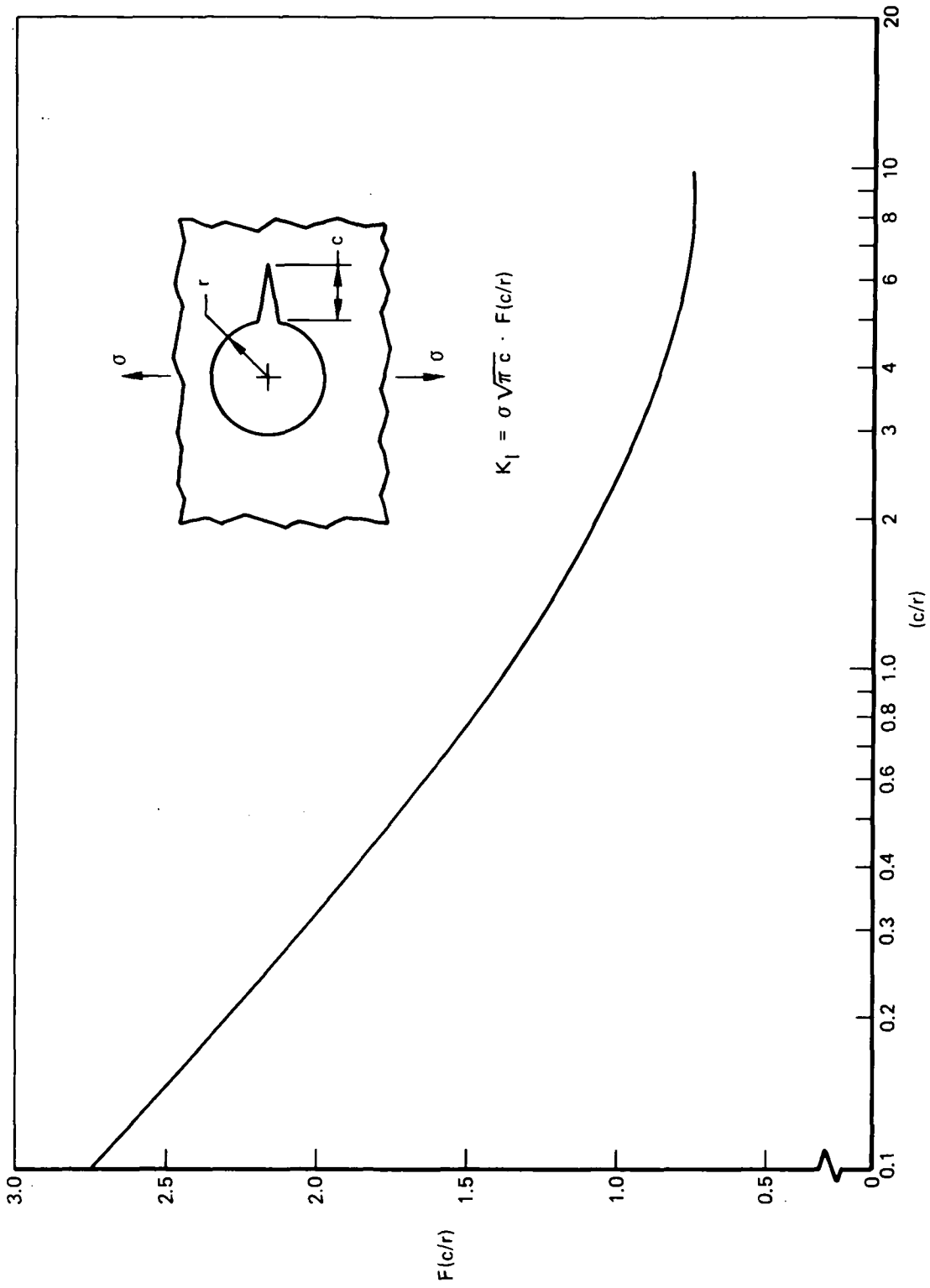


Figure 4-10:  $F(c/r)$  IN FAILURE CRITERION FOR FLAWS PROTRUDING FROM HOLES  
(REFERENCE 12)

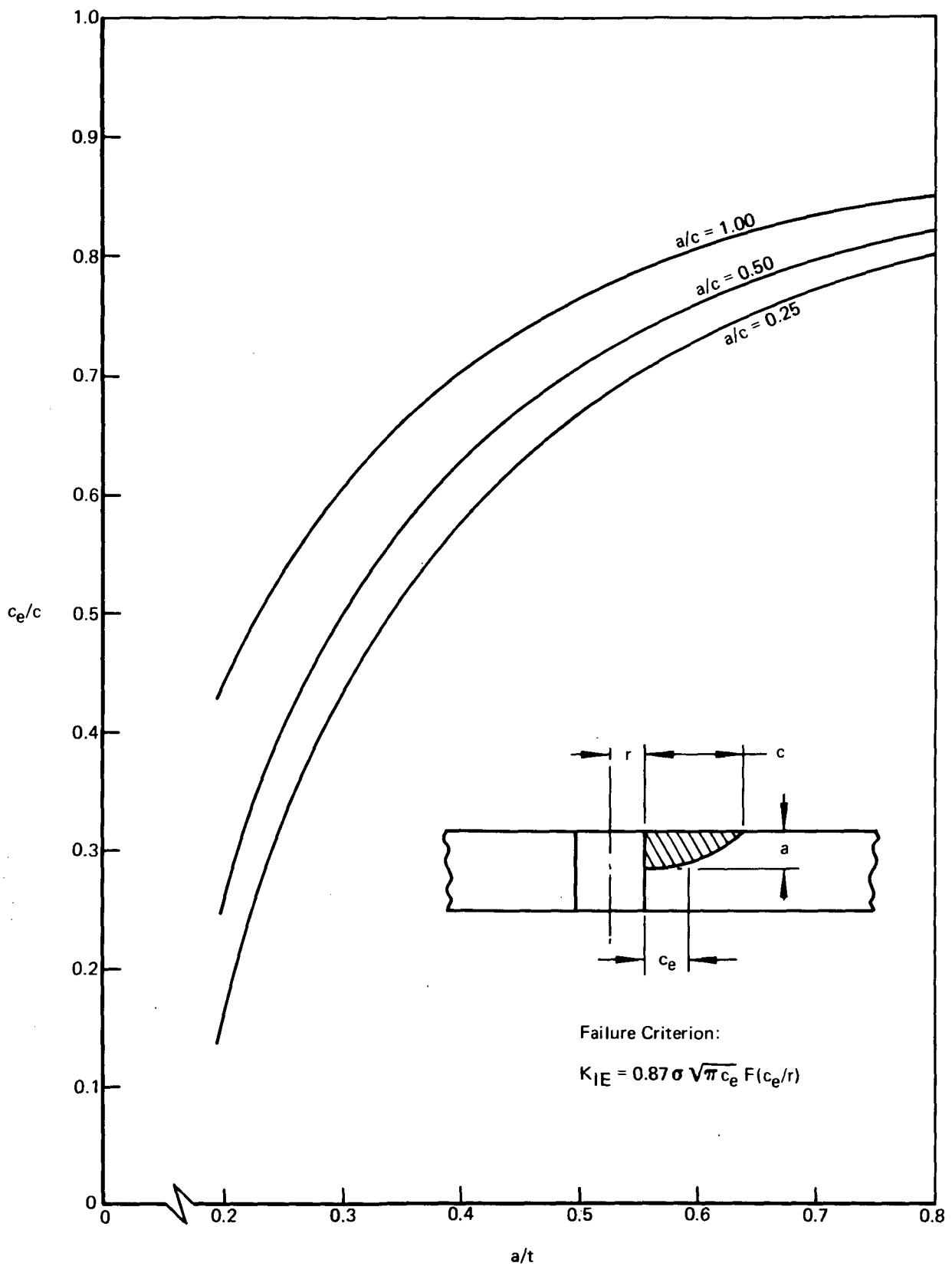
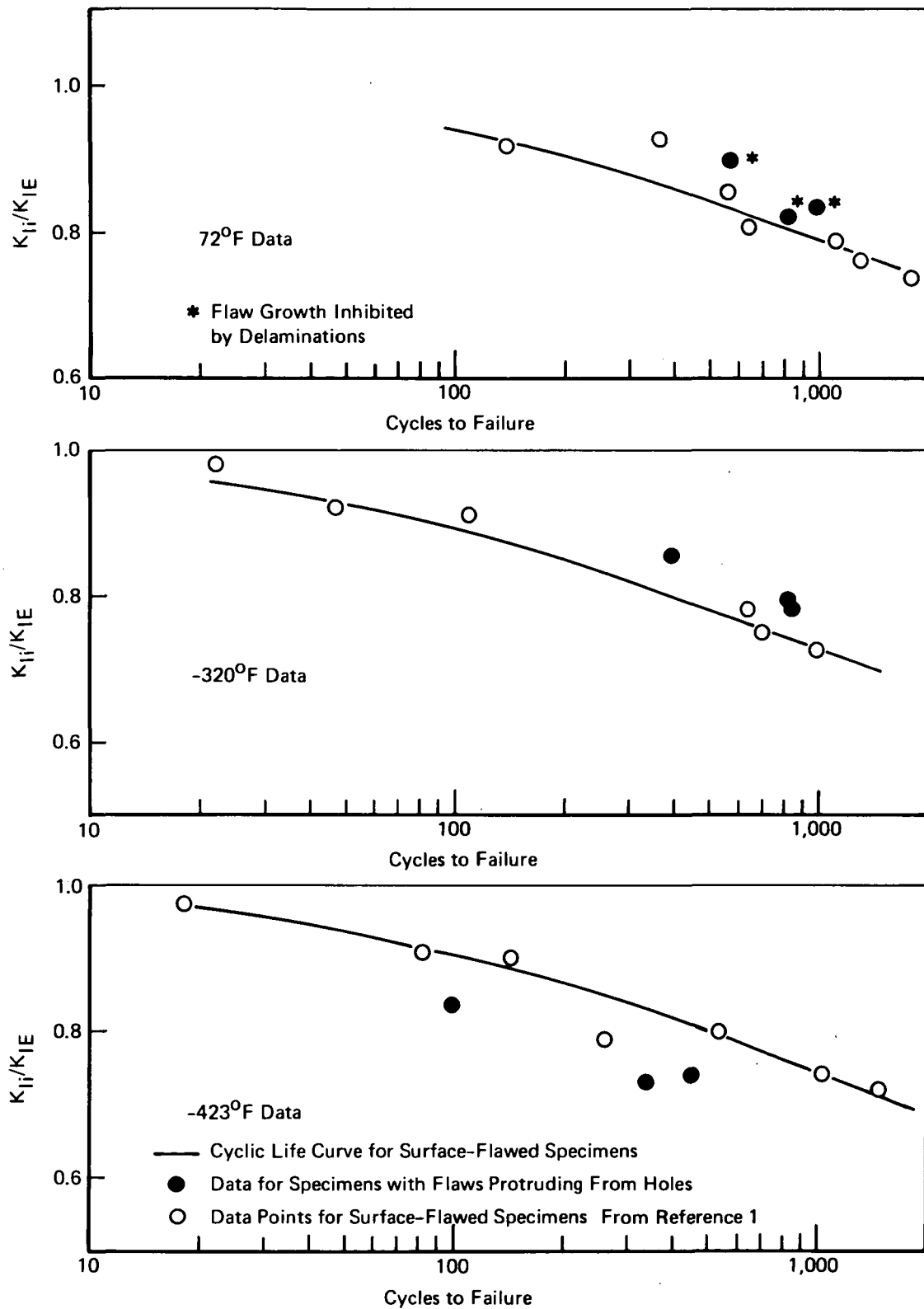
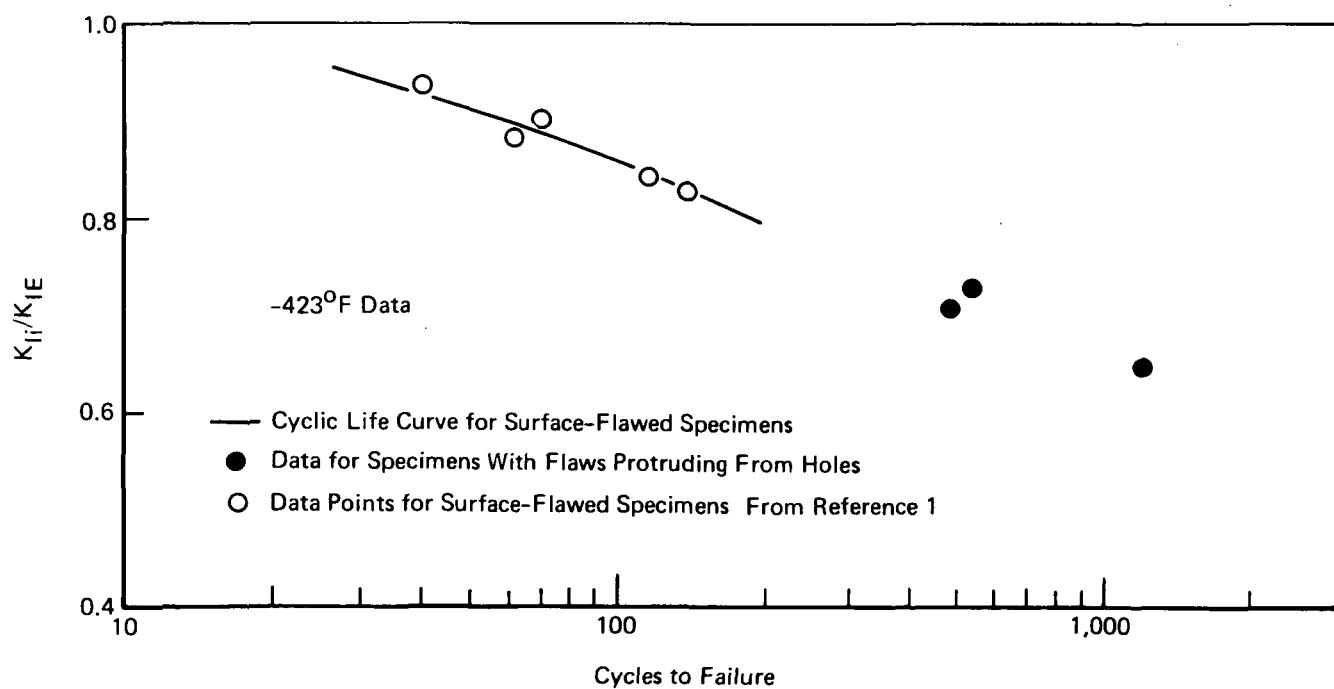
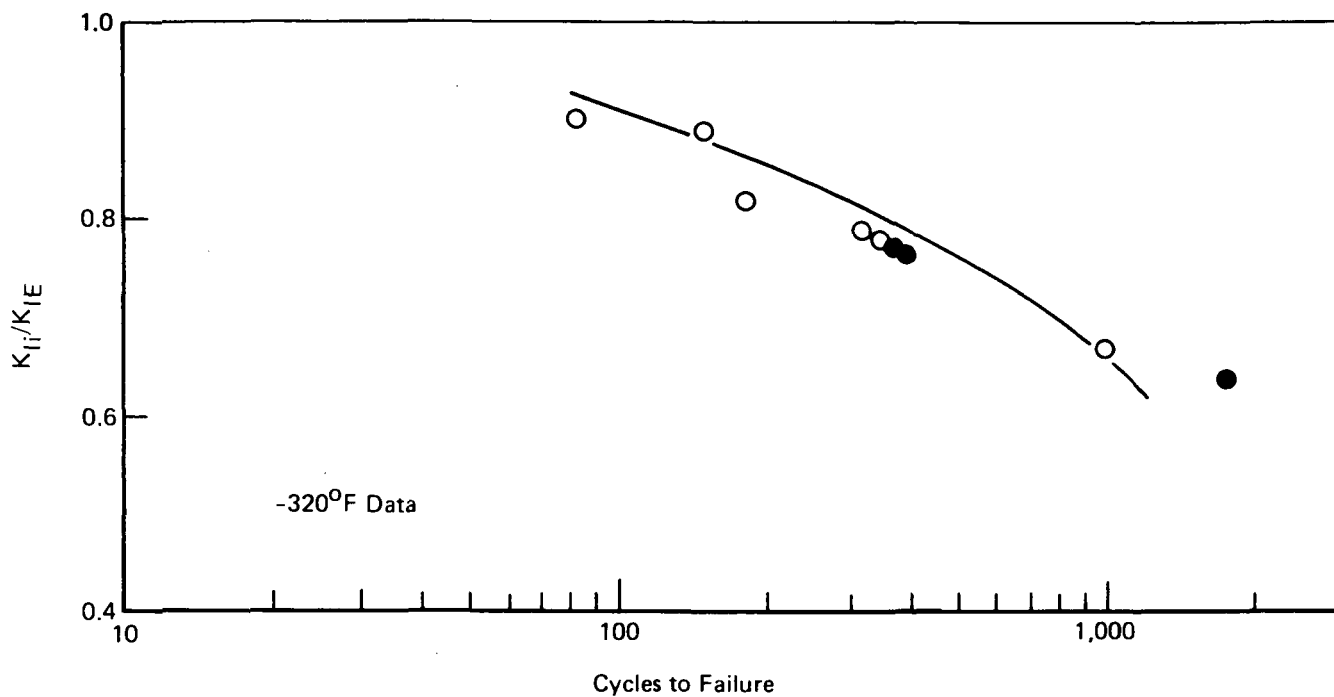


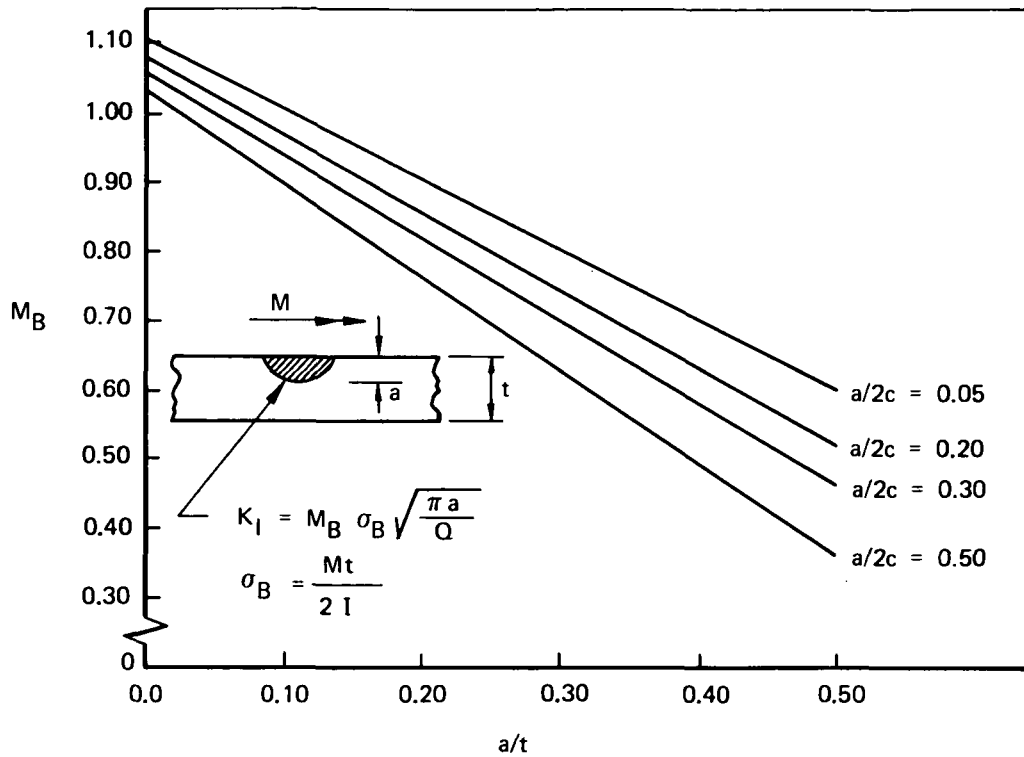
Figure 4-11: VALUES OF EFFECTIVE FLAW LENGTH FOR EMBEDDED FLAWS PROTRUDING FROM HOLES



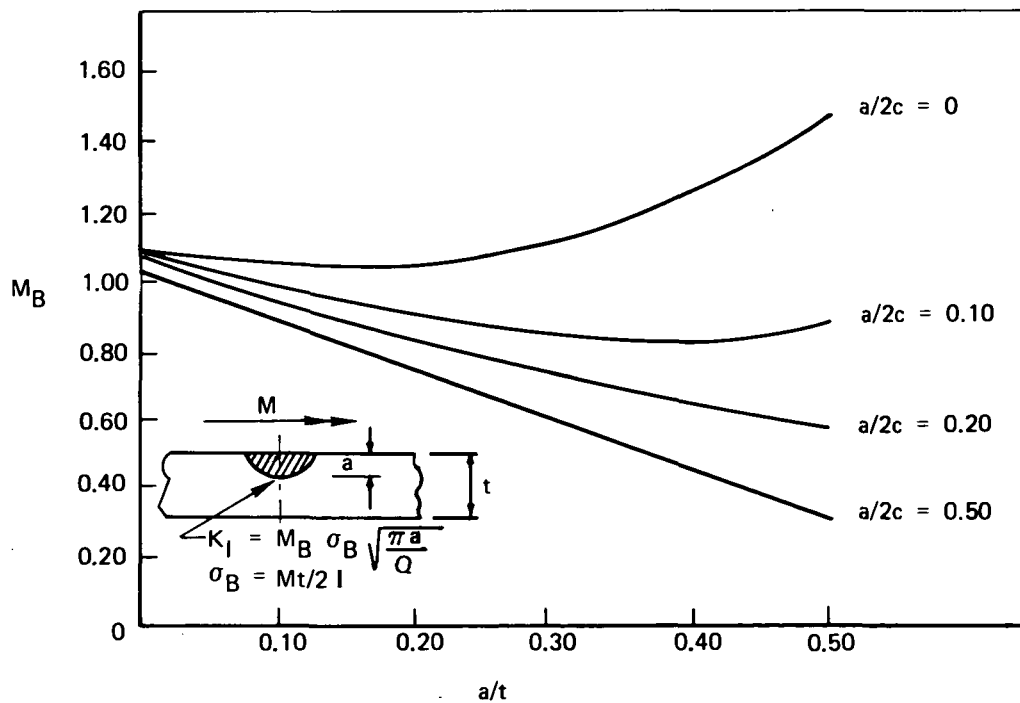
**Figure 4-12: FATIGUE DATA FOR 2219-T87 ALUMINUM SPECIMENS WITH FLAWS PROTRUDING FROM CIRCULAR HOLES**



**Figure 4-13: FATIGUE DATA FOR 5Al-2.5 Sn (ELI) TITANIUM SPECIMENS WITH FLAWS PROTRUDING FROM HOLES**



(b) SHAH'S SOLUTION



(a) SMITH'S SOLUTION

Figure 5-1: STRESS INTENSITY FOR SURFACE-FLAWED PLATES  
SUBJECTED TO BENDING STRESSES

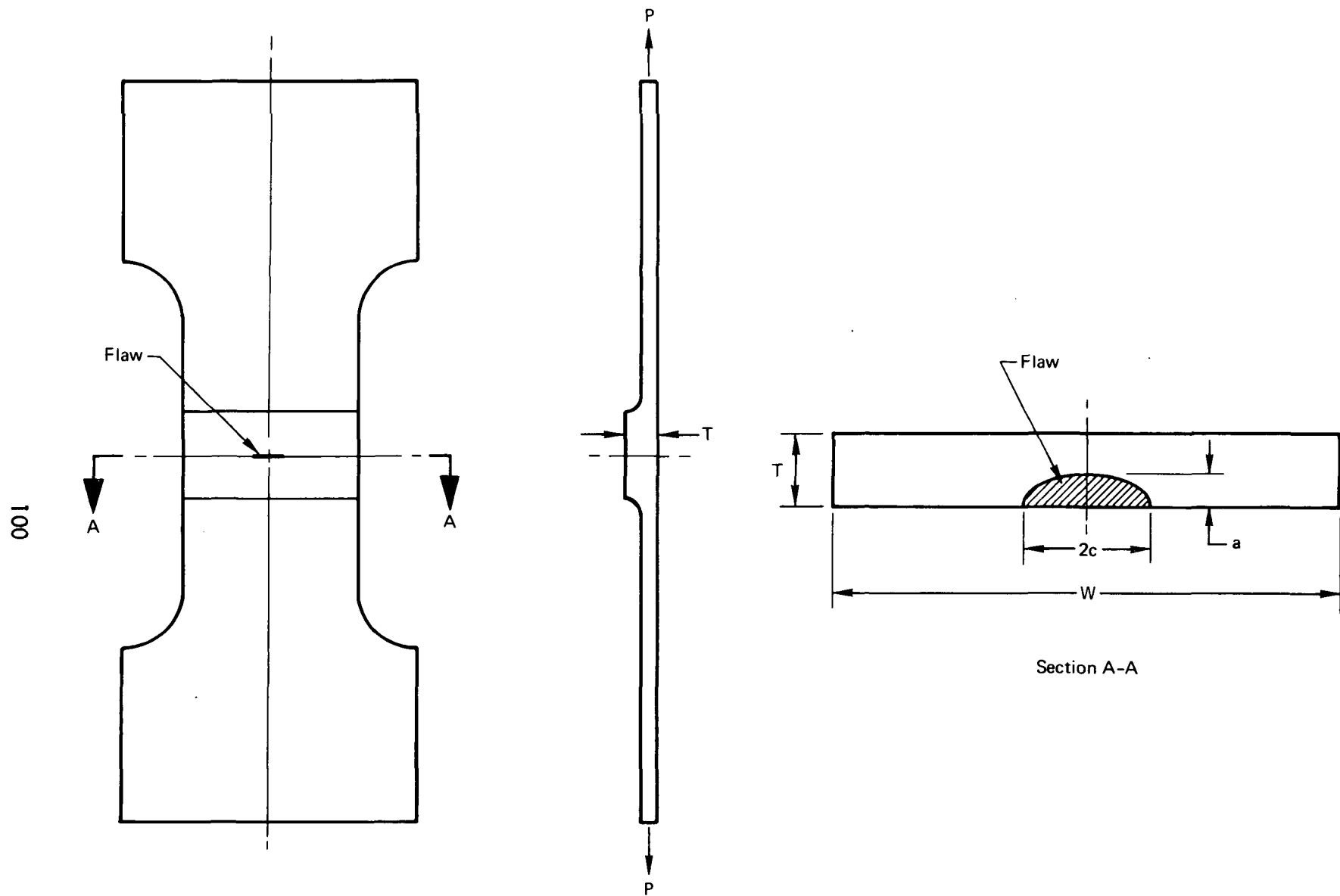


Figure 5-2: SPECIMEN CONFIGURATION FOR COMBINED BENDING/TENSION TESTS

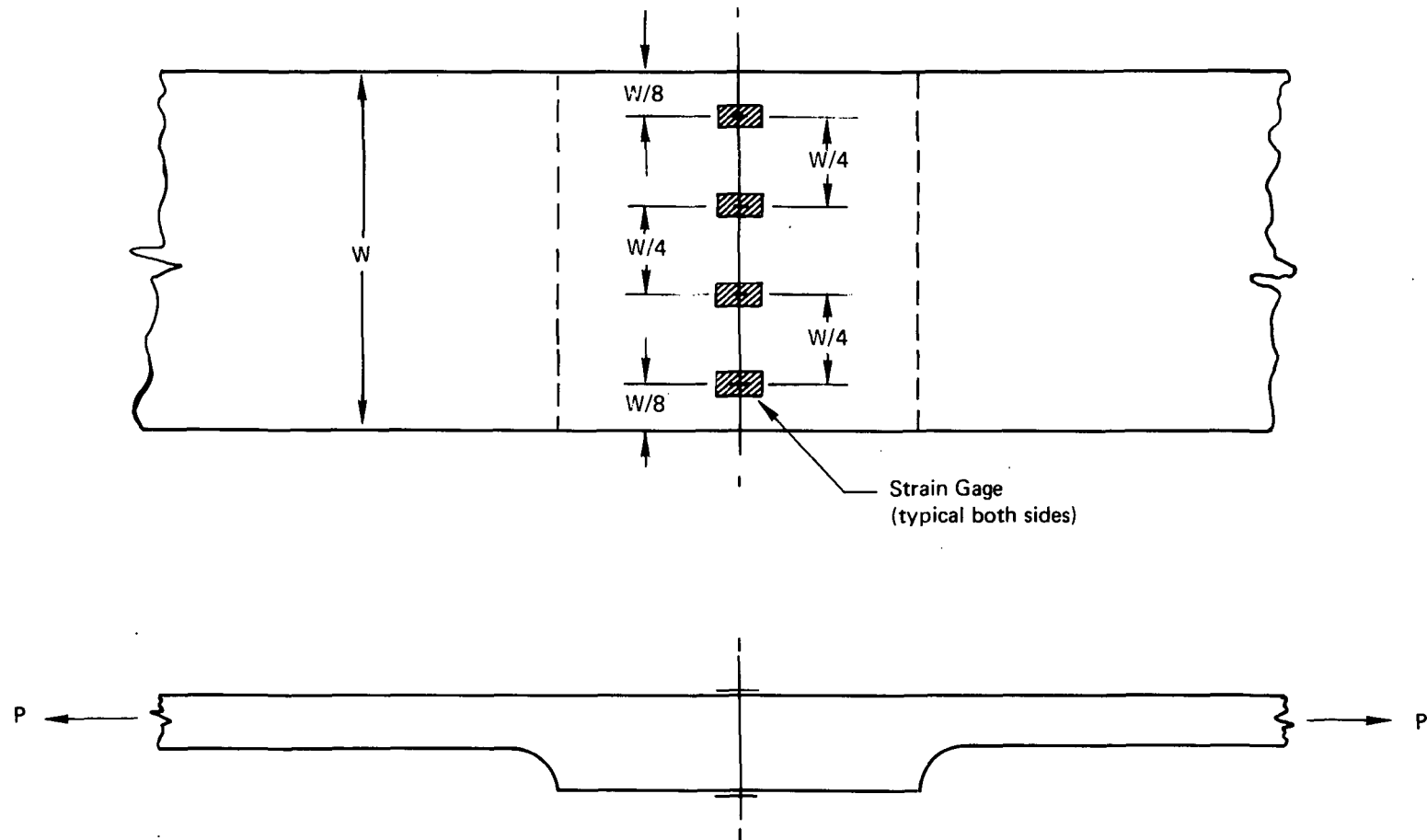
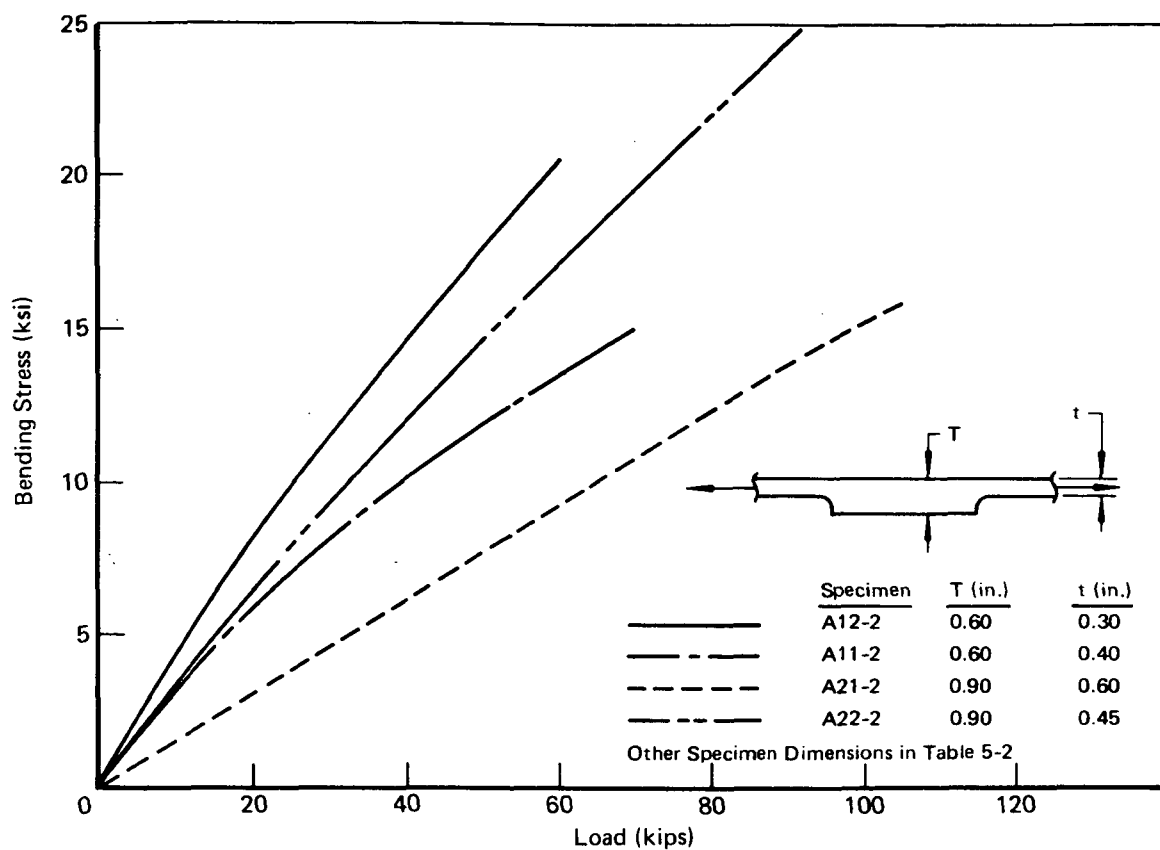
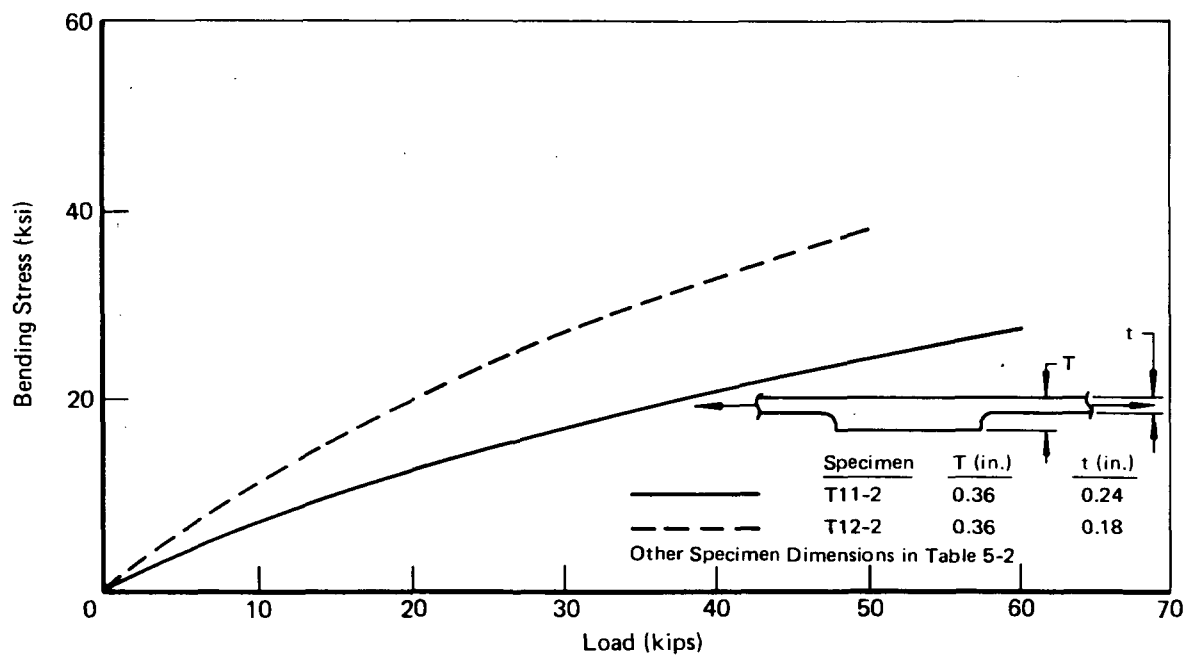


Figure 5-3: INSTRUMENTATION FOR CALIBRATING COMBINED BENDING/TENSION SPECIMENS



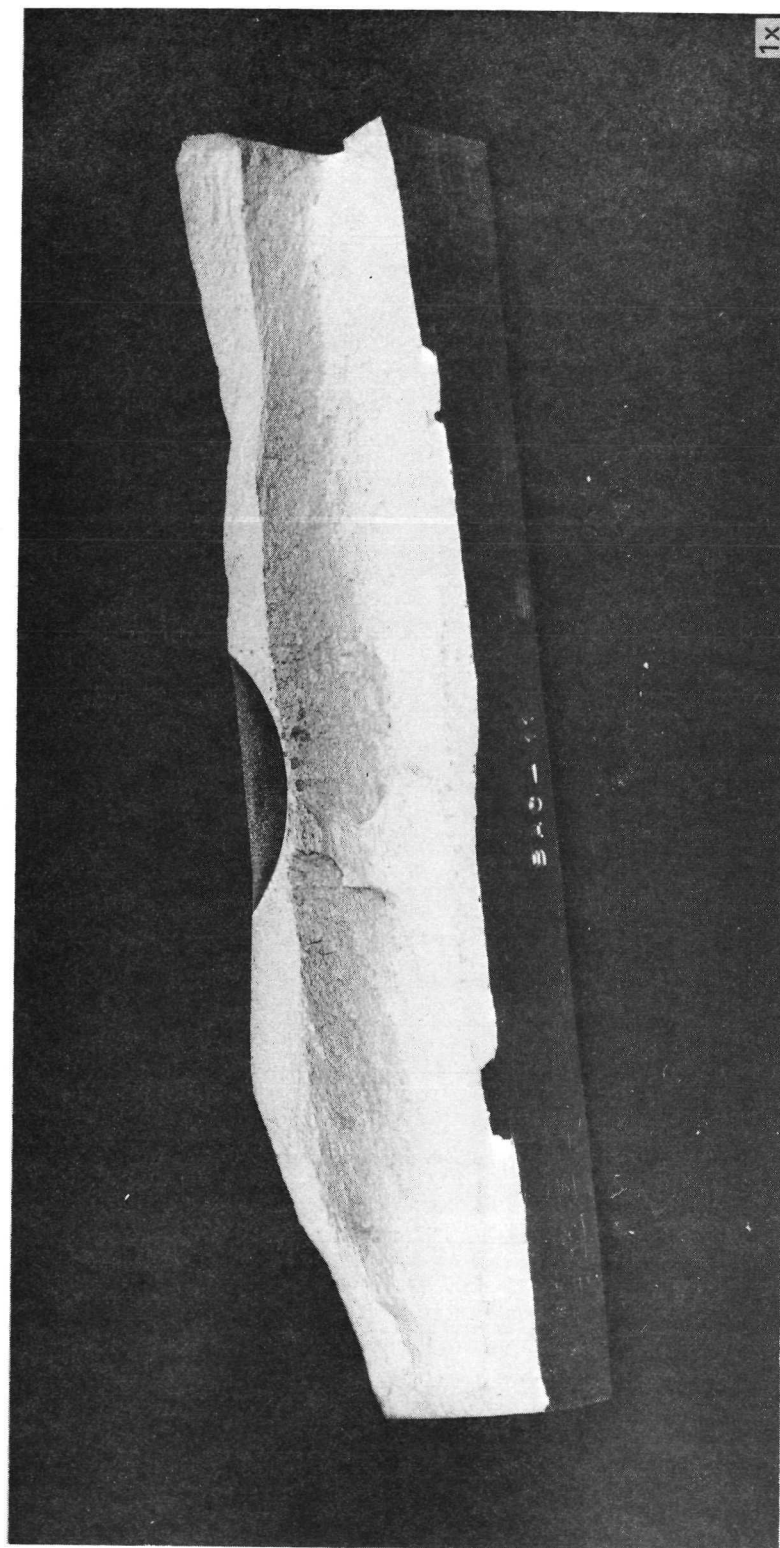


2219-T87 ALUMINUM SPECIMENS



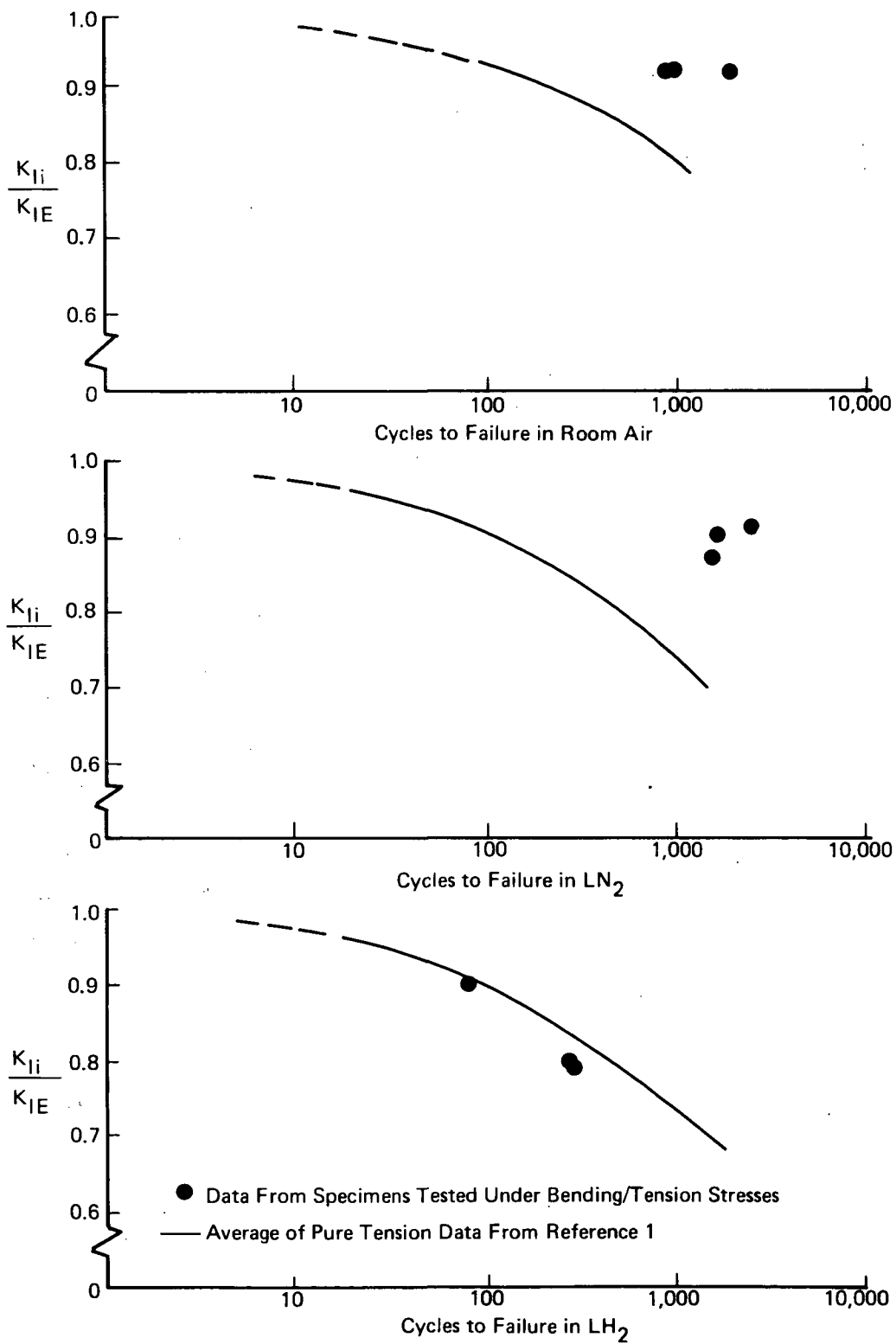
5Al-2.5Sn (ELI) TITANIUM SPECIMENS

Figure 5-4: LOAD-BENDING STRESS CALIBRATIONS FOR COMBINED BENDING AND TENSION SPECIMENS



SPECIMEN AC-11 TESTED AT RT

Figure 5-5: FRACTURE FACE OF SURFACE-FLAWED SPECIMEN FATIGUE TESTED UNDER COMBINED BENDING AND TENSION STRESSES



**Figure 5-6: FATIGUE DATA FOR 2219-T87 ALUMINUM SURFACE-FLAWED SPECIMENS SUBJECTED TO COMBINED BENDING/TENSION STRESSES OR PURE TENSILE STRESSES**

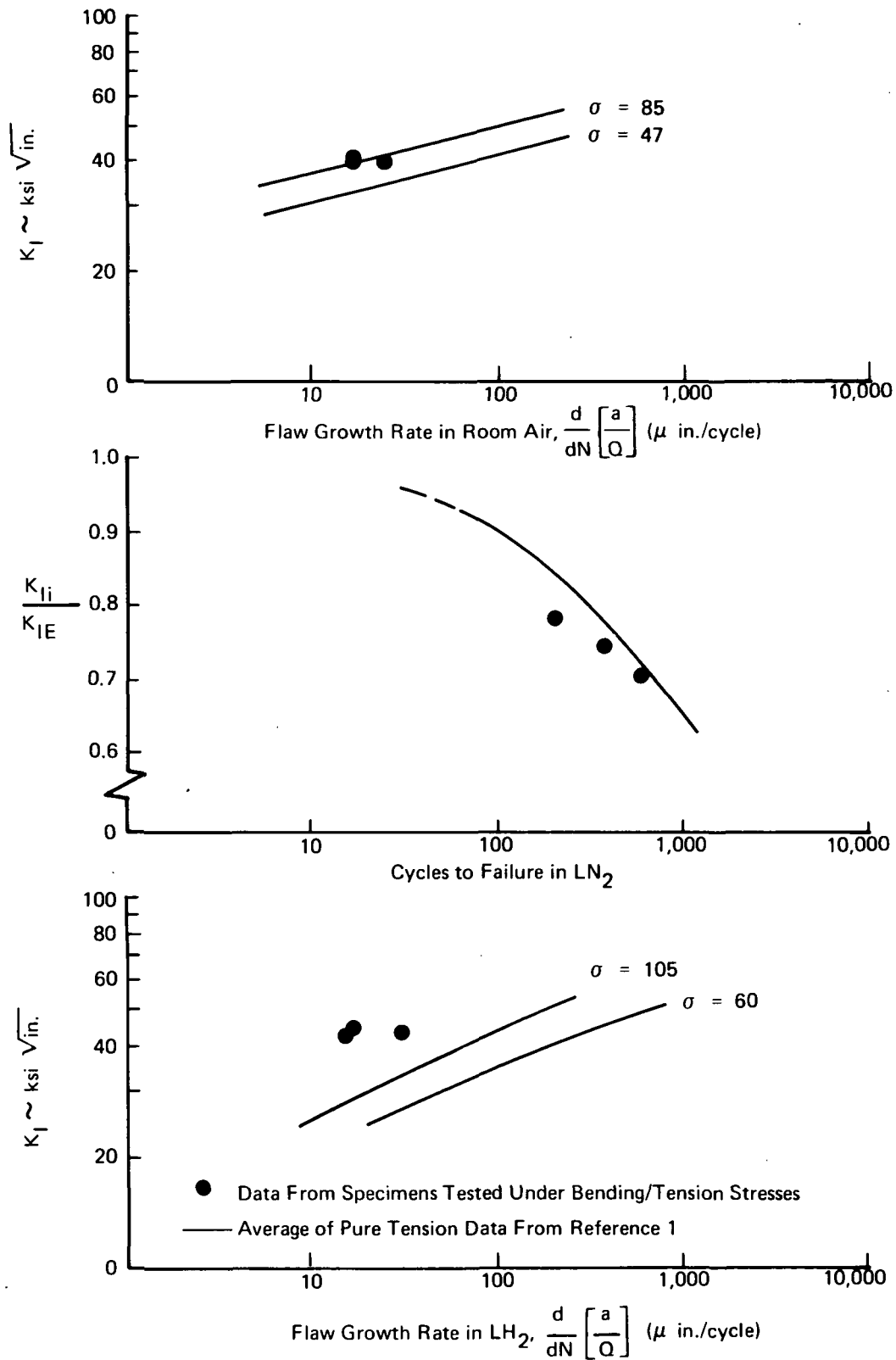


**Figure 5-7: FATIGUE DATA FOR 5Al-2.5Sn (ELI) TITANIUM SURFACE-FLAWED SPECIMENS SUBJECTED TO COMBINED BENDING/TENSION STRESSES OR PURE TENSILE STRESSES**

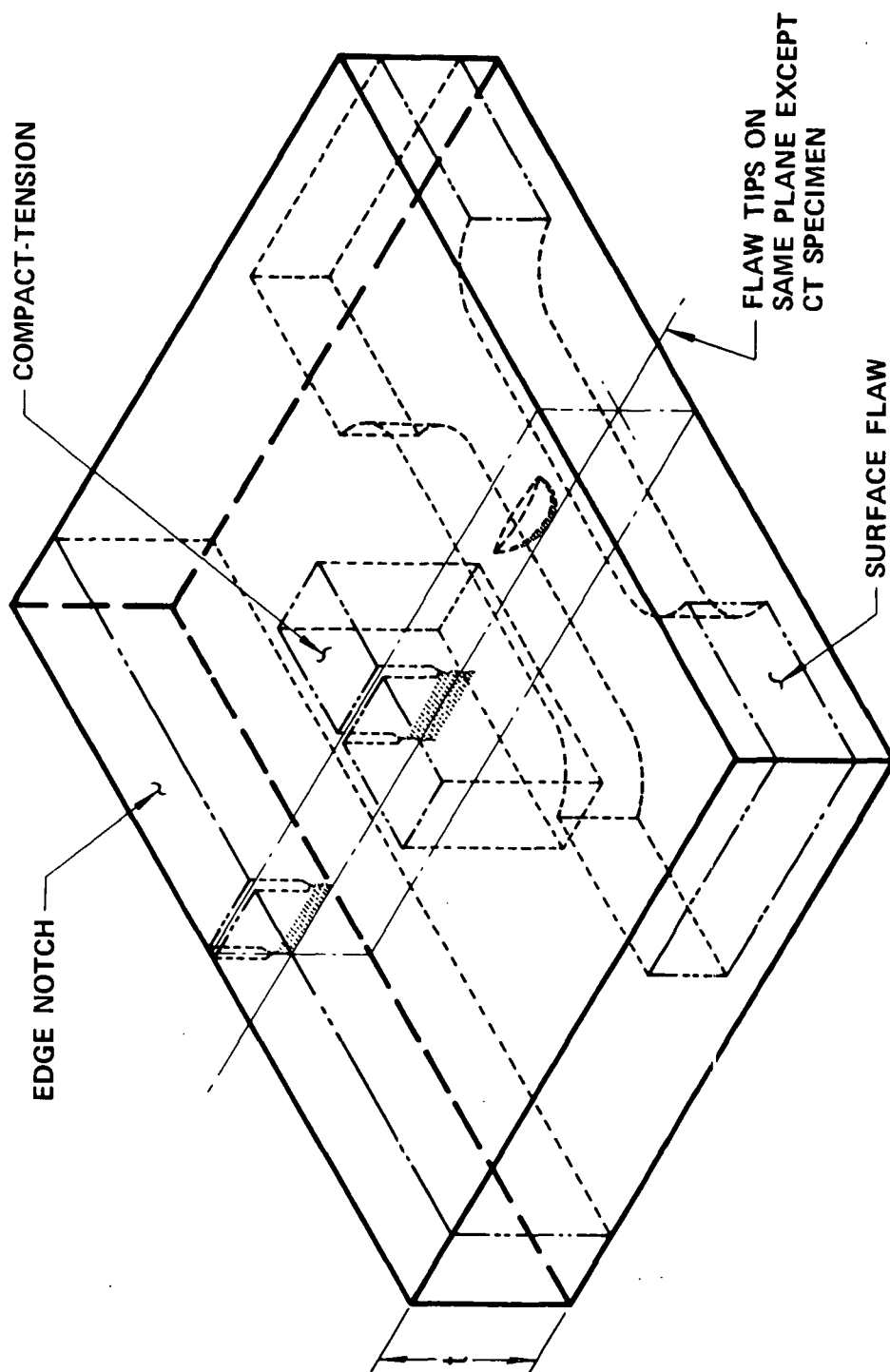
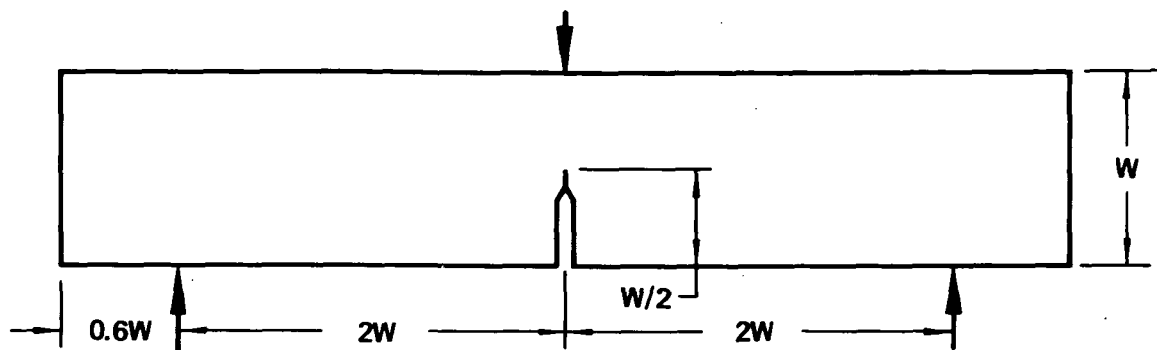


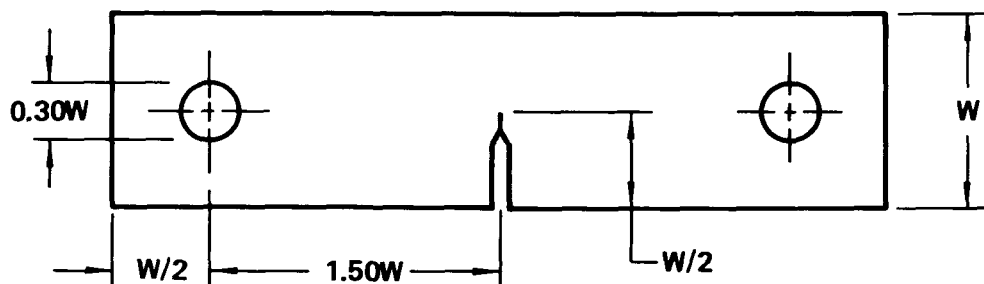
Figure 6-1: SPECIMEN LOCATION WITHIN PLATE



$W = 2.50$  Inches (6.350 Cm) For 2219-T87 Aluminum

$W = 0.75$  Inch (1.905 Cm) For 5Al-2.5Sn (ELI) Titanium

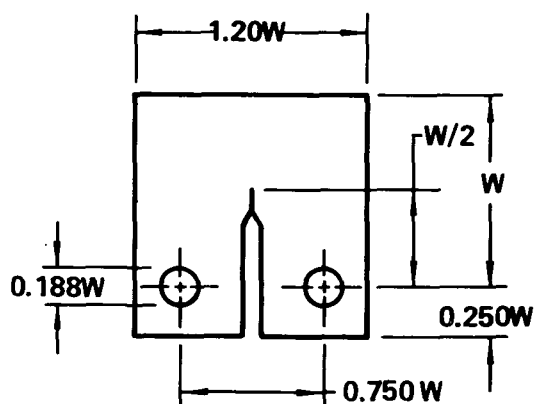
### SENB TEST SPECIMENS



$W = 2.50$  Inches (6.350 Cm) For 2219-T87 Aluminum

$W = 0.75$  Inch (1.905 Cm) For 5Al-2.5 Sn (ELI) Titanium

### SENT TEST SPECIMENS

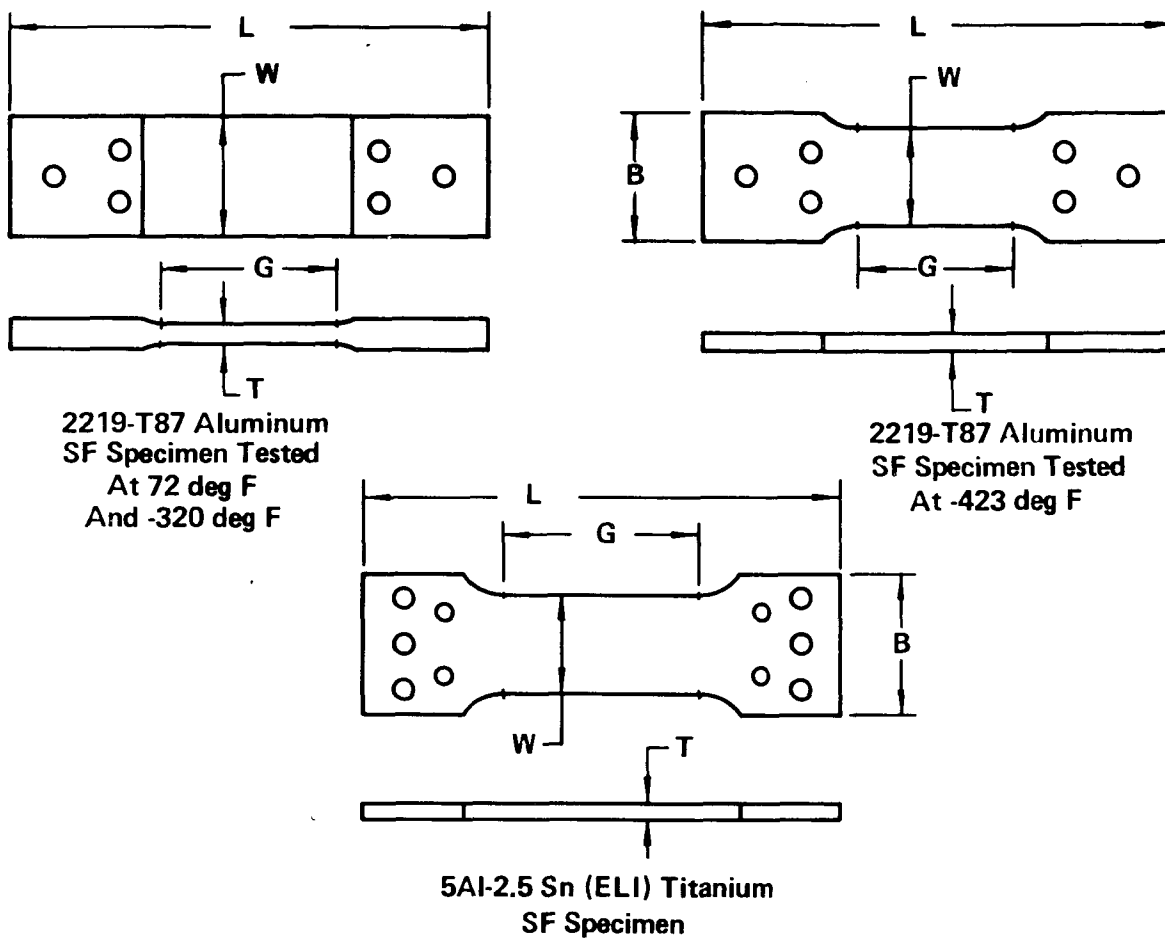


$W = 2.00$  Inches (5.08 Cm) For 2219-T87 Aluminum

$W = 0.60$  Inch (1.27 Cm) For 5Al-2.5 Sn (ELI) Titanium

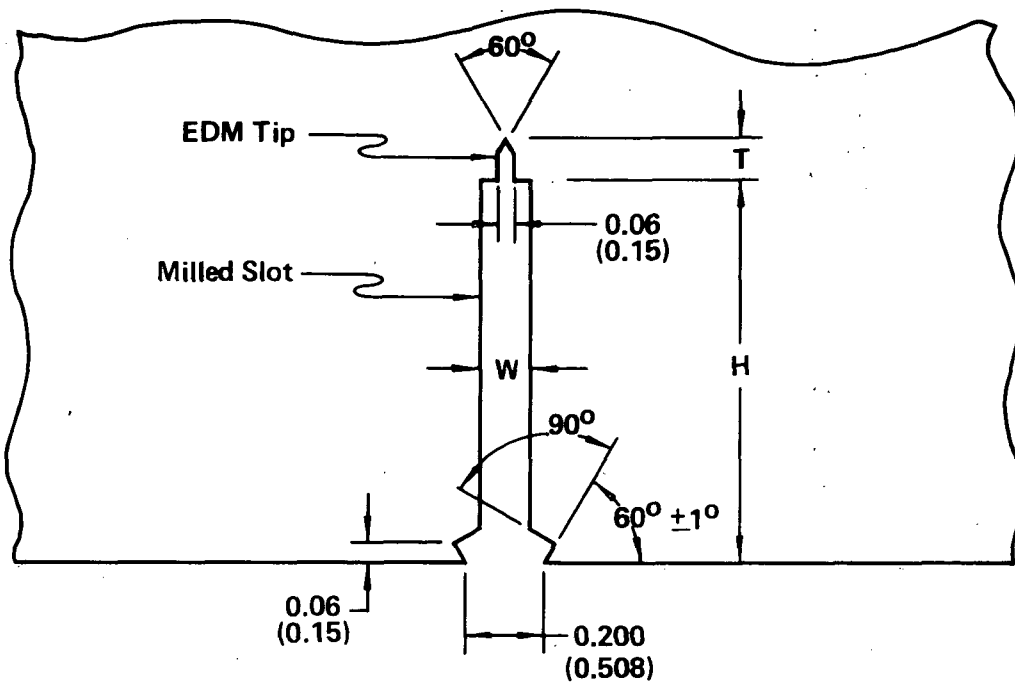
### CT TEST SPECIMENS

Figure 6-2: DETAILS OF SENB, SENT AND CT SPECIMENS



MATERIAL	TEST TEMPERATURE		L		B		W		G		T	
	deg F	deg C	In	Cm	In	Cm	In	Cm	In	Cm	In	Cm
2219-T87 Aluminum	72	22	24.0	61	6.00	15.2	6.00	15.2	9.00	22.9	1.10	2.79
	-320	-196	24.0	61	6.00	15.2	6.00	15.2	9.00	22.9	1.10	2.79
	-423	-253	24.0	61	6.50	16.5	5.00	12.7	8.00	20.3	1.00	2.54
5Al-2.5 Sn(ELI) Titanium	72		12.0	30.5	3.50	8.9	2.50	6.35	5.00	12.70	0.375	0.952
	-320											
	-423											

Figure 6-3: SPECIMEN DIMENSIONS FOR SF SPECIMENS USED IN CONFIGURATION EFFECT TESTS

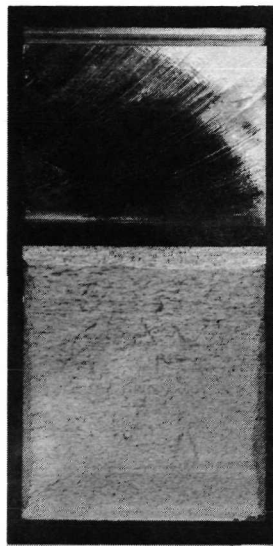


NOTE: Unbracketed Dimensions Are In Inches  
Bracketed Dimensions Are In Centimeters

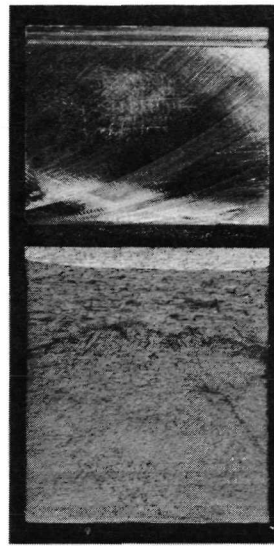
MATERIAL	SPECIMEN TYPE	H		T		W	
		In	Cm	In	Cm	In	Cm
2219-T87 Aluminum	SENB	1.00	2.54	0.10	0.25	0.125	0.318
	SENT	1.00	2.54	0.10	0.25	0.125	0.318
	CT	1.40	3.56	0.10	0.25	0.125	0.318
5Al-2.5 Sn(ELI) Titanium	SENB	0.20	0.51	0.05	0.13	0.100	0.254
	SENT	0.20	0.51	0.05	0.13	0.100	0.254
	CT	0.30	0.76	0.05	0.13	0.100	0.254

Figure 6-4: CRACK STARTER DETAILS FOR SENB, SENT AND CT SPECIMENS

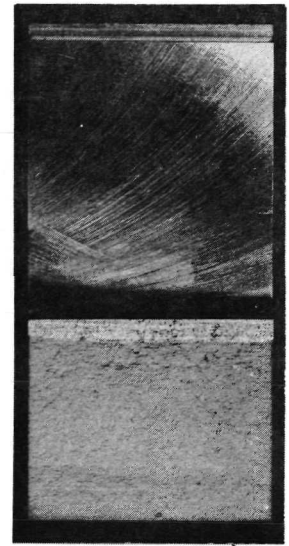




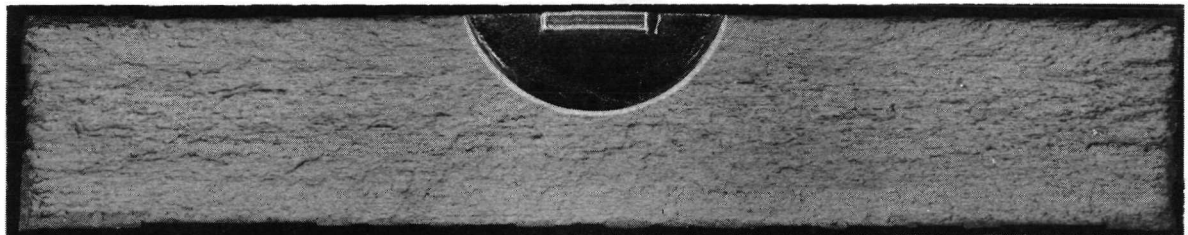
72 deg F  
SENB Specimen



-320 deg F  
SENT Specimen



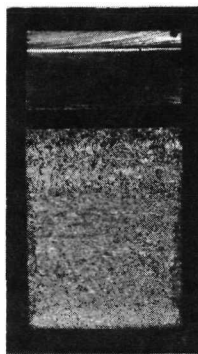
-423 deg F  
CT Specimen



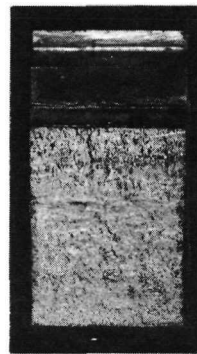
SF Specimen

-320 deg F

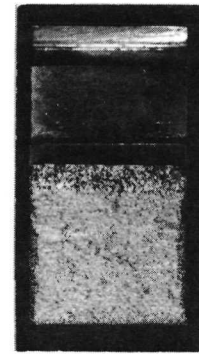
### 2219-T87 ALUMINUM SPECIMEN FRACTURE FACES



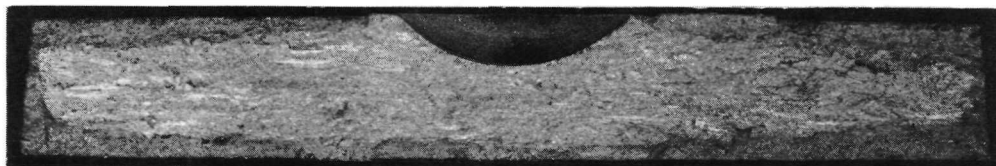
-423 deg F  
SENB Specimen



-423 deg F  
SENT Specimen



-423 deg F  
CT Specimen

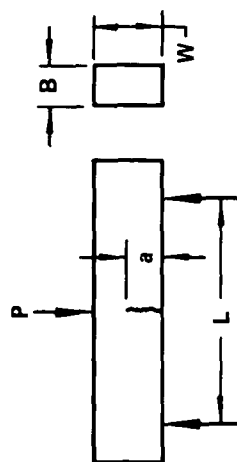
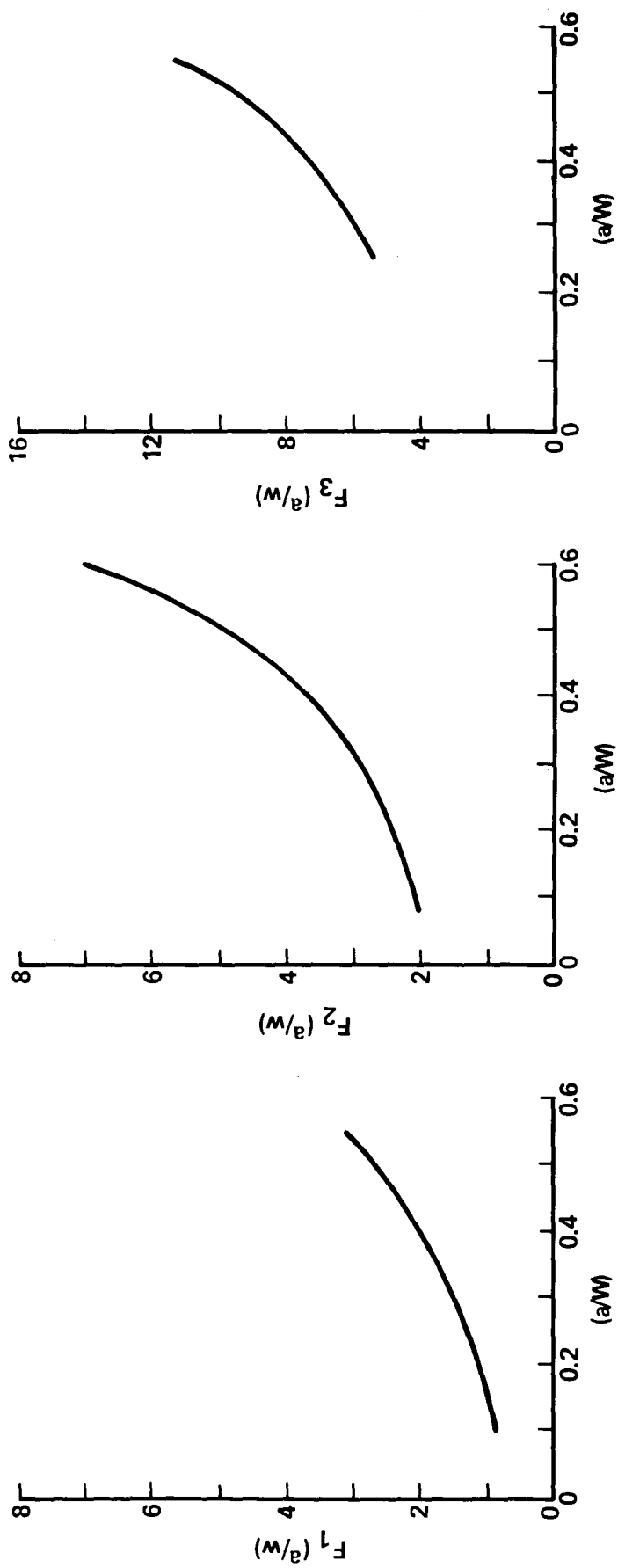


SF Specimen

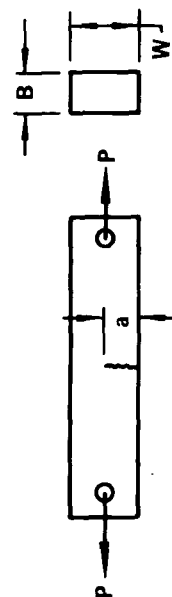
-423 deg F

### 5Al-2.5 Sn (ELI) TITANIUM SPECIMEN FRACTURE FACES

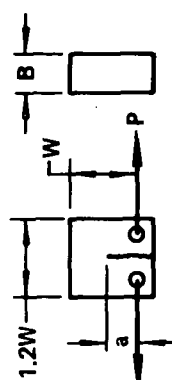
Figure 6-5: FRACTURE FACES OF TEST SPECIMENS



$$K = \frac{PL}{BW^{3/2}} \cdot F_1(a/W)$$



$$K = \frac{Pa^{1/2}}{BW} \cdot F_2(a/W)$$



$$K = \frac{P}{BW^{1/2}} \cdot F_3(a/W)$$

Figure 6-6: STRESS INTENSITY EXPRESSIONS FOR SENB, SENT AND CT SPECIMENS

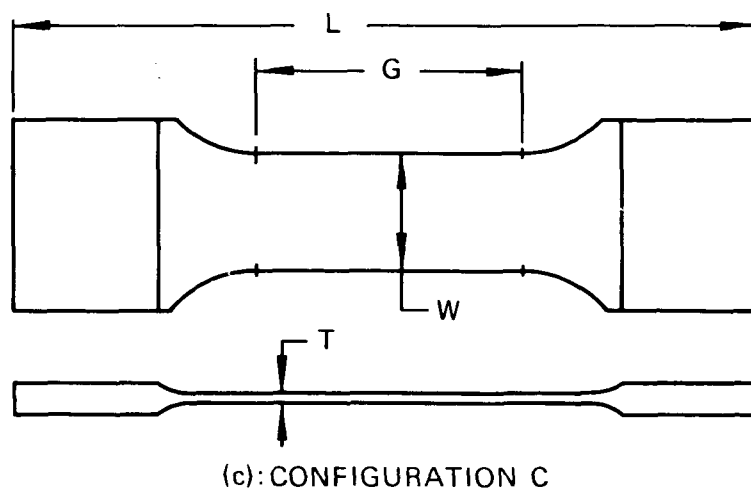
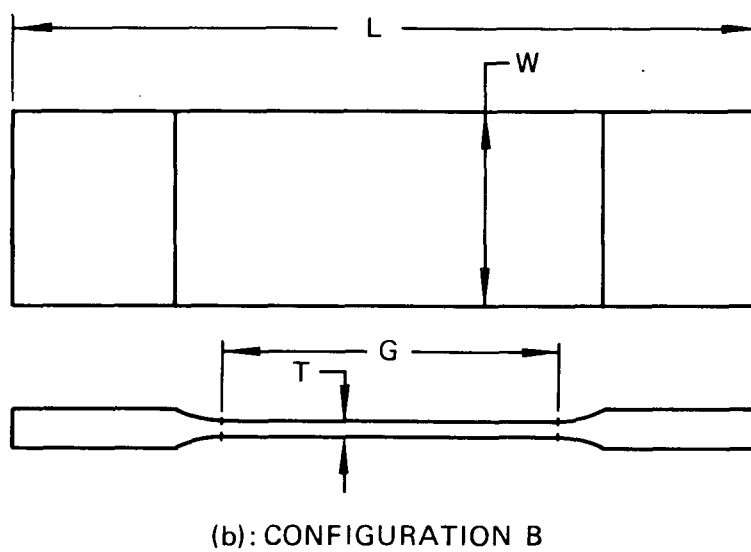
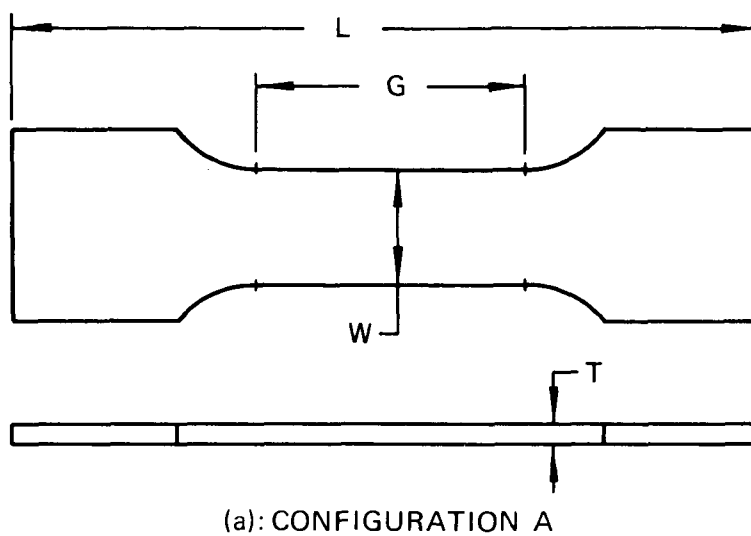


Figure 6-7: SPECIMEN CONFIGURATIONS FOR THICKNESS EFFECT TESTS

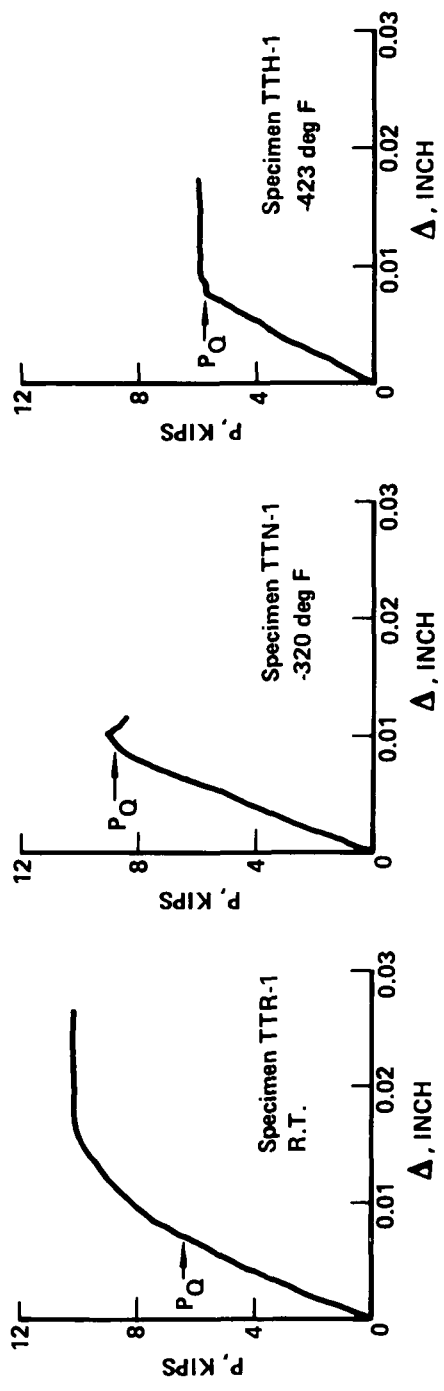
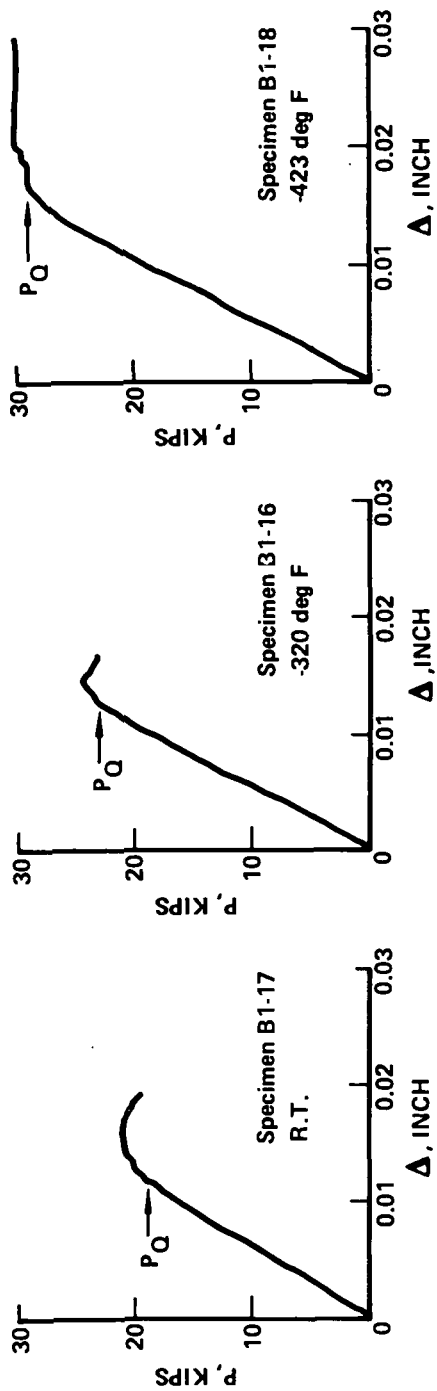


Figure 6-8: TEST RECORDS FOR SINGLE-EDGE-NOTCHED-TENSION SPECIMENS

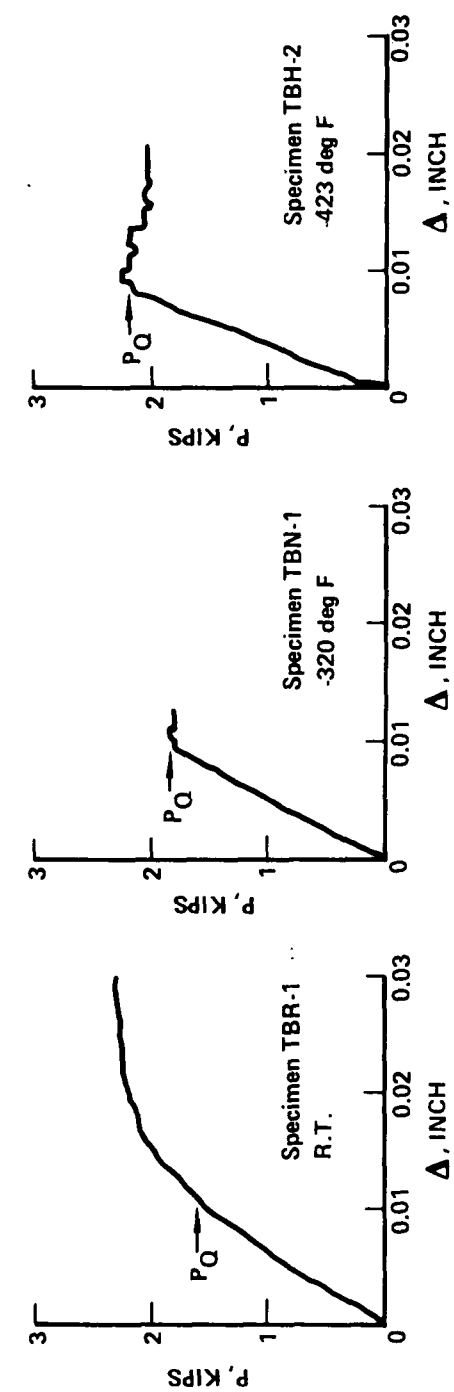
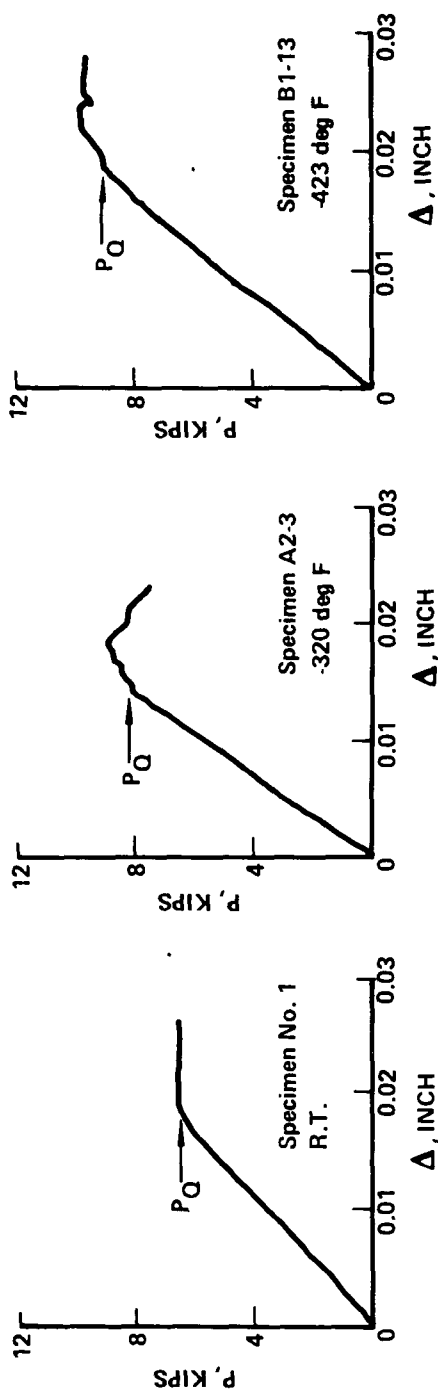
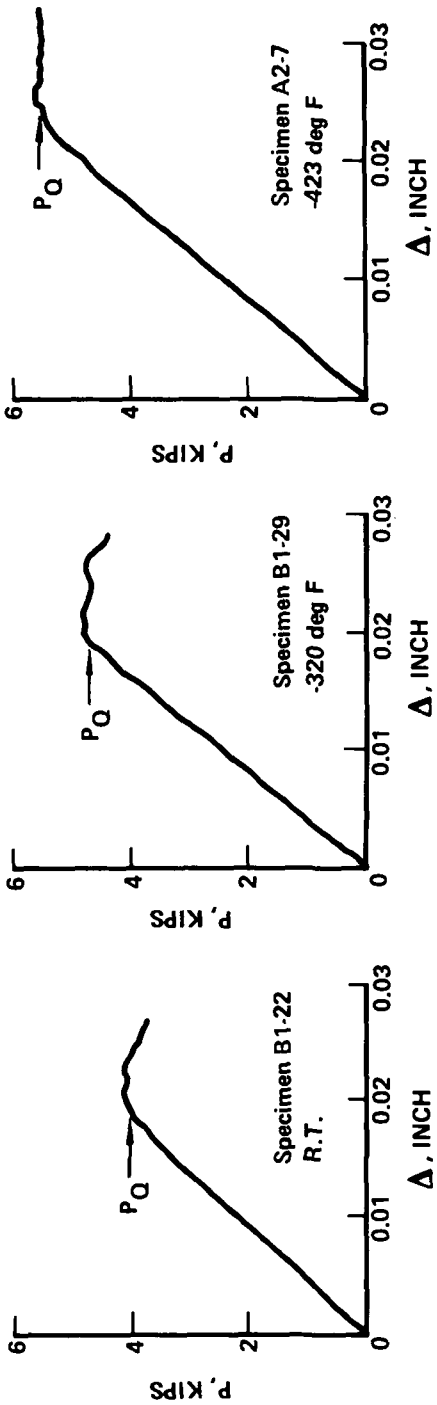
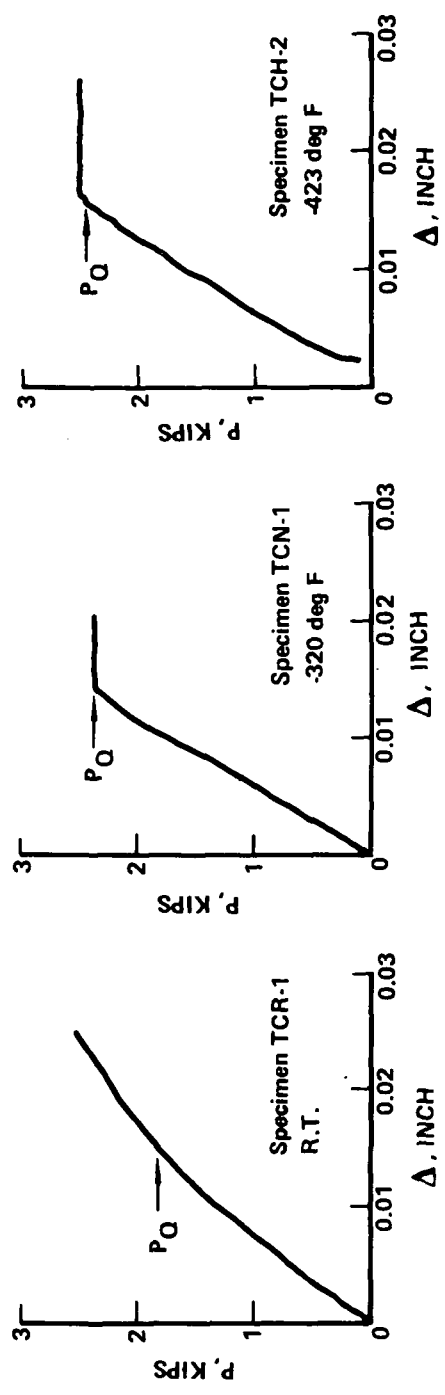


Figure 6-9: TEST RECORDS FOR SINGLE-EDGE-NOTCHED-BEND SPECIMENS



2219-T87 ALUMINUM CT SPECIMENS



Ti-5Al-2.5Sn(ELI) CT SPECIMENS

Figure 6-10: TEST RECORDS FOR COMPACT TENSION SPECIMENS

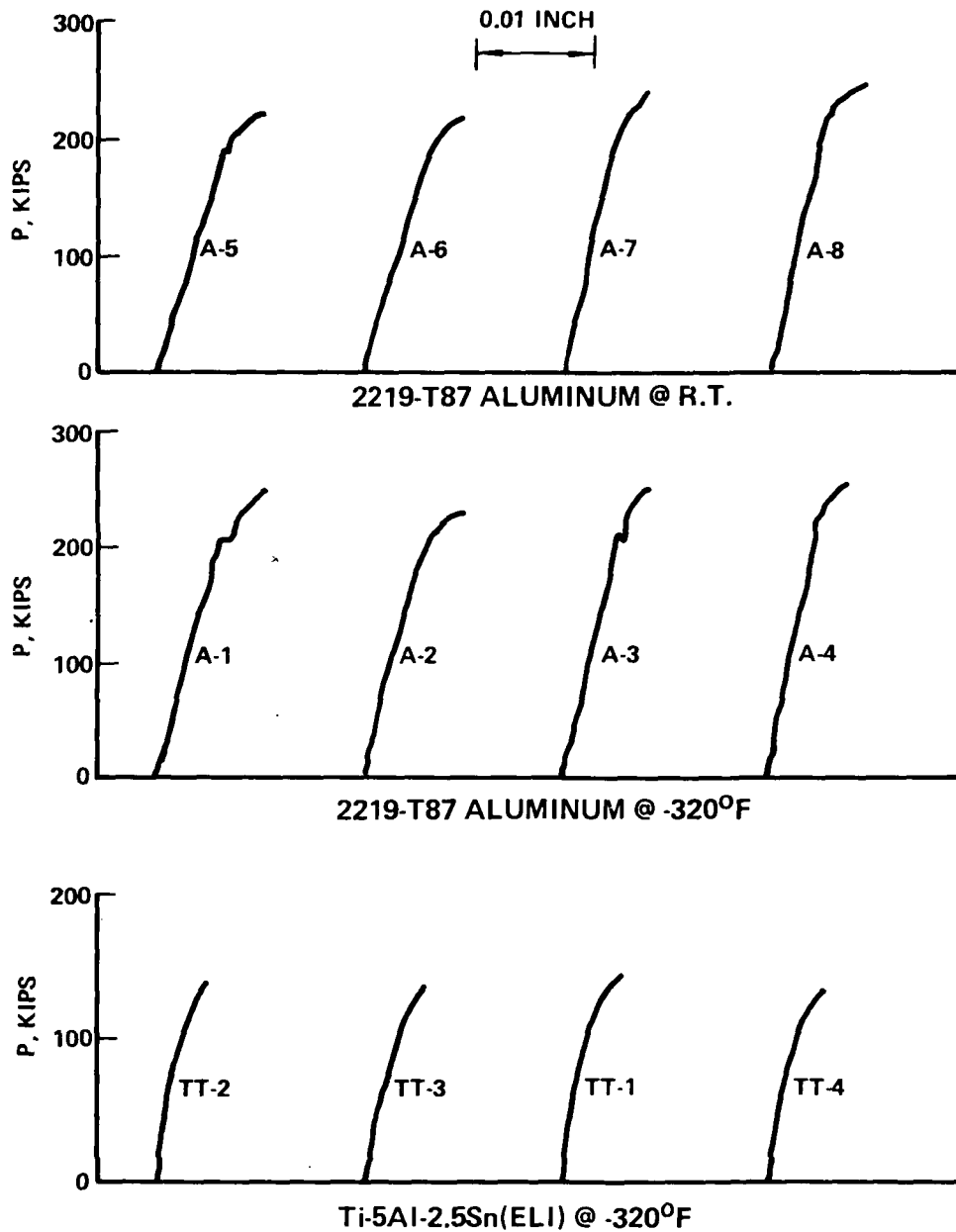


Figure 6-11: TEST RECORDS FOR SURFACE-FLAWED SPECIMENS

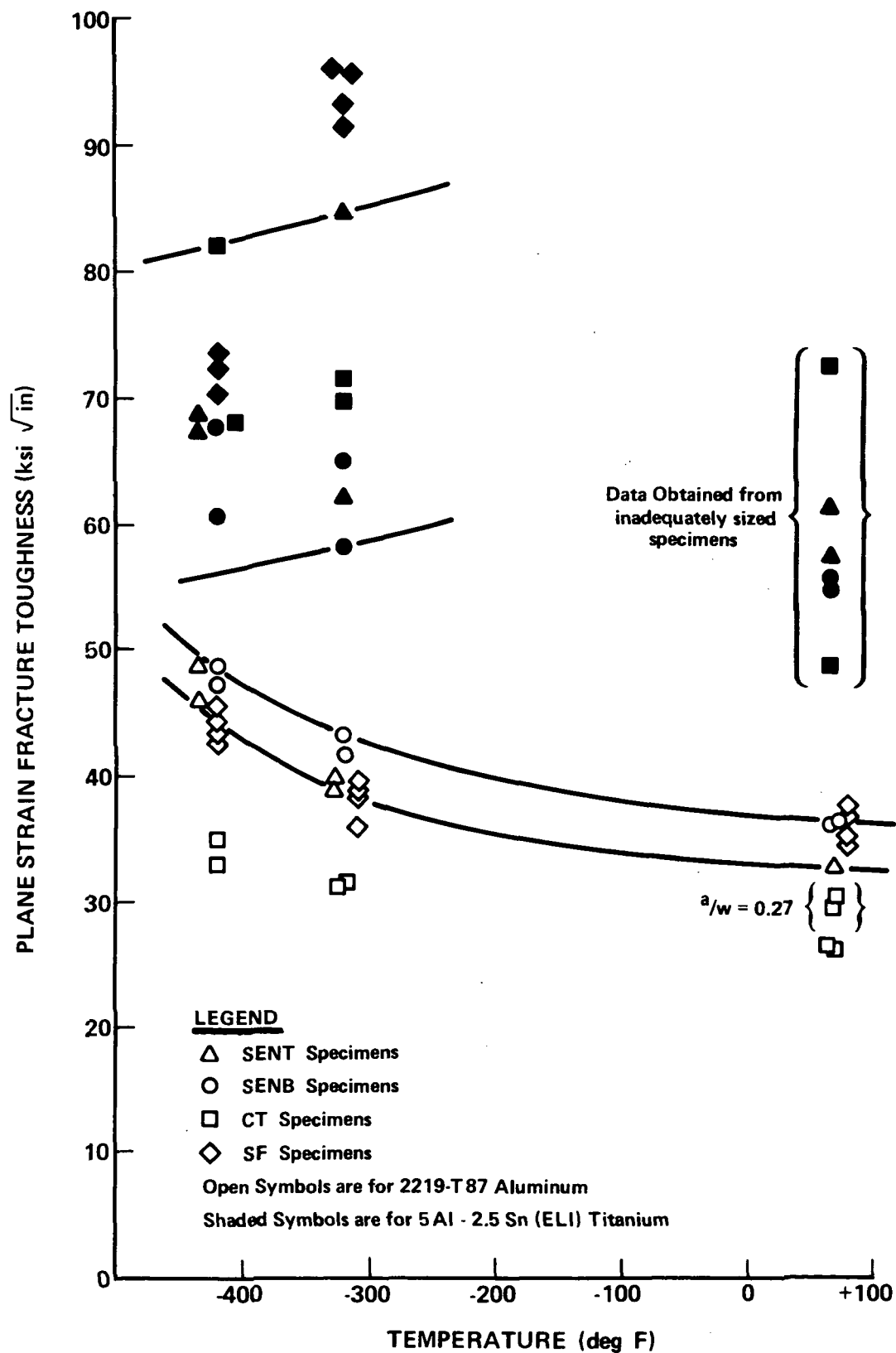
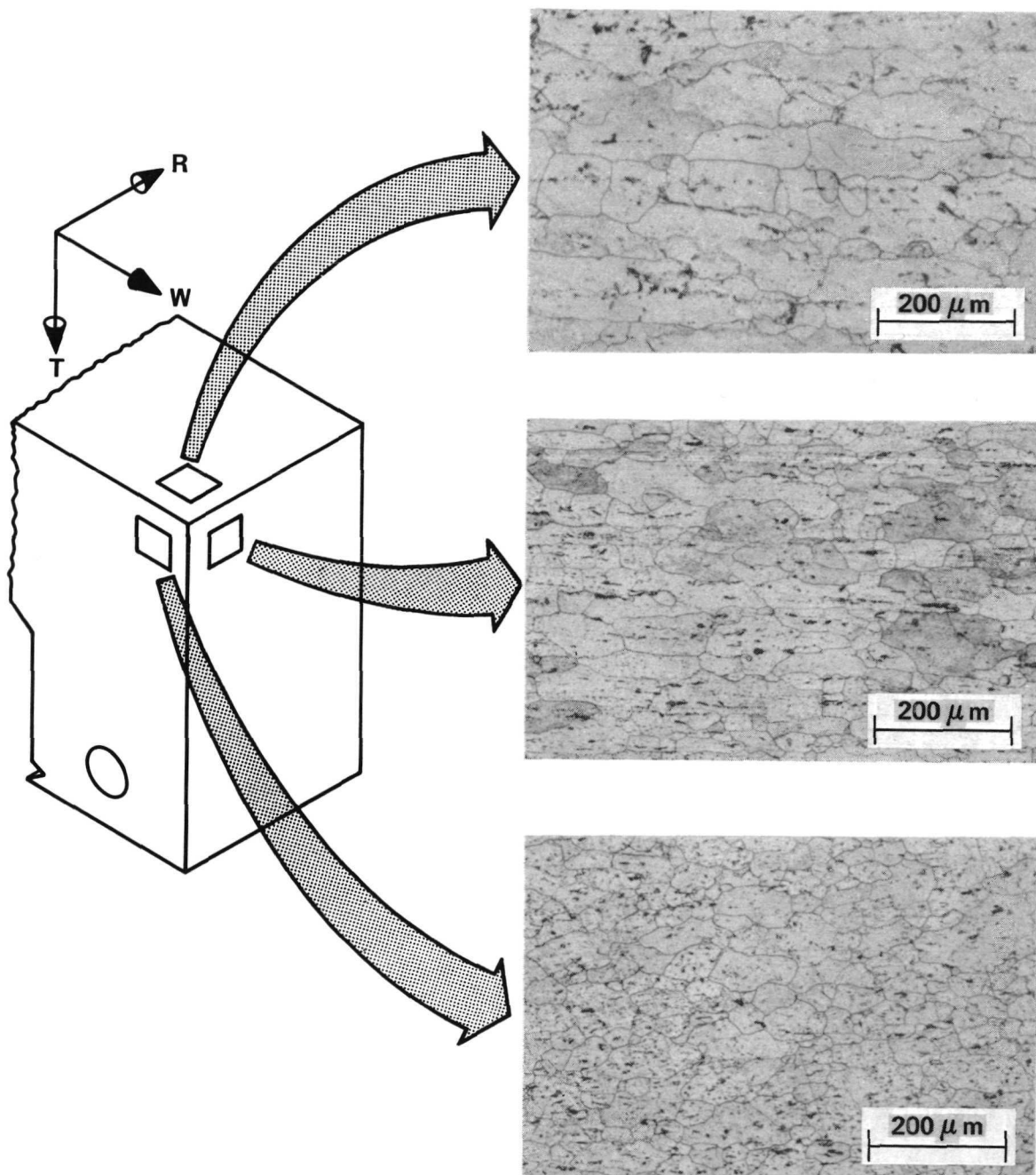


Figure 6-12: PLANE STRAIN FRACTURE TOUGHNESS DATA FOR 2219-T87 ALUMINUM AND 5Al-2.5 Sn(ELI) TITANIUM





Etchant: 1% HF, 1-1/2% HCL, 2-1/2% HNO<sub>3</sub>, BAL. H<sub>2</sub>O

Figure 6-13: MICROSTRUCTURAL INDICATIONS OF THICKNESS AND ROLLING DIRECTION IN 2219-T87 ALUMINUM CT SPECIMENS

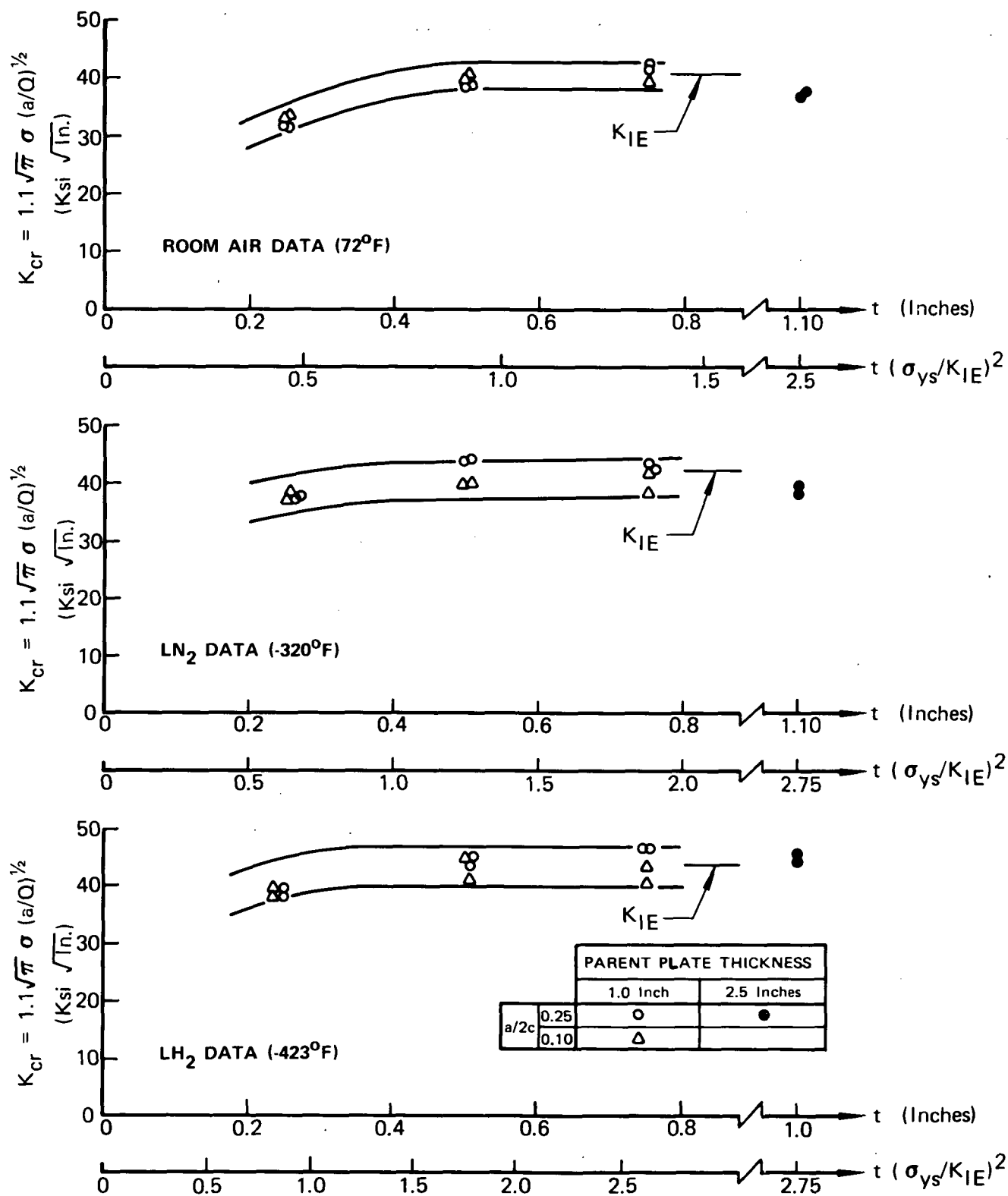


Figure 6-14: FRACTURE DATA FOR 2219-T87 ALUMINUM BASE METAL  
(Varied Thickness Surface-Flawed Specimen Tests)

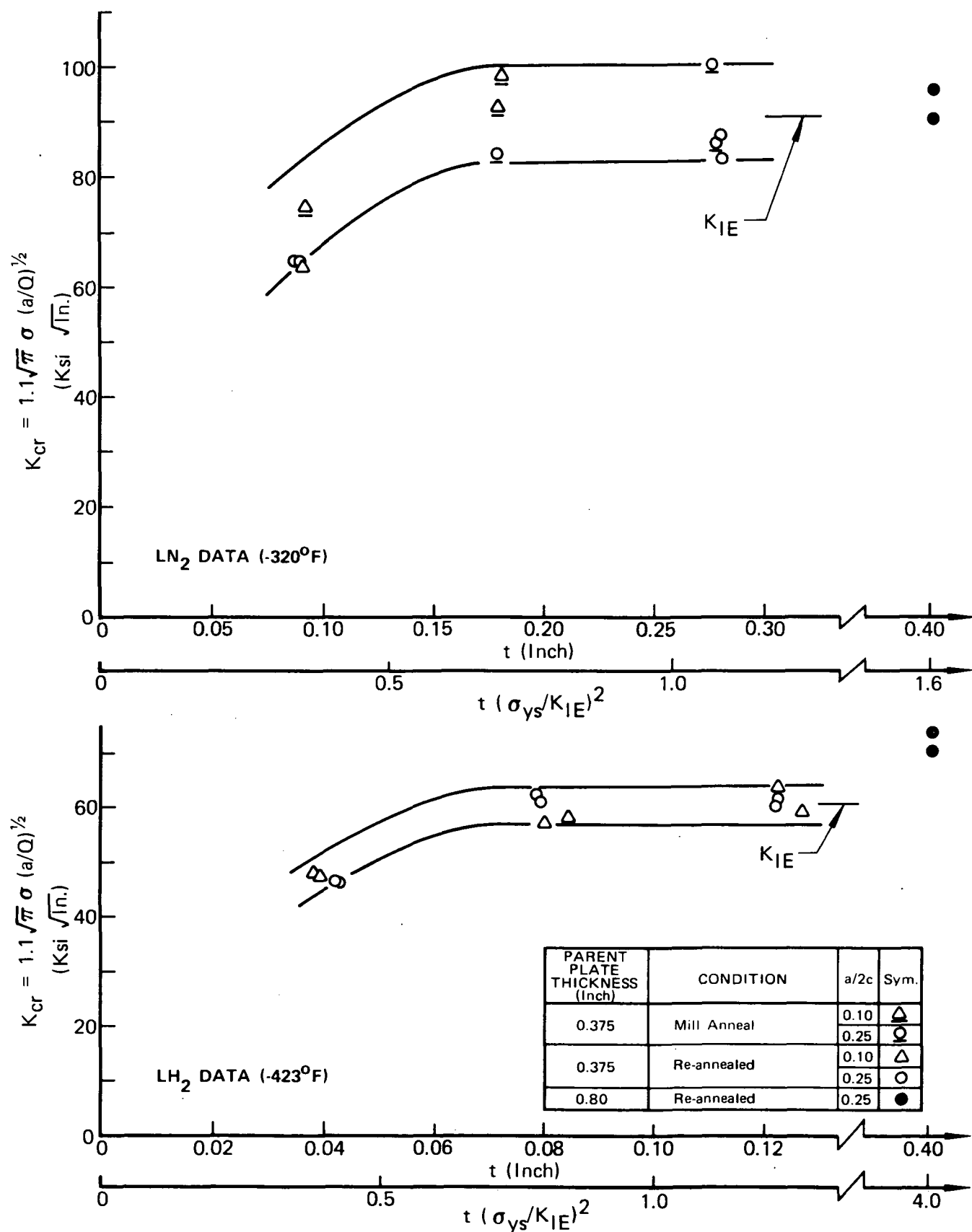


Figure 6-15: FRACTURE DATA FOR 5Al-2.5 Sn (ELI) TITANIUM BASE BASE METAL (Varied thickness Surface-Flawed Specimen Tests)

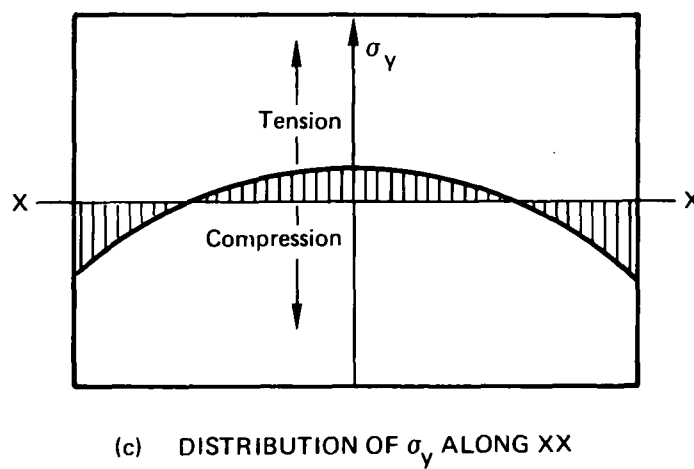
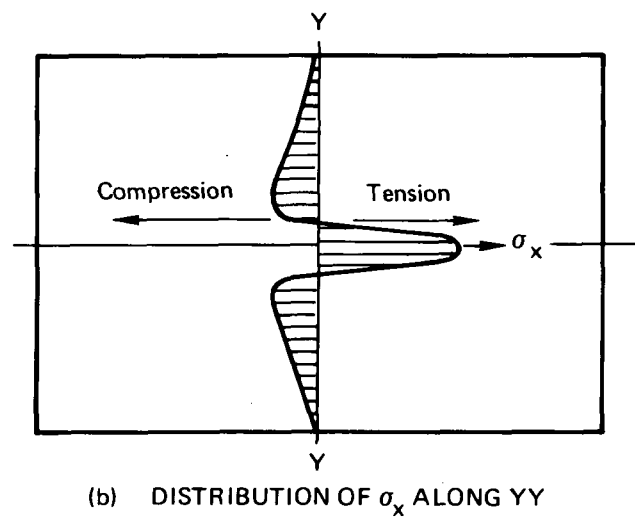
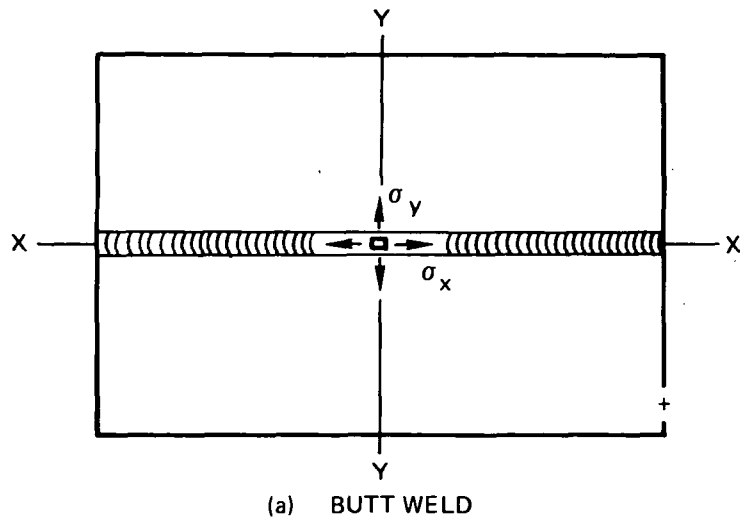
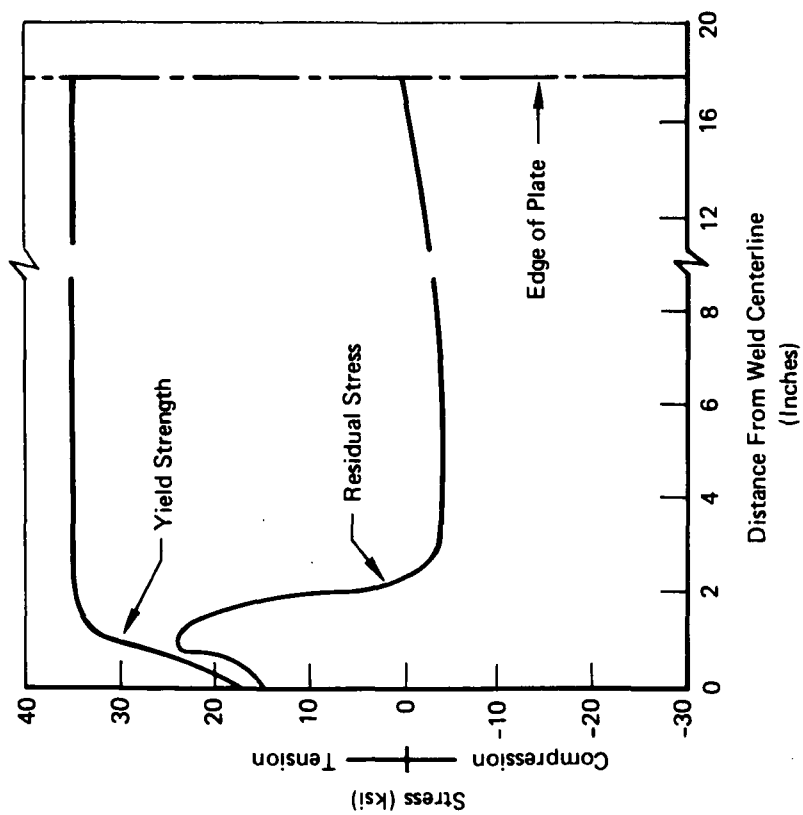
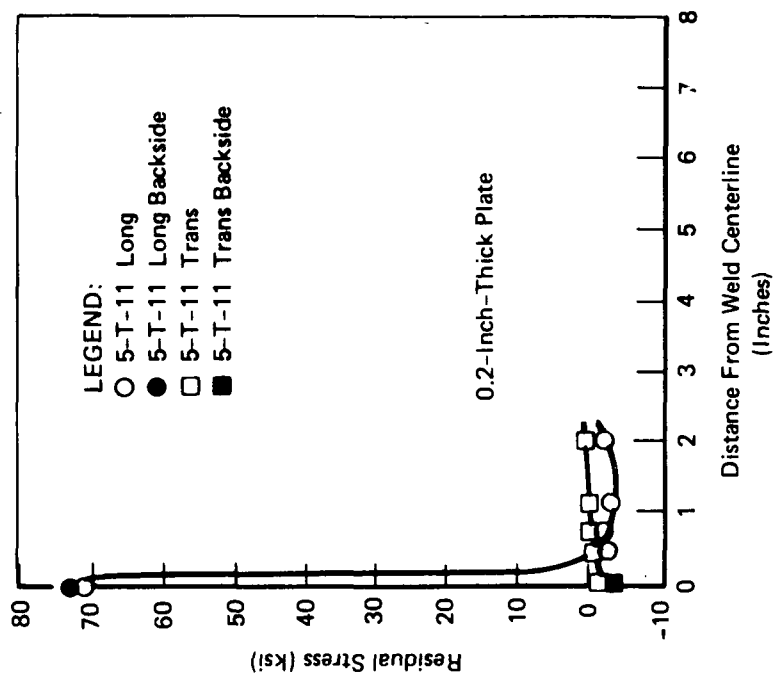


Figure 7-1: TYPICAL RESIDUAL STRESS DISTRIBUTION IN FLAT BUTT WELDED STEEL PLATES (REFERENCE 19)



**Figure 7-2: DISTRIBUTION OF YIELD STRENGTH AND LONGITUDINAL RESIDUAL STRESSES IN A WELDED 5456-H321 ALUMINUM PLATE (REFERENCE 20)**



**Figure 7-3: LONGITUDINAL AND TRANSVERSE RESIDUAL STRESSES IN AS-WELDED Ti-5Al-2.5Sn PANELS (REFERENCE 23)**

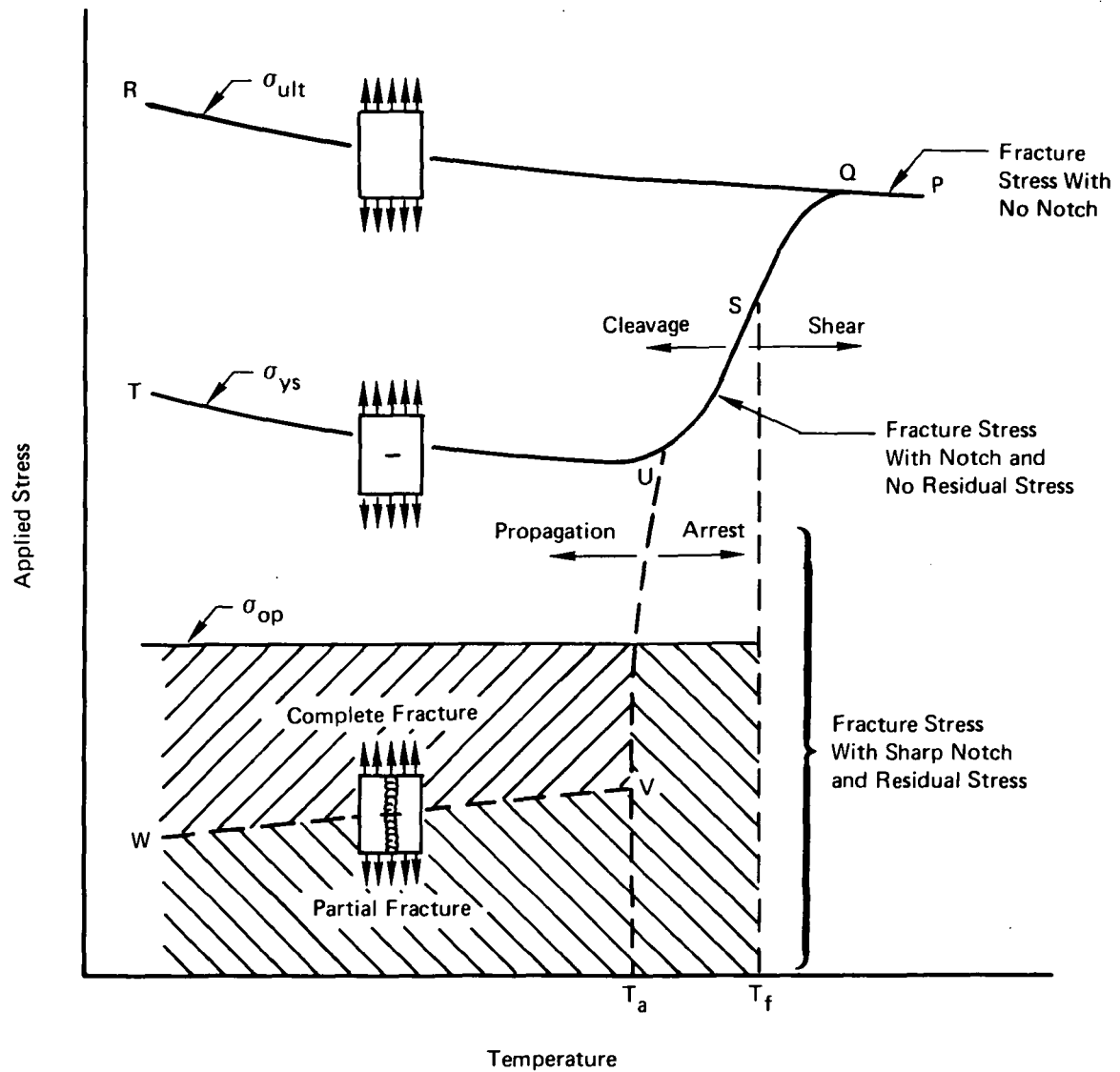
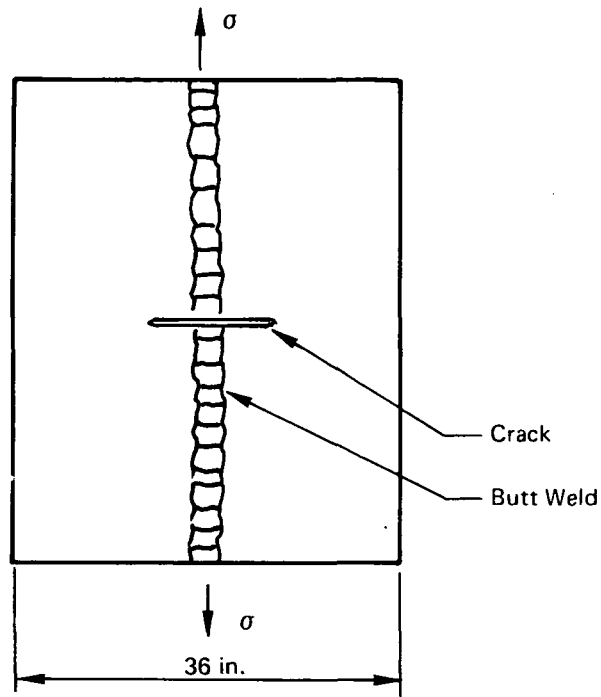
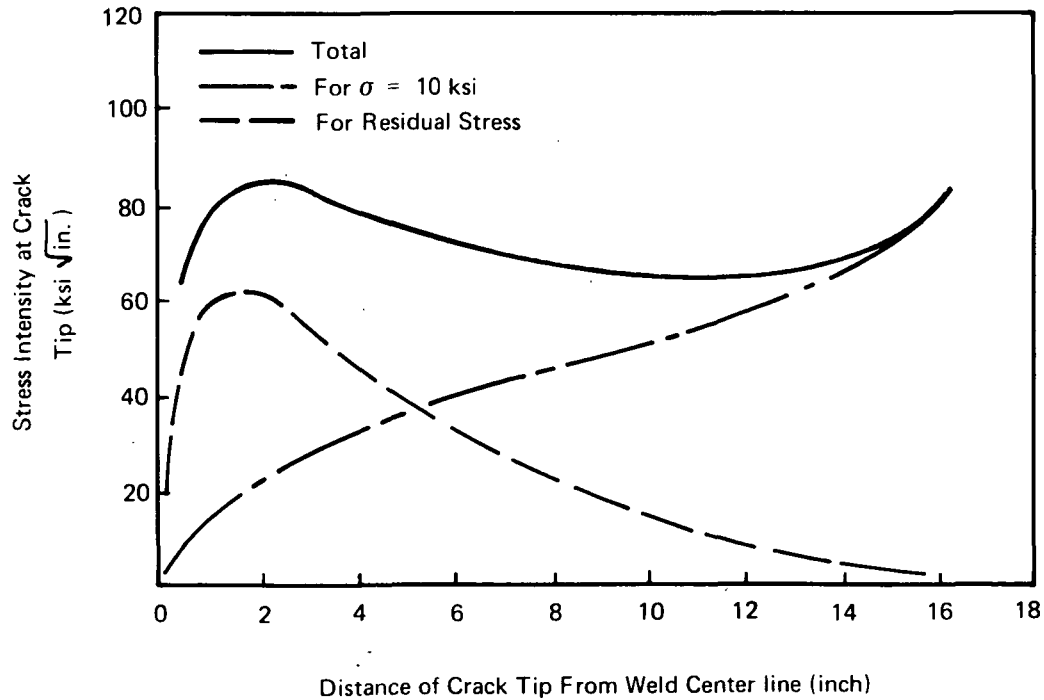


**Figure 7-4: EFFECTS OF SHARP NOTCH AND RESIDUAL STRESS ON FRACTURE STRENGTH OF STEEL WELDS (REFERENCE 29)**

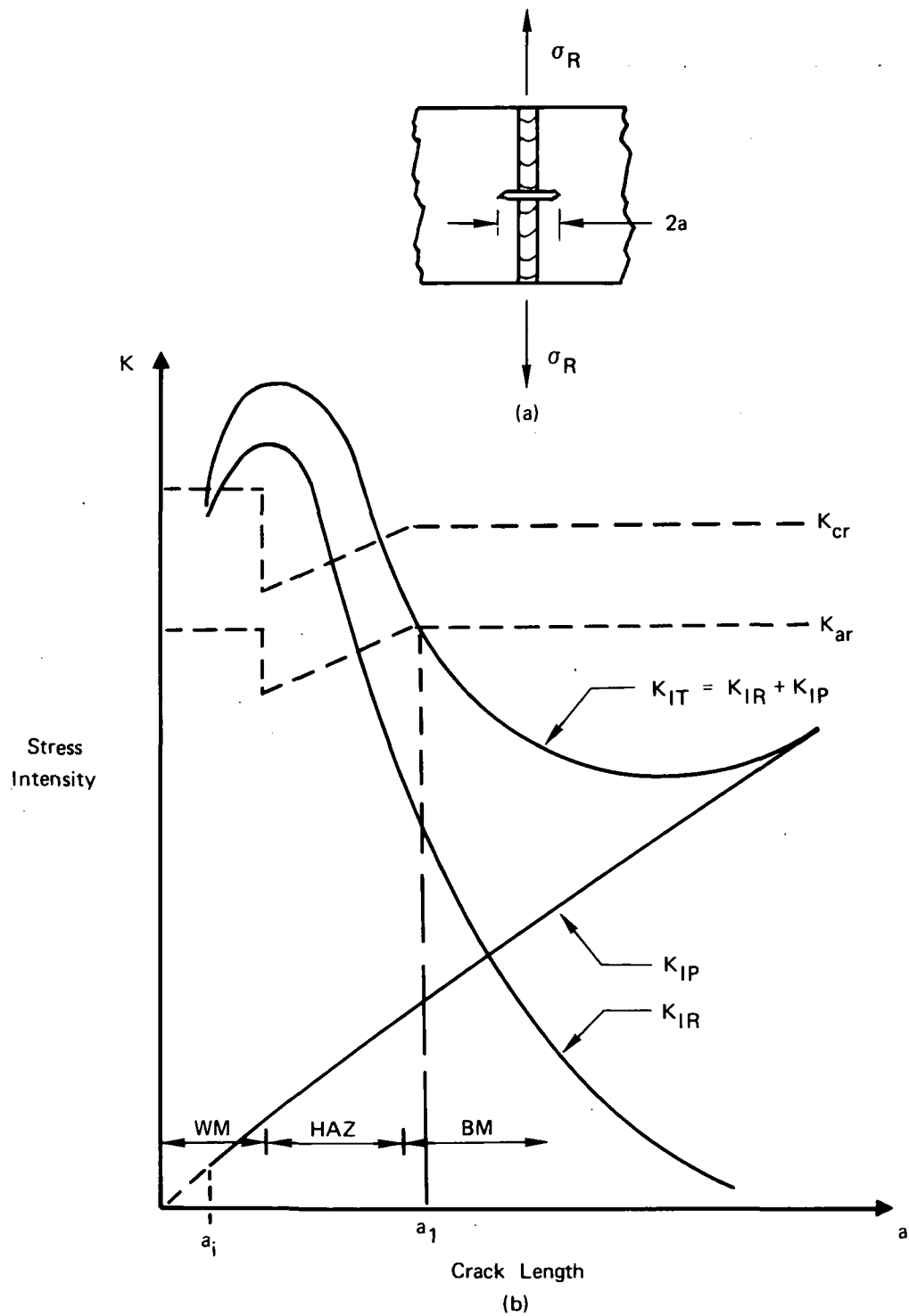


(a) SPECIMEN CONFIGURATION



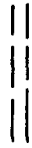

(b) STRESS INTENSITIES

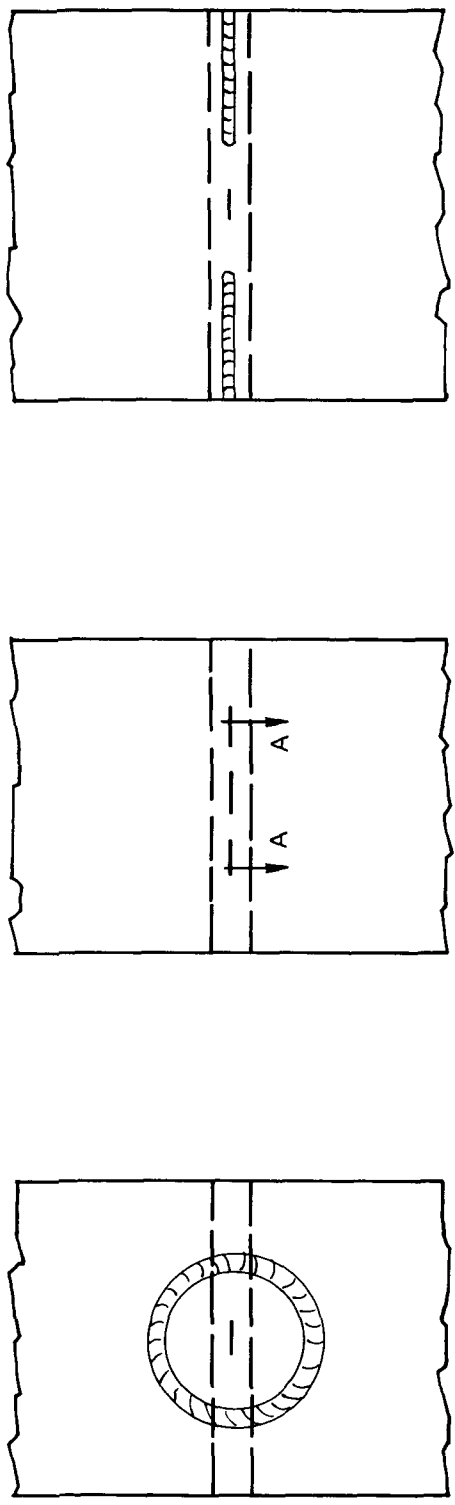
**Figure 7-5: CRACK TIP STRESS INTENSITY VALUES FOR BUTT WELDED SPECIMENS (REFERENCE 33)**



**Figure 7-6: SCHEMATIC ILLUSTRATIVE EXAMPLE OF THE APPLICATION OF FRACTURE MECHANICS TO ANALYSIS OF CRACK STABILITY IN A BUTT WELDED PLATE**



 Flush GTA Weld (Series I Only)  
 Electron Beam (EB) Weld



For Adding Tensile Residual Stress

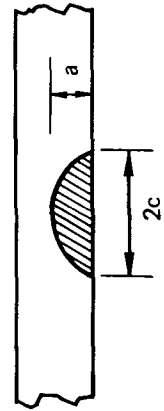
For Reference Specimens

For Adding Compressive Residual Stress

Gage Areas of Test Specimens

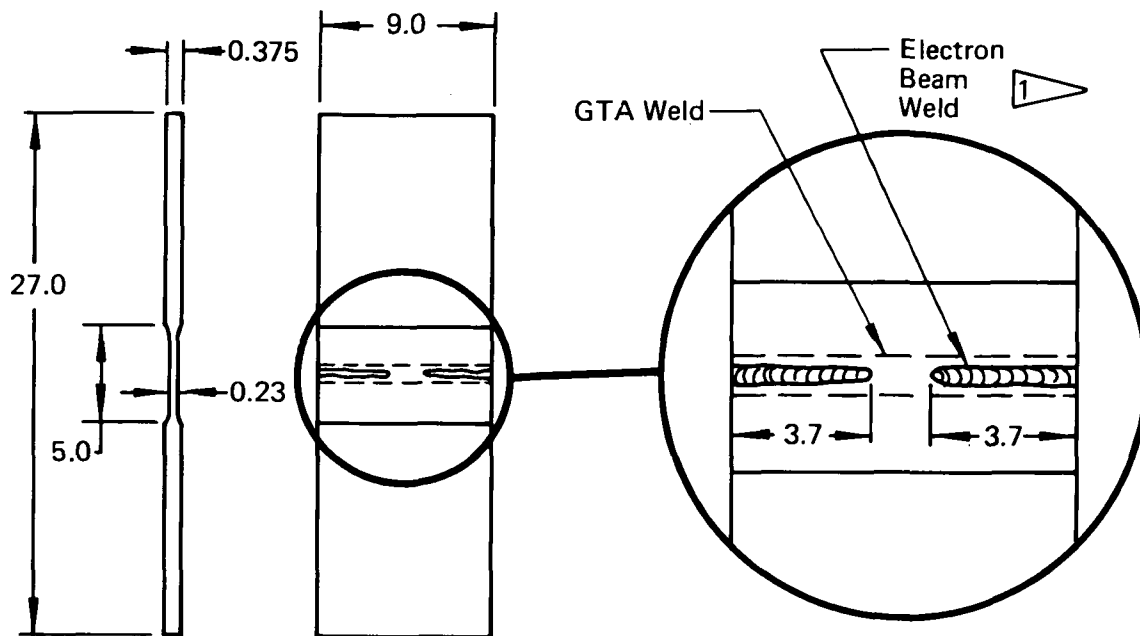
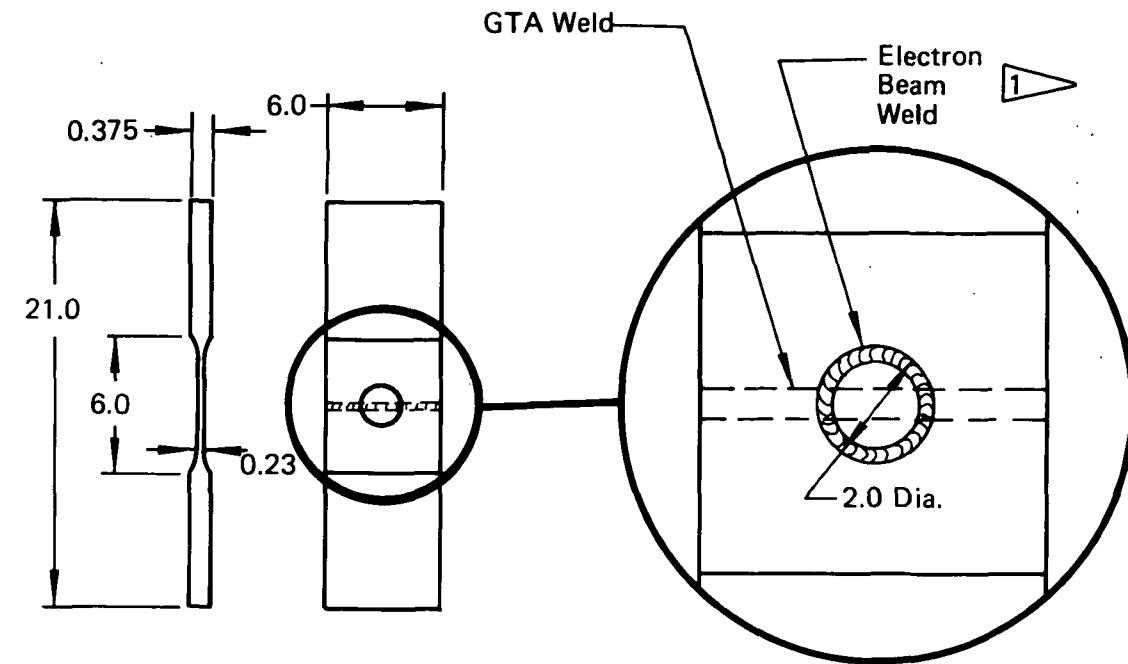
Production Sequence

1. Deposit GTA Weld (Series I Only)
2. Stress Relieve at 1,300°F for One Hour (Titanium Only)
3. Prepare Flaw
4. EB Weld to Generate Residual Stress



Section A-A  
(typical)

Figure 7-7: PRODUCTION SEQUENCES FOR RESIDUAL STRESS TEST SERIES I AND II



1 Full Penetration EB Weld, Deposit One Pass From Each Side With Slight Offset As Shown Below.

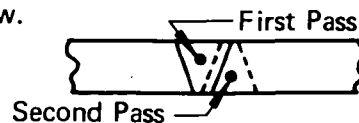


Figure 7-8: EB WELDING FOR 5Al-2.5Sn(ELI) TITANIUM TEST SERIES I AND II

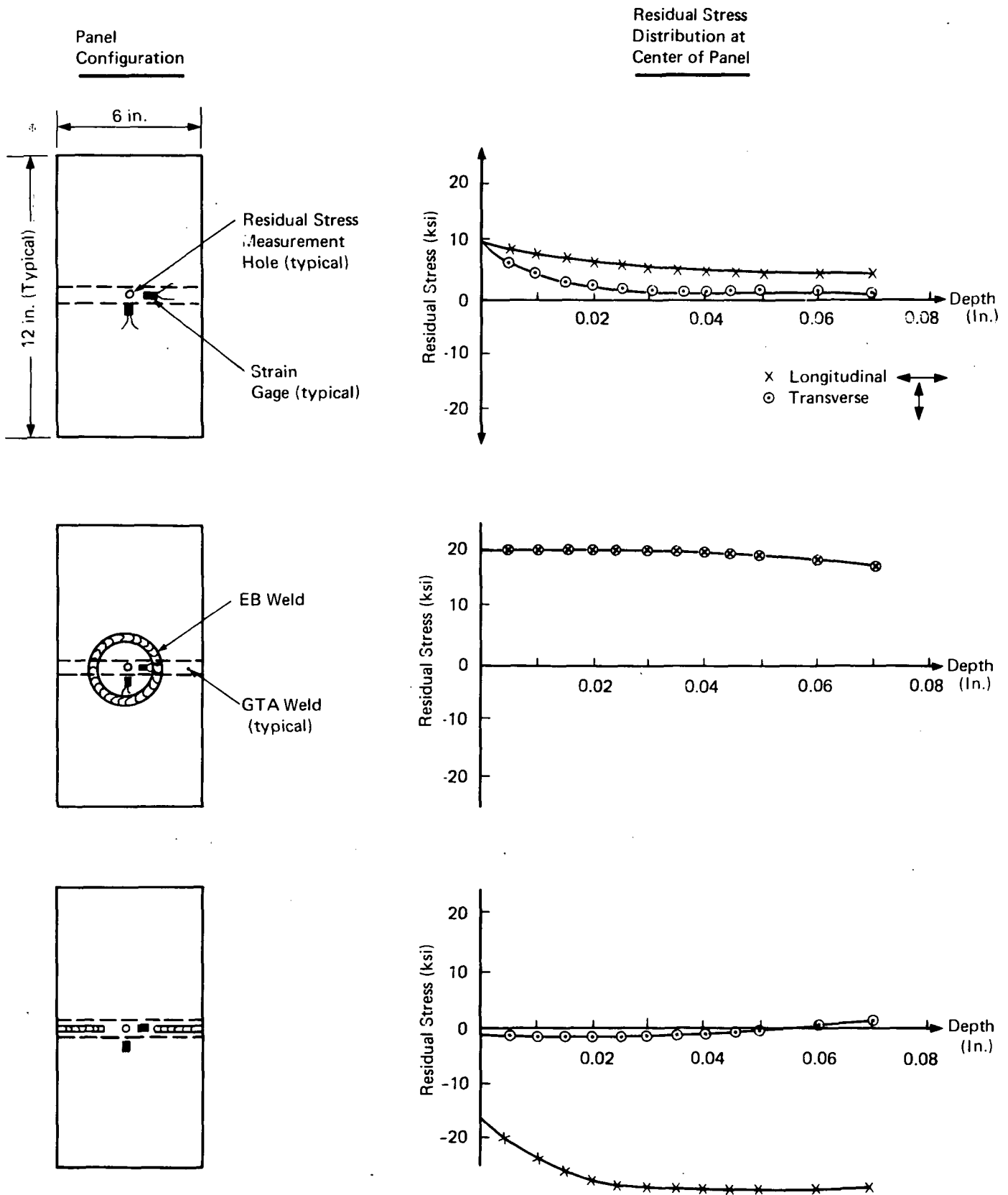


Figure 7-9: RESIDUAL STRESS MEASUREMENTS FOR 5Al-2.5Sn (ELI) TITANIUM ALLOY TEST SERIES I AND II

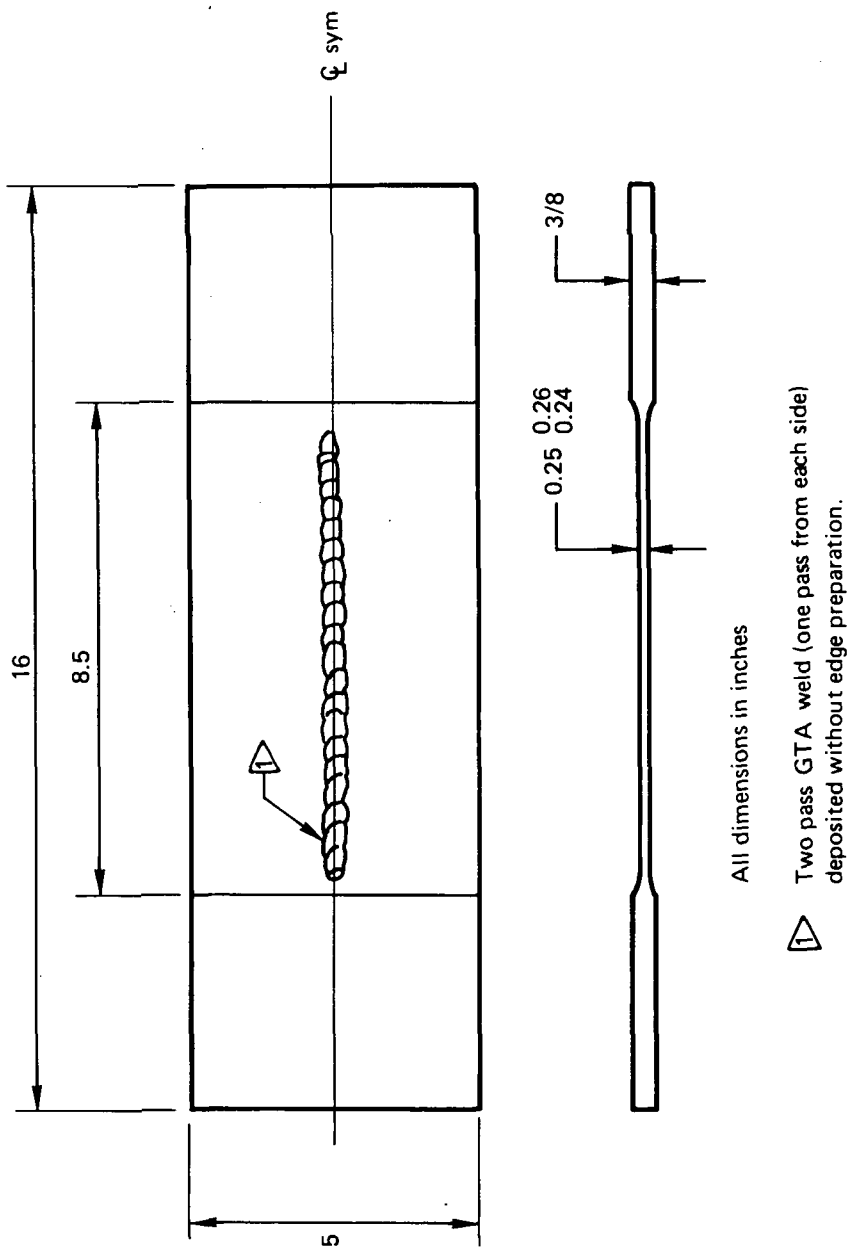


Figure 7-10: 5Al-2.5Sn (ELI) TITANIUM TEST SPECIMEN FOR RESIDUAL STRESS TEST SERIES III

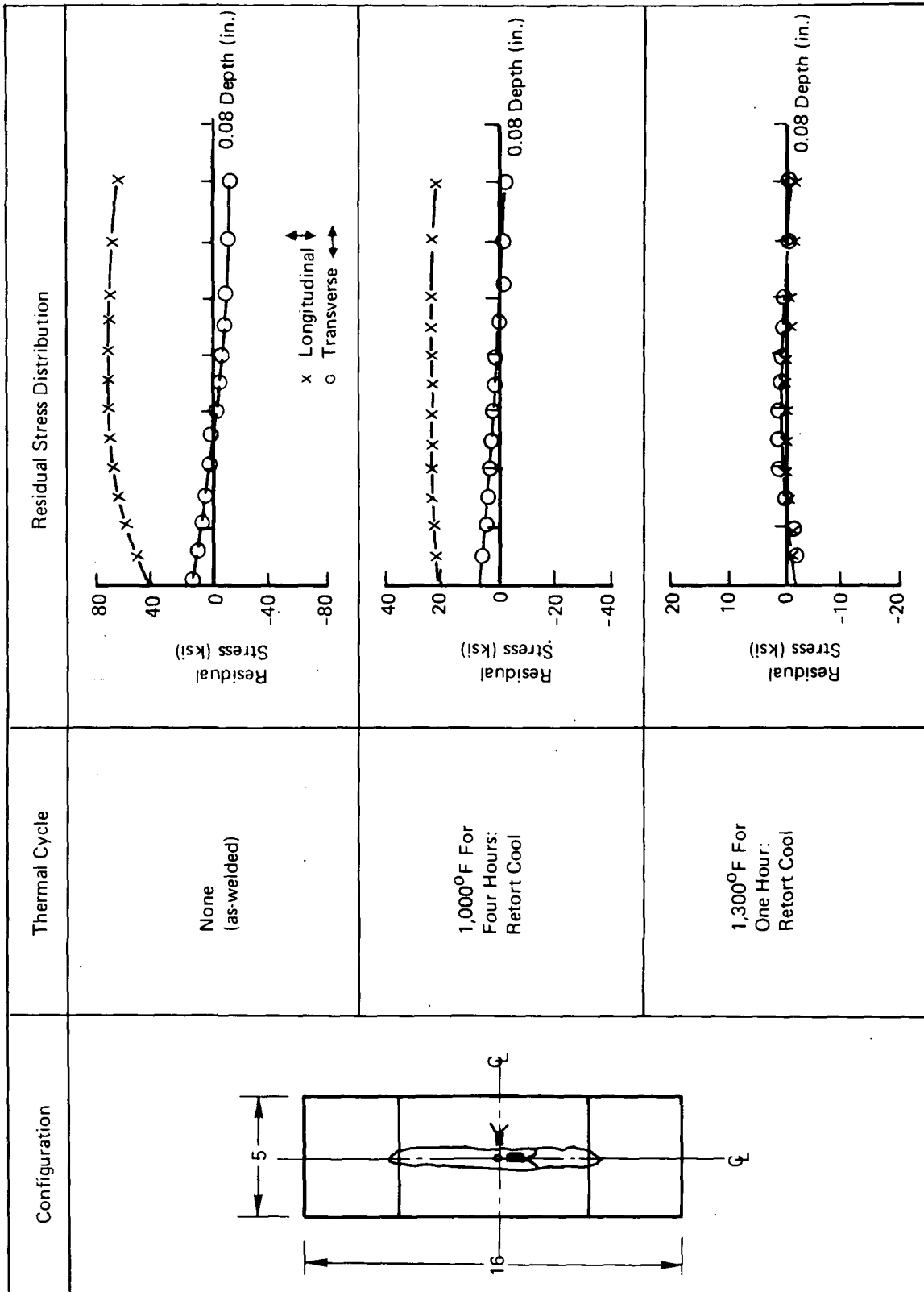


Figure 7-11: RESIDUAL STRESS MEASUREMENTS FOR 5Al-2.5Sn (ELI)  
TITANIUM ALLOY TEST SERIES III

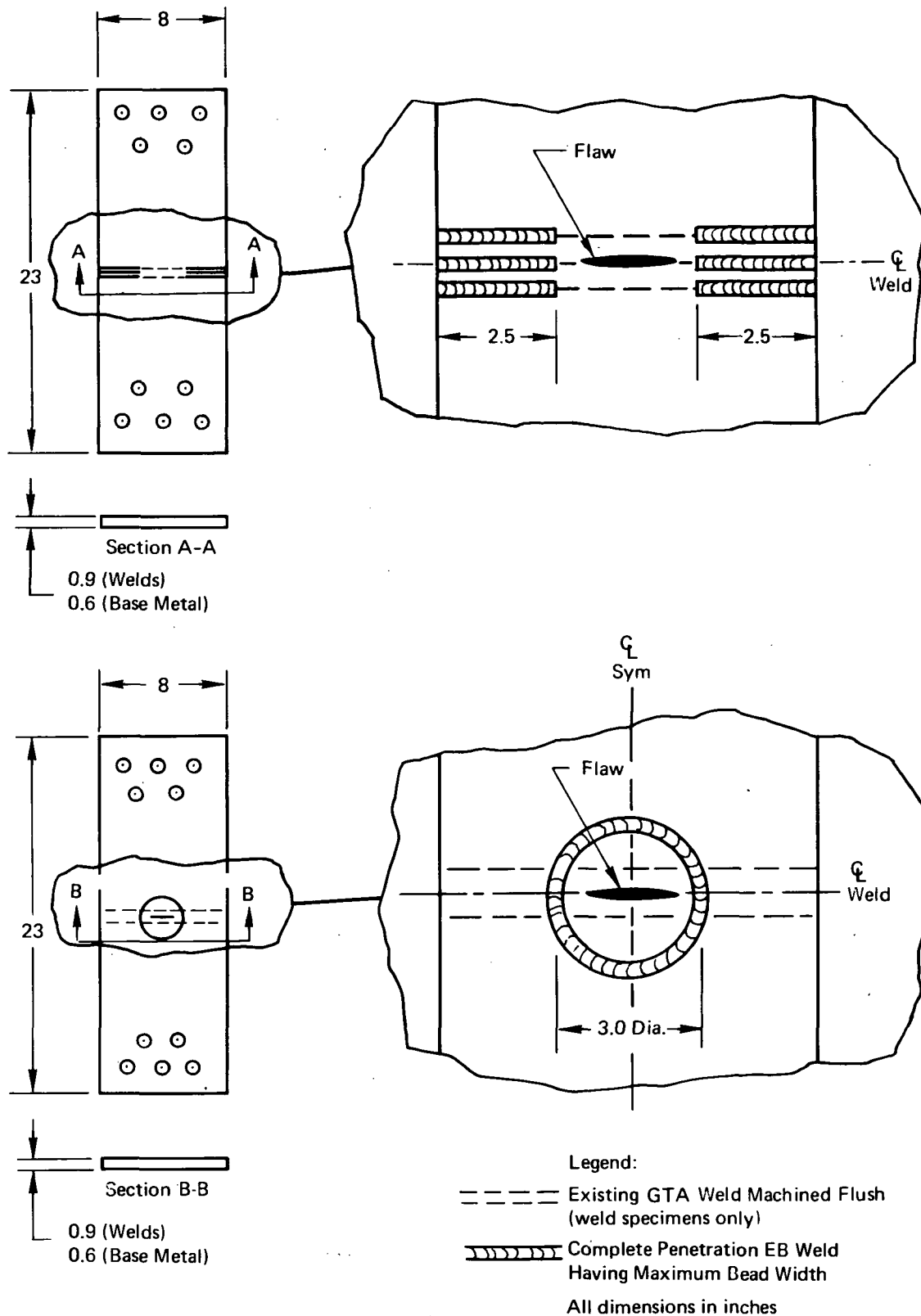


Figure 7-12: EB WELDING FOR 2219-T87 ALUMINUM RESIDUAL STRESS TEST SERIES I AND II

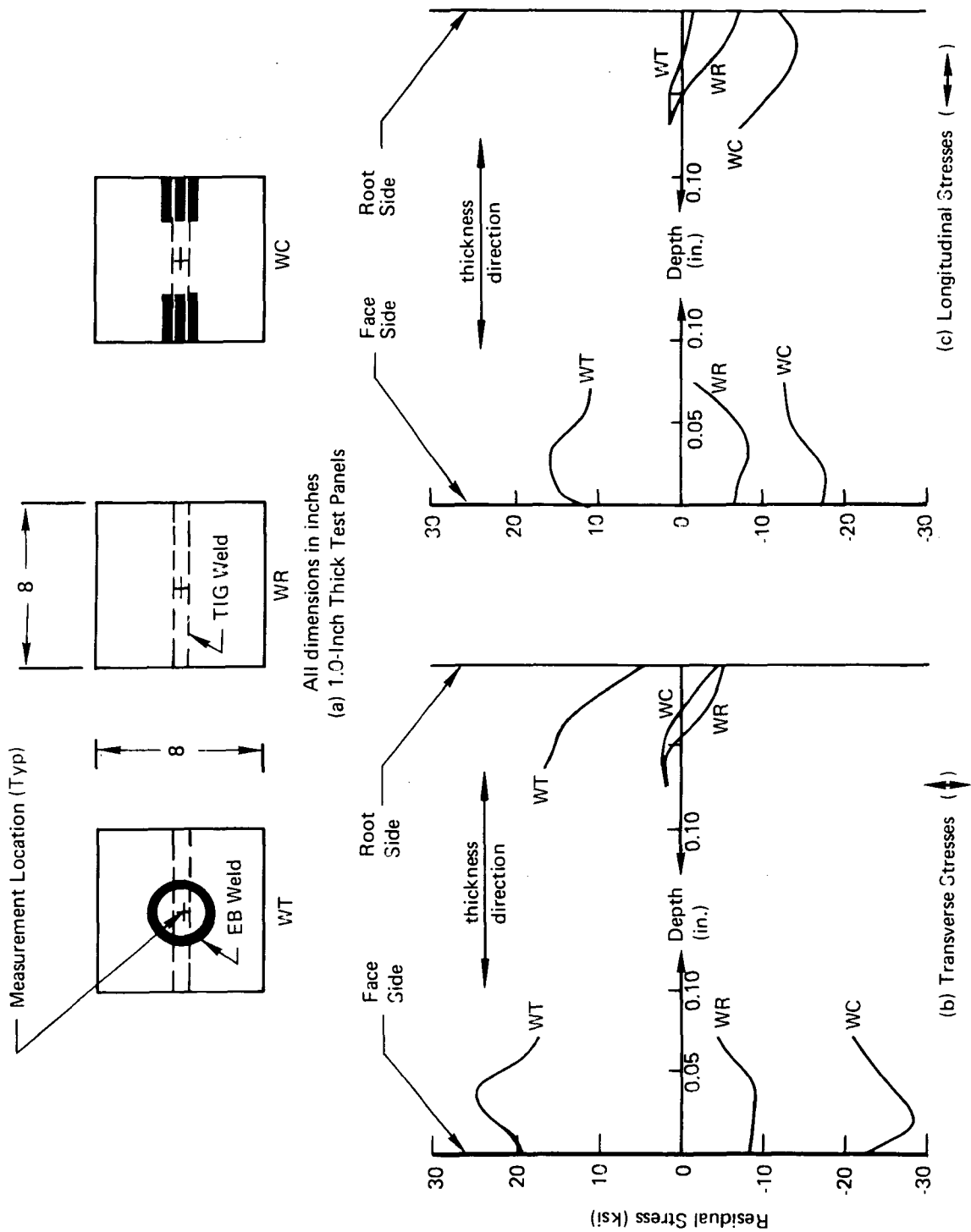


Figure 7-13: RESIDUAL STRESSES AT SURFACES OF 2219-T87 ALUMINUM  
SERIES I TEST SPECIMENS

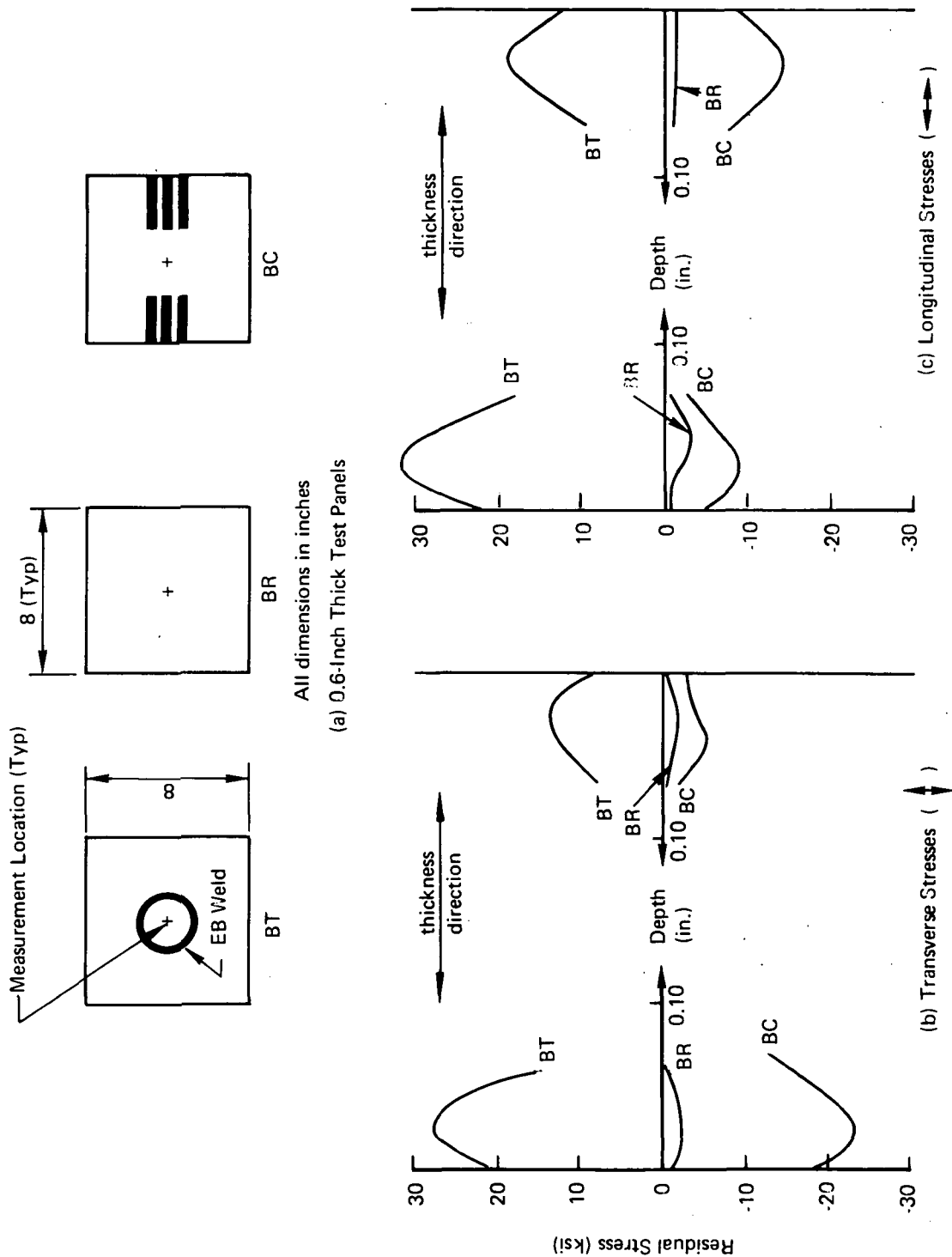
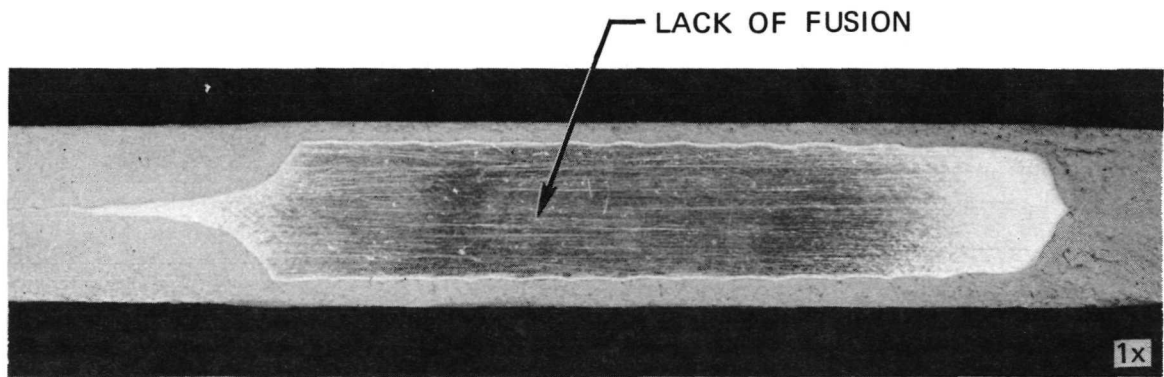
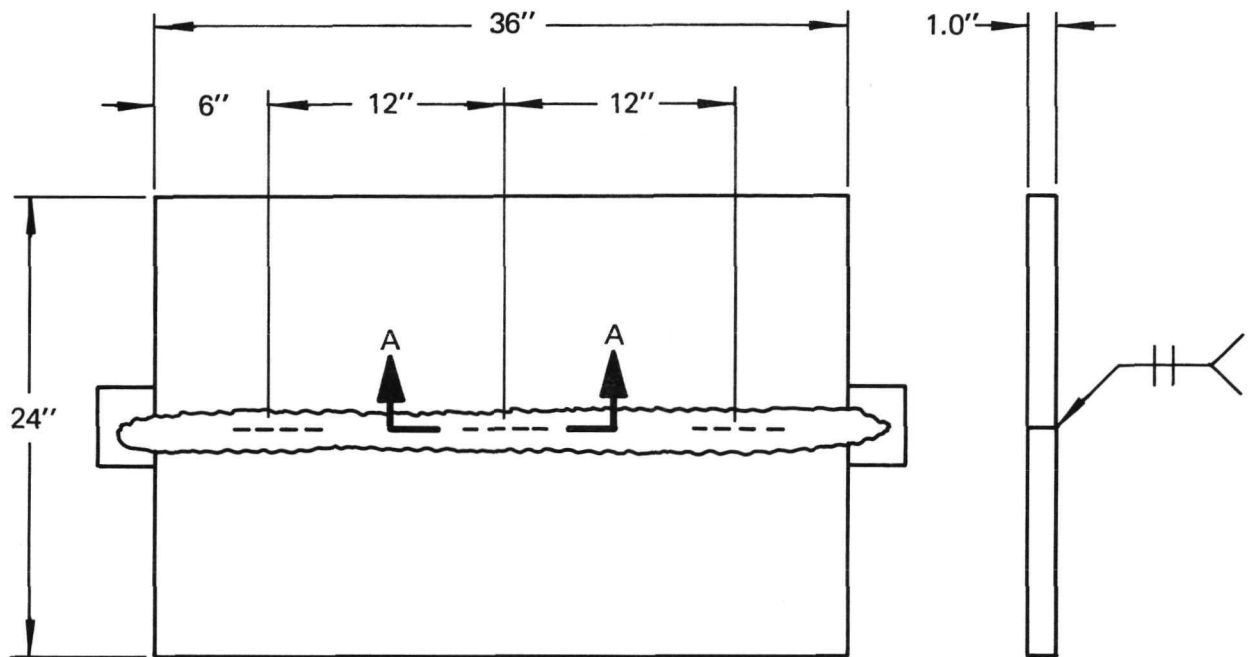


Figure 7-14: RESIDUAL STRESSES AT SURFACES OF 2219-T87 ALUMINUM  
SERIES II TEST SPECIMENS





SPECIMEN NO. 1-1

SECTION A-A (TYPICAL)

Figure 7-15: INTERNALLY FLAWED 2219-T87 ALUMINUM WELD PANELS

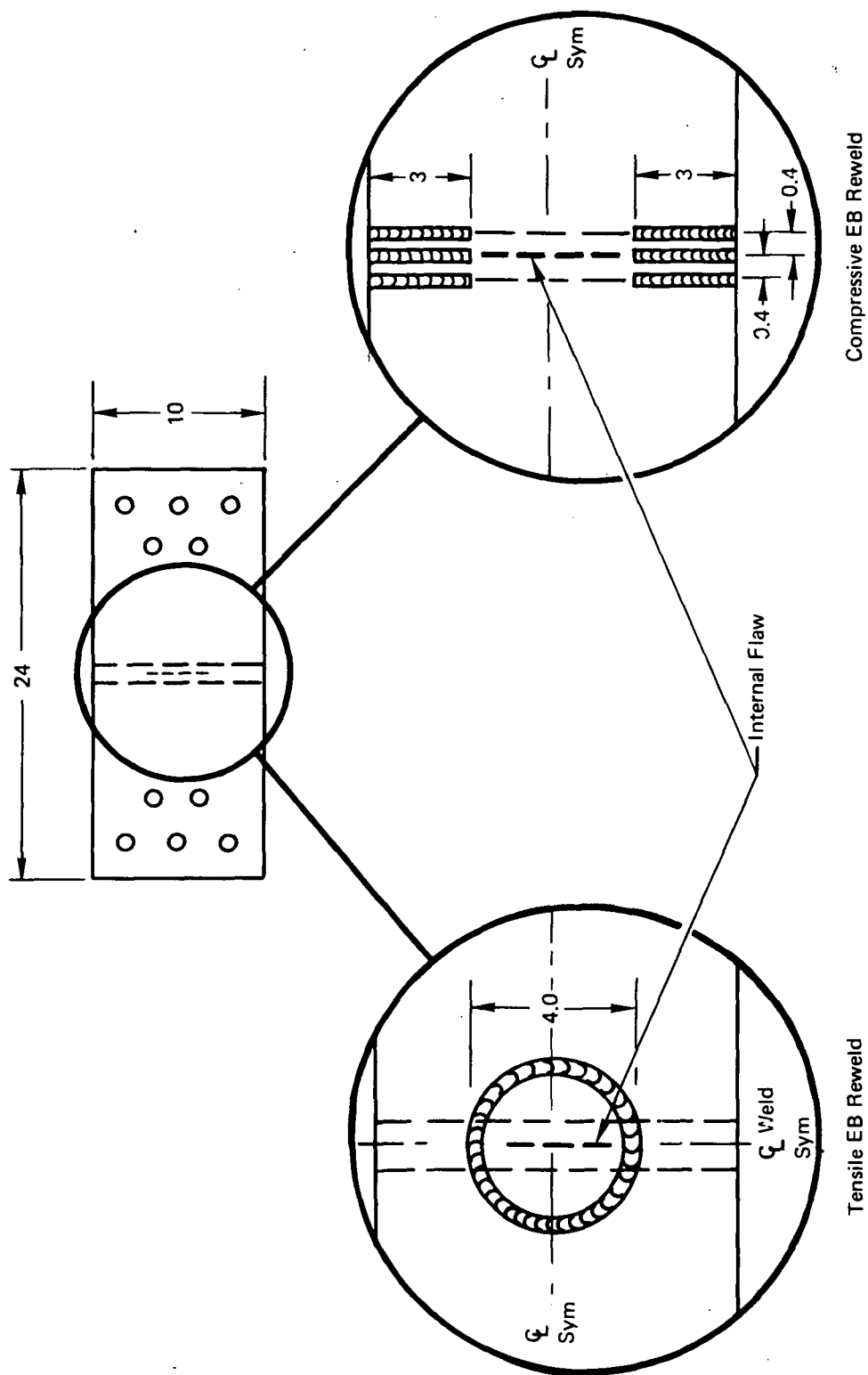
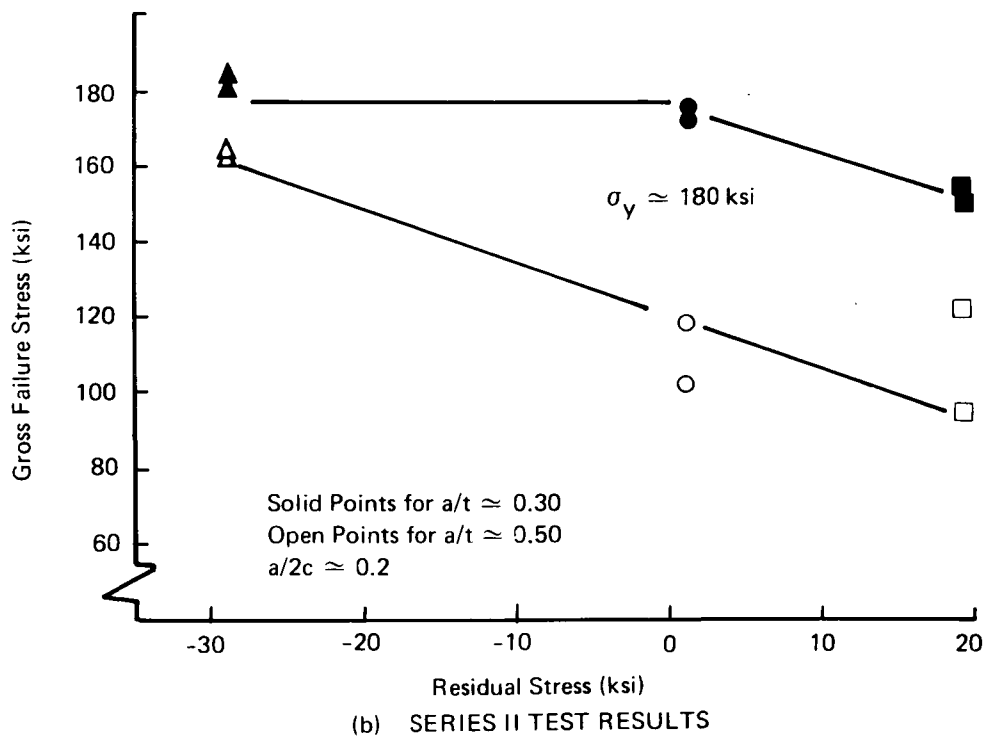
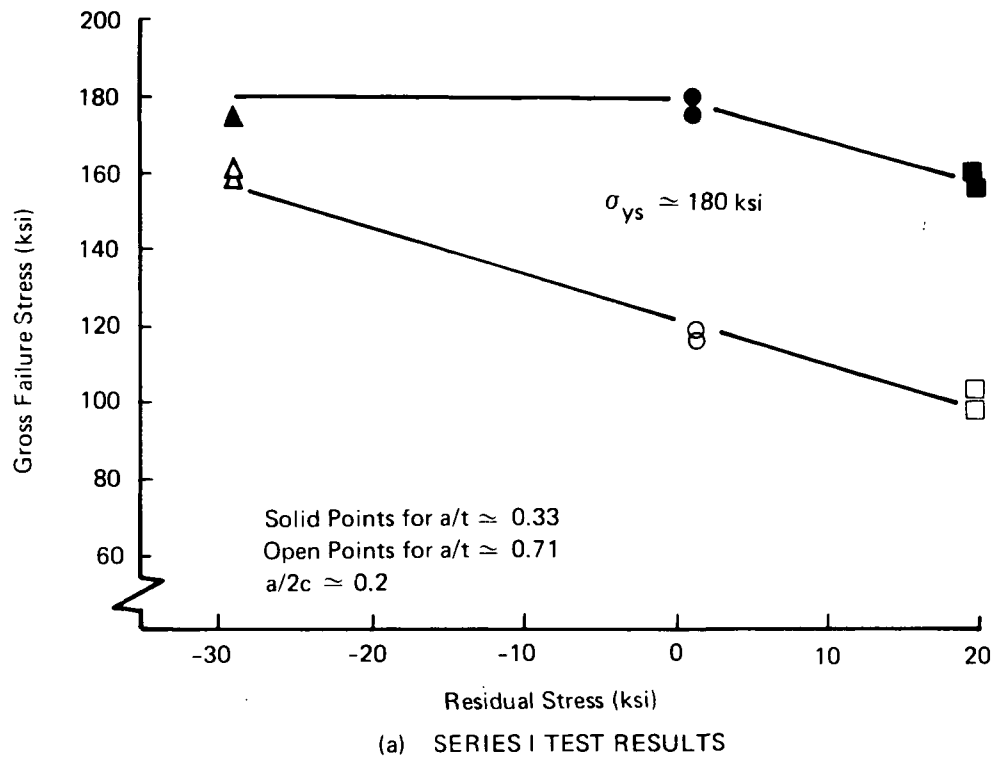
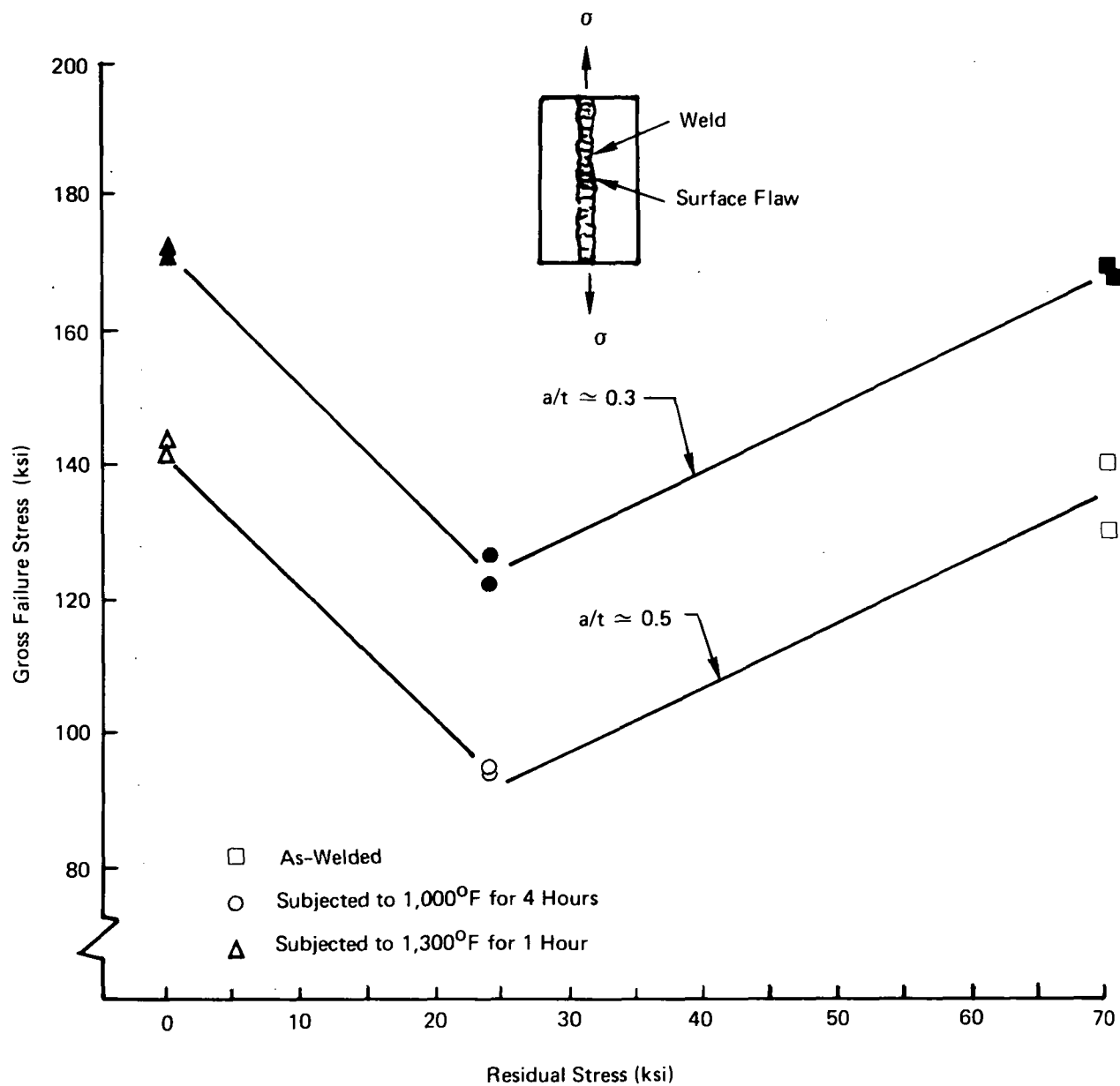


Figure 7-16: EB WELDING OF 2219-T87 ALUMINUM INTERNALLY FLAWED RESIDUAL STRESS SPECIMENS



**Figure 7-17: EFFECT OF RESIDUAL STRESS ON GROSS FAILURE STRESS FOR 5Al-2.5Sn (ELI) TITANIUM TEST SERIES I AND II**



**Figure 7-18: GROSS FAILURE STRESSES FOR 5Al-2.5Sn (ELI) TITANIUM TEST SERIES III**

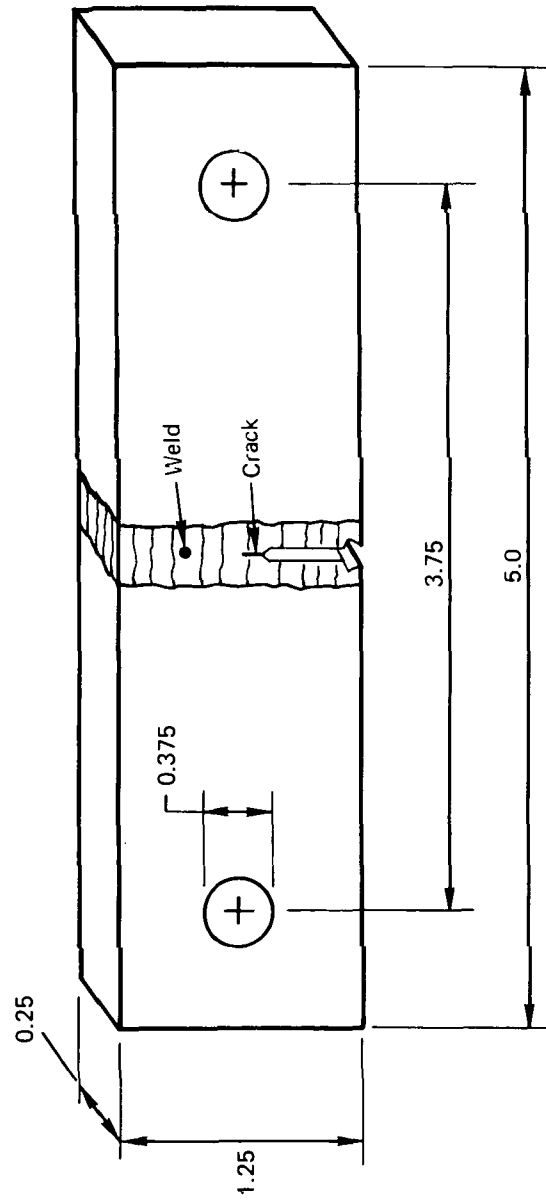
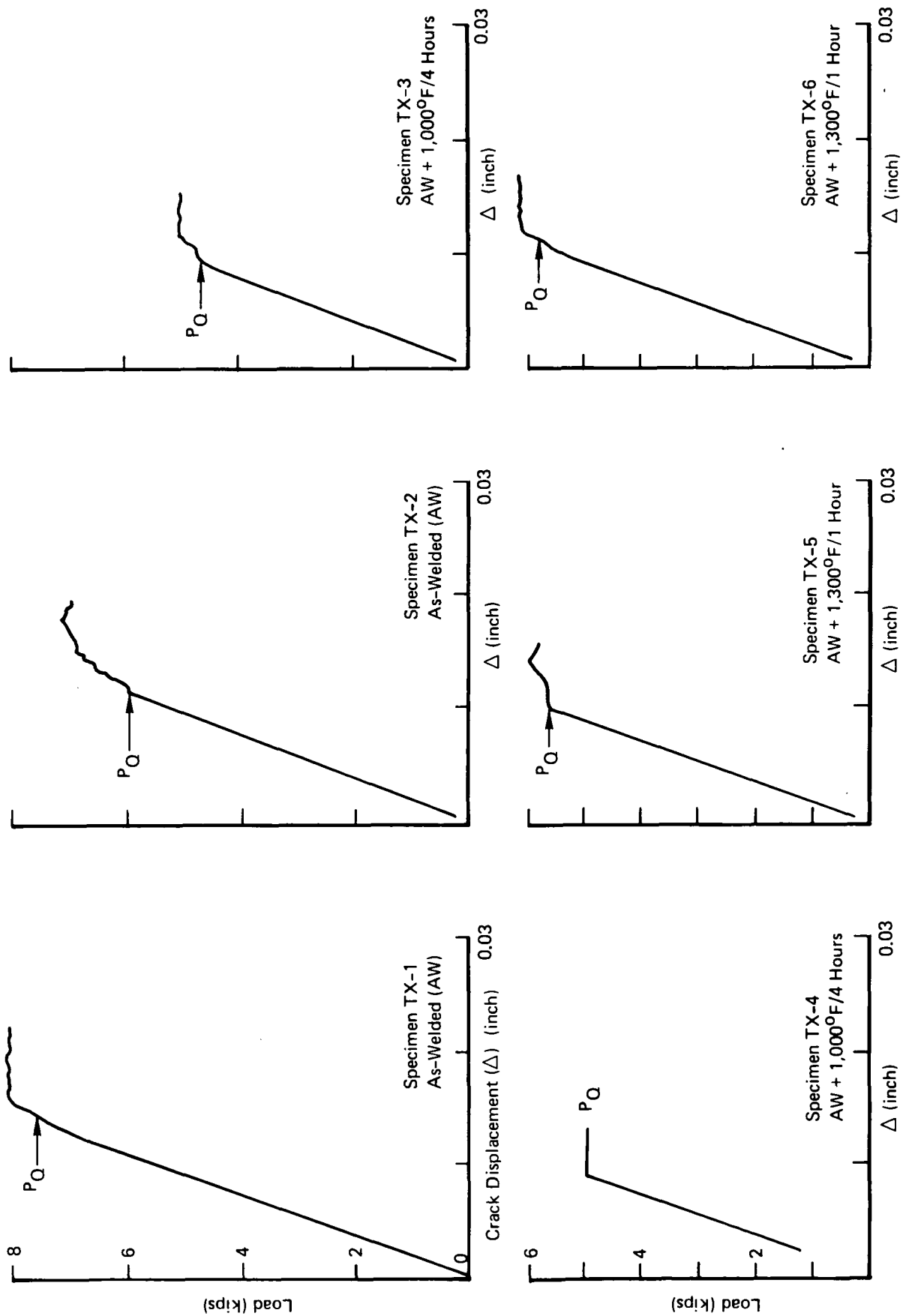


Figure 7-19: TEST SPECIMEN USED FOR EVALUATING EFFECT OF THERMAL CYCLES ON FRACTURE TOUGHNESS OF 5Al-2.5Sn (ELI) TITANIUM WELD CENTERLINES



**Figure 7-20: CRACK DISPLACEMENT VS LOAD TEST RECORDS FOR 5Al-2.5Sn (ELI) TITANIUM GTA WELD CENTERLINES IN SENT SPECIMENS**

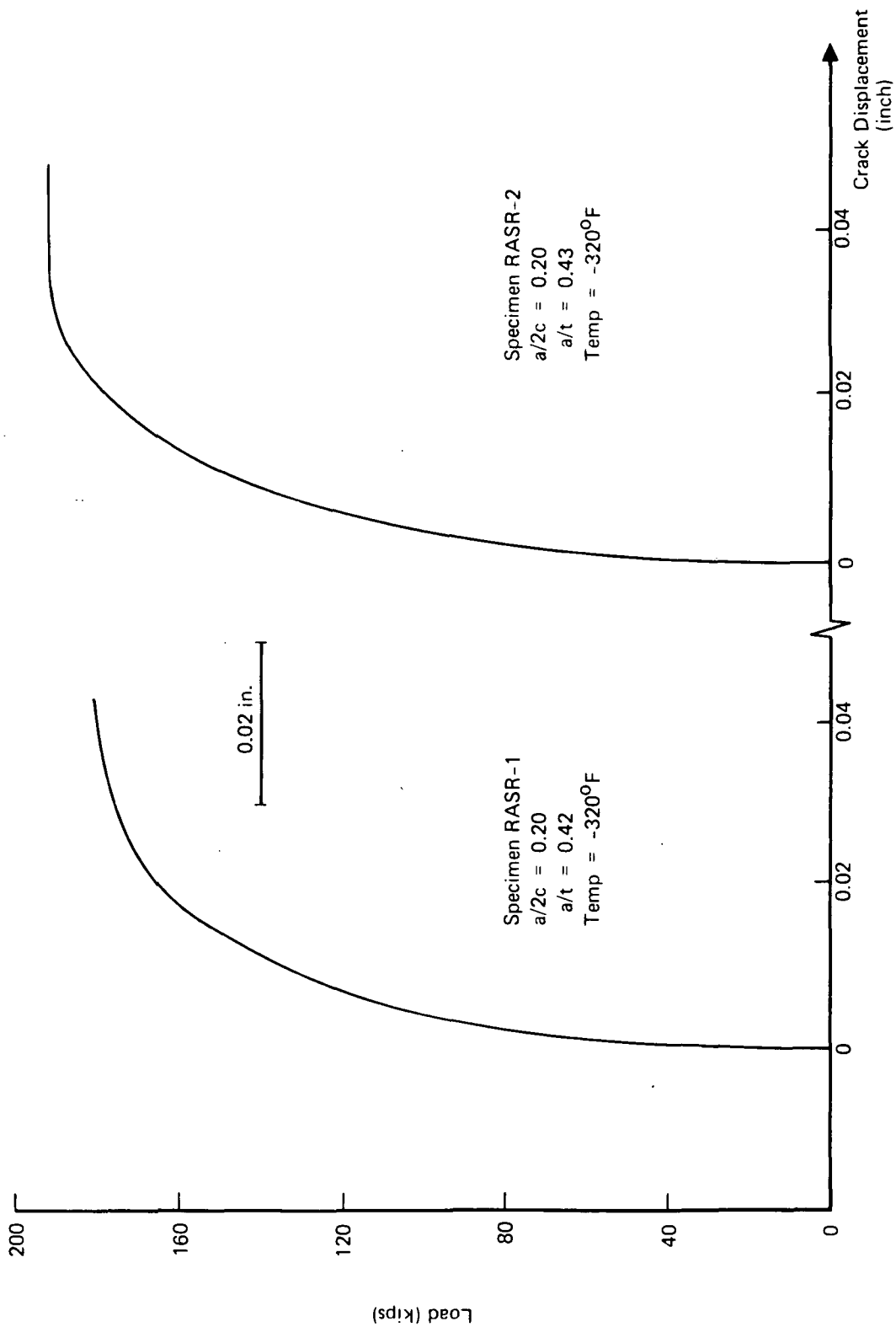


Figure 7-21: LOAD VS. CRACK DISPLACEMENT TEST RECORDS FOR SURFACE FLAWS AT 1-INCH-THICK 2219 ALUMINUM GTA WELD CENTERLINES

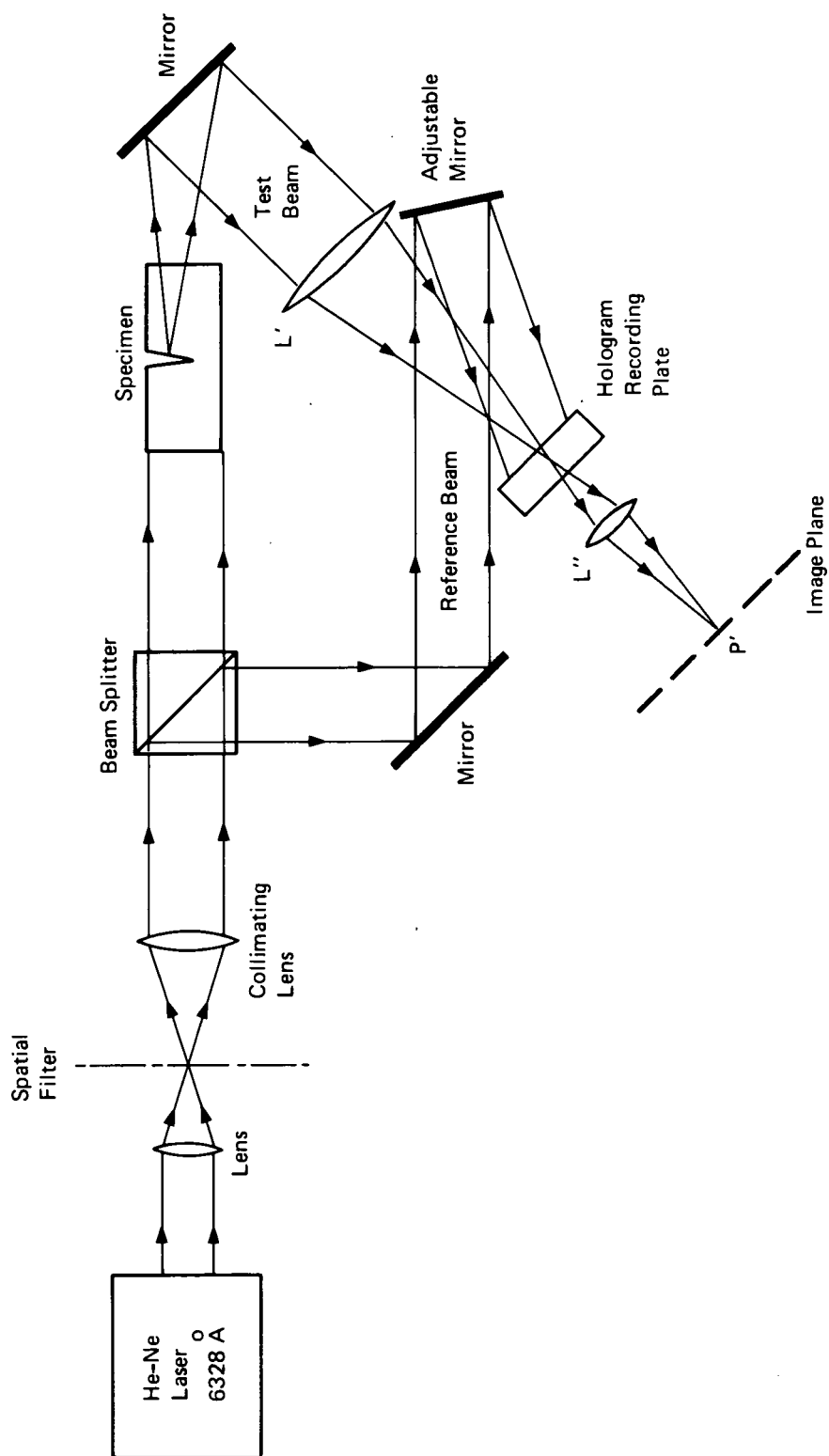
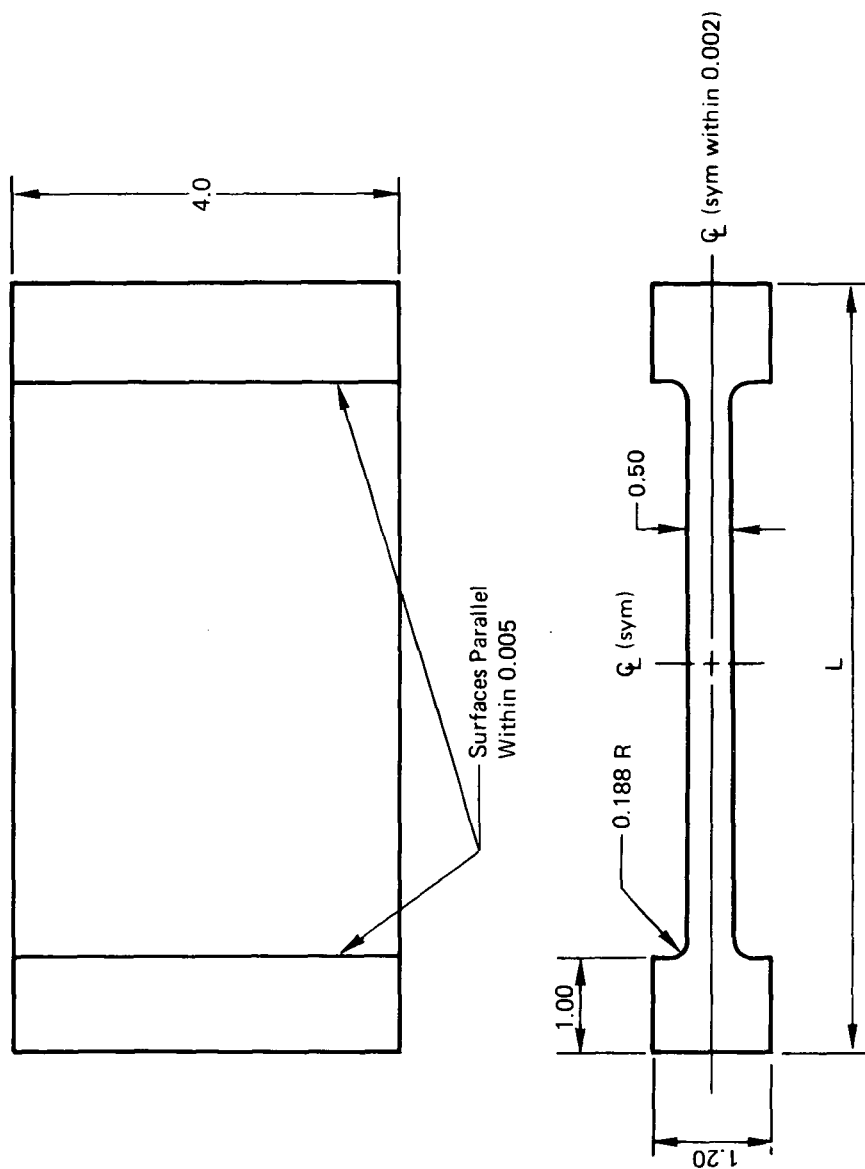


Figure 8-1: SCHEMATIC REPRESENTATION OF HOLOGRAPHIC TEST SETUP





All dimensions in inches

Figure 8-2: PLEXIGLAS TEST SPECIMEN

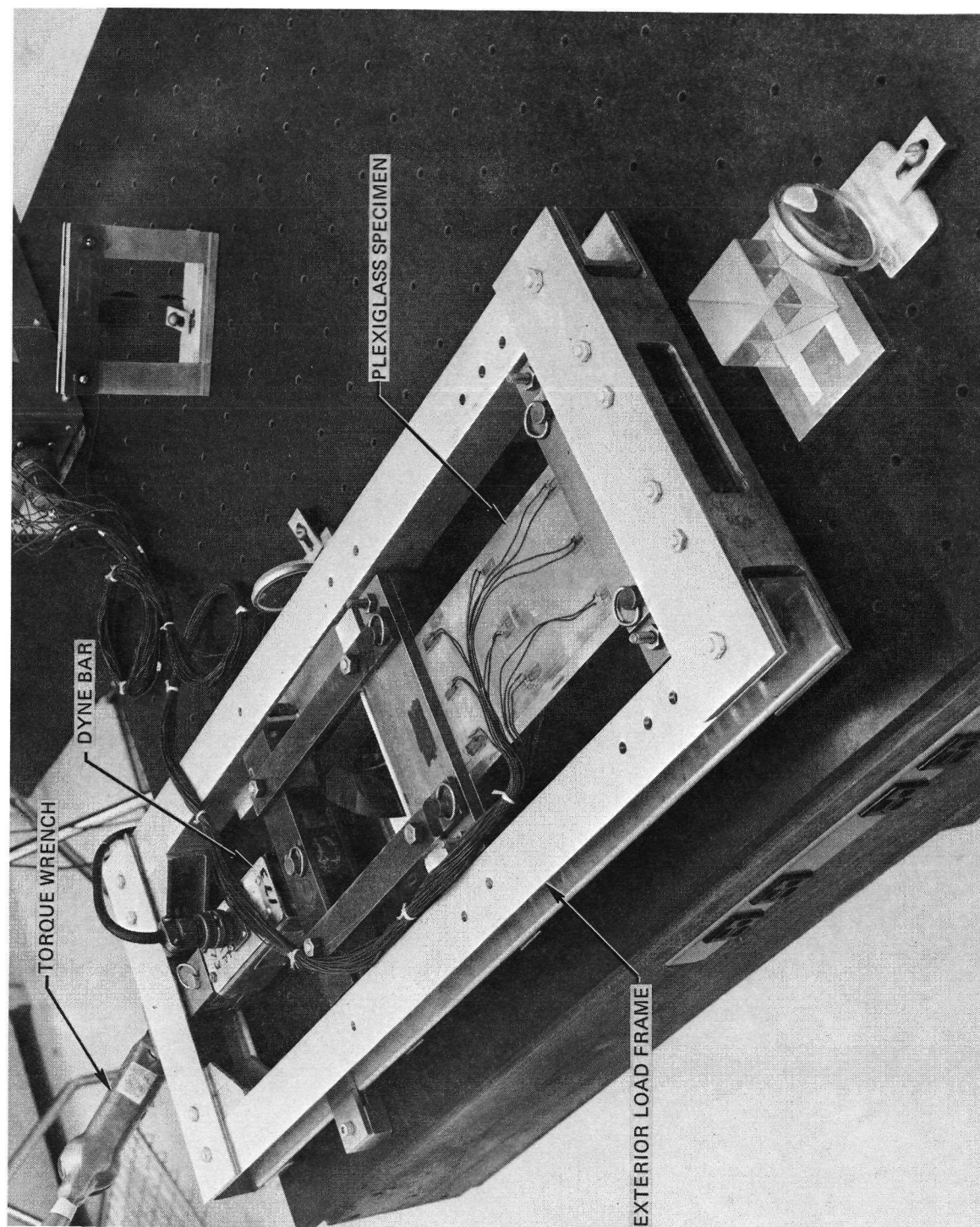
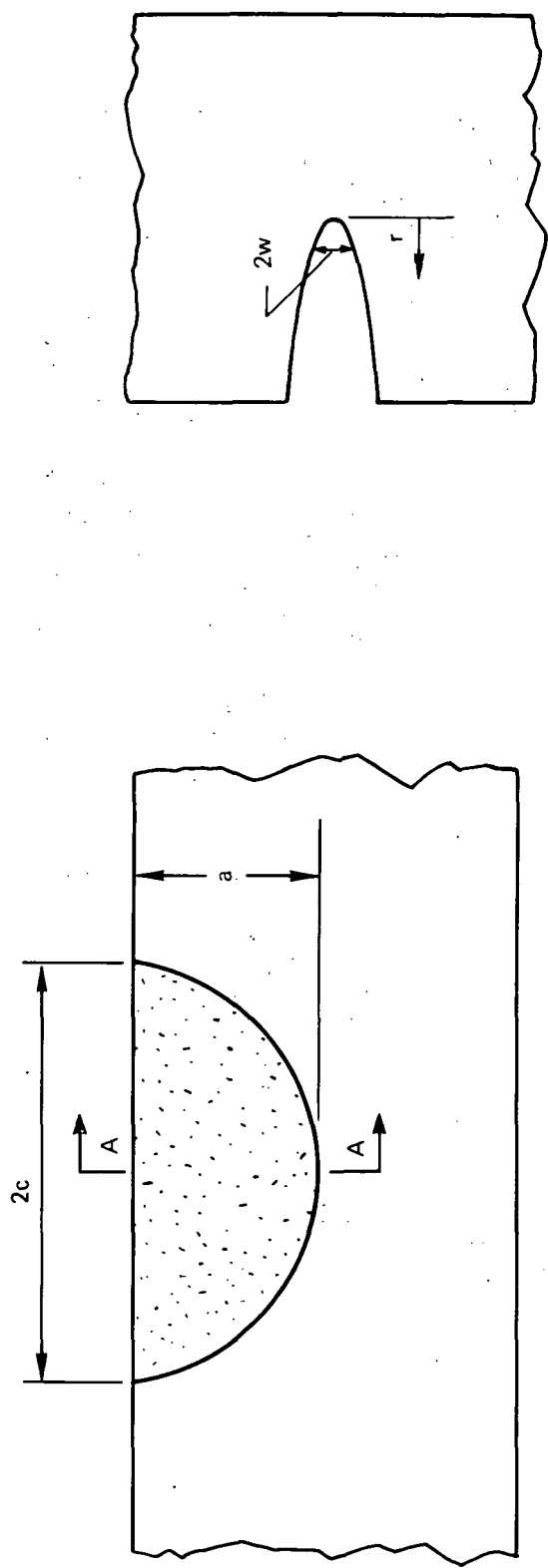
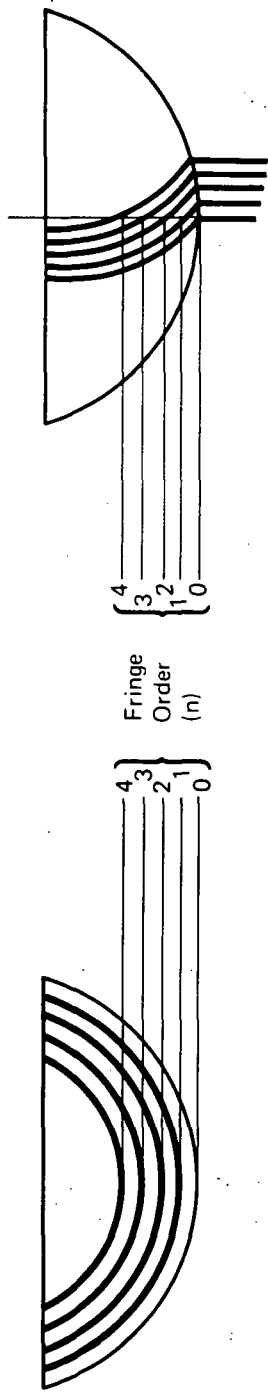


Figure 8-3: 2,000 POUND LOAD FIXTURE FOR LASER EXPERIMENT



(a) Flaw



(b) Schematic Representation of Interferogram

(c) Schematic Representation of Hologram

Figure 8-4: SCHEMATIC REPRESENTATION OF RESULTS

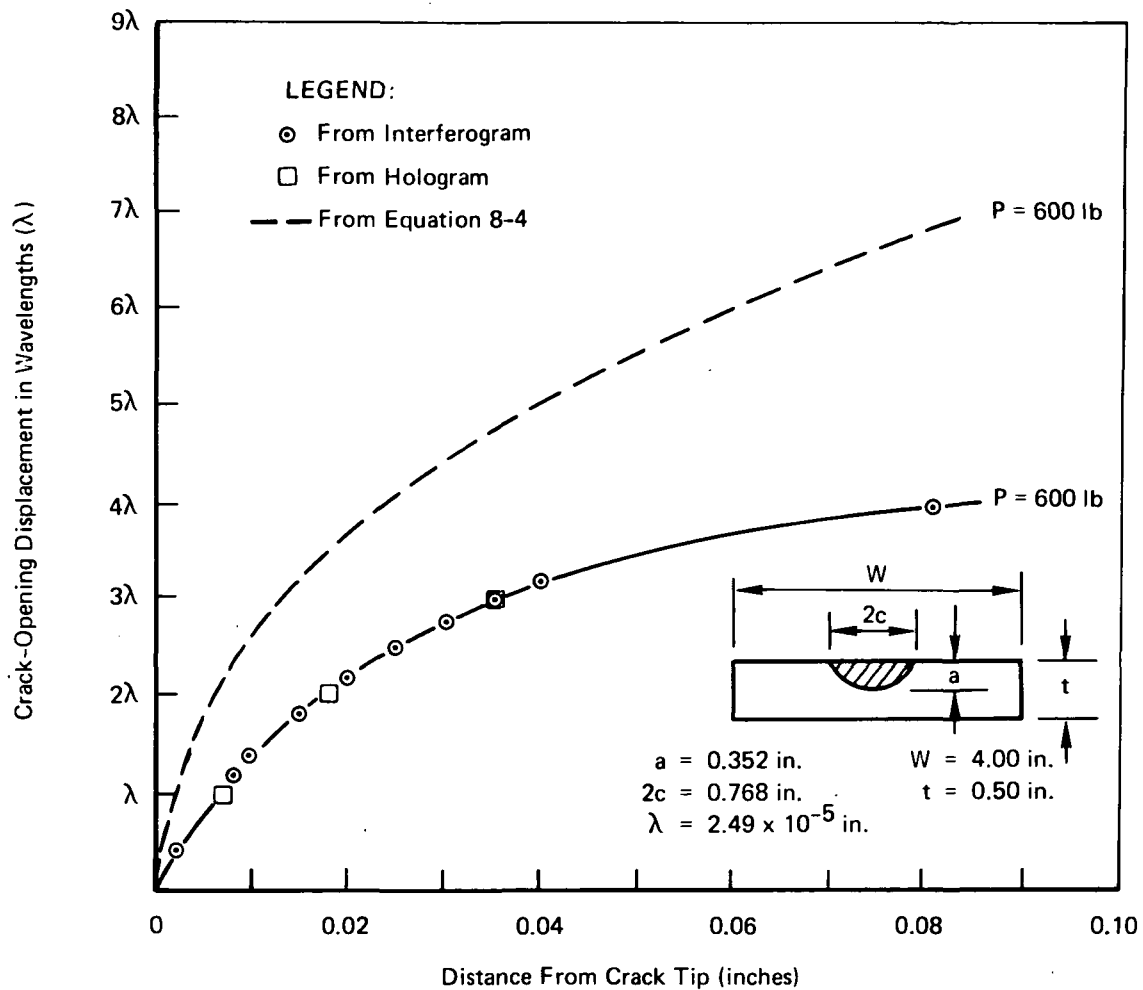


**Figure 8-5: CRACK-OPENING DISPLACEMENTS ALONG SEMIMINOR AXIS OF FIRST PLEXIGLAS SURFACE-FLAWED SPECIMEN**

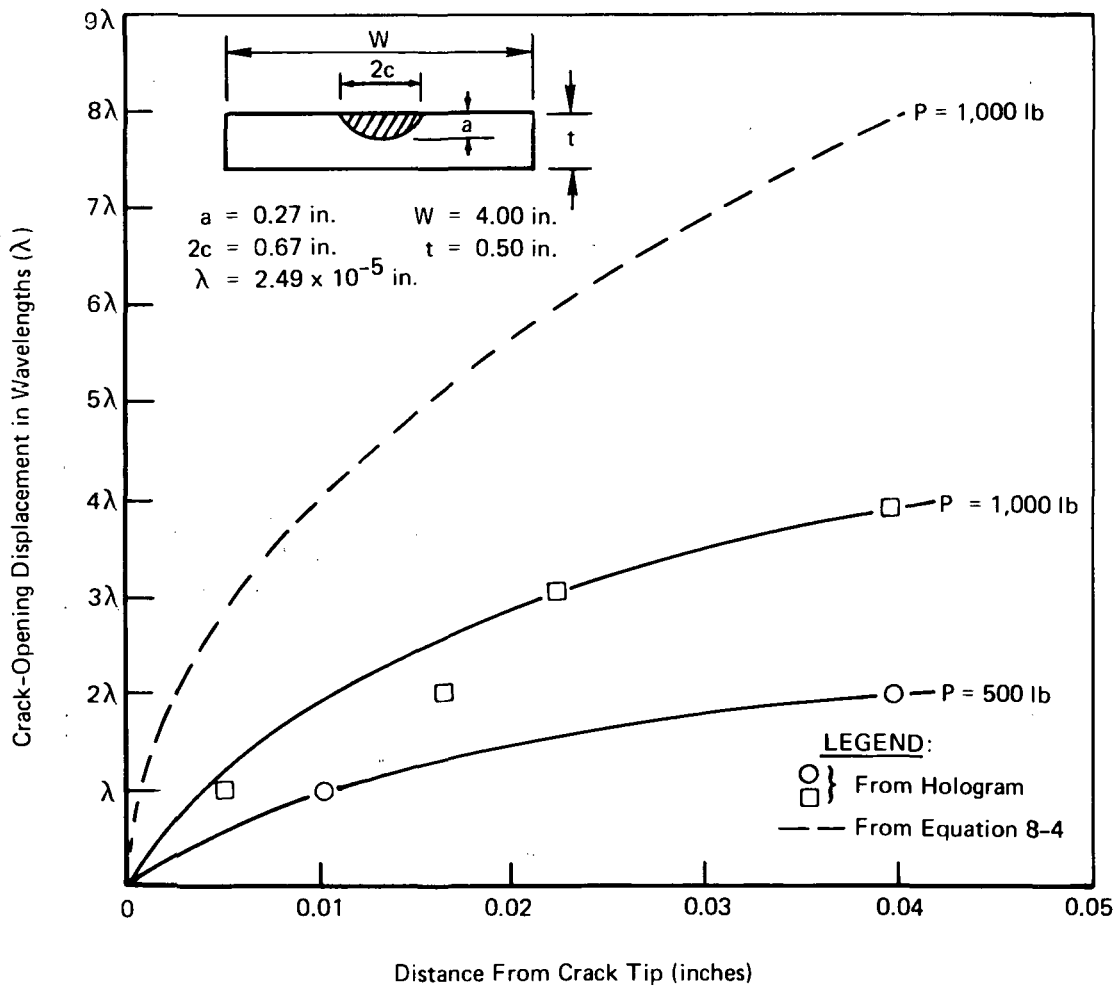
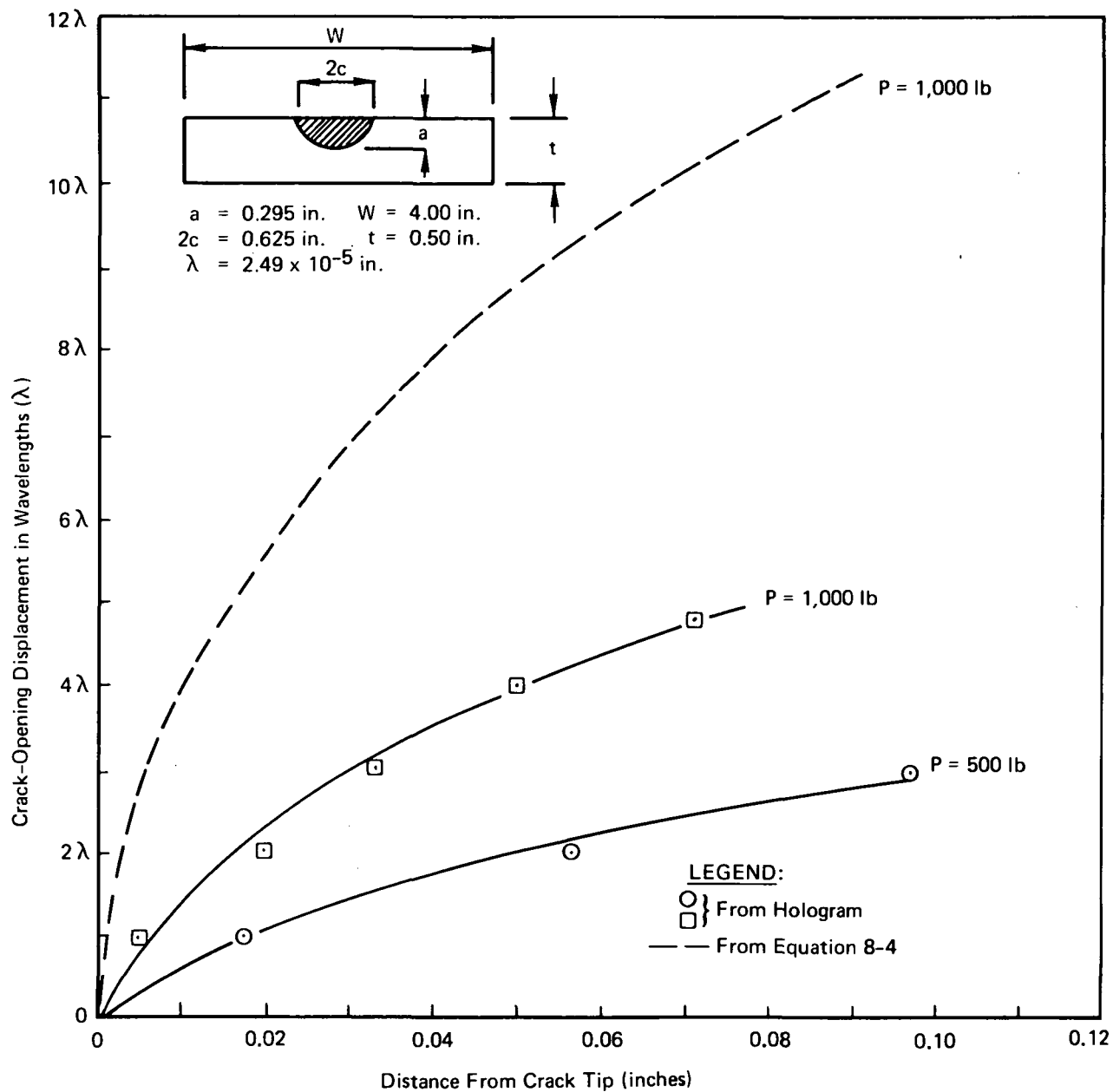
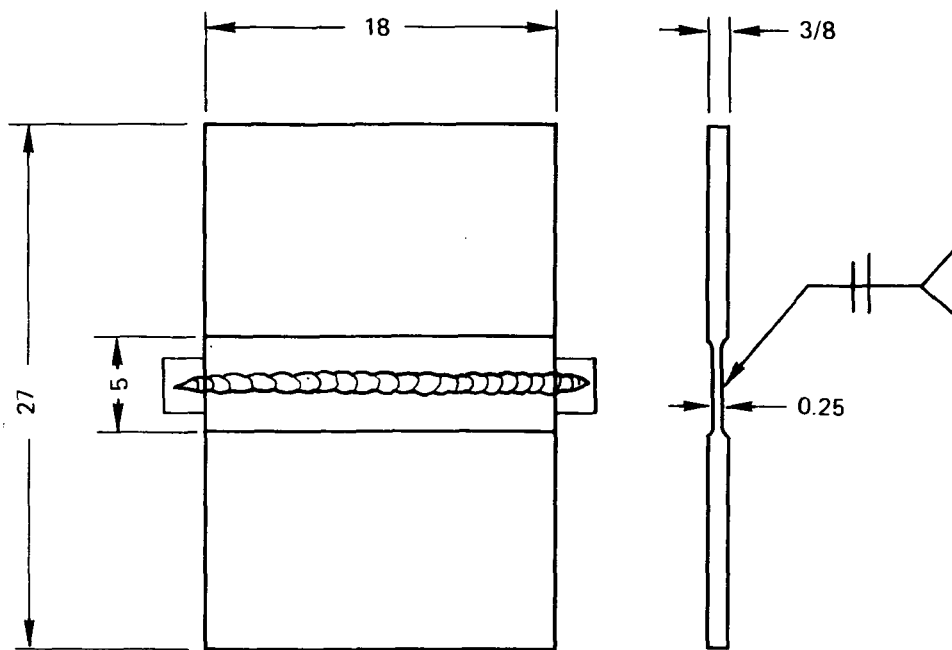


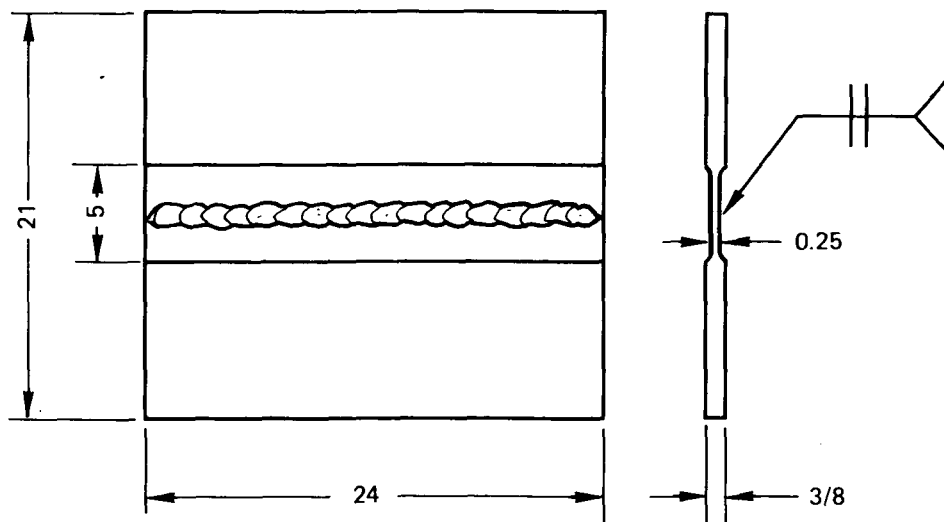
Figure 8-6: CRACK-OPENING DISPLACEMENTS ALONG SEMIMINOR AXIS  
 OF SECOND PLEXIGLAS SURFACE-FLAWED SPECIMEN



**Figure 8-7: CRACK-OPENING DISPLACEMENTS ALONG SEMIMINOR AXIS OF THIRD PLEXIGLAS SURFACE-FLAWED SPECIMEN**



Weld Panel For Specimens RC-1 Through 4



Weld Panel For Specimens RT-1 Through 4

Figure A-1: WELD PANELS FOR 5Al-2.5Sn (ELI) TITANIUM SPECIMENS

Table 3-1: CHEMICAL COMPOSITION OF MATERIALS

ELEMENT ( % by Weight ) ( Except as Noted )	2219-T87 ALUMINUM PLATE (Specification Limits)		5Al-2.5Sn (ELI) TITANIUM PLATE Heat No. 294327 (Actual Composition)
	Minimum	Maximum	
Copper	5.80	6.80	—
Silicon	—	0.20	—
Manganese	0.20	0.40	—
Magnesium	—	0.02	0.01
Iron	—	0.30	0.19
Chromium	—	—	—
Zinc	—	0.10	—
Vanadium	0.05	0.15	—
Tin	—	—	2.50
Carbon	—	—	0.02
Nitrogen	—	—	70 ppm
Oxygen	—	—	940 ppm
Hydrogen	—	—	94 ppm
Zirconium	0.10	0.25	—
Other Elements } Each	—	—	—
} Total	—	—	—
Titanium	0.10	0.20	Bal
Aluminum	Bal	Bal	5.10



Table 3-2: MECHANICAL PROPERTIES FOR 2219-T87 ALUMINUM  
PARENT METAL AND WELD METAL

Condition	Thickness (in.)	Test Temperature (°F)	Grain Direction (L=Longitudinal T=Transverse)	Ultimate Tensile Strength (ksi)	0.2% Offset Yield Strength (ksi)	Elongation in 2.0-Inch Gage Length
T87 Base Metal	1.0	72	T	69	53	8
		-320	T	85	66	12
		-423	T	100	59	11
	2.5	72	L	59	57	12
			T	59	55	10
		-320	L	87	70	12
			T	86	67	11
		-423	L	105	74	11
			T	101	73	10
As-Welded GTA Weld	1.0	72	-	40	20	8
		-320	-	56	25	9
		-423	-	67	27	11

**Table 3-3: MECHANICAL PROPERTIES FOR 5Al-2.5Sn (ELI) TITANIUM  
PARENT METAL AND WELD METAL**

Condition	Heat Treatment	Thickness (in.)	Test Temperature (°F)	Loading Direction (L= Longitudinal)	Ultimate Tensile Strength (ksi)	0.2% Offset Yield Strength (ksi)	Elongation in 2.0-Inch Gage Length
Base Metal	Mill Anneal (MA) 1,500°F/1/2 Hr	0.375	72	L	122	113	15
			-320	L	187	180	8
			-423	L	222	206	6
	1,550°F/8 Hr	0.375	72	L	119	114	14
			-320	L	190	179	9
			-423	L	209	196	5
	1,550°F/16Hr	0.80	72	L	114	108	14
			-320	L	176	173	8
			-423	L	201	187	3
GTA Weld Metal	1,200°F/1 Hr	0.25	72	—	126	117	11
			-320	—	192	184	9
			-423	—	224	204	7

Table 3-4: SUMMARY OF 5Al-2.5Sn (ELI) TITANIUM PROCESSING DETAILS

Test Program		Material Details		
Description	Location Within Report (Section)	Plate Thickness (inches)	Condition	Processing History
Determination of Combined Bending and Tension Stress Effects	5	0.375	Base Metal	Mill Anneal (1,500°F – 1/2 Hr – Air Cool)
Determination of Effects of Stress Fields Adjacent to Circular Holes	4	0.375	Base Metal	Mill Anneal
Determination of Residual Stress Effects	7	0.375	Base Metal	1. Mill Anneal 2. Stress Relieve (1,300°F – 1 Hour – Retort Cool)
			Welded	Variable: See Section 7
Determination of Surface Flawed Specimen Thickness Effects	6	0.375	Base Metal	1. Mill Anneal 2. 1,550°F – 8 Hrs – Retort Cool
Determination of Specimen Configuration Effects in Plane Strain Fracture Toughness Testing	6	0.80	Base Metal	1. Mill Anneal 2. 1,550°F – 16 Hour – Retort Cool

Table 3-5: MECHANICAL PROPERTIES OF CAST ACRYLIC MATERIAL

Number	Specimen		Test Temperature (°F)	Ultimate Tensile Strength (psi)	Young's Modulus (psi)	Poisson's Ratio
	Thickness (inches)	Area (in. <sup>2</sup> )				
1	0.1020	0.05096	72	4709.6	$4.50 \times 10^5$	—
2	0.0981	0.04915	72	4883.0	$4.86 \times 10^5$	0.373
3	0.1005	0.05065	72	4738.4	$4.70 \times 10^5$	0.378

Table 4-1: TEST PROGRAM FOR EVALUATING FRACTURE AT FLAWS  
PROTRUDING FROM CIRCULAR HOLES

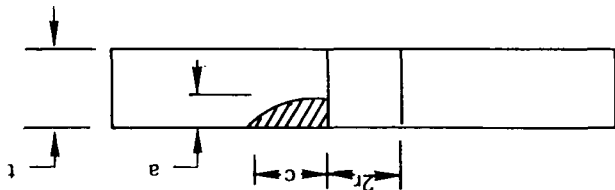
Flaw Configuration	Material	Test Type	Environment and Temp	t (in.)	$2r/t$	a/t	Number of Tests		
							a/c=0.25	a/c=0.50	a/c=1.00
	2219-T87 Aluminum	Static Fracture	LN <sub>2</sub> at -320°F	0.90	1.00	0.20	2	2	2
				0.80		0.50	2	2	2
				0.70		0.80	2	2	2
		Fatigue	Air at 72°F LN <sub>2</sub> at -320°F LH <sub>2</sub> at -423°F	0.90	0.50	0.20	2	2	2
				0.80		0.50	2	2	2
				0.70		0.80	2	2	2
	5Al-2.5Sn(ELI) Titanium	Static Fracture	LN <sub>2</sub> at -320°F	0.375	1.00	0.20	2	2	2
						0.50	2	2	2
						0.80	2	2	2
		Fatigue	Air at 72°F LN <sub>2</sub> at -320°F LH <sub>2</sub> at -423°F	0.375	0.50	0.20	2	2	2
						0.50	2	2	2
						0.80	2	2	2

Table 4-2: FRACTURE DATA FOR 2219-T87 ALUMINUM WITH FLAWS  
PROTRUDING FROM HOLES ( $2r/t = 0.5$ )

SPECIMEN			ENVIRONMENT		HOLE		FLAW VARIABLES				GROSS FAILURE STRESS (ksi)
Identification	Gage Thickness (inches)	Gage Width (inches)	Medium	Temperature (°F)	Diameter, $2r$ (inches)	$2r/t$	Flaw Depth, $a$ (inches)	Flaw Length, $c$ (inches)	$a/t$	$a/c$	
5HA22-1	0.9002	4.0005	LN <sub>2</sub>	-320	0.4495	0.499	0.190	0.710	0.211	0.268	47.6
5HA22-2	0.8995	4.0025	LN <sub>2</sub>	-320	0.4505	0.501	0.190	0.710	0.211	0.268	47.5
5HA25-1	0.9002	3.9965	LN <sub>2</sub>	-320	0.4500	0.500	0.205	0.356	0.228	0.576	48.5
5HA25-2	0.9010	3.9992	LN <sub>2</sub>	-320	0.4495	0.499	0.178	0.348	0.198	0.511	52.2
5HA21-1	0.9002	4.0012	LN <sub>2</sub>	-320	0.4500	0.500	0.166	0.166	0.184	1.000	52.9
5HA21-2	0.9005	3.9970	LN <sub>2</sub>	-320	0.4503	0.500	0.200	0.180	0.222	1.111	52.7
5HA52-1	0.7985	7.5040	LN <sub>2</sub>	-320	0.4000	0.501	0.400	1.610	0.501	0.248	39.6
5HA52-2	0.8002	7.5010	LN <sub>2</sub>	-320	0.3998	0.500	0.396	1.700	0.495	0.233	38.6
5HA55-1	0.7990	5.0045	LN <sub>2</sub>	-320	0.4002	0.501	0.388	0.710	0.486	0.546	42.5
5HA55-2	0.8005	5.0000	LN <sub>2</sub>	-320	0.4012	0.501	0.388	0.710	0.485	0.546	45.0
5HA51-1	0.6994	4.0036	LN <sub>2</sub>	-320	0.3994	0.571	0.430	0.455	0.615	0.945	50.6
5HA51-2	0.6995	4.0025	LN <sub>2</sub>	-320	0.4002	0.572	0.408	0.410	0.583	0.995	45.2
5HA82-1	0.6995	9.0050	LN <sub>2</sub>	-320	0.3500	0.500	0.525	2.170	0.751	0.242	30.2
5HA82-2	0.6999	9.0030	LN <sub>2</sub>	-320	0.3492	0.499	0.565	2.230	0.807	0.253	28.7
5HA85-1	0.6998	9.0060	LN <sub>2</sub>	-320	0.3500	0.500	0.520	1.060	0.743	0.491	43.6
5HA85-2	0.6980	9.0040	LN <sub>2</sub>	-320	0.3513	0.503	0.550	1.050	0.788	0.524	37.4
5HA81-1	0.7998	4.0001	LN <sub>2</sub>	-320	0.3500	0.438	0.575	0.560	0.719	1.027	43.1
5HA81-2	0.7993	4.0005	LN <sub>2</sub>	-320	0.3495	0.437	0.555	0.550	0.694	1.009	43.7

Table 4-3: FRACTURE DATA FOR 2219-T87 ALUMINUM WITH FLAWS  
PROTRUDING FROM HOLES ( $2r/t = 1.0$ )

SPECIMEN			ENVIRONMENT		HOLE		FLAW VARIABLES				GROSS FAILURE STRESS (ksi)
Identification	Gage Thickness (inches)	Gage Width (inches)	Medium	Temperature (°F)	Diameter, $2r$ (inches)	$2r/t$	Flaw Depth, $a$ (inches)	Flaw Length, $c$ (inches)	$a/t$	$a/c$	
1HA22-1	0.9000	4.9985	LN <sub>2</sub>	-320	0.8995	0.999	0.216	0.685	0.240	0.315	39.0
1HA22-2	0.8995	5.0025	LN <sub>2</sub>	-320	0.9005	1.001	0.190	0.660	0.211	0.288	42.0
1HA25-1	0.8990	5.0015	LN <sub>2</sub>	-320	0.9008	1.002	0.192	0.340	0.214	0.565	41.8
1HA25-2	0.8992	5.0002	LN <sub>2</sub>	-320	0.9008	1.002	0.196	0.350	0.218	0.560	42.7
1HA21-1	0.8995	3.9993	LN <sub>2</sub>	-320	0.9004	1.001	0.186	0.172	0.207	1.081	43.5
1HA21-2	0.8995	4.0015	LN <sub>2</sub>	-320	0.8995	1.000	0.176	0.158	0.196	1.114	42.3
1HA52-1	0.7990	7.5020	LN <sub>2</sub>	-320	0.7998	1.001	0.396	1.530	0.496	0.259	31.0
1HA52-2	0.8001	7.5000	LN <sub>2</sub>	-320	0.7995	0.999	0.370	1.620	0.462	0.228	35.1
1HA55-1	0.8000	7.5000	LN <sub>2</sub>	-320	0.7998	1.000	0.400	0.710	0.500	0.563	35.5
1HA55-2	0.8004	7.5000	LN <sub>2</sub>	-320	0.8003	1.000	0.395	0.685	0.494	0.577	35.5
1HA51-1	0.7985	3.9975	LN <sub>2</sub>	-320	0.8001	1.002	0.410	0.400	0.513	1.025	36.3
1HA51-2	0.7995	4.0005	LN <sub>2</sub>	-320	0.8004	1.001	0.404	0.400	0.505	1.010	37.0
1HA82-1A	0.6990	9.0110	LN <sub>2</sub>	-320	0.7005	1.002	0.550	2.130	0.787	0.258	21.6
1HA82-2	0.6995	9.0050	LN <sub>2</sub>	-320	0.6995	1.000	0.520	2.230	0.743	0.233	25.8
1HA85-1	0.7008	9.0020	LN <sub>2</sub>	-320	0.7005	1.000	0.520	0.965	0.742	0.539	33.7
1HA85-2	0.7010	9.0010	LN <sub>2</sub>	-320	0.7001	0.999	0.540	1.000	0.770	0.540	33.0
1HA81-1	0.7000	3.9972	LN <sub>2</sub>	-320	0.6990	0.999	0.565	0.550	0.807	1.027	32.7
1HA81-2	0.6996	4.0024	LN <sub>2</sub>	-320	0.7000	1.001	0.560	0.560	0.800	1.000	35.3

Table 4-4: FRACTURE DATA FOR 5Al-2.5Sn (ELI) TITANIUM WITH FLAWS  
PROTRUDING FROM HOLES ( $2r/t = 0.5$ )

SPECIMEN			ENVIRONMENT		HOLE		FLAW VARIABLES				GROSS FAILURE STRESS (ksi)
Identification	Gage Thickness (inches)	Gage Width (inches)	Medium	Temperature (°F)	Diameter, $2r$ (inches)	$2r/t$	Flaw Depth, $a$ (inches)	Flaw Length, $c$ (inches)	$a/t$	$a/c$	
5HT22-1	0.3858	1.9988	LN <sub>2</sub>	-320	0.1860	0.482	0.092	0.260	0.238	0.354	134.8
5HT22-2	0.3905	2.0028	LN <sub>2</sub>	-320	0.1860	0.476	0.098	0.268	0.251	0.366	116.4
5HT25-1	0.3775	2.0004	LN <sub>2</sub>	-320	0.1840	0.487	0.066	0.136	0.175	0.485	147.6
5HT25-2	0.3833	2.0014	LN <sub>2</sub>	-320	0.1840	0.480	0.074	0.140	0.193	0.529	139.3
5HT21-1	0.3920	2.0002	LN <sub>2</sub>	-320	0.1860	0.474	0.076	0.084	0.194	0.905	144.7
5HT21-2	0.3812	1.9971	LN <sub>2</sub>	-320	0.1880	0.493	0.074	0.066	0.194	1.121	155.6
5HT52-1	0.3815	4.0010	LN <sub>2</sub>	-320	0.1920	0.503	0.192	0.750	0.503	0.256	78.4
5HT52-2	0.3705	4.0008	LN <sub>2</sub>	-320	0.1880	0.518	0.192	0.750	0.518	0.256	77.9
5HT55-1	0.3880	2.0005	LN <sub>2</sub>	-320	0.1850	0.477	0.176	0.384	0.454	0.458	100.5
5HT55-2	0.3885	2.0006	LN <sub>2</sub>	-320	0.1850	0.476	0.190	0.352	0.489	0.540	97.8
5HT51-1	0.3835	1.9982	LN <sub>2</sub>	-320	0.1860	0.485	0.182	0.200	0.475	0.910	112.2
5HT51-2	0.3877	1.9984	LN <sub>2</sub>	-320	0.1860	0.480	0.180	0.180	0.464	1.000	121.3
5HT82-1	0.3700	5.4495	LN <sub>2</sub>	-320	0.1860	0.503	0.300	1.200	0.811	0.250	64.8
5HT82-2	0.3748	5.5014	LN <sub>2</sub>	-320	0.1880	0.502	0.300	1.180	0.800	0.254	62.5
5HT85-1	0.3824	2.7492	LN <sub>2</sub>	-320	0.1860	0.486	0.288	0.620	0.753	0.465	80.4
5HT85-2	0.3920	2.7514	LN <sub>2</sub>	-320	0.1850	0.472	0.300	0.620	0.765	0.484	81.1
5HT81-2	0.3868	1.9970	LN <sub>2</sub>	-320	0.1860	0.481	0.306	0.280	0.791	1.093	97.2
5HT81-2	0.3874	2.0000	LN <sub>2</sub>	-320	0.1860	0.480	0.280	0.308	0.723	1.100	100.7



Table 4-5: FRACTURE DATA FOR 5Al-2.5Sn (ELI) TITANIUM WITH FLAWS  
PROTRUDING FROM HOLES ( $2r/t = 1.0$ )

SPECIMEN			ENVIRONMENT		HOLE		FLAW VARIABLES				GROSS FAILURE STRESS (ksi)
Identification	Gage Thickness (inches)	Gage Width (inches)	Medium	Temperature (°F)	Diameter, $2r$ (inches)	$2r/t$	Flaw Depth, $a$ (inches)	Flaw Length, $c$ (inches)	$a/t$	$a/c$	
1HT22-1	0.3875	2.7497	LN <sub>2</sub>	-320	0.3740	0.965	0.076	0.285	0.196	0.267	107.9
1HT22-2	0.3901	2.7485	LN <sub>2</sub>	-320	0.3735	0.957	0.090	0.290	0.231	0.310	99.8
1HT25-1	0.3870	1.9980	LN <sub>2</sub>	-320	0.3760	0.972	0.086	0.132	0.222	0.652	99.8
1HT25-2	0.3794	1.9965	LN <sub>2</sub>	-320	0.3740	0.986	0.080	0.132	0.211	0.506	105.7
1HT21-1	0.3805	2.0006	LN <sub>2</sub>	-320	0.3750	0.986	0.072	0.070	0.189	1.029	122.2
1HT21-2	0.3835	1.9982	LN <sub>2</sub>	-320	0.3750	0.978	0.074	0.068	0.193	1.088	110.9
1HT52-1	0.3855	5.5025	LN <sub>2</sub>	-320	0.3745	0.971	0.182	0.725	0.472	0.251	69.5
1HT52-2	0.3821	5.5018	LN <sub>2</sub>	-320	0.3745	0.980	0.190	0.725	0.497	0.262	67.3
1HT55-1	0.3830	2.7470	LN <sub>2</sub>	-320	0.3740	0.977	0.190	0.350	0.496	0.543	78.9
1HT55-2	0.3835	2.7495	LN <sub>2</sub>	-320	0.3740	0.975	0.180	0.380	0.469	0.474	79.2
1HT51-1	0.3795	1.9980	LN <sub>2</sub>	-320	0.3735	0.984	0.182	0.178	0.480	1.022	89.9
1HT51-2	0.3740	1.9998	LN <sub>2</sub>	-320	0.3730	0.997	0.204	0.196	0.545	1.041	87.4
1HT82-1	0.3737	5.5015	LN <sub>2</sub>	-320	0.3735	0.999	0.300	1.170	0.803	0.256	55.9
1HT82-2	0.3854	5.5015	LN <sub>2</sub>	-320	0.3730	0.968	0.300	1.170	0.785	0.256	52.3
1HT85-1	0.3824	5.5005	LN <sub>2</sub>	-320	0.3745	0.979	0.288	0.620	0.753	0.465	58.1
1HT85-2	0.3920	5.5012	LN <sub>2</sub>	-320	0.3755	0.958	0.300	0.620	0.765	0.484	71.0
1HT81-1	0.3755	2.7480	LN <sub>2</sub>	-320	0.3730	0.996	0.308	0.276	0.820	1.116	77.2
1HT81-2	0.3926	2.7485	LN <sub>2</sub>	-320	0.3750	0.955	0.296	0.296	0.754	1.000	79.0

Table 4-6: FATIGUE DATA FOR SPECIMENS CONTAINING FLAWS PROTRUDING FROM HOLES

MATERIAL	SPECIMEN			HOLE AND CRACK DETAILS									NOTES
	Identification	Gage Thickness (inches)	Gage Width (inches)	Hole Diameter (inches)	Initial Flaw Depth (inches)	Initial Flaw Length (inches)	Final Flaw Depth (inches)	Final Flaw Length (inches)	Environment	Temperature (°F)	Peak Cyclic Stress (ksi)	Applied Loading Cycles	
2219-T87 ALUMINUM	HACR-1	0.807	4.02	0.402	0.164	0.146	●	●	Air	72	42.0	814	<p>All specimens except T1/air cycled to failure</p> <p>● Could not be detected</p> <p>■ 150 cycles applied with <math>\sigma = 37.8</math> ksi followed by 718 cycles with <math>\sigma = 42.0</math> ksi</p>
	HACR-2	0.801	4.04	0.402	0.170	0.156	●	●	Air	72	42.0	975	
	HACR-3	0.805	4.01	0.402	0.178	0.150	●	●	Air	72	45.0	564	
	HACN-1	0.805	4.01	0.402	0.176	0.150	●	●	LN <sub>2</sub>	-320	■	817	
	HACN-2	0.803	4.03	0.402	0.166	0.140	●	●	LN <sub>2</sub>	-320	42.0	868	
	HACN-3	0.804	4.01	0.402	0.180	0.148	●	●	LN <sub>2</sub>	-320	45.0	392	
	HACH-1	0.802	4.00	0.402	0.168	0.148	●	●	LH <sub>2</sub>	-423	45.5	98	
	HACH-2	0.804	4.00	0.402	0.166	0.144	●	●	LH <sub>2</sub>	-423	41.0	339	
	HACH-3	0.804	4.00	0.402	0.176	0.150	●	●	LH <sub>2</sub>	-423	41.0	446	
5A1-2.5Sn (ELI) TITANIUM	HTC-1R	0.371	2.00	0.185	0.088	0.075	0.170	0.107	Air	72	80.0	1,000	
	HTC-2R	0.370	2.00	0.185	0.080	0.070	0.144	0.099	Air	72	80.0	1,000	
	HTC-3R	0.368	2.00	0.185	0.075	0.075	●	●	LN <sub>2</sub>	-320	95.0	1,734	
	HTC-4N	0.368	2.00	0.185	0.080	0.077	●	●	LN <sub>2</sub>	-320	115.0	382	
	HTC-5N	0.365	2.00	0.185	0.070	0.074	●	●	LN <sub>2</sub>	-320	115.0	374	
	HTC-7H	0.367	2.00	0.185	0.075	0.075	●	●	LH <sub>2</sub>	-423	81.7	539	
	HTC-8H	0.372	2.00	0.185	0.071	0.075	●	●	LH <sub>2</sub>	-423	80.5	471	
	HTC-9H	0.371	2.00	0.185	0.082	0.076	●	●	LH <sub>2</sub>	-423	71.3	1,191	

Table 4-7: FRACTURE TOUGHNESS TEST RESULTS FOR MATERIALS USED IN FRACTURE TESTS OF SPECIMENS WITH FLAWS PROTRUDING FROM HOLES

SPECIMEN				CRACKING DETAILS					TEST CONDITIONS			RESULTS			
Material	Type	Identification	Thickness (inches)	Width (inches)	$(K_I^f)_{\max}$ (ksi $\sqrt{\text{in.}}$ )	$(K_I^f)_{\max} / (K_I^f)_{\min}$	Number of Cycles to Grow Crack in Thousands	Crack Depth, a (inches)	Crack Length, 2c (inches)	Environment	Temperature (°F)	Loading Rate (ksi/min)	Gross Section Failure Stress (ksi)	$\frac{\text{Gross Stress}}{\text{Yield Stress}}$	$K_{Ic}^E$ (ksi $\sqrt{\text{in.}}$ )
2219-T87 Aluminum	Surface Flawed	2A1N-1	0.750	10.01	10	0.06	7.0	0.290	2.89	LN <sub>2</sub>	-320	40	37.2	0.55	39
		2A1N-2	0.750	10.01	10	0.06	11.0	0.290	2.89				40.4	0.59	42
		2A3N-1	0.753	7.00	10	0.06	14.0	0.380	1.44				43.4	0.64	44
		2A32-2	0.749	7.00	10	0.06	14.0	0.380	1.44	LN <sub>2</sub>	-320	40	42.4	0.62	43
Ti6Al-2.5Sn (ELI) Titanium	Surface Flawed	A-1	0.360	2.75	18	0.06	4.0	0.151	0.500	LN <sub>2</sub>	-320	100	123.0	0.68	75
		A-2	0.358	2.75	18	0.06	7.0	0.150	0.498				126.5	0.70	78
		A-3	0.362	2.75	18	0.06	3.0	0.151	0.495				119.3	0.66	72
		A-4	0.358	2.75	18	0.06	5.0	0.150	0.498	LN <sub>2</sub>	-320	100	118.0	0.66	72

Table 4-8: SUMMARY OF CALCULATED PARAMETERS USED TO ESTIMATE CYCLIC LIFE FOR SPECIMENS WITH FLAWS PROTRUDING FROM HOLES

Material	Temperature (°F)	Specimen Number	Peak Cyclic Stress (ksi)	$C_e$ (inches)	$F(C_e/r)$	$K_{II} \sqrt{0.87Q/\pi C_e} \cdot F(C_e/r)$ ksi $\sqrt{\text{in.}}$	$K_{IE} \sqrt{\text{in.}}$ ksi	$K_{II}/K_{IE}$	Estimated Cyclic Life (see section 4.2.2)	Actual Cyclic Life
2219-T87 Aluminum	72	HACR-1	42.0	0.070	1.95	33.4	41	0.81	660	814
	72	HACR-2	42.0	0.076	1.90	33.9	41	0.82	600	975
	72	HACR-3	45.0	0.080	1.87	36.7	41	0.89	230	564
	-320	HACN-1	42.0	0.078	1.88	34.0	43	0.79	470	817
	-320	HACN-2	42.0	0.071	1.94	33.5	43	0.78	530	868
	-320	HACN-3	45.0	0.080	1.87	36.7	43	0.86	170	392
	-423	HACH-1	45.5	0.074	1.92	36.6	45	0.81	410	98
	-423	HACH-2	41.0	0.072	1.94	32.9	45	0.73	1,150	339
	-423	HACH-3	41.0	0.080	1.87	33.4	45	0.74	900	446
5A1-2.5 Sn (ELL) Titanium	-320	HTC-3R	95.0	0.032	1.96	51.2	75	0.68	850	1,734
	-320	HTC-4N	115.0	0.038	1.85	63.8	75	0.85	225	382
	-320	HTC-5N	115.0	0.031	1.98	61.7	75	0.82	310	374
	-423	HTC-7H	81.7	0.032	1.96	44.0	60	0.73	300	539
	-423	HTC-8H	80.5	0.030	1.99	42.8	60	0.71	350	471
	-423	HTC-9H	71.3	0.037	1.87	39.0	60	0.65	510	1,191

Table 5-1: COMBINED BENDING AND TENSION STRESS TEST PROGRAM

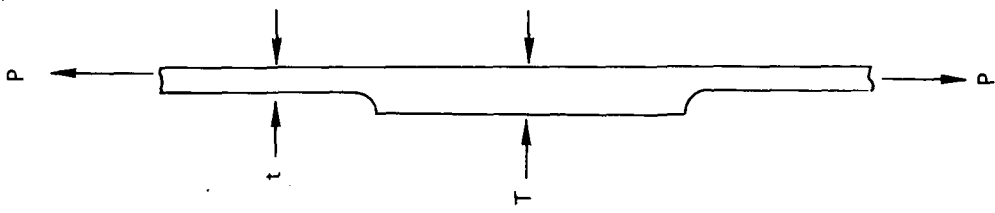
Specimen Configuration	Material	Test Type	Test Temp	a/2c	T (in.)	$\frac{T}{t}$	$\frac{a}{T}$	No. Tests
	2219-T87 Aluminum Base Metal	Static Fracture	-320°F	0.125	0.60	1.00	0.25	1
						1.50	0.25	1
						2.00	0.50	1
						1.00	0.25	1
						2.00	0.50	1
						1.00	0.50	1
	5Al-2.5Sn (ELI) Titanium Base Metal	Fatigue	72°F -320°F -423°F	0.25	0.90	2.0	0.33	3
						1.00	0.50	1
						2.00	0.25	1
						1.00	0.50	1
						2.00	0.25	1
						1.00	0.50	1
	5Al-2.5Sn (ELI) Titanium Base Metal	Static Fracture	-320°F	0.125	0.36	1.00	0.25	1
						1.50	0.25	1
						2.00	0.50	1
						1.00	0.25	1
						2.00	0.25	1
						1.00	0.50	1
	Fatigue	Fatigue	72°F -320°F -423°F	0.25	0.36	2.0	0.42	3
						2.0	0.56	3
						2.0	0.24	3
						2.0	0.42	3
						2.0	0.56	3
						2.0	0.24	3

Table 5-2: TEST RESULTS FOR SURFACE-FLAWED SPECIMENS SUBJECTED TO COMBINED BENDING AND TENSION STRESSES

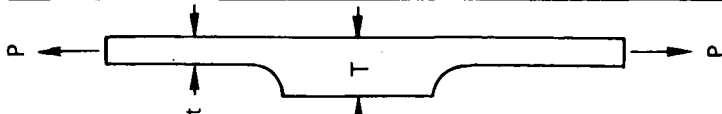
Configuration	Specimen					Flaw		Results		Remarks	
	Material	Number	Width, W (in.)	T (in.)	t (in.)	Depth, <sup>a</sup> (in.)	Width, 2c (in.)	Maximum Applied Load (kips)	Maximum Gross Stress (ksi)		
	2219-T87 Aluminum	A11-1	9.02	0.599	0.599	0.310	2.46	236.6	43.8	Failed at Flaw	
		A11-2	4.50	0.600	0.400	—	—	—	—	—	Not Tested
		A11-3	9.00	0.600	0.400	0.420	2.48	161.0	29.8	Failed at Flaw	
		A12-1	4.50	0.599	0.599	0.158	1.21	156.3	58.0	Failed at Flaw	
		A12-2	4.51	0.600	0.300	—	—	—	—	—	Not Tested
		A12-3	8.99	0.599	0.300	—	—	136.5	—	—	Failed at Grip
		A21-1	7.00	0.900	0.900	0.430	1.72	277.2	44.0	Failed at Flaw	
		A21-2	4.50	0.901	0.601	—	—	150.9	—	—	Failed at Grip
		A21-3	9.00	0.903	0.601	0.480	1.76	267.4	32.9	Failed at Flaw	
	A22-1	4.50	0.899	0.899	0.200	0.86	243.0	60.0	Failed at Flaw		
	A22-2	4.50	0.901	0.450	—	—	—	—	—	Not Tested	
	A22-3	8.11	0.901	0.450	—	—	196.5	—	—	Failed at Grip	
	5A1-2.5Sn (ELI) Titanium	T11-1	5.20	0.388	0.388	—	—	—	160.0	—	Did Not Fail
		T11-2	3.00	0.358	0.239	—	—	—	—	—	Not Tested
		T11-3	6.00	0.361	0.240	0.200	1.49	121.3	56.0	Failed at Flaw	
T12-1		2.75	0.388	0.388	—	—	—	160.0	—	Did Not Fail	
T12-2		3.00	0.357	0.179	—	—	—	57.0	—	Failed at Grip	
T12-3		6.00	0.363	0.182	—	—	—	108.0	—	Failed at Grip	
T21-1		2.75	0.382	0.382	0.170	0.71	115.9	110.3	Failed at Flaw		
T21-2		2.50	0.361	0.241	—	—	—	96.4	—	Failed at Grip	
T21-3		3.00	0.362	0.242	—	—	—	98.8	—	Failed at Grip	
T22-1	2.75	0.387	0.387	0.080	0.355	136.0	88.8	Failed at Flaw			
T22-2	2.00	0.363	0.181	—	—	71.0	—	—	Failed at Grip		
T22-3	2.50	0.360	0.180	0.200	0.780	63.0	70.0	Failed at Flaw			

Table 5-3: EVALUATION OF TEST RESULTS FOR SURFACE-FLAWED SPECIMENS  
SUBJECTED TO COMBINED BENDING AND TENSION STRESSES

Specimen		Flaw		Max Stresses		Estimated $K_{cr}$ (ksi√in.)	Failure Load $P_{max}$ (kips)	$\frac{P_{max}}{(P_{cr})_1^{**}}$	$\frac{P_{max}}{(P_{cr})_2^*}$	REMARKS
Number	Thickness (in.)	Depth, a (in.)	Width, 2c (in.)	Tensile Stress $\sigma_T$ (ksi)	Estimated Bending Stress $\sigma_B$ (ksi)					
A11-3	0.600	0.420	2.48	29.8	16.5	45	161.0	0.88	1.04	Specimens Failed at Flaw Plane
A21-3	0.903	0.480	1.76	32.9	20.1	45	136.5	0.91	0.91	
T22-3	0.360	0.200	0.78	70.0	50.0	77	63.0	1.11	1.10	
T11-3	0.361	0.200	1.49	56.0	42.7	77	121.3	1.15	1.03	
A12-3	0.599	0.30	2.40	25.3	22.9	45	136.5	0.82	0.93	Specimens Failed in Grips. Flaw Depths and Widths Are Estimated Values.
A21-2	0.901	0.23	0.90	37.2	22.3	45	150.9	0.92	0.90	
A22-3	0.901	0.45	1.80	26.9	29.0	45	196.5	0.97	0.97	
T12-3	0.363	0.18	1.44	49.5	39.6	45	108.0	0.71	0.80	
T21-3	0.362	0.18	0.72	91.0	36.6	77	98.8	0.99	0.99	
T21-2	0.361	0.09	0.36	106.8	40.6	77	96.4	0.89	0.88	
T22-2	0.363	0.09	0.36	97.7	60.0	77	71.0	0.90	0.89	

\*\*  $(P_{cr})_1$  is estimated failure load using Equation 5-4 and  $M_B$  values from Figure 5-1b.

\*  $(P_{cr})_2$  is estimated failure load using Equation 5-4 and  $M_B$  values from Figure 5-1a.

Table 5-4: RESULTS FOR FATIGUE TESTS OF SURFACE-FLAWED SPECIMENS SUBJECTED TO COMBINED BENDING AND TENSION STRESSES

Material	Specimen			Initial Conditions				Test Conditions				Number of Applied Loading Cycles, N	Final Condition				Evaluation			Remarks			
	Identification	Configuration	Gage Width (in.)	Gage Thickness (in.)	Flaw Depth, $a_f$ (in.)	Flaw Length $2c_f$ (in.)	Flaw Size, (a/O) $_f$ (in.)	$K_{If}$ ksi $\sqrt{in.}$	Test Type	Loading Profile	Medium		Temperature (°F)	Minimum Tensile Stress (ksi)	Maximum Bending Stress (ksi)	Flaw Depth, $a_f$ (in.)	Flaw Length, $2c_f$ (in.)	Flaw Size, (a/O) $_f$ (in.)	$K_{If}$ ksi $\sqrt{in.}$		$\frac{(K_{If} + K_{If})}{2}$ ksi $\sqrt{in.}$	$\Delta(a/O)$ (in.)	$\Delta(a/O) / N$ $\mu$ . in./cycle
22:9:187 Aluminum	AC-11	Fig 4-1	6.50	0.903	0.29	1.32	-	37.9	↔ Fatigue ↔	↔ Zero-to-Tension ↔	Room	72	30.0	18.3	●	-	-	-	-	-	-	● Specimen Delaminated	
	AC-12	↔	6.51	0.906	0.30	1.31	-	37.9	↔	↔	Air	72	30.0	18.3	●	-	-	-	-	-	-		
	AC-13	↔	6.50	0.901	0.30	1.31	-	37.7	↔	↔	↔	72	30.0	18.3	●	-	-	-	-	-	-		
	ACN-1	↔	6.25	0.901	0.29	1.30	-	39.4	↔	↔	LN <sub>2</sub>	-320	31.5	19.1	●	-	-	-	-	-	-		
	ACH-2	↔	6.25	0.901	0.29	1.28	-	38.9	↔	↔	LN <sub>2</sub>	-320	31.5	19.1	●	-	-	-	-	-	-		
	AC-10	↔	6.50	0.901	0.30	1.30	-	37.5	↔	↔	LN <sub>2</sub>	-320	30.0	18.3	●	-	-	-	-	-	-		
	ACH-1	↔	6.25	0.907	0.29	1.29	-	34.9	↔	↔	LH <sub>2</sub>	-423	28.0	17.1	■	-	-	-	-	-	-	■ Could not be Detected	
	ACH-3	↔	6.25	0.902	0.31	1.33	-	35.3	↔	↔	LH <sub>2</sub>	-423	28.0	17.1	■	-	-	-	-	-	-		
	ACR-3	Fig 4-1	6.25	0.903	0.28	1.28	-	39.7	↔	↔	LH <sub>2</sub>	-423	32.0	19.4	■	-	-	-	-	-	-		
SAI-255 niELTi Titanium	TCR-1	Fig 4-1	2.50	0.360	0.141	0.565	0.099	41.5	↔ Fatigue ↔	↔ Zero-to-Tension ↔	Room	72	47.0	38.3	1,000	0.206	0.648	0.125	40.3	40.9	0.026	26	Specimens Were Not Cycled to Failure
	TCR-2	↔	2.50	0.352	0.136	0.560	0.097	41.4	↔	↔	Air	72	47.0	38.3	1,000	0.228	0.690	0.134	40.2	40.8	0.037	37	
	TCR-3	↔	2.50	0.360	0.136	0.562	0.098	41.9	↔	↔	↔	72	47.0	38.3	1,000	0.212	0.645	0.125	40.4	41.2	0.027	27	
	TCN-1	↔	2.50	0.360	0.186	0.780	-	59.2	↔	↔	LN <sub>2</sub>	-320	63.0	45.7	200	■	-	-	-	-	-	-	■ Could not be Detected
	TCN-2	↔	2.50	0.360	0.187	0.775	-	56.5	↔	↔	LN <sub>2</sub>	-320	60.0	44.5	360	■	-	-	-	-	-	-	
	TCN-3	↔	2.50	0.358	0.182	0.788	-	53.7	↔	↔	LN <sub>2</sub>	-320	56.0	42.6	600	■	-	-	-	-	-	-	
	TCH-1	↔	2.50	0.356	0.086	0.334	0.059	42.8	↔	↔	LH <sub>2</sub>	-423	60.0	44.5	396	0.125	0.364	0.071	44.7	43.8	0.012	30.3	Specimens Failed in Grips
	TCH-2	↔	2.50	0.359	0.080	0.332	0.056	40.1	↔	↔	LH <sub>2</sub>	-423	57.0	43.1	490	0.107	0.334	0.063	40.6	40.4	0.007	14.2	
	TCH-3	Fig 4-1	2.00	0.353	0.082	0.348	0.058	43.0	↔	↔	LH <sub>2</sub>	-423	60.0	44.5	554	0.112	0.356	0.067	43.3	43.2	0.009	16.2	



Table 6-1: TEST PROGRAM

PURPOSE	MATERIAL	PARENT PLATE THICKNESS (Inch)	SPECIMEN TYPE	APPROXIMATE SPECIMEN THICKNESS $\times (\nu \gamma_S / K_{IC})^2$ (Inch)	SURFACE FLAW PARAMETERS		NUMBER OF TESTS AT		
					a/2c	a/t	72°F	-320°F	-423°F
SPECIMEN CONFIGURATION EFFECT TESTS	2219-T87 ALUMINUM	2.50	SENB SENT CT SF SF	2.50	- - - 0.25 0.40	- - - 0.3 0.5	2 2 2 2 2	2 2 2 2 2	2 2 2 2 2
	5Al-2.5 Sn (ELI) TITANIUM	0.80	SENB SENT CT SF SF	2.50	- - - 0.25 0.40	- - - 0.4 0.5	2 2 2 2 2	2 2 2 2 2	2 2 2 2 2
SURFACE-FLAWED SPECIMEN THICKNESS EFFECT TESTS	2219-T87 ALUMINUM	1.00	SF	1.88	0.10 0.25	0.4 0.5	2 2	2 2	2 2
				1.25	0.10 0.25	0.4 0.5	2 2	2 2	2 2
				0.63	0.10 0.25	0.4 0.5	2 2	2 2	2 2
				0.31	0.10 0.25	0.7 0.8	2 2	2 2	2 2
	5Al-2.5 Sn (ELI) TITANIUM	0.375	SF	1.88	0.10 0.25	0.4 0.5	NONE	2 2	2 2
				1.25	0.10 0.25	0.4 0.5		2 2	2 2
				0.63	0.10 0.25	0.4 0.5		2 2	2 2
				0.31	0.10 0.25	0.7 0.8		2 2	2 2

Table 6-2: FRACTURE TOUGHNESS TEST RESULTS FOR 2219-T87 ALUMINUM  
(SENB, SENT And CT Specimens)

SPECIMEN				CRACK DETAILS								TEST CONDITIONS					RESULTS				REMARKS
TYPE	IDENTIFICATION	THICKNESS, B (inch)	DEPTH, W (inch)	TEST LENGTH, L (inch)	(K <sub>I</sub> ) <sub>max</sub> (Ksi/√in.)	(K <sub>I</sub> ) <sub>min</sub> / (K <sub>I</sub> ) <sub>max</sub>	NUMBER OF CYCLES TO GROW LAST 0.10 IN. OF FATIGUE CRACK	CRACK LENGTHS (Inch)					ENVIRONMENT	TEMPERATURE (deg F)	LOADING RATE (1000 Lbs/Min)	MAX LOAD (1000 Lbs)	P <sub>Q</sub> (1000 Lbs)	K <sub>Q</sub> (Ksi/√in.)	K <sub>Ic</sub> (Ksi/√in.)		
								At Surface "a <sub>1</sub> "	At 1/4 Point "a <sub>2</sub> "	At Centerline "a <sub>3</sub> "	At 1/4 Point "a <sub>4</sub> "	At Surface "a <sub>5</sub> "								AVG. CRACK LENGTH, (a <sub>2</sub> + a <sub>3</sub> + a <sub>4</sub> ) / 3 (Inch)	
SENT	B1-17	1.252	2.491	7.50	9.7	0.06	47,000	1.20	1.23	1.23	1.21	1.20	AIR	72	25.0	20.70	19.10	32.8	---		
	A2-5	1.255	2.485				50,000	1.18	1.20	1.20	1.20	1.19	LN <sub>2</sub>	-320	30.0	24.70	24.00	39.9	---		
	B1-16	1.252	2.489				47,000	1.18	1.20	1.22	1.22	1.20	LN <sub>2</sub>	-320	30.0	24.60	23.10	39.0	---		
	B1-18	1.253	2.482				47,000	1.17	1.20	1.22	1.21	1.18	LH <sub>2</sub>	-423	30.0	29.50	28.65	48.9	---		
SENT	B1-19	1.252	2.491	7.50	9.7	0.06	45,000	1.21	1.23	1.23	1.21	1.17	LH <sub>2</sub>	-423	30.0	27.80	26.80	46.0	---		
SENB	1	1.250	2.500	10.00	12.0	0.06	280,000	1.25	1.27	1.27	1.26	1.24	Air	72	10.0	6.56	6.53	---	36.2		
	B1-14	1.250	2.500				60,000	1.19	1.23	1.25	1.25	1.22	Air	72	10.0	6.96	6.94	---	36.4		
	B1-15	1.254	2.502				64,000	1.23	1.24	1.24	1.22	1.18	LN <sub>2</sub>	-320	12.0	8.30	7.98	---	41.6		
	A2-3	1.249	2.502				60,000	1.22	1.23	1.23	1.21	1.18	LN <sub>2</sub>	-320	12.0	8.72	8.36	---	43.3		
	B1-12	1.253	2.502				60,000	1.17	1.23	1.25	1.23	1.21	LH <sub>2</sub>	-423	10.0	9.65	9.21	---	48.8		
SENB	B1-13	1.255	2.503	10.00	12.0	0.06	60,000	1.22	1.23	1.23	1.21	1.17	LH <sub>2</sub>	-423	10.0	9.75	9.18	---	47.2		
CT	B1-21	1.252	2.001	2.401	12.2	0.06	37,000	1.11	1.14	1.14	1.14	1.11	Air	72	5.0	3.98	3.88	---	26.4		
	B1-22	1.252	2.002	2.402			35,000	1.07	1.08	1.12	1.12	1.11	Air	72	5.0	4.13	4.05	---	26.1		
	B1-23	1.251	2.001	2.400			31,000	1.10	1.13	1.14	1.15	1.11	LN <sub>2</sub>	-320	6.0	4.82	4.60	---	31.4		
	B1-29	1.249	2.001	2.401			35,000	1.09	1.12	1.14	1.12	1.10	LN <sub>2</sub>	-320	6.0	4.82	4.72	---	31.3		
	A2-6	1.251	2.000	2.400			35,000	1.03	1.11	1.11	1.11	1.09	LH <sub>2</sub>	-423	6.0	5.40	5.10	---	33.0		
	A2-7	1.252	2.002	2.402	12.2	0.06	30,000	1.07	1.10	1.10	1.09	1.07	LH <sub>2</sub>	-423	6.0	5.60	5.53	---	35.0		
	ACL-1	1.255	2.002	2.402	11.4	0.06	84,000	0.53	0.54	0.54	0.52	0.52	Air	72	5.0	10.72	9.70	30.4	---		
CT	ACL-2	1.255	2.002	2.402	11.4	0.06	85,000	0.53	0.54	0.54	0.52	0.52	Air	72	5.0	10.90	9.48	29.7	---		

Table 6-3: FRACTURE TOUGHNESS TEST RESULTS FOR 5Al-2.5 Sn(ELI) TITANIUM  
(SENB, SENT And CT Specimens)

SPECIMEN			CRACK DETAILS							TEST CONDITIONS			RESULTS				REMARKS				
TYPE	IDENTIFICATION	THICKNESS, B (inch)	DEPTH, W (inch)	TEST LENGTH, L (inch)	(K <sub>I</sub> ) <sub>max</sub> (Ksi √in.)	(K <sub>I</sub> ) <sub>min</sub> / (K <sub>I</sub> ) <sub>max</sub>	NUMBER OF CYCLES TO GROW LAST 0.10 - IN. OF FATIGUE CRACK	CRACK LENGTHS (Inch)					ENVIRONMENT	TEMPERATURE (deg F)	LOADING RATE (1000 Lbs/Min)	MAX LOAD (1000 Lbs)		P <sub>Q</sub> (1000 Lbs)	K <sub>Q</sub> (Ksi √in.)	K <sub>Ic</sub> (Ksi √in.)	
								At Surface "a <sub>1</sub> "	At 1/4 Point "a <sub>2</sub> "	At Centerline "a <sub>3</sub> "	At 1/4 Point "a <sub>4</sub> "	At Surface "a <sub>5</sub> "					AVG. CRACK LENGTH, (a <sub>2</sub> + a <sub>3</sub> + a <sub>4</sub> ) / 3 (inch)				
SENT	TTR-10	0.402	0.750	2.50	24.2	0.06	116,000	0.348	0.352	0.354	0.352	0.348	0.353	Air	72	10.0	10.19	6.40	57.5	---	B < 2.5 (K <sub>Q</sub> /σ <sub>ys</sub> ) <sup>2</sup>
-	TTR-20	0.404	0.751	-	27.9	-	78,000	0.380	0.380	0.380	0.380	0.380	0.380	Air	72	10.0	---	5.92	61.4	---	
-	TTN-10	0.402	0.746	-	22.9	-	123,000	0.340	0.362	0.366	0.362	0.346	0.363	LN <sub>2</sub>	-320	10.0	9.16	8.80	84.7	---	K <sub>Ic</sub> /E > 0.0012 in <sup>1/2</sup>
-	TTN-20	0.401	0.748	-	27.5	-	82,000	0.366	0.374	0.380	0.378	0.370	0.377	LN <sub>2</sub>	-320	10.0	6.43	6.00	62.4	---	
-	TTTH-10	0.400	0.751	-	32.0	-	62,000	0.400	0.404	0.404	0.404	0.404	0.404	LH <sub>2</sub>	-423	5.0	5.92	5.70	69.0	---	K <sub>Ic</sub> /E > 0.0012 in <sup>1/2</sup>
SENT	TTH-20	0.401	0.751	2.50	31.2	0.06	81,000	0.398	0.400	0.400	0.400	0.400	0.400	LH <sub>2</sub>	-423	5.0	5.95	5.72	67.6	---	
SENB	TBR-10	0.402	0.750	3.00	17.4	0.06	104,000	0.408	0.408	0.408	0.408	0.392	0.408	Air	72	3.0	2.30	1.60	55.6	---	B < 2.5 (K <sub>Q</sub> /σ <sub>ys</sub> ) <sup>2</sup>
-	TBR-20	0.401	0.749	-	22.8	-	26,000	0.380	0.394	0.398	0.396	0.376	0.396	Air	72	3.0	2.36	1.68	54.8	---	
-	TBN-10	0.404	0.752	-	22.6	-	12,000	0.380	0.390	0.394	0.390	0.380	0.391	LN <sub>2</sub>	-320	3.0	1.83	1.83	58.3	---	Valid K <sub>Ic</sub> Numbers
-	TBN-20	0.399	0.750	-	24.3	-	10,000	0.400	0.404	0.404	0.404	0.402	0.404	LN <sub>2</sub>	-320	3.0	1.87	1.87	65.1	---	
-	TBH-10	0.401	0.750	-	16.5	-	38,000	0.380	0.396	0.396	0.396	0.392	0.396	LH <sub>2</sub>	-423	2.0	1.94	1.85	---	60.8	B < 2.5 (K <sub>Q</sub> /σ <sub>ys</sub> ) <sup>2</sup>
SENB	TBH-20	0.400	0.751	3.00	15.4	0.06	40,000	0.366	0.378	0.386	0.384	0.370	0.383	LH <sub>2</sub>	-423	2.0	2.27	2.20	---	67.9	
CT	TCR-10	0.402	0.592	0.718	33.7	0.06	19,000	0.346	0.350	0.352	0.344	0.282	0.349	Air	72	3.0	2.55	1.81	72.5	---	B < 2.5 (K <sub>Q</sub> /σ <sub>ys</sub> ) <sup>2</sup>
-	TCR-20	0.399	0.602	0.722	22.3	-	20,000	0.278	0.290	0.292	0.288	0.268	0.290	Air	72	3.0	2.63	1.66	48.8	---	
-	TCN-10	0.401	0.602	0.722	23.2	-	42,000	0.278	0.290	0.302	0.296	0.282	0.296	LN <sub>2</sub>	-320	3.0	2.38	2.38	71.8	---	B < 2.5 (K <sub>Q</sub> /σ <sub>ys</sub> ) <sup>2</sup>
-	TCN-20	0.399	0.602	0.722	22.3	-	35,000	0.266	0.286	0.290	0.290	0.282	0.291	LN <sub>2</sub>	-320	3.0	2.41	2.27	66.9	---	
-	TCH-10	0.398	0.599	0.719	24.0	-	48,000	0.292	0.300	0.302	0.298	0.280	0.300	LH <sub>2</sub>	-423	3.0	2.66	2.62	82.0	---	K <sub>Ic</sub> /E > 0.0012 in <sup>1/2</sup>
CT	TCH-20	0.401	0.602	0.722	25.2	0.06	43,000	0.280	0.288	0.288	0.288	0.280	0.288	LH <sub>2</sub>	-423	3.0	2.49	2.35	68.1	---	

Table 6-4: FRACTURE TOUGHNESS TEST RESULTS FOR 2219-T87 ALUMINUM  
(SF Specimens)

SPECIMEN				CRACK DETAILS							TEST CONDITIONS			RESULTS		
TYPE	IDENTIFICATION	THICKNESS, $t$ (Inch)	WIDTH, $W$ (Inch)	$(K_{Ic})_{max}$ (Ksi $\sqrt{In.}$ )	$(K_{Ic})_{min}/(K_{Ic})_{max}$	NUMBER OF CYCLES TO GROW CRACK IN THOUSANDS	CRACK DEPTH, $a$ (Inch)	CRACK LENGTH, $2c$ (Inch)	$a/2c$	$a/t$	ENVIRONMENT	TEMPERATURE (deg F)	LOADING RATE (1000 Lbs/Min)	GROSS SECTION FAILURE STRESS (Ksi)	GROSS STRESS YIELD STRESS	$K_{Ic}$ (Ksi $\sqrt{In.}$ ) *
SURFACE FLAWED	A-5	1.097	6.00	12.4	0.06	5.0	0.532	1.360	0.391	0.488	AIR	72	230	33.6	0.61	34.7
	A-6	1.094	5.99	12.5	0.06	5.0	0.545	1.390	0.392	0.498	AIR	72	230	33.8	0.61	35.1
	A-7	1.094	6.00	12.0	0.06	7.0	0.366	1.475	0.248	0.335	AIR	72	230	36.9	0.67	37.0
	A-8	1.096	6.01	12.1	0.06	8.0	0.360	1.485	0.242	0.328	AIR	72	230	37.5	0.68	37.7
	A-1	1.102	6.01	12.4	0.06	4.0	0.539	1.370	0.393	0.489	LN <sub>2</sub>	-320	240	37.4	0.55	38.6
	A-2	1.098	6.00	12.4	0.06	5.0	0.540	1.370	0.394	0.492	LN <sub>2</sub>	-320	240	34.8	0.51	35.9
	A-3	1.102	6.01	12.0	0.06	8.0	0.368	1.480	0.249	0.334	LN <sub>2</sub>	-320	240	39.5	0.58	39.6
	A-4	1.100	6.01	11.9	0.06	6.5	0.360	1.480	0.243	0.327	LN <sub>2</sub>	-320	240	38.6	0.57	38.3
	A-9	1.002	5.00	12.0	0.06	5.5	0.480	1.285	0.375	0.479	LH <sub>2</sub>	-423	220	42.5	0.58	42.5
	A-10	1.000	5.01	12.0	0.06	5.0	0.480	1.285	0.374	0.475	LH <sub>2</sub>	-423	220	43.2	0.59	43.1
	A-11	1.004	5.00	11.3	0.06	7.0	0.313	1.310	0.240	0.309	LH <sub>2</sub>	-423	220	47.0	0.64	44.3
	A-12	1.004	5.00	11.3	0.06	6.0	0.305	1.310	0.236	0.304	LH <sub>2</sub>	-423	220	48.7	0.67	45.9

$$* K_{Ic} = 1.1 \sqrt{\pi} \sigma \sqrt{a/Q}$$

Table 6-5: FRACTURE TOUGHNESS TEST RESULTS FOR 5Al-2.5Sn(ELI) TITANIUM  
(SF Specimens)

SPECIMEN				CRACK DETAILS							TEST CONDITIONS			RESULTS		
TYPE	IDENTIFICATION	THICKNESS, $t$ (Inch)	WIDTH, $W$ (Inch)	$(K_{Ic})_{max}$ (Ksi $\sqrt{In.}$ )	$(K_{Ic})_{min}/(K_{Ic})_{max}$	NUMBER OF CYCLES TO GROW CRACK IN THOUSANDS	CRACK DEPTH, $a$ (Inch)	CRACK LENGTH, $2c$ (Inch)	$a/2c$	$a/t$	ENVIRONMENT	TEMPERATURE (deg F)	LOADING RATE (1000 Lbs/Min)	GROSS SECTION FAILURE STRESS (Ksi)	GROSS STRESS YIELD STRESS	$K_{Ic}$ (Ksi $\sqrt{In.}$ ) *
SURFACE FLAWED	TT-1	0.379	2.50	18.8	0.06	7.0	0.180	0.455	0.396	0.475	LN <sub>2</sub>	-320	140	153.0	0.88	93.3
	TT-2	0.375	2.50	19.6	0.06	3.0	0.177	0.470	0.377	0.472	LN <sub>2</sub>	-320	140	147.1	0.85	96.2
	TT-3	0.377	2.50	19.7	0.06	4.0	0.149	0.580	0.257	0.395	LN <sub>2</sub>	-320	140	145.4	0.84	95.8
	TT-4	0.374	2.50	19.3	0.06	5.0	0.143	0.575	0.249	0.383	LN <sub>2</sub>	-320	140	142.5	0.82	91.5
	TT-5	0.375	2.50	17.3	0.06	7.0	0.146	0.440	0.332	0.389	LH <sub>2</sub>	-423	110	125.5	0.67	72.5
	TT-6	0.377	2.50	17.3	0.06	3.0	0.166	0.450	0.367	0.440	LH <sub>2</sub>	-423	110	117.0	0.63	---
	TT-7	0.376	2.50	20.3	0.06	7.0	0.149	0.615	0.242	0.396	LH <sub>2</sub>	-423	110	108.8	0.58	73.6
	TT-8	0.376	2.50	18.6	0.06	2.0	0.140	0.565	0.248	0.372	LH <sub>2</sub>	-423	110	114.0	0.61	70.5

**Table 6-6: RESULTS FOR FRACTURE TESTS OF 2219-T87 ALUMINUM  
SURFACE-FLAWED SPECIMENS TESTED AT 72°F IN ROOM AIR  
(Specimen Thickness & Flaw Shape Varied)**

CONFIGURATION (See Figure 6-7)	IDENTIFICATION	SPECIMEN				CRACK DETAILS				LOADING RATE (1,000 psi/min)	GROSS SECTION FAILURE STRESS (Ksi)	$K_{Gr} = 1.1 \sqrt{\pi} \sigma \sqrt{a/Q}$ (ksi√in.)
		LENGTH, L (Inch)	GAGE LENGTH, G (Inch)	GAGE WIDTH, W (Inch)	GAGE THICKNESS, T (Inch)	$(K_I)_{max}$ (Ksi √in.)	NUMBER OF CYCLES TO GROW CRACK IN THOUSANDS	CRACK DEPTH, a (Inch)	CRACK LENGTH, 2c (Inch)			
B	2A1R-1	24.0	8.0	10.00	0.750	10.4	7.0	0.284	2.89	40	38.1	38.6
B	2A1R-2	↑	↑	10.00	0.743	10.7	11.0	0.300	2.89	↑	42.8*	46.1*
B	2A3R-1	↑	↑	7.00	0.752	10.0	14.0	0.360	1.44	↑	41.6	41.9
B	2A3R-2	↑	↑	7.00	0.752	10.1	15.0	0.370	1.44	↑	42.1	42.7
B	1A1R-1	↓	↓	7.00	0.502	9.1	35.0	0.220	1.93	↓	44.3	40.6
B	1A1R-2	24.0	8.0	7.00	0.505	8.7	24.0	0.195	1.93	40	45.7	40.2
A	1A3R-1	16.0	6.0	3.49	0.498	8.3	15.0	0.250	0.96	50	46.0	38.5
A	1A3R-2	↑	↑	3.50	0.493	8.3	14.0	0.240	0.95	↑	46.6	38.6
C	6A1R-1	↑	↑	3.50	0.250	10.5	2.0	0.109	0.98	↑	50.4	33.3
C	6A1R-2	↑	↑	3.50	0.248	9.0	13.0	0.102	0.99	↑	51.9	33.6
A	6A3R-1	↑	↑	2.50	0.248	7.2	9.0	0.118	0.49	↑	53.3	31.9
A	6A3R-2	↑	↑	2.50	0.251	7.1	15.0	0.118	0.49	↑	53.0	31.8
C	3A1R-1	↑	↑	3.00	0.117	5.6	5.0	0.084	0.84	↑	45.3	—
C	3A1R-2	↑	↑	3.00	0.126	5.7	23.0	0.088	0.84	↑	45.4	—
A	3A3R-1	↓	↓	2.50	0.126	6.6	9.0	0.100	0.42	↓	50.5	—
A	3A3R-2	16.0	6.0	2.50	0.130	6.5	9.0	0.100	0.41	50	50.9	—

\*DELAMINATION

**Table 6-7: RESULTS FOR FRACTURE TESTS OF 2219-T87 ALUMINUM  
SURFACE-FLAWED SPECIMENS TESTED AT -320°F IN LN<sub>2</sub>  
(Specimen Thickness & Flaw Shape Varied)**

CONFIGURATION (See Figure 6-7)	IDENTIFICATION	SPECIMEN				CRACK DETAILS				LOADING RATE (1,000 psi/min)	GROSS SECTION FAILURE STRESS (Ksi)	$K_{Gr} = 1.1 \sqrt{\pi} \sigma \sqrt{a/Q}$ (ksi√in.)
		LENGTH, L (Inch)	GAGE LENGTH, G (Inch)	GAGE WIDTH, W (Inch)	GAGE THICKNESS, T (Inch)	$(K_I)_{max}$ (Ksi √in.)	NUMBER OF CYCLES TO GROW CRACK IN THOUSANDS	CRACK DEPTH, a (Inch)	CRACK LENGTH, 2c (Inch)			
B	2A1N-1	24.0	8.0	10.00	0.750	10.3	8.5	0.290	2.89	40	37.2	38.5
B	2A1N-2	↑	↑	10.00	0.750	10.4	8.5	0.290	2.89	↑	40.4	42.0
B	2A3N-1	↑	↑	7.00	0.753	10.1	14.0	0.380	1.44	↑	43.4	43.8
B	2A3N-2	↑	↑	7.00	0.749	10.1	14.0	0.380	1.44	↑	42.4	42.7
B	1A1N-1	↑	↑	7.00	0.500	8.8	28.0	0.208	1.92	↑	45.1	39.8
B	1A1N-2	24.0	8.0	7.00	0.499	8.8	23.0	0.204	1.92	40	46.6	39.9
A	1A3N-1	16.0	6.0	3.50	0.494	8.3	13.0	0.244	0.95	50	52.4	43.4
A	1A3N-2	↑	↑	3.50	0.494	8.3	13.0	0.240	0.95	↑	53.9	44.6
C	6A1N-1	↑	↑	3.50	0.247	9.1	11.0	0.106	0.96	↑	57.5	37.3
C	6A1N-2	↑	↑	3.50	0.250	9.1	15.0	0.104	0.97	↑	59.3	38.4
A	6A3N-1	↑	↑	2.50	0.246	7.3	12.0	0.127	0.50	↑	61.3	37.4
A	6A3N-2	↑	↑	2.50	0.250	7.3	13.0	0.128	0.49	↑	61.9	37.7
C	3A1N-1	↑	↑	3.00	0.128	5.6	15.0	0.084	0.84	↑	52.5	—
C	3A1N-2	↑	↑	3.00	0.126	5.4	17.0	0.088	0.84	↑	52.3	—
A	3A3N-1	↓	↓	2.50	0.129	6.6	9.0	0.100	0.42	↓	59.2	—
A	3A3N-2	16.0	6.0	2.50	0.128	6.6	9.0	0.101	0.42	50	59.1	—

**Table 6-8: RESULTS FOR FRACTURE TESTS OF 2219-T87 ALUMINUM SURFACE-FLAWED SPECIMENS TESTED AT -423°F IN LH<sub>2</sub> (Specimen Thickness & Flaw Shape Varied)**

SPECIMEN						CRACK DETAILS				LOADING RATE (1,000 psi/min)	GROSS SECTION FAILURE STRESS (Ksi)	$K_{IC} = 1.1 \sqrt{\pi \sigma \sqrt{a/Q}}$ (Ksi√in.)
CONFIGURATION (See Figure 6-7)	IDENTIFICATION	LENGTH, L (Inch)	GAGE LENGTH, G (Inch)	GAGE WIDTH, W (Inch)	GAGE THICKNESS, T (Inch)	$(K_{IC})_{max}$ (Ksi√in.)	NUMBER OF CYCLES TO GROW CRACK IN THOUSANDS	CRACK DEPTH, a (Inch)	CRACK LENGTH, 2c (Inch)			
B	2A1H-1	24.0	8.0	10.00	0.744	10.3	8.0	0.288	2.88	40	42.5	44.1
B	2A1H-2	↑	↑	10.00	0.747	10.4	9.5	0.296	2.88	↑	39.3	41.0
B	2A3H-1	↑	↑	7.00	0.750	10.1	15.0	0.378	1.44	↑	46.7	47.2
B	2A3H-2	↑	↑	7.00	0.751	10.1	14.0	0.384	1.44	↑	46.6	47.2
B	1A1H-1	↓	↓	7.00	0.503	8.8	23.0	0.204	1.90	↓	51.3	45.2
B	1A1H-2	24.0	8.0	7.00	0.504	8.8	20.0	0.210	1.92	40	46.9	41.5
A	1A3H-1	16.0	6.0	3.49	0.497	8.2	15.0	0.244	0.96	50	53.0	43.9
A	1A3H-2	↑	↑	3.50	0.497	8.2	14.0	0.240	0.96	↑	54.9	45.4
C	6A1H-1	↑	↑	3.50	0.246	9.2	14.0	0.112	0.97	↑	60.6	40.2
C	6A1H-2	↑	↑	3.50	0.250	9.1	15.0	0.108	0.99	↑	59.2	38.7
A	6A3H-1	↑	↑	2.50	0.248	7.1	14.0	0.120	0.49	↑	64.3	38.6
A	6A3H-2	↑	↑	2.50	0.253	7.2	14.0	0.122	0.49	↑	66.1	40.0
C	3A1H-1	↑	↑	3.00	0.125	5.5	18.5	0.090	0.85	↑	54.1	—
C	3A1H-2	↑	↑	3.00	0.128	5.3	20.0	0.086	0.85	↑	53.2	—
A	3A3H-1	↓	↓	2.50	0.128	6.6	11.0	0.103	0.42	↓	61.8	—
A	3A3H-2	16.0	6.0	2.50	0.129	6.6	10.0	0.105	0.42	50	60.8	—

**Table 6-9: RESULTS FOR FRACTURE TESTS OF MILL ANNEALED 5Al-2.5 Sn (ELI) TITANIUM SURFACE-FLAWED SPECIMENS TESTED AT -320°F IN LN<sub>2</sub> (Specimen Thickness & Flaw Shape Varied)**

SPECIMEN						CRACK DETAILS				LOADING RATE (1,000 psi/min)	GROSS SECTION FAILURE STRESS (Ksi)	$K_{IC} = 1.1 \sqrt{\pi \sigma \sqrt{a/Q}}$ (Ksi√in.)
CONFIGURATION (See Figure 6-7)	IDENTIFICATION	LENGTH, L (Inch)	GAGE LENGTH, G (Inch)	GAGE WIDTH, W (Inch)	GAGE THICKNESS, T (Inch)	$(K_{IC})_{max}$ (Ksi√in.)	NUMBER OF CYCLES TO GROW CRACK IN THOUSANDS	CRACK DEPTH, a (Inch)	CRACK LENGTH, 2c (Inch)			
A	2T3N-1	16.0	5.0	2.50	0.279	19.2	5.0	0.150	0.56	140	134.6	85.9
A	2T3N-2	↑	↑	2.50	0.276	19.0	3.0	0.132	0.56	140	158.5	100.2
A	1T3N-1	↑	↑	2.50	0.178	15.3	28.0	0.086	0.35	170	165.4	83.9
A	1T1N-1	↑	↑	2.50	0.180	17.3	21.0	0.082	0.71	170	170.3	98.1
A	1T1N-2	↓	↓	2.50	0.178	19.0	13.0	0.070	0.70	170	170.4	92.3
A	6T1N-1	16.0	5.0	2.50	0.092	12.4	22.0	0.040	0.38	175	180.0	74.1

Table 6-10: RESULTS FOR FRACTURE TESTS OF RE-ANNEALED 5Al-2.5 Sn (ELI)  
TITANIUM SURFACE-FLAWED SPECIMENS TESTED AT -320°F IN LN<sub>2</sub>  
(Specimen Thickness & Flaw Shape Varied)

SPECIMEN						CRACK DETAILS				LOADING RATE (1,000 psi/min)	GROSS SECTION FAILURE STRESS (ksi)	$K_{IC} = 1.1\sqrt{\pi a}\sqrt{a/Q}$ (ksi√in.)
CONFIGURATION (See Figure 6-7)	IDENTIFICATION	LENGTH, L (Inch)	GAGE LENGTH, G (Inch)	GAGE WIDTH, W (Inch)	GAGE THICKNESS, T (Inch)	$(K_{IC})_{max}$ (Ksi √in.)	NUMBER OF CYCLES TO GROW CRACK IN THOUSANDS	CRACK DEPTH, a (Inch)	CRACK LENGTH, 2c (Inch)			
A	2T3N-1A	16.0	5.0	2.50	0.280	21.6	4.0	0.131	0.55	140	135.0	83.3
A	2T3N-2A	↑	↑	2.50	0.277	21.6	3.5	0.126	0.56	140	141.4	87.2
A	6T1N-2			2.50	0.090	13.0	4.0	0.032	0.36	175	171.8	63.8
A	6T3N-1			2.50	0.088	12.8	6.0	0.042	0.18	175	176.6	64.2
A	6T3N-2			2.50	0.090	12.7	11.0	0.042	0.18	175	176.7	64.2
A	3T1N-1			2.50	0.046	12.4	5.0	0.031	0.31	150	150.6	—
A	3T1N-2			2.49	0.049	12.3	4.0	0.030	0.32	150	158.2	—
A	3T3N-1			2.49	0.043	11.6	2.0	0.035	0.15	150	163.4	—
A	3T3N-2	16.0	5.0	2.50	0.051	11.6	4.0	0.035	0.15	150	169.4	—

Table 6-11: RESULTS FOR FRACTURE TESTS OF RE-ANNEALED 5Al-2.5 Sn (ELI)  
TITANIUM SURFACE-FLAWED SPECIMENS TESTED AT -423°F IN LH<sub>2</sub>  
(Specimen Thickness & Flaw Shape Varied)

SPECIMEN						CRACK DETAILS				LOADING RATE (1,000 psi/min)	GROSS SECTION FAILURE STRESS (Ksi)	$K_{IC} = 1.1\sqrt{\pi a}\sqrt{a/Q}$ (ksi√in.)
CONFIGURATION (See Figure 6-7)	IDENTIFICATION	LENGTH, L (Inch)	GAGE LENGTH, G (Inch)	GAGE WIDTH, W (Inch)	GAGE THICKNESS, T (Inch)	$(K_{IC})_{max}$ (Ksi √in.)	NUMBER OF CYCLES TO GROW CRACK IN THOUSANDS	CRACK DEPTH, a (Inch)	CRACK LENGTH, 2c (Inch)			
A	2T1H-1	16.0	5.0	2.50	0.127	14.4	15.0	0.044	0.47	150	143.9	59.7
A	2T1H-2	↑	↑	2.50	0.123	14.6	8.0	0.045	0.47	150	152.2	64.7
A	2T3H-1			2.50	0.122	14.0	7.0	0.053	0.24	150	155.1	62.3
A	2T3H-2			2.50	0.122	14.1	9.5	0.056	0.24	150	150.9	61.3
A	1T1H-1			2.50	0.085	12.3	5.0	0.031	0.32	175	166.7	59.1
A	1T1H-2			2.50	0.080	12.1	4.0	0.030	0.33	175	165.8	58.1
A	1T3H-1			2.50	0.078	11.9	4.0	0.037	0.17	175	185.0	63.8
A	1T3H-2			2.50	0.079	11.9	4.0	0.037	0.17	175	181.5	62.4
A	6T1H-1			2.49	0.040	9.0	17.0	0.016	0.16	190	186.0	48.1
A	6T1H-2			2.49	0.040	8.9	13.0	0.016	0.16	190	187.3	48.6
A	6T3H-1			2.50	0.043	8.6	21.0	0.020	0.08	190	190.4	46.7
A	6T3H-2			2.50	0.042	8.6	28.0	0.020	0.08	190	191.3	46.9
A	3T1H-1			2.49	0.020	8.3	4.0	0.014	0.14	175	175.7	—
A	3T1H-2			2.50	0.021	7.7	8.0	0.012	0.13	175	178.7	—
A	3T3H-1			2.50	0.024	7.7	15.0	0.015	0.07	190	193.7	—
A	3T3H-2	16.0	5.0	2.49	0.019	7.7	19.0	0.015	0.07	190	185.9	—

**Table 7-1: TEST PROGRAM FOR EVALUATING RESIDUAL STRESS EFFECTS  
IN 5Al-2.5Sn (ELI) TITANIUM**

Test Series	Flaw Location and Orientation	Flaw Geometry		Test Temp (°F)	Residual Stress Level		
		Type	Depth Thickness (a/t)		Reference + Tensile	Reference	Reference + Compressive
I	Weld $\perp$ : Flaw Plane II to Longitudinal Weld Axis	Surface Flaw	0.25	-320	2	2	2
			0.50		2	2	2
II	Parent Metal Flaw Plane $\perp$ to Rolling Direction	Surface Flaw	0.25	-320	2	2	2
			0.50		2	2	2
III	Weldment: Flaw Plane $\perp$ to Longitudinal Weld Axis	Surface Flaw	0.25	-320	2	2	2
			0.50		2	2	2

Note: Numbers Indicate Duplicate Tests

**Table 7-2: TEST PROGRAM FOR EVALUATING RESIDUAL STRESS EFFECTS  
IN 2219-T87 ALUMINUM**

Test Series	Flaw Location And Orientation	Flaw Geometry		Test Temp (°F)	Residual Stress Level		
		Type	Depth Thickness (a/t)		Reference + Tensile	Reference	Reference + Compressive
I	Weld $\perp$ : Flaw Plane II to Longitudinal Weld Axis	Surface Flaw	0.6	-320	2	2	2
II	Parent Metal Flaw Plane $\perp$ to Transverse Direction	Surface Flaw	0.6	-320	2	2	2
III	Weld $\perp$ : Flaw Plane II to Longitudinal Weld Axis	Internal Flaw	0.3	-320	3	3	3



Table 7-3: TEST PROGRAM FOR EVALUATING RESIDUAL STRESS EFFECTS  
ON CYCLIC FLAW GROWTH RATES

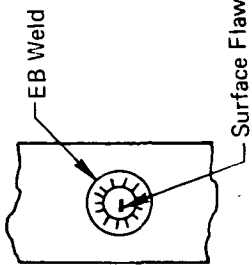
Specimen Configuration	Alloy	Number of Tests		
		72°F	-320°F	-423°F
	2219-T87 Aluminum	3	3	3
	5Al-2.5Sn (ELI) Titanium	3	3	3

Table 7-4: TEST RESULTS FOR 5Al-2.5Sn (ELI) TITANIUM RESIDUAL STRESS TEST SERIES I

SPECIMEN			TEST DETAILS					RESULTS						
Number	Thickness, T (inches)	Width, W (inches)	Temperature (°F)	Flaw Depth, a (inches)	Flaw Width, 2c (inches)	Flaw Shape, a/2c	Flaw Depth-to-Thickness Ratio, a/T	Gross Failure Stress, $\sigma_p$ (ksi)	Net Failure Stress (ksi)	Approximate Residual Stress, $\sigma_R$ (ksi)	Flaw Size, a/Q (inches)	$K_{IR}^*$ ( $\text{ksi} \sqrt{\text{in.}}$ )	$K_{IP}^{**}$ ( $\text{ksi} \sqrt{\text{in.}}$ )	$K_{cr} = K_{IR} + K_{IP}$ ( $\text{ksi} \sqrt{\text{in.}}$ )
RR-1	0.223	3.01	-320	0.076	0.392	0.20	0.34	179.7	186.2	2	0.069	1.1	99.5	100.6
RR-2	0.234	3.00	-320	0.074	0.394	0.19	0.32	175.7	181.6	2	0.068	1.1	96.0	97.1
RR-3	0.222	4.00	-320	0.135	0.705	0.19	0.61	117.4	128.2	2	0.114	2.0	111.4	113.4
RR-4	0.226	4.00	-320	0.138	0.705	0.20	0.61	118.3	129.2	2	0.116	2.0	113.2	115.2
RT-1	0.226	4.00	-320	0.079	0.394	0.20	0.35	158.8	163.2	19	0.070	10.7	89.4	100.1
RT-2	0.238	4.00	-320	0.081	0.398	0.20	0.34	157.7	162.0	19	0.072	10.7	89.0	99.7
RT-3	0.234	4.00	-320	0.143	0.710	0.20	0.61	102.8	112.4	19	0.115	18.1	97.8	115.9
RT-4	0.242	4.00	-320	0.132	0.705	0.19	0.55	101.7	110.0	19	0.109	16.1	86.4	102.5
RC-1	0.236	5.50	-320	0.076	0.410	0.19	0.32	175.5	178.8	-28	0.070	-15.6	97.5	81.9
RC-2	0.234	6.00	-320	0.075	0.396	0.19	0.32	183.8	1	-28	0.069	-15.7	103.6	87.9
RC-3	0.237	6.01	-320	0.142	0.740	0.19	0.60	158.0	167.7	-28	0.124	-27.3	154.0	126.7
RC-4	0.232	6.01	-320	0.128	0.728	0.18	0.55	158.3	167.0	-28	0.116	-25.9	146.5	120.5

$$* K_{IR} = 1.1 \sqrt{\pi} \sigma_R \sqrt{a/Q} \cdot M_K$$

$$** K_{IP} = 1.1 \sqrt{\pi} \sigma_P \sqrt{a/Q} \cdot M_K$$

1 Failed in Grip

Table 7-5: TEST RESULTS FOR 5Al-2.5Sn (ELI) TITANIUM RESIDUAL STRESS TEST SERIES II

SPECIMEN			TEST DETAILS					RESULTS						
Number	Thickness, T (inches)	Width, W (inches)	Temperature (°F)	Flaw Depth, a (inches)	Flaw Width, 2c (inches)	Flaw Shape, a/2c	Flaw Depth-to- Thickness Ratio, a/T	Gross Failure Stress, $\sigma_p$ (ksi)	Net Failure Stress (ksi)	Approximate Residual Stress, $\sigma_R$ (ksi)	Flaw Size, a/Q (inches)	$K_{IR}^*$ (ksi $\sqrt{\text{in.}}$ )	$K_{IP}^{**}$ (ksi $\sqrt{\text{in.}}$ )	$K_{IR}^{cr} = K_{IR} + K_{IP}$ (ksi $\sqrt{\text{in.}}$ )
RMR-1	0.260	3.00	-320	0.072	0.390	0.19	0.28	174.4	179.4	2	0.067	1.1	92.4	93.5
RMR-2	0.256	3.00	-320	0.074	0.390	0.19	0.29	174.5	179.3	2	0.068	1.1	93.2	94.3
RMR-3	0.248	4.00	-320	0.140	0.710	0.20	0.57	101.9	110.6	2	0.114	1.8	92.0	93.8
RMR-4	0.255	4.00	-320	0.142	0.700	0.20	0.56	118.7	128.5	2	0.116	1.9	107.3	109.2
RMT-1	0.250	4.00	-320	0.080	0.388	0.21	0.32	151.7	155.5	19	0.068	10.3	82.7	93.0
RMT-2	0.253	4.00	-320	0.081	0.392	0.21	0.32	153.4	157.3	19	0.070	10.5	84.8	95.3
RMT-3	0.257	4.00	-320	0.136	0.725	0.19	0.53	94.6	103.3	19	0.111	16.3	81.1	97.4
RMT-4	0.252	4.00	-320	0.124	0.668	0.19	0.49	122.8	130.9	19	0.106	15.0	96.8	111.8
RMC-1	0.221	6.00	-320	0.070	0.395	0.18	0.32	183.9	187.0	-28	0.067	-15.1	99.4	84.3
RMC-2	0.245	6.00	-320	0.084	0.420	0.20	0.34	178.5	182.0	-28	0.076	-16.2	103.7	87.5
RMC-3	0.260	6.00	-320	0.128	0.700	0.18	0.49	161.2	168.8	-28	0.118	-23.6	136.2	112.6
RMC-4	0.257	6.00	-320	0.119	0.690	0.17	0.46	163.2	170.3	-28	0.112	-22.3	129.7	107.4

$$* K_{IR} = 1.1 \sqrt{\pi} \sigma_R \sqrt{a/Q} \cdot M_K$$

$$** K_{IP} = 1.1 \sqrt{\pi} \sigma_P \sqrt{a/Q} \cdot M_K$$

Table 7-6: TEST RESULTS FOR 5AI-2.5Sn (ELI) TITANIUM RESIDUAL STRESS TEST SERIES III

SPECIMEN			TEST DETAILS					RESULTS				
Number	Thickness, T (inches)	Width, W (inches)	Temperature (°F)	Flaw Depth, a (inches)	Flaw Width, 2c (inches)	Flaw Shape, a/2c	Flaw Depth-to-Thickness Ratio, a/T	Gross Failure Stress, $\sigma_p$ (ksi)	Net Failure Stress (ksi)	Approximate Residual Stress, $\sigma_R$ (ksi)	Flaw Size, a/Q (inches)	$K_{cr}^*$ (ksi $\sqrt{\text{in.}}$ )
RLT-1	0.255	3.01	-320	0.073	0.406	0.18	0.29	169.9	175.2	70	0.067	—
RLT-2	0.249	3.01	-320	0.071	0.402	0.18	0.29	169.4	174.6	70	0.066	—
RLT-3	0.249	4.00	-320	0.100	0.478	0.21	0.40	140.3	145.8	70	0.082	—
RLT-4	0.245	4.00	-320	0.106	0.480	0.22	0.43	130.1	135.6	70	0.083	—
RLR-1	0.247	3.01	-320	0.068	0.384	0.18	0.28	126.9	130.5	24	0.058	74.5
RLR-2	0.248	3.01	-320	0.069	0.390	0.18	0.28	122.0	125.6	24	0.059	72.5
RLR-3	0.253	4.00	-320	0.113	0.478	0.24	0.45	94.4	98.5	24	0.083	77.1
RLR-4	0.251	4.00	-320	0.115	0.480	0.24	0.45	93.7	98.0	24	0.083	76.6
RLC-1	0.255	3.00	-320	0.076	0.396	0.19	0.30	172.4	177.9	0	0.068	93.0
RLC-2	0.247	3.00	-320	0.076	0.396	0.19	0.30	172.5	178.2	0	0.068	93.1
RLC-3	0.241	4.00	-320	0.117	0.396	0.30	0.49	140.7	147.4	0	0.079	87.9
RLC-4	0.255	4.00	-320	0.118	0.396	0.30	0.46	143.0	149.5	0	0.079	89.3

$$* K_{cr} = 1.1 \sqrt{\pi (\sigma_p + \sigma_R)} \sqrt{a/Q} \cdot M_K$$

Table 7-7: FRACTURE TEST RESULTS FOR 5Al-2.5Sn (ELI) TITANIUM GTA WELD CENTERLINES SUBJECTED TO VARIOUS THERMAL CYCLES

SPECIMEN					CRACK DETAILS				TEST CONDITIONS			RESULTS			
Type	Identification	Thickness (in.)	Width (in.)	Length (in.)	Thermal Processing	(Kt) max.	(Kt) max./ (Kt) min.	No. of Fatigue Cycles to Grow Crack (1,000's)	Crack Length (in.)	Environment	Temperature (°F)	Loading Rate (1,000 lb/min)	Failure Load (lb)	P <sub>Q</sub> (1,000 lb)	K <sub>Q</sub> (ksi $\sqrt{\text{in.}}$ )
						ksi $\sqrt{\text{in.}}$									
Single Edge Notched Tension	TX-1	0.234	1.254	3.75	None (AW)	30	0.06	37	0.570	LN <sub>2</sub>	-320	6	8,180	7,700	86.5
	TX-2	0.234	1.253	3.75	None (AW)	30	0.06	50	0.585	LN <sub>2</sub>	-320	6	7,180	6,000	71.1
	TX-3	0.234	1.254	3.75	AW + 1,000°F - 4 hr.	30	0.06	27	0.570	LN <sub>2</sub>	-320	6	5,060	4,750	53.6
	TX-4	0.236	1.256	3.75	AW + 1,000°F - 4 hr.	30	0.06	20	0.580	LN <sub>2</sub>	-320	6	5,000	5,000	58.0
	TX-5	0.233	1.254	3.75	AW + 1,300°F - 1 hr.	30	0.06	15	0.595	LN <sub>2</sub>	-320	6	5,980	5,600	69.0
	TX-6	0.235	1.256	3.75	AW + 1,300°F - 1 hr.	30	0.06	15	0.590	LN <sub>2</sub>	-320	6	6,060	5,800	68.9

Table 7-8: RESULTS FOR 2219-T87 ALUMINUM RESIDUAL STRESS TEST SERIES I  
(Surface-Flawed Specimens Fractured at -320°F in LN<sub>2</sub>)

SPECIMEN			SURFACE FLAW DETAILS					Residual Stress Level	Gross Failure Stress, $\sigma_p$ (ksi)	$\frac{\sigma_p}{\sigma_{ys}}$
Number	Thickness, T (inches)	Width, W (inches)	Location	Depth, a (inches)	Width, 2c (inches)	Shape, a/2c	Depth-to-Thickness Ratio, a/T			
RASR-1	0.899	7.81	↑	0.38	1.93	0.20	0.42	↑	25.0	1.00
RASR-2	0.897	7.81		0.39	1.93	0.20	0.43	As Welded	27.3	1.10
RASR-3	0.894	7.80		0.61	2.52	0.24	0.68	(AW)	23.5	0.95
RASR-4	0.898	7.81		0.61	2.52	0.24	0.68	↑	23.0	0.93
RAST-1	0.898	7.80		0.38	1.93	0.20	0.42	↑	24.4	0.98
RAST-2	0.898	7.81	Weld	0.38	1.93	0.20	0.42	AW	24.3	0.98
RAST-3	0.899	7.81	℄	0.58	2.52	0.23	0.64	Tensile	22.4	0.90
RAST-4	0.898	7.80		0.58	2.52	0.23	0.65	↑	21.9	0.88
RASC-1	0.898	7.81		0.42	1.92	0.22	0.47	↑	28.3	1.14
RASC-2	0.897	7.80		0.40	1.93	0.21	0.45	AW	27.4	1.10
RASC-3	0.891	7.80		0.67	2.54	0.26	0.75	Compressive	23.0	0.93
RASC-4	0.892	7.81	↑	0.61	2.52	0.24	0.58	↑	23.5	0.95

Table 7-9: RESULTS FOR 2219-T87 ALUMINUM RESIDUAL STRESS TEST SERIES II  
(Surface-Flawed Specimens Fractured at -320°F in LN<sub>2</sub>)

SPECIMEN			SURFACE FLAW DETAILS					Residual Stress Level	Gross Failure Stress, $\sigma_p$ (ksi)	$\frac{\sigma_p}{\sigma_{ys}}$
Number	Thickness, T (inches)	Width, W (inches)	Location	Depth, a (inches)	Width, 2c (inches)	Shape, a/2c	Depth-to-Thickness Ratio, a/T			
RAR-1	0.603	8.00	↑ Base Metal	0.42	2.22	0.19	0.58	As Rolled (AR)	32.3	0.49
RAR-2	0.597	8.00		0.42	2.22	0.19	0.38		32.0	0.49
RAT-1	0.302	8.00	↑ Base Metal	0.41	2.00	0.21	0.70	AR + Tension	41.3	0.63
RAT-2	0.306	8.00		0.41	2.19	0.19	0.70		41.0	0.62
RAC-1	0.301	8.00	↑	0.42	2.22	0.19	0.70	AR + Compressive	33.1	0.50
RAC-2	0.301	8.00		0.42	2.23	0.19	0.70		34.5	0.52

Table 7-10: RESULTS FOR 2219-T87 ALUMINUM RESIDUAL STRESS TEST SERIES III  
(Internally Flawed Welds Fractured at  $-320^{\circ}\text{F}$  in  $\text{LN}_2$ )

SPECIMEN			FLAW DETAILS			Residual Stress Level	Gross Failure Stress, $\sigma_p$ (ksi)	Net Section Failure Stress, $\sigma_N$ (ksi)	$\frac{\sigma_N}{\sigma_{ys}}$
Number	Thickness, T (inches)	Width, W (inches)	Location	Depth, $2a$ (inches)	Depth-to-Thickness Ratio, $a/T$				
1	0.93	10.00	←	0.53	0.68	As Welded	25.4	33.6	1.35
2	0.93	10.00		0.53	0.68	(AW)	23.8	31.7	1.28
5	0.93	10.00		0.61	0.66		24.4	32.2	1.30
3	0.94	10.00	Weld	0.50	0.64	AW	24.6	33.0	1.33
4	0.94	10.00	→	0.60	0.64	Compressive	24.4	32.7	1.32
6	0.93	10.00		0.63	0.68		24.8	33.5	1.35
7	0.92	10.00		0.53	0.68	AW	18.0	24.2	0.98
8	0.93	10.00		0.60	0.65	Tension	20.4	26.9	1.08
9	0.92	10.00	→	0.52	0.58		20.0	26.8	1.08

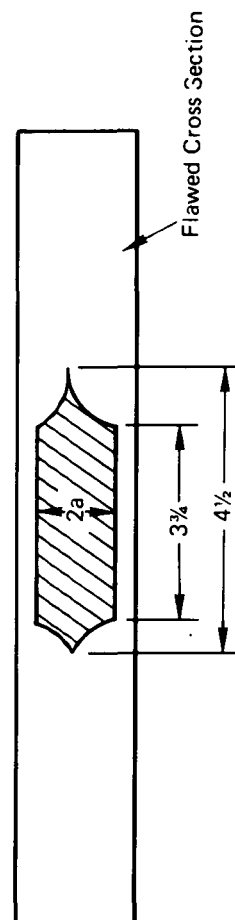




Table 7-11: RESULTS FOR CYCLIC TESTS OF 5Al-2.5Sn (ELI) TITANIUM SPECIMENS CONTAINING RESIDUAL STRESSES

Specimen			Test Conditions				Initial Flaw Parameters			Final Flaw Parameters			Applied Loading Cycles	Notes
Number	Thickness (in.)	Width (in.)	Medium	Loading Profile	Peak Cyclic Stress (ksi)	Approximate Residual Stress (ksi)	Depth, $a_i$ (in.)	Width, (2c) <sub>i</sub> (in.)	K <sub>I</sub> <sub>i</sub> <sup>b</sup> (ksi in.)	Depth, $a_f$ (in.)	Width, 2c <sub>f</sub> (in.)	K <sub>I</sub> <sub>f</sub> <sup>b</sup> (ksi in.)		
-1	0.258	4.00	Amb Air	Sinusoidal 0-100-0	80.0	19	0.084	0.42	55.4	0.156	0.51	80.8	1,000	a Could not be Determined b $K_{I1} = 1.95 (\sigma_R + \sigma_P) \times \sqrt{(a/Q)}$ M <sub>K</sub>
-2	0.258	4.00			75.0	19	0.080	0.41	50.7	0.140	0.43	65.3	1,000	
-3	0.258	4.00			70.0	19	0.070	0.40	44.6	0.102	0.41	53.2	1,000	
-4	0.258	4.00	LN <sub>2</sub>	Sinusoidal 0-100-0	100.0	19	0.072	0.40	60.2	a	a	—	357	
-5	0.252	4.00			100.0	19	0.065	0.38	57.2	a	a	—	438	
-6	0.256	4.00			90.0	19	0.079	0.40	56.6	a	a	—	704	
-7	0.256	3.99	LH <sub>2</sub>	Sinusoidal 0-100-0	71.0	19	0.073	0.39	44.4	a	a	—	928	
-8	0.254	3.99			71.0	19	0.080	0.41	46.7	a	a	—	549	
-9	0.257	3.99			71.0	19	0.065	0.39	42.0	a	a	—	384	

Table 7-12: EVALUATION OF CYCLIC FLAW GROWTH DATA FOR 5Al-2.5Sn (ELI)  
TITANIUM SURFACE-FLAWED SPECIMENS CONTAINING RESIDUAL STRESSES

Data Source	Specimen No.	Temp/Env (°F)	K <sub>IE</sub> (ksi in.)	C* (σ <sub>o</sub> = 100 ksi)	Notes
Table 7-11	-1	72/Air	120 <sup>a</sup>	1.7 x 10 <sup>-12</sup>	a Estimated Using Data From Ref 1 and 15
	-2			1.1 x 10 <sup>-12</sup>	
	-3			1.2 x 10 <sup>-12</sup>	
	-4	-320/LN <sub>2</sub>	94 <sup>b</sup>	2.9 x 10 <sup>-12</sup>	b From Table 7-5 c From Figure 6-21
	-5			3.1 x 10 <sup>-12</sup>	
	-6			1.6 x 10 <sup>-12</sup>	
Reference 1	-7	-423/LH <sub>2</sub>	62 <sup>c</sup>	2.9 x 10 <sup>-12</sup>	
	-8			3.9 x 10 <sup>-12</sup>	
	-9			9.1 x 10 <sup>-12</sup>	
		72/Air	120	6.7 x 10 <sup>-12</sup>	
		-320/LN <sub>2</sub>	61	5.8 x 10 <sup>-12</sup>	
		-423/LH <sub>2</sub>	50	20.0 x 10 <sup>-12</sup>	

$$* \frac{d}{dN} (a/Q) = C(\sigma_o/\sigma)^2 \left(1 + \frac{K_{min}}{\Delta K}\right)^m (\Delta K)^4 \left(1 - \frac{K_{max}}{K_{IE}}\right)^{-0.2}$$

Table 7-13: RESULTS FOR CYCLIC TESTS OF 2219-T87 ALUMINUM SPECIMENS CONTAINING RESIDUAL STRESSES

Specimen			Test Conditions				Initial Flaw Parameters			Final Flaw Parameters			Applied Loading Cycles	Notes
Number	Thickness (in.)	Width (in.)	Medium	Loading Profile	Peak Cyclic Stress (ksi)	Approximate Residual Stress (ksi)	Depth, $a_i$ (in.)	Width, $2c_i$ (in.)	$K_{II} \sqrt{in.}$	Depth, $a_f$ (in.)	Width, $2c_f$ (in.)	$K_{IF}$ in. ksi		
-1	0.61	7.98	Amb Air	Sinusoidal 0-100-0	42.0	+	0.244	0.96	-	-	-	-	0 <sup>a</sup>	a Specimen Failed at Circular Eb Weld ( $P_{cr} = 203$ kips) b Specimen Delaminated No Depthwise Growth c Growth Inhibited by Delaminations
-5	0.60	7.98			41.0	+	0.254	0.94	-	-	-	-	20 <sup>b</sup>	
-6	0.59	7.98			38.0	+	0.248	0.94	-	-	-	-	317 <sup>b</sup>	
-2	0.61	7.98	LN <sub>2</sub>	Sinusoidal 0-100-0	41.0	+	0.240	0.94	-	0.38	1.42	-	342	
-3	0.61	7.98			41.0	+	0.238	0.97	-	0.35 <sup>c</sup>	1.75	-	1,097	
-4	0.61	7.98			41.0	+	0.244	0.94	-	0.38 <sup>c</sup>	1.80	-	755	

DISTRIBUTION LIST FOR FINAL REPORT NASA CR-72659  
CONTRACT NAS 3-12016

INVESTIGATION OF FLAW GEOMETRY AND LOADING EFFECTS  
ON PLANE STRAIN FRACTURE IN METALLIC STRUCTURES

THE BOEING COMPANY  
Seattle, Washington

<u>RECIPIENT (R)</u>	<u>DESIGNEE (D)</u>	<u>COPIES TO</u>
		<u>R      D</u>
NASA-Lewis Research Center		
Attn: Contracting Officer, MS 500-313		1
Liquid Rocket Technology Branch, MS 500-209		1
Technical Report Control Office, MS 5-5		1
Technology Utilization Office, MS 3-16		1
AFSC Liaison Office, MS 501-3		1
Library, MS 60-3		1
Office of Reliability & Quality Assurance		1
MS 500-111		
D. L. Nored, Chief, LRTB, MS 500-209		1
G. T. Smith, Project Manager, MS 49-1		18
R. H. Kemp, MS 49-1		1
W. F. Brown, Jr., MS 105-1		1
2100 Brookpart Road		
Cleveland, Ohio 44135		
National Aeronautics & Space Administration		
Attn: RPX/Chief, Liquid Experimental Engineering		1
KT/Technology Utilization Office		1
R-1/M B. Ames, Jr.		1
MTG/J. G. Malament		1
MHE/N G. Peil		1
RWM/J. J. Gangler		1
RWS/D. A. Gilstead		1
Library		1
Washington, D.C. 20546		
NASA Scientific & Technical Information Facility		1
Attn: NASA Representative		
P.O. Box 33		
College Park, MD 20740		

<u>RECIPIENT (R)</u>	<u>DESIGNEE (D)</u>	<u>COPIES TO</u>	
		<u>R</u>	<u>D</u>
NASA-Marshall Space Flight Center			
Attn: S&E-ASTN-AA/C. Lifer		1	
S&E-ASTN-ASR/C. Crockett		1	
S&E-ASTN-AS/H. Coldwater		1	
Marshall Space Flight Center, AL 35812			
NASA Scientific & Technical Information Facility		6	
P.O. Box 33			
College Park, MD 20740			
NASA-Ames Research Center		1	
Attn: Library	Hans M. Mark		
Moffett Field, CA 94035	Mission Analysis Div.		
NASA-Flight Research Center		1	
Attn: Library			
P.O. Box 273			
Edwards, CA 93523			
NASA-Goddard Space Flight Center	Merland L. Moseson,	1	
Attn: Library	Code 620		
Greenbelt, MD 20771			
NASA-John F. Kennedy Space Center	Dr. Kurt H. Debus	1	
Attn: Library			
Kennedy Space Center, FL 32931			
NASA-Langley Research Center	E. Cortright	1	
Attn: Library	R. W. Leonard		
Hampton, VA 23365	H. Hardrath		
NASA-Manned Spacecraft Center	R. E. Johnson	1	
Attn: Library	L. St. Leger		
Houston, TX 77001			
NASA-Marshall Space Flight Center	Hans G. Paul	1	
Attn: Library	Leon J. Hastings		
Huntsville, AL 35812	James Thomas		
	Dale Burrows		
	I. G. Yates		
	Clyde Nevins		
	J. Blumrich		
Jet Propulsion Laboratory	Joe Lewis	1	
Attn: Library			
4800 Oak Grove Drive			
Pasadena, CA 91103			
Defense Documentation Center		1	
Attn: TISIA			
Cameron Station, Building 5			
5010 Duke Street			
Alexandria, VA 22314			

<u>RECIPIENT (R)</u>	<u>DESIGNEE (D)</u>	<u>COPIES TO</u>	
		<u>R</u>	<u>D</u>
Commanding Officer U.S. Army Research Office (Durham) Attn: Library Box CM, Duke Station Durham, NC 27706		1	
U.S. Army Missile Command Attn: Document Section Redstone Scientific Information Center Redstone Arsenal, AL 35808	Dr. W. Wharton	1	
Arnold Engineering Development Center Attn: Library Air Force Systems Comman Tallahona, TN 37389	R. H. K. Doetsch	1	
Aeronautical Systems Division Air Force Systems Command Attn: Library Wright-Patterson Air Force Base, Ohio 45433	C. F. Tiffany D. L. Schmidt, Code ARSCNC-2	1	
Air Force Systems Command Andrews Air Force Base Attn: Library Washington, D.C. 20332	Capt. S. W. Bowen, SCLT	1	
Air Force Rocket Propulsion Laboratory (RPM) Attn: Library Edwards, CA 93523		1	
Air Force Office of Scientific Research Attn: Library Washington, D.C. 20333	Dr. J. F. Masi, SREP	1	
Director (Code 6180) U.S. Naval Research Laboratory Attn: Library Washington, D.C. 20390	H. W. Carhart J. M. Krafft	1	
Air Force Aero Propulsion Laboratory Research. & Technology Division Air Force Systems Comman United States Air Force Attn: APRP (Library) Wright-Patterson Air Force Base, Ohio 45433	R. Quigley C. M. Donaldson	1	
Aerojet Liquid Rocket Company Attn: Technical Library 2484-2015A P.O. Box 15847 Sacramento, Cal. 95813	R. Stiff	1	
Aeronutronic Division of Philco Ford Corp. Attn: Technical Information Department Ford Road Newport Beach, CA 92663	Dr. L. H. L	1	

<u>RECIPIENT (R)</u>	<u>DESIGNEE (D)</u>	<u>COPIES TO</u>	
		<u>R</u>	<u>D</u>
Aerospace Corporation Attn: Library-Documents 2400 E. El Segundo Blvd. Los Angeles, CA 90045	J. G. Wilder	1	
Bell Aerosystems, Inc. Attn: Library Box 1 Buffalo, NY 14240	T. Reinhardt W. M. Smith	1	
Instruments & Life Support Division Bendix Corporation Attn: Library P.O. Box 4508 Davenport, IA 52808	W. M. Carlson	1	
Chemical Propulsion Information Agency Applied Physics Laboratory 8621 Georgia Avenue Silver Springs, MD 20910	Tom Reedy	1	
Chrysler Corporation Missile Division Attn: Library P.O. Box 2628 Detroit, MI	John Gates	1	
Chrysler Corporation Space Division Attn: Library P.O. Box 29200 New Orleans, LA 70129		1	
University of Denver Denver Research Institute Attn: Security Office P.O. Box 10127 Denver, CO 80210		1	
Republic Aviation Fairchild Hiller Corporation Farmington, Long Island, NY		1	
General Dynamics/Convair Aerospace Attn: Library P.O. Box 1128 San Diego, CA 92112	Jack Jensen W. Witzel	1	
Missiles and Space Systems Center General Electric Company Valley Forge Space Technology Center Attn: Library P.O. Box 8555 Philadelphia, Penn. 19101	A. Cohen F. Schultz	1	
Grumman Aircraft Engineering Corporation Attn: Library Bethpage, Long Island, NY	Joseph Gavin W. Ludwig	1	

RECIPIENT (R)	DESIGNEE (D)	COPIES TO	
		R	D
IIT Research Institute Technology Center Attn: Library Chicago, Ill. 60616	C. K. Hersh	1	
Ling-Temco-Vought Corporation Attn: Library P.O. Box 5907 Dallas, Tex. 75222		1	
Lockheed Missiles and Space Company Attn: Library P.O. Box 504 Sunnyvale, CA 94087	R. E. Lewis	1	
Stanford Research Institute Attn: Library 3333 Ravenswood Avenue Menlo Park, CA 94025	Dr. Gerald Marksman	1	
TRW Systems Inc. Attn: Tech. Lib. Doc. Acquisitions One Space Park Redondo Beach, CA 90278		1	
TRW TAPCO Division 23555 Euclid Avenue Cleveland, Ohio 44117	P. T. Angell E. A. Stigerwald	1	
United Aircraft Corporation Corporate Library Attn: Library 400 Main Street East Hartford, Conn. 06108	Dr. David Rix Erle Martin Frank Owen Wm. E. Taylor	1	
United Aircraft Corporation Pratt & Whitney Division Florida Research & Development Center Attn: Library P.O. Box 2691 West Palm Beach, Fl. 33402	R. J. Coar Dr. Schmitke	1	
Western Division McDonnell Douglas Astronautics Attn: Library 5301 Bolsa Avenue Huntington Beach, Cal. 92647	B. V. Whiteson R. Rowe	1	
McDonnell Douglas Aircraft Corporation Attn: Library P.O. Box 516 Lambert Field, MO 63166	R. A. Herzmark	1	



RECIPIENT (R)	DESIGNEE (D)	COPIES TO	
		R	D
Rocketdyne Division North American Rockwell Inc. Attn: Library, Department 596-306 6633 Canoga Avenue Canoga Park, CA 91304	Dr. R. J. Thompson S. F. Iacobellis	1	
Space & Information Systems Division North American Rockwell Inc. Attn: Library 12214 Lakewood Blvd. Downey, Cal.	J. Colipriest	1	
Northrop Space Laboratories Attn: Library 3401 West Broadway Hawthorne, CA	Dr. William Howard	1	
Purdue University Attn: Library (Technical). Lafayette, Ind. 47907	Dr. Bruce Reese	1	
Vought Astronautics Attn: Library Box 5907 Dallas, Tex.		1	
Wright-Patterson Air Force Base Attn: AFFML Wright-Patterson Air Force Base, Ohio 45433		1	
Wright-Patterson Air Force Base Attn: AFDL Wright-Patterson Air Force Base, Ohio 45433	R. E. Headrick (Code MANE)	1	
Department of the Army U.S. Army Material Command Attn: AMCRD-RC Washington, D.C. 20315		1	
Bureau of Naval Weapons Department of the Navy Attn: RRRE-6 Washington, D.C. 20360		1	
Commander U.S. Naval Ordnance Laboratory Attn: Library White Oak Silver Springs, Md. 20910		1	
Sandia Corporation Attn: H. E. Montgomery Sandia Base Albuquerque, N.M. 87115		1	

<u>RECIPIENT (R)</u>	<u>DESIGNEE (D)</u>	<u>COPIES TO</u>	
		<u>R</u>	<u>D</u>
Thiokol Chemical Corporation Wasatch Division Attn: Library Section P.O. Box 524 Brigham City, Utah 84302		1	
Brunswick Corporation Defense Products Division Attn: J. Carter P.O. Box 4594 43000 Industrial Avenue Lincoln, Neb. 68504		1	
Carnegie Institute of Technology Department of Civil Engineering Attn: Library Pittsburgh, Penn. 15213		1	
Westinghouse Research Laboratories Attn: Library Beulah Road, Churchill Borough Pittsburgh, Penn. 15235	W. K. Wilson G. T. Wessel	1	
Frankford Arsenal Attn: 1320, Library Philadelphia, Penn. 19137	Carl Carman	1	
Cornell University Department of Materials Science & Engineering Attn: Library Ithaca, N.Y. 14850	H. H. Johnson	1	
Director Special Projects Office Department of the Navy Washington, D.C. 20360		1	
New York University Attn: Library University Heights New York, N.Y.		1	
General Dynamics Attn: Library P.O. Box 748 Fort Worth, Tex. 76101	D. E. Westerheide	1	
Brunswick Corporation Defense Products Division Attn: Library P.O. Box 4594 43000 Industrial Avenue Lincoln, Neb.	J. Carter	1	

RECIPIENT (R)	DESIGNEE (D)	COPIES TO	
		R	D
Garrett Corporation Airesearch Division Attn: Library Phoenix, Ariz. 85036		1	
Brown University Attn: Technical Library Providence, R.I.	Dr. P. F. Maeder Dr. J. R. Rice	1	
Case Western Reserve University Attn: Technical Library 10090 Euclid Avenue Cleveland, Ohio 44115		1	
Pennsylvania State University Attn: Library State College, Penn.		1	
California Institute of Technology Attn: Library (Technical) Pasadena, Cal.		1	
Massachusetts Institute of Technology Attn: Library Cambridge, Mass.		1	
Atomic Energy Commission Division of Reactor Development & Technology Washington, D.C. 20767	N. Grossman		1
Naval Ship Research & Development Center Annapolis Division Annapolis, Md. 21402	W. V. Smith		1
U.S. Army Aviation Materials Lab Ft. Eustis, Va. 23604	J. N. Danials SAVFE-AS		1
U.S. Army Engineering R & D Labs Gas Turbine Test Facility Fort Belvoir, Va. 22060	W. Crim		1
Battelle Memorial Institute Attn: Library 505 King Avenue Columbus, Ohio 43201	Dr. Halbert Dr. G. Hahn C. Federson	1	1
Franklin Institute Research Labs Attn: Library Benjamin Franklin Parkway Philadelphia, Penn. 19103	J. Rumbarger	1	1
National Science Foundation Engineering Division Attn: Library 1800 G. Street, N.W. Washington, D.C. 20540		1	

<u>RECIPIENT (R)</u>	<u>DESIGNEE (D)</u>	COPIES TO	
		<u>R</u>	<u>D</u>
Naval Ship Research and Development Center Code 526 Washington, D.C. 20007	Dr. W. B. Morgan	1	
AEC-NASA Space Nuclear Propulsion Office, NPO NASA Headquarters Germantown, Md.	F. C. Schwenk N. J. Gerstein	1	1